Chapter 5

Magnetic Data and Interpretation

5.1 Introduction

Magnetic data are important in constraining marine geophysical models in continental margin environments due to the fundamentally different magnetic signature of continental and oceanic crust. Their greatest importance, however, is in dating oceanic crust through the identification of seafloor spreading anomalies and the correlation of these anomalies to the geomagnetic time-scale (e.g. Vine & Matthews [1963]). Identification of seafloor spreading anomalies on the Wilkes Land sector of the Antarctic margin, however, is difficult, primarily because of the slow and variable spreading rates at the South-East Indian Ridge (SEIR) between Australia and Antarctica prior to the onset of fast spreading in the Eocene [Cande & Mutter, 1982; Tikku & Cande, 1999].

A slow mid-ocean ridge spreading rate causes several normal and reverse polarity periods to occur in a spatially limited area. This results in the complex superposition of anomalies associated with each switch from normal to reverse field polarity. The anomaly sequence between breakup and the Eocene on the Antarctic and southern Australian margins is difficult to model and interpret. Hence, a number of questions remain regarding the identification of the oldest seafloor spreading anomaly on the Antarctic margin. Recent studies on the conjugate southern Australian margin indicate that anomaly 33o[1] represents breakup at 83 Ma [Sayers *et al.*, 2001]. This interpretation, however, conflicts with previous interpretations by Tikku & Cande [1999], Veevers [1986], and other workers as discussed below.

Magnetic data were acquired along each multi-channel seismic (MCS) line of surveys GA-228 and GA-229. An *Elsec 7706* proton precession magnetometer was utilised throughout surveying. Both total magnetic field and magnetic anomaly values (calculated using IGRF2000 [IAGA, 2000]) were provided by the geophysical contractor. The data have been filtered using a three point de-spiking and interpolation process to smooth

[1] subscripts o and y refer respectively to the old and young edges of the normal polarity period of an individual geomagnetic chron. Normal polarity periods are indicated by the subscript n, e.g. 33n refers to the entire normal polarity period of Chron 33.

irregular 'drop-outs', but have not been diurnally corrected. Accordingly, temporal magnetic field variations as well as remanent and induced magnetisations are included in the total magnetic field measurements.

Marine geophysical surveys in the Southern Ocean have been acquiring magnetic data since the 1950's. Although not as thoroughly surveyed as other ocean regions there is relatively good data coverage between the SEIR (which runs approximately east-west at 50°S) and 60°S. However, south of 60°S the coverage is much sparser. This is particularly unfortunate given that this is the region of most ambiguous seafloor spreading anomaly identification. All data used in this study are corrected to IGRF2000 [IAGA, 2000] to assure uniformity in anomaly calculation. Data are projected onto a north-south azimuth to allow consistent comparison. This orientation was chosen as it is approximately orthogonal to the trend of the SEIR between the Australian and Antarctic Plates.

The acquisition of ∼10,000 km of magnetic anomaly data along the Wilkes Land margin represents a major increase in available data in this region. The early spreading history of Wilkes Land and southern Australia, based on previously available data, remains uncertain (e.g. Tikku & Cande [1999]). Hence, spreading rate modelling was undertaken to constrain the identification of seafloor spreading anomalies in GA-228 and GA-229 data and investigate the timing of breakup between Antarctica and Australia.

5.2 Magnetic Modelling

Introduction

Magnetic modelling is crucial in the testing of seafloor spreading models, and therefore in dating sections of oceanic crust. As a potential field method it can not provide a unique solution as there are infinite source distributions possible for any given magnetic anomaly data. However, it remains a means of testing geologically reasonable hypotheses and constraining important variables, namely spreading rate and age of oceanic crust.

The magnetism of the rocks that comprise the Earth's crust is highly variable and can be acquired in a variety of ways. Magnetisation can be transient (i.e. dependent upon the presence of an ambient magnetic field), this is known as induced magnetisation. It can also be permanent (i.e. unaffected by changes in ambient field strength), this is known as remanent magnetisation. The relative importance of these two types of magnetisation is primarily a function of the local geological environment, e.g. rock type, cooling history, grain-size, metamorphic/alteration history.

When placed in a magnetic field, rocks and sediments may become magnetised by induction, a result of dipoles aligning under the presence of an ambient field. The dipole

moment per unit volume is defined as the induced magnetisation (J_i), this quantity is proportional to the strength of the ambient field (F). The constant of proportionality is defined as the magnetic susceptibility (k) such that,

$$J_i = kF$$

Susceptibilities of common minerals vary significantly, from -0.0001 (quartz) to 6 (magnetite) SI units, depending on their proportional content of paramagnetic, diamagnetic, ferromagnetic and ferrimagnetic material. Studies of induced rock magnetism primarily consider induced magnetisation of ferrimagnetic mineral grains [Dunlop, 1995].

The magnetism of the Earth's crust is largely controlled by ferrimagnetic mineral distribution. There are two such important mineral groups; the titanomagnetite series and pyrhhotite. In most rocks, particularly oceanic basalts, titanomagnetites are the primary source of magnetisation (e.g. Smith & Banerjee [1986]). Titanomagnetites exhibit a continuous solid solution between the *Fe* rich endmember (magnetite) and the *Ti* rich endmember (ulvöspinel) [Blanchard *et al.*, 1976]. The susceptibility of common rocks tends to be proportional to magnetite content and typically decreases with decreasing grain size [Stacey, 1967; Kent & Gee, 1994].

As magnetite and other ferrimagnetic minerals cool to below the Curie temperature (T_c) a large proportion of magnetic domains come to have moments which are aligned in the ambient field direction. This produces a permanent natural or Thermal Remanent Magnetisation (TRM) that persists in the absence of any external field. Many rocks with high titanomagnetite content, such as oceanic crust basalts, acquire a remanent magnetisation (J_r) as they cool. However, as oceanic crust ages, layer 2 basalts are altered and their magnetisation is reduced, although a record of the geomagnetic field is retained [Kent & Gee, 1994].

Total magnetisation (J) (i.e. the quantity measured by total field magnetometers) is the sum of induced and remanent magnetisation,

$$J = J_i + J_r$$

the induced and remanent components are both vectors and must be added accordingly. The magnitude J controls anomaly amplitude and its direction controls the anomaly shape. The ratio of the *magnitude* of J_r to J_i (i.e. J_r/J_i) is defined as the Königsberger ratio (Q).

Linear magnetic anomalies in oceanic crust that record seafloor spreading (e.g. Vine & Matthews [1963]) result almost entirely from TRM. Induced magnetisation associated with the present-day ambient geomagnetic field is also present, but the Königsberger ratio of oceanic crust tends to be large [Dunlop, 1995]. The fine grain size of titanomagnetites

in oceanic crust, resulting from initial quenching and later surface oxidation, inhibits any motion of magnetic domains within the crystal lattice and, therefore inhibits induced magnetisation. Hence, only remanent magnetisation is usually taken into account in analysis of magnetic anomalies in ocean basins.

Gee *et al.* [1989] investigated the contribution of induced magnetisation at seamounts and concluded that although remanent magnetisation is dominant, up to one-sixth of the total magnetisation may be accounted for by induced magnetisation. It is difficult to determine any departures from the assumptions regarding Königsberger ratios in oceanic basalts at passive margins as no drill-holes have as yet penetrated deeply into oceanic crust beneath thick marginal sediments. Therefore, at continental margins and other environments possibly affected by hydrothermal alteration and structural deformation, the relative contribution of remanent and induced components is less certain than in deep ocean basins.

5.2.1 Previous Work

The most detailed study of magnetic anomalies in the southeast Indian Ocean was undertaken by Weissel & Hayes [1972]. Weissel & Hayes [1971] and Weissel & Hayes [1972] divided the region south of Australia into three longitudinal zones on the basis of contrasts in magnetic, morphologic, and seismologic parameters (Figure 5.1). They investigated asymmetry in spreading, the effect of variable palaeoinclinations, and magnetic anomaly amplitude variations. Weissel & Hayes [1972] noted distinct amplitude differences among,

1. magnetic anomalies of different ages,
2. magnetic lineations of the same age but located on opposing ridge flanks, and
3. magnetic anomalies of the same age and on the same ridge flank but from the different longitudinal zones.

The oldest magnetic anomaly sequence identified by Weissel & Hayes [1972] was 19-21, with *"perhaps an indication of anomaly 22"* in the Great Australian Bight and near the Antarctic continent. Hence, they interpreted Australia-Antarctic separation to have occurred in the Early Eocene (53 Ma), based on the Heirtzler *et al.* [1968] geomagnetic reversal time scale. However, a relative paucity of data on the Antarctic margin forced interpretations of Weissel & Hayes [1972] to include unconstrained interpolations of great distance (>150 km) between shiptrack data.

The lineation identified as anomaly 22 by Weissel & Hayes [1972] does not lie adjacent to the coast on either the southern Australian or Antarctic margin, due to the presence of Magnetic Quiet Zones (MQZ) [Weissel & Hayes, 1972]. The spreading rate model of Weissel & Hayes [1972], for their zone A (128-138°E), is shown in Figure 5.2. Variable

Figure 5.1: Shiptrack magnetic anomaly data utilised by Weissel & Hayes [1971]. Zones A-C are divided on the basis of magnetic, morphologic, and seismologic properties. Earthquake epicentres are indicated by black dots.

half spreading rates of between 22 mm/yr and 38 mm/yr were interpreted based on this model. The fit between the observed and modelled profiles is good from the spreading centre to approximately anomaly 18. Spreading rate differs by only 2 mm/yr for north and south flanks (faster to the south) after anomaly 5 time. From anomaly 5 to anomaly 13 time, modelled spreading rates are faster to the north by between 5 mm/yr and 9 mm/yr. Spreading rates prior to anomaly 13 are, again, almost the same on both flanks.

A number of problems associated with the breakup age interpreted by Weissel & Hayes [1972] were noted in the mid-late 1970s and early 1980s. Boeuf & Doust [1975] and Denham & Brown [1976] interpreted foreset bedding in seismic reflection data in Upper Cretaceous strata, and suggested that they indicate the development of a marine depositional environment prior to the early Tertiary. Willcox [1978] also interpreted seismic reflection data to indicate Lower Cretaceous sediments overlying purported Eocene aged oceanic crust. König [1980] noted that the model of Weissel & Hayes [1972] did not explain the presence of a distinct, laterally extensive magnetic anomaly between anomalies interpreted as 20 and 21 by Weissel & Hayes [1972].

In particular, Cande & Mutter [1982] questioned aspects of the identification of anomaly 22 south of Australia and the fit of the model and observed data for the older

Figure 5.2: Spreading rate model of Weissel & Hayes [1972] and two-dimensional synthetic magnetic anomalies for zone A computed for selected sequences of anomalies. Representative observed profiles (indicated by arrows) shown for comparison with synthetic profiles. Note that spreading rates are in cm/yr.

part of the anomaly sequence (anomalies 19-22). On re-examination of the magnetic anomaly pattern, Cande & Mutter [1982] concluded that anomalies 19-22 were better modelled as anomalies 20-34 using a variable spreading rate, Figure 5.3. Accordingly, Cande & Mutter [1982] interpreted that breakup occurred between 86-110 Ma, during the Cretaceous Long Normal Polarity epoch (KLNP), based on the Heirtzler *et al.* [1968] geomagnetic reversal time scale. The anomaly sequence interpreted by Weissel & Hayes [1972] subsequent to anomaly 18n time was accepted by Cande & Mutter [1982].

Although the revised interpretation of the magnetic anomaly sequence suggested that breakup occurred at or before anomaly 34 time, the actual age of breakup remained uncertain. Due to the presence of the broad MQZ, of enigmatic origin, the age of breakup was difficult to estimate [Cande & Mutter, 1982]. Two alternative age constraints were suggested by Cande & Mutter [1982] based on two different geological scenarios:

1. *"If the MQZ is floored by subsided continental crust or perhaps remnants of the original pre-breakup rift valley, and if the basement high at its southern side marks the ocean/continent boundary , then we date the age of this boundary as approximately 90*

m.y. B.P. by extrapolating beyond anomaly 34 using a spreading rate of 4.5 mm/yr."

2. If the MQZ is formed in part by seafloor spreading during the Cretaceous long normal polarity period (KLNP) then *"the age of breakup could be anywhere between 112 m.y. (the age of M0) and 90 m.y."*.

The revised anomaly identifications and seafloor spreading model of Cande & Mutter [1982] included an interval of slow-spreading from 90-43 Ma. They cite the correlation of the boundaries of this period with times of global plate reorganisations, as a possible catalyst for significant spreading rate changes.

Modelling by Cande & Mutter [1982] indicated that anomalies that had been interpreted as anomalies 20-22 closely resembled a very slow spreading rate (4.5 mm/yr) model of anomalies 21-34. The key to this model was that each anomaly corresponds to the combined effect of several polarity reversals. A comparison of the models of Weissel & Hayes [1972] and Cande & Mutter [1982] is shown in Figure 5.3.

Figure 5.3: Spreading rate models of Weissel & Hayes [1972] and Cande & Mutter [1982] and two-dimensional synthetic magnetic anomalies computed for the sequence of anomalies older than 13n. Observed profiles from surveys Eltanin 37 and Eltanin 41 are shown for comparison. Model B is the preferred model of Cande & Mutter [1982]. Figure after Cande & Mutter [1982].

Geologically, there was no conclusive evidence contraindicating the interpretation of Cande & Mutter [1982]. The *"breakup unconformity"* interpreted by Falvey [1974] in the Otway Basin was reinterpreted by Cande & Mutter [1982] as an unconformity associated

with a eustatic sea level change. They correlate the unconformity with a lowering of eustatic sea level at the base Tertiary as inferred by both Vail *et al.* [1977] and Pitman [1978].

Veevers [1986] accepted the major points of the Cande & Mutter [1982] model but believed it was possible to further constrain the broad breakup age implied by the limits of the KLNP, 86-112 Ma. Veevers [1986] reinterpreted the positive magnetic anomaly that marks the oceanward edge of the MQZ, interpreted previously as anomaly 22 by Weissel & Hayes [1972] and anomaly 34 by Cande & Mutter [1982], as an edge-effect, caused by magnetic oceanic crust abutting essentially non-magnetic continental crust (i.e. the COB). Based on this interpretation of the COB location, consistently approximately 45 km landwards of anomaly 34y, and a spreading half-rate of 4.5 mm/yr, Veevers [1986] interpreted the age of breakup as 96 Ma. This age was *"...rounded to 95±5 Ma to account for uncertainties in the initial rate of spreading and the exact location of the COB"*.

The notion of a mid-Cretaceous breakup age persisted throughout the 1990s and was used ubiquitously as a basis for interpretation. Tikku & Cande [1999] reinvigorated the debate over the age of breakup for Australia-Antarctica and refined further the spreading rate model for the southeast Indian Ridge since initial separation. Reconstructions based on the revised anomaly identifications of Tikku & Cande [1999] also encountered problems involving large amounts of continental overlap involving the South Tasman Rise (STR), Tasmania, and Victoria Land (Antarctica). They offered two alternative hypotheses to account for this overlap:

1. Continental extension and/or deformation of oceanic crust in the Australia-Antarctic Basin, or

2. That magnetic anomalies older than anomaly 31 in the Australia-Antarctic Basin are not isochrons.

Tikku & Cande [1999] question the validity of the suggestion by Veevers [1986] that the seaward edge of the MQZ is the COB anomaly, since it is unclear that this distinctive magnetic anomaly is associated directly with the COB for the entire span of the Australia Antarctic Basin (AAB). Tikku & Cande [1999] also introduce a new spreading rate model, based on Cande & Mutter [1982], of the SEIR for the Late Cretaceous to early Tertiary. The major departure from the earlier model of Cande & Mutter [1982] is the introduction of a period of *"ultra-slow spreading"* (∼1.5 mm/yr) between anomaly 31o and 24o time. The inclusion of this period further improved the fit of the modelled and observed magnetic anomaly profiles. The Tikku & Cande [1999] model includes a continental edge-effect at 95 Ma, similar to that modelled by Veevers [1986], however, they do not necessarily suggest that this is representative of the COB.

Reconstructions carried out by Tikku & Cande [1999], based on their revised anomaly

and rotation interpretation, provides two particularly important indications:

1. The quiet zone boundary (QZB) anomaly is not an isochron as its rotation pole is inconsistent with those of later spreading anomalies.

2. That reconstructions using rotation poles based on anomalies 34y, 33o, and 32y result in continental overlap between Tasmania and the western STR.

Tikku & Cande [1999] suggest a number of possibilities to explain these problems:

1. The western STR is incorrectly located in recent reconstructions (e.g. Royer & Rollet [1997]).

2. There may have been substantial northeast-southwest extension in the Bass Strait region or in the conjugate area of Wilkes and Victoria Land since 80 Ma. It is also possible, though difficult to assess, that the required extension may have occurred in the poorly known Wilkes Land interior basins.

3. Like the QZB anomaly it is possible that anomalies 32y, 33o and 34y are not isochrons.

The most recent geophysical and geological interpretation of data from the southern margin of Australia, [Sayers *et al.*, 2001] further revised the Australia-Antarctica breakup age. Sayers *et al.* [2001] identify a 50-120 km continent-ocean transition (COT) zone in the Great Australian Bight using recently acquired deep seismic reflection, and gravity and magnetic data. The COT is characterised by a thin apron of post-breakup sediments overlying complexly deformed sediments and intruded crust that is bounded landward by a basement ridge and seawards by rugged basement, interpreted as oceanic crust. The COT is interpreted to be floored by extended continental lithosphere and accordingly the COB is defined between the COT and oceanic crust, the model proposed by Sayers *et al.* [2001] is shown in Figure 5.4.

In the model of Sayers *et al.* [2001], the COB is located seaward of anomaly 34y and just landward of anomaly 33o as interpreted by Tikku & Cande [1999]. Sayers *et al.* [2001] therefore conclude that the anomaly interpreted previously as 34y is not a seafloor spreading anomaly and that breakup occurred around 33o time. It should be noted, however, that the magnetic models created by Sayers *et al.* [2001] are not referenced in any way to a geomagnetic reversal time scale. Oceanic crustal segments are given positive or negative *"apparent susceptibilities"* to simulate normal or reverse remanently magnetised blocks. The block edges are *"...placed where the data demands a change in magnetic properties"*. The model includes only six reversely polarised blocks, however, the labelled anomalies (18 to 33o) corresponds to at least 15 magnetic field reversals. Despite the shortcomings of this magnetic model, the important result from this study is that anomaly 34y is interpreted to overlie stretched continental, rather than oceanic, crust.

Figure 5.4: Structural model of Sayers *et al.* [2001] (Figure 7) across the Ceduna Sub-basin in the Great Australian Bight. Stretched continental crust is interpreted to underlie the magnetic anomaly previously interpreted as a seafloor spreading anomaly associated with Chron 34.

Methodologies: Previous Studies

Conventional sea floor spreading anomaly modelling was undertaken by Weissel & Hayes [1972], Cande & Mutter [1982], Veevers [1987] and Tikku & Cande [1999]. Each of these studies utilised a constant thickness (0.5 km) magnetic source layer to represent layer 2 of oceanic crust. The upper surface of this source layer was based either on bathymetry filtered of short-wavelength features (e.g. Weissel & Hayes [1972]), or an assumed constant, crustal depth (e.g. Cande & Mutter [1982]).

The magnetic source layer was assumed by each of the above workers to be 500 m thick. This assumption is based on studies that indicate the source of magnetic anomalies over young oceanic crust is predominantly the upper 500-1000 m of oceanic layer 2 (e.g. Irving [1970] and Levi [1983]). Source layers comprised blocks of alternately normal and reverse TRM of equal magnitude. The polarities of model blocks are constrained by the geomagnetic time scale and an assumed spreading rate model. There is an assumption of zero magnetisation due to induction. This conforms to the generally valid assumption that the remanent magnetisation component is the first order control on the measured total magnetisation vector in oceanic crust.

Modelling with a flat source body of constant thickness (and constant susceptibility) results in no lateral variation in susceptibility. Accordingly the modelled induced magnetisation component is non-variable. The modelled magnetic anomalies due to such a model are entirely a result of the juxtaposition of remanently magnetised blocks with opposing directions of polarity. Weissel & Hayes [1972] explicitly state and justify using only the TRM, citing the lack of significant crustal topography and the typically high Königsberger ratios of oceanic basalts.

The rationale behind this methodology, which has been successfully applied in many of the world's ocean basins, is that a unique pattern of magnetic lineations can be generated and preserved at an active spreading ridge, and that this sequence of anomalies can be matched by a simple model based on a geomagnetic time scale and assumed spreading rates. In the simplest case where no induced component is included, a single Königsberger ratio or remanent magnetisation vector amplitude is utilised, and sharp block edges are juxtaposed, there will be a degree of misfit between the simple model and the observed data. However, even in this situation there typically exist characteristic anomalies that can be *matched* between the modelled and observed data.

The relatively simple methodology outlined above was not followed by Sayers *et al.* [2001], they instead follow an object-oriented approach to modelling. Sayers *et al.* [2001] base their models on seismic interpretations and good fits between observed and modelled profiles that are achieved. In the Sayers *et al.* [2001] model, magnetic source bodies within

the oceanic crust are *"...inferred from changes in the magnetic signal alone, in accord with standard practice"*. The magnetic sources in the models of Sayers *et al.* [2001] exhibit variable depth, thickness, susceptibility, and TRM magnitude. However, there is no basis to infer changes in magnetic properties of rocks on the basis of seismic character, and there is very little variability of seismic character in oceanic crust. Accordingly, this methodology is poorly constrained and not suited to the modelling of seafloor spreading.

Spreading around the SEIR has been primarily north-south (relative to present-day pole locations) since very early separation [Weissel & Hayes, 1972; Cande & Mutter, 1982]. If the SEIR maintained an east-west trend and the Earth's magnetic field was described by a geocentric axial dipole through the Cainozoic, then the declination of the ambient field should have been near zero throughout rifting [Weissel & Hayes, 1972]. Accordingly Weissel & Hayes [1972] assumed a direction of 0° for the horizontal component of the TRM in their modelling, this assumption has been accepted in subsequent modelling studies. [Weissel & Hayes, 1972] calculated anomalies assuming remanent inclinations of ±85°, ±74°, and ±59°, which correspond to latitudes of formation of 80°, 60°, and 40° respectively (assuming an axial dipole field). Subsequent studies by Cande & Mutter [1982] and Tikku & Cande [1999] assume a remanent inclination of ±74°.

5.2.2 Methodology: This Study

A conventional sea floor spreading modelling methodology was utilised in this study. However, as seismic reflection data constrains basement topography, the effect of including variable depth source layers was tested. Tikku & Cande [1999] were restricted to assuming a constant depth magnetic source layer at 5.5 km, as they did not have constraints on basement topography. Variations in both the remanent and induced magnetisations are introduced by including a variable magnetic source layer.

The computational method of Talwani & Heirtzler [1964] was used to compute the magnetic anomalies associated with two-dimensional irregular polygons, extending to infinity in the positive-x direction (Figure 5.5). The horizontal (ΔX) and vertical (ΔZ) magnetic field strength at any given point, associated with an arbitrary polygon, are given by,

$$\Delta X = 2(M_x.P - M_z.Q) \tag{5.1}$$

$$\Delta Z = 2(M_x.Q - M_z.P) \tag{5.2}$$

where M_x and M_z are the components of the magnetisation resolved in the x and z directions respectively, and where

$$P = \frac{(z_2 - z_1)^2}{(z_2 - z_1)^2 + (x_1 - x_2)^2}(\phi_1 - \phi_2) + \frac{(z_2 - z_1)(x_1 - x_2)}{(z_2 - z_1)^2 + (x_1 - x_2)^2} log\frac{r_2}{r_1} \tag{5.3}$$

$$Q = \frac{(z_2 - z_1)(x_1 - x_2)}{(x_2 - x_1)^2 + (x_1 - x_2)^2}(\phi_1 - \phi_2) + \frac{(z_2 - z_1)^2}{(x_2 - x_1)^2 + (x_1 - x_2)^2} log \frac{r_2}{r_1} \quad (5.4)$$

where x_1, x_2, z_1, z_2, r_1, r_2, ϕ_1 and ϕ_2 are illustrated in Figure 5.5.

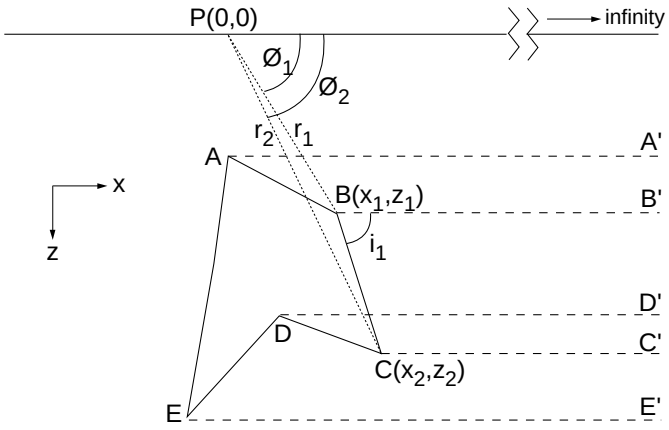

Figure 5.5: Schematic representation of an arbitrary polygon and the method of Talwani & Heirtzler [1964] for two-dimensional modelling of magnetic anomalies.

Similarly to Weissel & Hayes [1972], remanent inclinations of ±85° to ±65° were tested during modelling. A remanent inclination of ±80°, similar to the present-day inclination for the Wilkes Land margin sector of the Southern Ocean, was selected for further modelling. Remanent declination was assumed to be 0°, in accord with previous studies based on the analysis and assumptions of Weissel & Hayes [1972]. An ambient field strength of -66,000 nT was assumed, based on IGRF models [IAGA, 2000]. A remanent magnetisation amplitude of 4 Am^{-1} and magnetic susceptibility of 0.05 SI units were assumed throughout modelling, these are within the ranges specified by Telford *et al.* [1990] and typical of oceanic crust. For this ambient field, and the selected remanent magnetisation palaeoinclination and amplitude, and magnetic susceptibility, the Königsberger ratio of remanent to induced magnetisation is ∼2. The magnitude of the Königsberger ratio alters only the amplitude of calculated anomalies.

The geomagnetic reversal time-scale of Cande & Kent [1995] was used for all modelling. The age bounds of the normal polarity chrons important in discussing magnetic anomalies from the AAB, from the mid-Oligocene to the KLNP (Chron 11 to Chron 34), are detailed in Table 5.1.

Magnetic anomaly	Period (Ma)
11	29.4 - 30.1
12	30.5 - 30.9
13	33.1 - 33.5
18	38.4 - 40.1
20	42.5 - 43.8
21	46.3 - 47.9
22	49.0 - 49.7
24	52.4 - 53.3
27	60.9 - 61.3
31	67.7 - 68.7
33	73.6 - 79.1
34	83 - 118

Table 5.1: Normal magnetic polarity intervals important in the discussion of magnetic anomalies from the AAB. Intervals are from the geomagnetic reversal time-scale of Cande & Kent [1995].

Model Constraints

As there exists a greater quantity of data across the young oceanic crust flanking the SEIR relative to the older oceanic crust at the Wilkes Land margin, and as the magnetisation of oceanic crust is reduced with time (e.g. Kent & Gee [1994]), magnetic anomaly identification is easier in the central AAB relative to its margins. Accordingly, determining spreading rate variations is also easier in the central AAB. Figure 5.6 shows shiptrack plots of five separate cruises by the *R/V Eltanin* which cross the SEIR at least once. The observed magnetic anomaly and bathymetry profiles (projected as north-south profiles) for each of these crossings of the SEIR are shown in Figure 5.7. It is possible to correlate characteristic magnetic anomalies based on amplitude and form (i.e. amplitude and shape) between the profiles. These anomalies can be correlated to modelled anomalies of a synthetic profile created using an assumed spreading rate (31 mm/yr) and the geomagnetic reversal time-scale.

Characteristic magnetic anomalies are most readily correlatable on profiles acquired between 125°E and 140°E (Figure 5.7). Lack of data continuity and changes in anomaly form make it difficult to correlate anomalies east and west of the central AAB. Anomaly amplitude differs significantly between profile ELT35 (western AAB) and ELT41A (eastern AAB). Peak-to-peak amplitudes of anomalies across the SEIR and the adjacent flanks

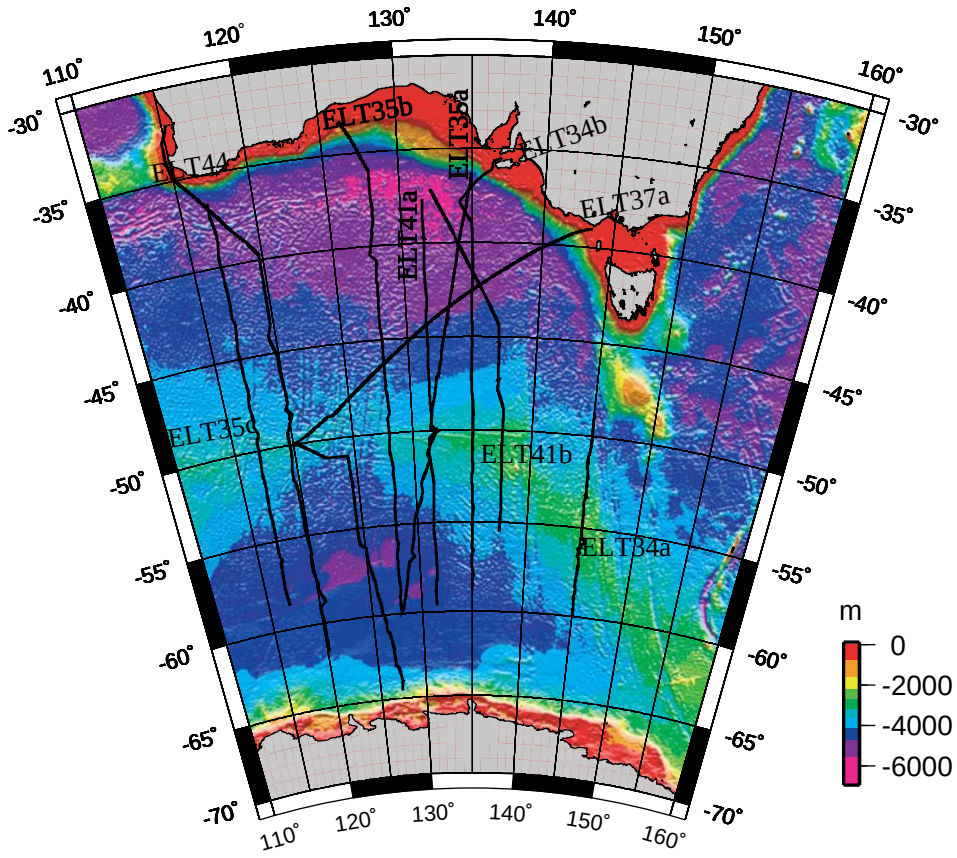

Figure 5.6: Shiptrack plot of Eltanin cruises ELT34, ELT35, ELT37, ELT41 and ELT44, each which cross the SEIR at least once. The satellite derived bathymetry [Smith & Sandwell, 1994], illuminated from the north, illustrates the position of the current spreading ridge system.

in ELT41A data reach up to 600 nT, whereas the largest amplitude anomalies in ELT35 data are ∼300 nT.

The depths to the ridge crest (and hence the minimum depth of the magnetic source layer) are not significantly different between zones A, B, and C. Likewise, the present-day ambient magnetic field is approximately equal in magnitude and inclination in each zone. Hence, it is unlikely the variable along-ridge anomaly amplitude is a function of source depth variation or differences in the present-day magnetic field. Weissel & Hayes [1972] attributed the variation in amplitude to either a thinner magnetic source layer beneath the ridge crest of zone C and/or, a contrast in the magnetic properties of the crust extruded at the ridge crest in the different zones. Weissel & Hayes [1972] provide a detailed analysis of anomaly characteristics as they relate to constant spreading rate episodes and to intervals of asymmetric spreading in the different longitudinal zones.

Despite the lateral variations in anomaly patterns, an ordered anomaly pattern oc-

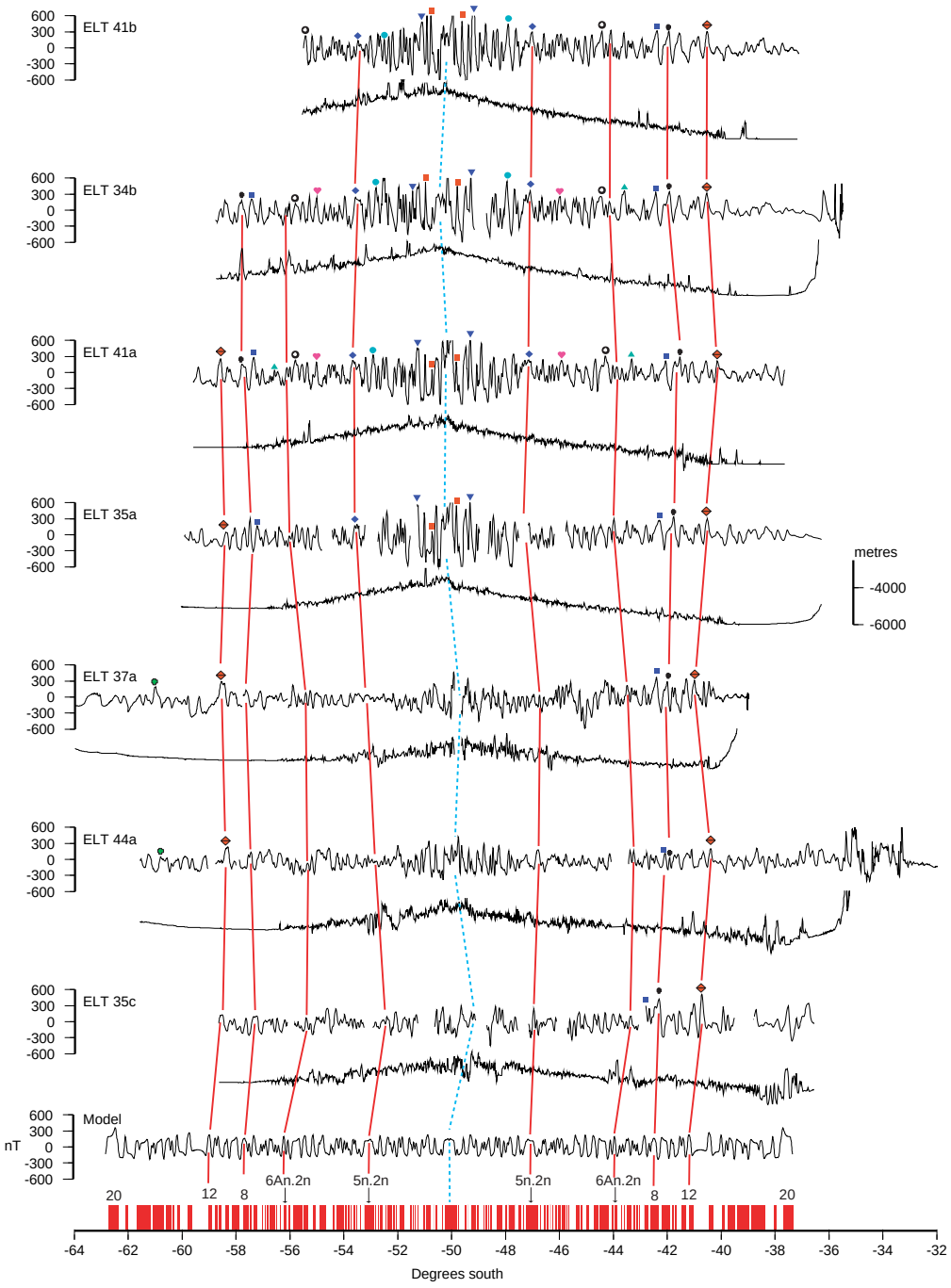

Figure 5.7: Observed magnetic anomaly and bathymetry profiles (located in Figure 5.6) across the SEIR, projected onto a north-south section and correlated to a synthetic model. Symbols and solid linking lines indicate confidently correlatable magnetic anomalies. Dashed light blue line indicates local zero age oceanic crust at the centre of the spreading ridge. Model assumes a half spreading rate of 31 mm/yr, constant depth and thickness of source layer, and a remanent magnetisation of 4 Am^{-1}.

curring north and south of the current SEIR is evident. Figure 5.8 illustrates the detailed correlation of observed and modelled anomalies for the southern flank of the SEIR from the present-day to anomaly 13n time (∼33Ma). The model was created assuming a spreading rate of 31 mm/yr, which was selected after a number of iterations with different spreading rates. The characteristic form of the anomalies labelled in Figure 5.8 are well simulated by the modelled profile, providing a high level of confidence in the spreading rate assumed in creating the model. This indicates spreading has proceeded at an average half-rate of ∼31 mm/yr since at least anomaly 13n (∼33Ma). To assess the spreading rates between anomaly 13 time and breakup, profiles extending further south are required.

To test the fit of a spreading rate model with the anomaly sequence prior to anomaly 13n, an end point within the geomagnetic time scale is required. What factors influence the choice of such an endpoint? Stratigraphic evidence of early rift basin development allows an upper (older) temporal limit for the onset of seafloor spreading. Commercial drilling results from the southern rift system of Australia (e.g.

Between 160 Ma and 118 Ma the longest single normal or reverse polarity period (i.e. time period with no reversals) is less than 2 My. 118 Ma marks the onset of the KLNP in the geomagnetic time scale (anomaly 34n), a period of ∼35 My of normal polarity with no reversals. If seafloor spreading initiated prior to this period, then an extent of relatively magnetically featureless oceanic crust flanked by positive edge-effect anomalies would be expected in observed magnetic data from the southeast Indian Ocean. No magnetic data from the southern Australian or Wilkes Land margins include evidence of such a long period without reversals. Accordingly, the *oldest* probable seafloor spreading anomaly is likely to be anomaly 34n, clearly this logic does not rule out that the oldest anomaly is not *younger* than anomaly 34n. An age of 90 Ma is assumed as a provisional endpoint here, this may be revised upwards or downwards depending on modelling results.

Extending a magnetic model to 90 Ma with a spreading rate[2] of 31 mm/yr results in,

1. a very poor anomaly fit between modelled and measured sections for the sequence of anomalies older than 17o, and

2. the southern extent of the modelled seafloor anomaly sequence (34o) occurring at a latitude of ∼74°S.

At a latitude of 74°S, anomaly 34n occurs approximately 900 km south of the Antarctic coastline. The obvious implications of this model being that spreading rates much lower than 31 mm/yr prevailed from breakup to anomaly 17o time (∼38 Ma), and/or that breakup occurred much later than 90 Ma.

[2]spreading rate implies half rates only unless explicityly stated otherwise

Figure 5.9 shows that reducing the modelled spreading rate by a factor of about two, from 31 mm/yr to 15 mm/yr, prior to 18y time still provides a poor fit between modelled and observed anomalies for the sequence older than anomaly 17, and predicts anomaly 34n to occur landward of the Antarctic coast. An average spreading rate of 6 mm/yr is required between 90 Ma and anomaly 18y time to limit the landward extent of the modelled profile to the base of the continental slope (Figure 5.9b). For the model illustrated in Figure 5.9b the positive anomaly associated with Chron 34 is aligned with the anomaly (labelled *A* in Figure 5.9) that has been previously been identified as anomaly 22 (e.g. Weissel & Hayes [1972]) and anomaly 34 (e.g. Cande & Mutter [1982]).

The *A* anomaly is a common feature in magnetic profiles from the Wilkes Land margin. It is characterised by a relatively broad (∼50 km) wavelength positive anomaly with an average peak-to-peak amplitude of 200 nT. Tikku & Cande [1999] question the interpretation of this feature as a seafloor spreading anomaly, whether the anomaly is caused by remanently magnetised oceanic crust has not been unequivocally resolved.

The indication from these relatively simple models, and assuming breakup at ∼90 Ma, is that a change in spreading rates occurred at the SEIR after anomaly 17 time. An average spreading rate of ∼6 mm/yr is implied for the interval from breakup to anomaly 17 time, whereas an average spreading rate of ∼31 mm/yr is implied from anomaly 17 time to the present-day.

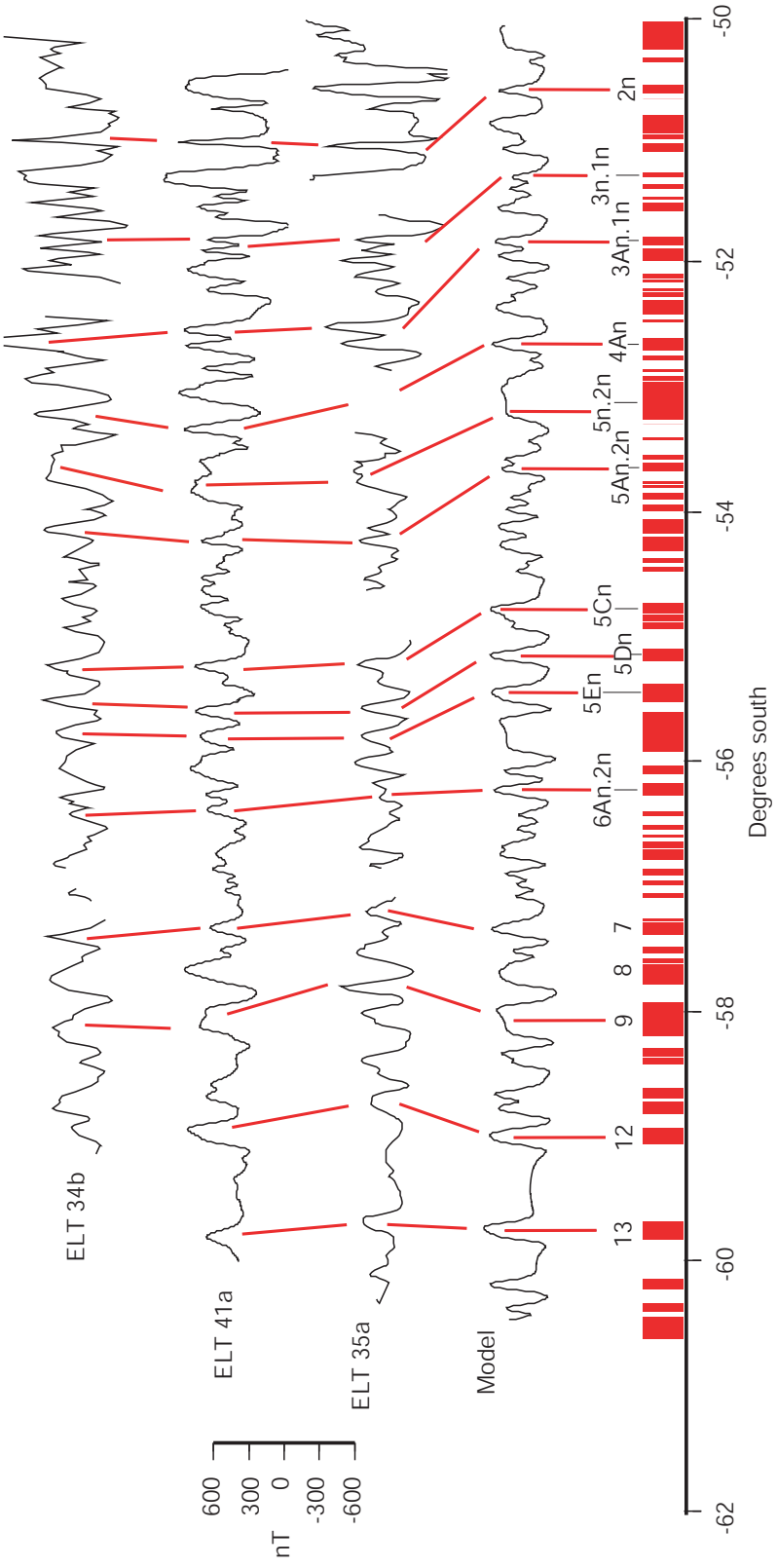

Figure 5.8: Comparison of observed and calculated magnetic anomalies over the southern flank of the SEIR. Characteristic anomaly sequences can be confidently correlated between observed and modelled profiles. Model parameters as for Figure 5.7.

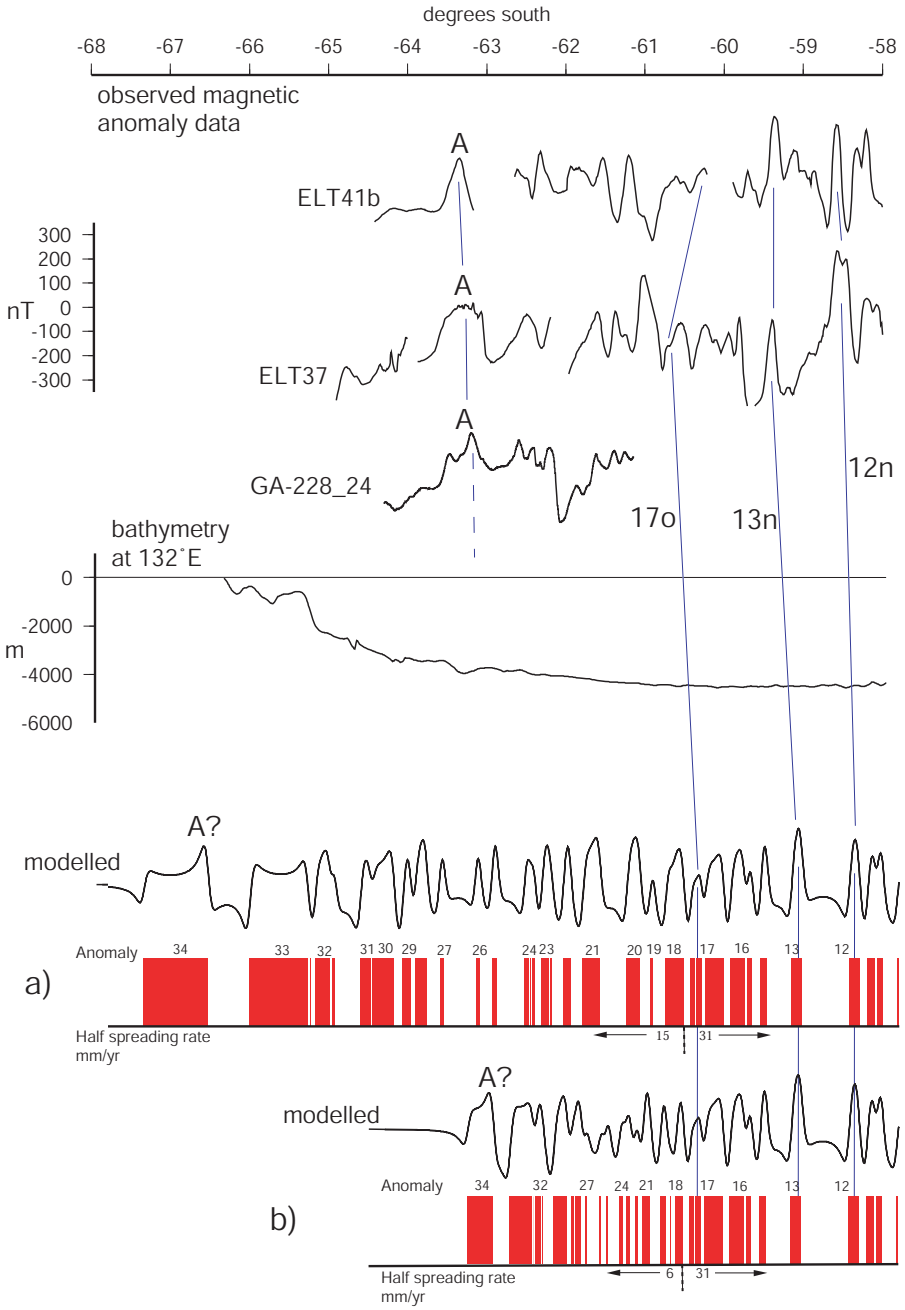

Figure 5.9: Comparison of observed and modelled magnetic anomaly profiles across the Wilkes Land margin. The anomaly sequence younger than ~17o is well modelled by a spreading rate of 31 mm/yr. b) A spreading rate of 15 mm/yr prior to 17o results in the model terminating south of the Antarctic coastline. c) For a spreading rate of 6 mm/yr prior to 17o the model terminates at the base of the continental slope. Bathymetry profile is from Smith & Sandwell [1994]. Model parameters as for Figure 5.7.

5.2.3 Variable Spreading Rate Modelling

In an attempt to improve the fit between the modelled and observed anomaly sequence older than anomaly 17o, variable spreading rates were introduced. By varying modelled spreading rates, for specific intervals of the geomagnetic time-scale, it is possible to alter the width of modelled anomalies. Hence, it is possible to improve the fit between modelled and measured magnetic anomalies. As the modelling above illustrates, spreading rates are much lower from breakup to anomaly 17o relative to anomaly 17o to the present-day. Slow spreading rates result in the interference of anomalies associated with each magnetic polarity reversal. It is possible that for very slow spreading rates, a single anomaly peak or trough may be caused by multiple bodies of alternating TRM polarity.

Initial models were extended to a time point within 34n that created a positive source body (for a given spreading rate) capable of producing an anomaly similar in character to the observed anomaly *A*. Figure 5.10 shows confidently correlated anomalies as solid lines and more contentious correlations as dashed lines for a number of lines that traverse the Wilkes Land margin. Correlation of modelled anomalies to GA-228 and GA-229 data is difficult as these survey lines terminate northwards at ∼61°S, which is ubiquitously south of the recent (∼17o to the present day) well formed anomaly sequence. The modelled data is Gaussian filtered with a 15 km full width filter (1σ ∼2.5 km) to account for the smearing effects of very slow spreading rates [Schouten & McCamy, 1972].

The spreading rate model illustrated in Figure 5.10 extends to approximately 89 Ma. The temporal end point is somewhat unconstrained in these models, as by increasing or decreasing the spreading rate before 34y (for a constant width body) the time end point can be moved back or forward in time. The spreading rate for 34y time and older is assumed to be the same as for the reversal period between 34y and 33o, which can be constrained by the modelling process.

This spreading rate model is broadly consistent with the model of Tikku & Cande [1999]. The decrease to 22 mm/yr between 18y and 18o and then 10 mm/yr from 18o to 21y mimics their spreading rate model. This model introduces a spreading rate of 7.5 mm/yr for the period between 21y and 22y, a period modelled with a spreading rate of 6.5 mm/yr by Tikku & Cande [1999]. This spreading rate model results in a modelled profile that simulates accurately observed data from anomalies 11 to 21. Survey GA-228 data terminate northwards at approximately the expected location of anomaly 18. A well-developed anomaly sequence is observed from ∼61-62°S. This sequence is characterised by a small positive anomaly on the seaward flank of the younger of two similar amplitude and wavelength, positive anomalies, which are separated by a distinct trough. This sequence can be confidently correlated with the modelled sequence for Chrons 19-20-21.

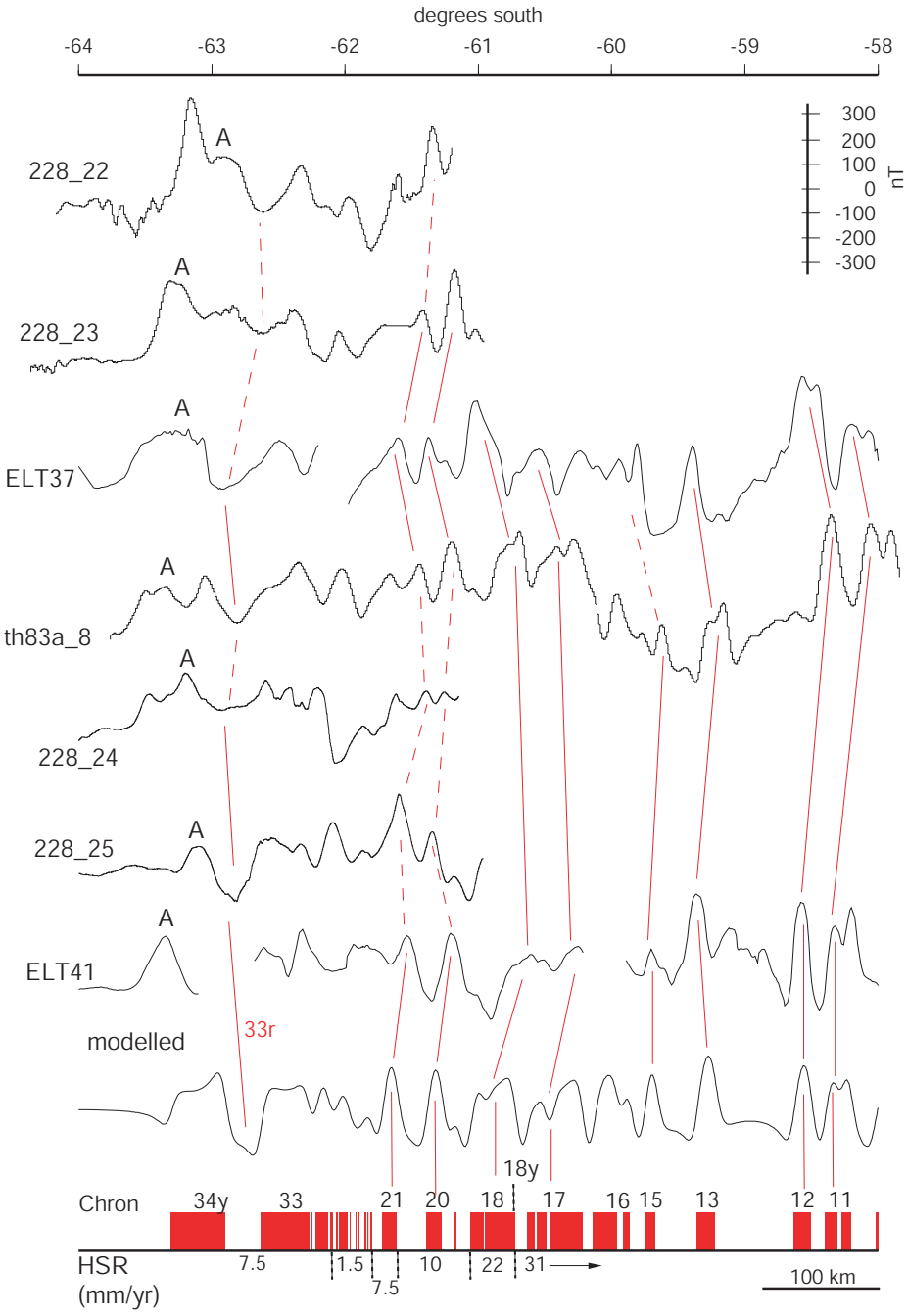

Figure 5.10: Comparison of observed and modelled magnetic anomaly profiles for a variable Half-Spreading Rate (HSR) model. The spreading rate of 31 mm/yr from present to anomaly 18y aligns the modelled characteristic sequence of anomalies 11-12-13 relative to the observed data. The 19-20-21 anomaly sequence is the oldest confidently identified sequence along the margin. Confident correlations are indicated by solid lines and estimated correlations by dashed lines.

This is the oldest anomaly sequence that can be confidently correlated for the full width of the AAB.

A very slow spreading rate of 1.5 mm/yr is introduced from 22y to 32y. This differs from the model of Tikku & Cande [1999], which only introduced such a slow rate between 24o and 31o. This spreading rate change was introduced to try and better fit the modelled and observed profiles. The model comprises a distinct double anomaly that matches the form of the observed data. However, south of anomaly 21 it becomes increasingly difficult to simulate the observed data and the quality of fit decreases significantly. Given the very slow spreading rate (1.5 mm/yr) modelled during this interval, it is not surprising that the fit is less well-developed between observed and modelled data. When such slow spreading rates occur, multiple periods of reversal are essentially 'piggy-backed' or stacked onto a relatively narrow section of oceanic crust and the complex interference of individual anomalies results.

South of the region modelled with a very slow spreading rate, the modelled spreading rate is increased to 7.5 mm/yr, which contrasts with a rate of 5 mm/yr in Tikku & Cande [1999]. The higher spreading rate improves the fit and alignment of the observed and modelled profiles south of the region of very slow spreading. The modelled positive anomaly associated with Chron 33n can be correlated to observed data on relatively few profiles, e.g. GA-228_25 (Figure 5.10). However, the trough observed at ~62.5°S can be correlated confidently between many profiles and is well simulated by the modelled trough associated with the reverse polarity interval of Chron 33 (i.e. 33r). Landward of this trough, anomaly *A* can be correlated across a number of lines. However, a large degree of variation in the form of the anomaly is observed. In this model, anomaly *A* correlates to the positive anomaly associated with Chron 34n. However, the modelled anomaly only simulates the form of a limited number of the anomalies labelled *A*, e.g. GA-228_24 and th83a_8 (Figure 5.10).

The broad correlation between modelled and observed anomalies supports the proposed spreading rate model. However, it does not vindicate the assumption that breakup occurred during Chron 34n. The next test applied to constrain breakup age is to assume breakup occurred during 33n. This would imply a breakup age of between approximately 80My and 74My. In suggesting breakup during Chron 33n, it is necessary to assess whether the full anomaly sequence, from anomaly *A* in the south through to the well constrained anomaly 21 in the north, can be modelled utilising 33n as a temporal starting point. It has already been shown that if anomaly *A* is not a seafloor spreading anomaly then the sequence of anomalies northward of this anomaly could be modelled using the spreading rate distribution outlined above.

To align the positive anomaly associated with Chron 33n to the observed anomaly

A, without shifting the well fit 19-20-21 anomaly sequence, requires increased spreading rates from anomaly 21o to 33o. Figure 5.11 shows two variable spreading rate models, both of which terminate at 33o. In the first of these models a spreading rate of 5 mm/yr is introduced between anomaly 22y and 32y, this spreading rate increase is sufficient to locate modelled anomaly 33 in line with anomaly *A*. However, the modelled trough associated with the reversal period between 32y and 31o is too narrow relative to the trough observed immediately northward of anomaly *A*. The fit of modelled to observed anomalies between this trough and anomaly 21 is also not very good. In the second spreading rate model, the spreading rate between anomaly 31o and 32y is increased to 12 mm/yr, this increases the modelled trough width to more closely approximate the observed trough. However, the fit of other anomalies is not improved relative to the first model. As the spreading rate is progressively increased, the number of individual modelled anomalies increases (i.e. there is less interference due to greater source separation), however, the observed sequence typically contains only 2-3 positive anomalies from Chron 21o to 32y.

Subsequent modelling with progressively younger terminations encounter the same problems as are evident for the 33n time ending model. The total number of anomalies modelled when spreading rates are increased (necessary to force younger age crust to reach a southern termination that allows anomaly *A* to be modelled) increases as individual anomalies begin to become distinct, this results in a calculated profile containing more anomalies than the measured profiles. In conjunction with this problem is the lack of a reversal period of great enough temporal extent (or spatial extent with reasonable spreading rates) to model the distinctive trough northward of anomaly *A*. Hence, it is possible to model anomaly *A* using several starting points, however, such starting points poorly simulate the remainder of the anomaly sequence.

This stepwise process, which has sought as much to eliminate possibilities as to vindicate any given age of breakup and temporal distribution of spreading rates, has illustrated that if anomaly *A* is a seafloor spreading anomaly, then it is associated with seafloor spreading commencing during late 34n time (approximately 90 Ma). Profiles calculated using this time point as the model terminus simulate relatively closely observed profiles, indicating that anomaly *A* is likely either associated with seafloor spreading anomaly 34, or remanently magnetised intrusive and volcanic rocks of 34n age.

Modelling thus far has assumed a constant depth to the top and bottom of the magnetised source layer. Seismic reflection data, however, reveals the actual crustal topography, showing trough to peak elevations of up to 2000 m are relatively common. One possible source of error therefore in the modelling is the contribution of a varying depth to the magnetised source layer.

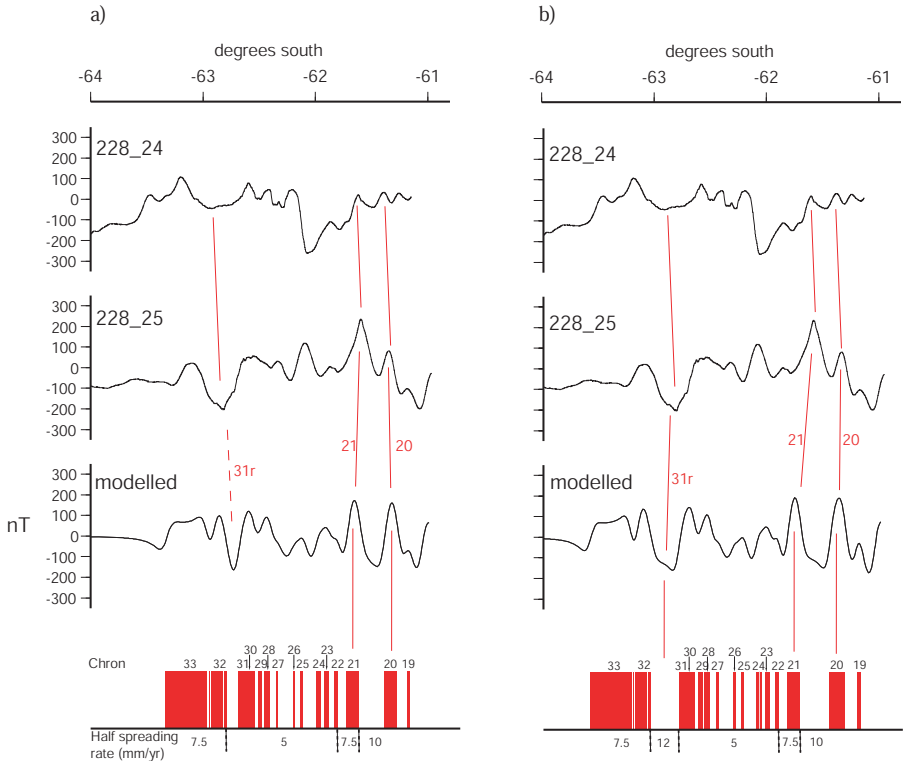

Figure 5.11: Modelled magnetic anomalies for two variable half spreading rate models. Model endpoint is anomaly 33n. There is a poor fit between observed and calculated profiles for these models. a) Modelled 31r trough is too narrow relative to observed data. b) Modelled 31r trough wavelength has been increased by increasing the spreading rate for the reversal period between 32y and 31o time, however, the overall correlation between modelled and observed anomalies is not improved. Model parameters as for Figure 5.7.

5.2.4 Variable Crustal Topography Modelling

For a variable depth magnetic source layer, lateral variations in susceptibility are introduced that did not exist in previous models. This results in an induced magnetisation component in the modelled total magnetisation. This component will remain very small, relative to the remanent component of total magnetisation, where the Königsberger ratio is large (i.e. ≥ 2). Lateral variation in the remanent component of the total magnetisation results from juxtaposed blocks of reverse and normal polarity as modelled above, however, further variation, and associated changes in the remanent magnetisation component of the modelled total magnetisation, is also introduced by the variable source depth.

The effect of incorporating basement topography on the remanent component of the total magnetisation was tested by creating a model that included both variable source depth and TRM polarity reversals. This approach requires the simple block bodies created in earlier models to have surfaces controlled by the observed crustal topography. To create models for each GA-228 and GA-229 line the interpreted basement depth was combined with the optimal spreading rate model determined previously (e.g. Figure 5.10). To minimise edge effects, a flat extension with no remanent magnetisation was added to the southern termination of the model. Figure 5.12 illustrates the small changes in the modelled field associated with a non-uniform source depth model, the topographic effect on the remanent component (that is, the effect of changing the surface of a block of any polarity) is minor. The depth variation of the crustal layer is negligible relative to the distance between the measurement surface and source layer. Accordingly, the dominant remanent magnetisation component is that resulting from the juxtaposition of remanently magnetised blocks with opposing polarity.

The induced magnetisation field component in oceanic crust is minor relative to remanent magnetisation, as the Königsberger ratio is typically large in oceanic crust as discussed previously. However, the relationship between remanent and induced magnetisation of continental crust is far more variable and complicated (e.g. Dunlop [1995]). As continental margins represent the boundary between oceanic and continental crust, variation in the magnitude of the K

To investigate the induced magnetisation associated with crustal topography, source bodies were created utilising an upper surface constrained by the depth converted basement surface (as interpreted from MCS data). The magnetic source layer was assumed to be 500 m thick and comprise a constant magnetic susceptibility. To avoid large-amplitude edge-effects, the source layer was extended to the north and south as a flat continuous body. An example of the induced magnetisation component associated with basement

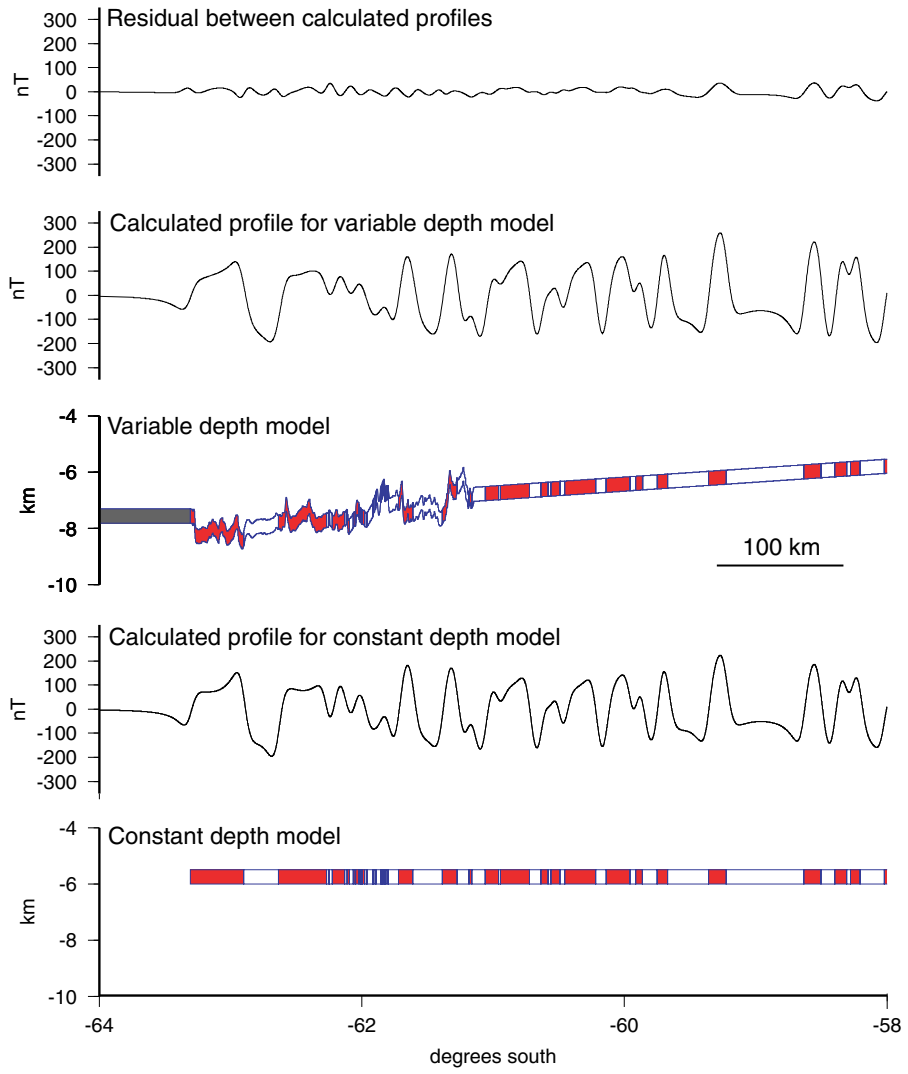

Figure 5.12: Comparison of modelled anomalies for constant and variable depth magnetic source layers. The introduction of a variable depth introduces very little variation, as illustrated by the very small signal amplitude in the residual profile. The depth variation is insignificant relative to the distance between the measurement surface and source layer. Model parameters as for Figure 5.7.

topography, calculated for three values of magnetic susceptibility (k), is shown in Figure 5.13.

Modelled induced magnetisation anomalies for susceptibilities of 0.05 and 0.1 SI are of negligible amplitude relative to observed anomalies (Figure 5.13). Only for an unrealistically large susceptibility of 0.5 SI do modelled anomalies exceed 40 nT. However, for this susceptibility, the two positive anomalies observed at ~62.5°S are well simulated by modelled anomalies. Modelling of other lines, however, provides no further evidence of a

correlation between basement topography and observed magnetic anomalies

Increasing the thickness of the magnetic source layer does not produce modelled anomalies of similar amplitude to observed anomalies, as it does not increase lateral variation in susceptibility. The depth of the source layer (∼7 km) relative to the topographic variation is such that a constant susceptibility and constant thickness source layer does not produce large amplitude anomalies. It is possible to produce induced magnetisation anomalies of greater amplitude, however, this requires variations in source layer thickness and/or susceptibility to be introduced. Unlike depth to basement, neither magnetic susceptibility or source layer thickness can be independently constrained from seismic reflection data. Other than variation in the observed magnetic data, there are no constraints on how these parameters vary, and there is no *a priori* reason to assign different susceptibility values to any specific section of oceanic crust (other than to improve the fit of a model). As there is an infinite number of source distribution solutions for any observed anomaly sequence, changing parameters such as susceptibility with no geological or geophysical basis provides no insight into anomaly identification or breakup age determination.

Modelling of the induced field component indicates that induced magnetisation anoma-

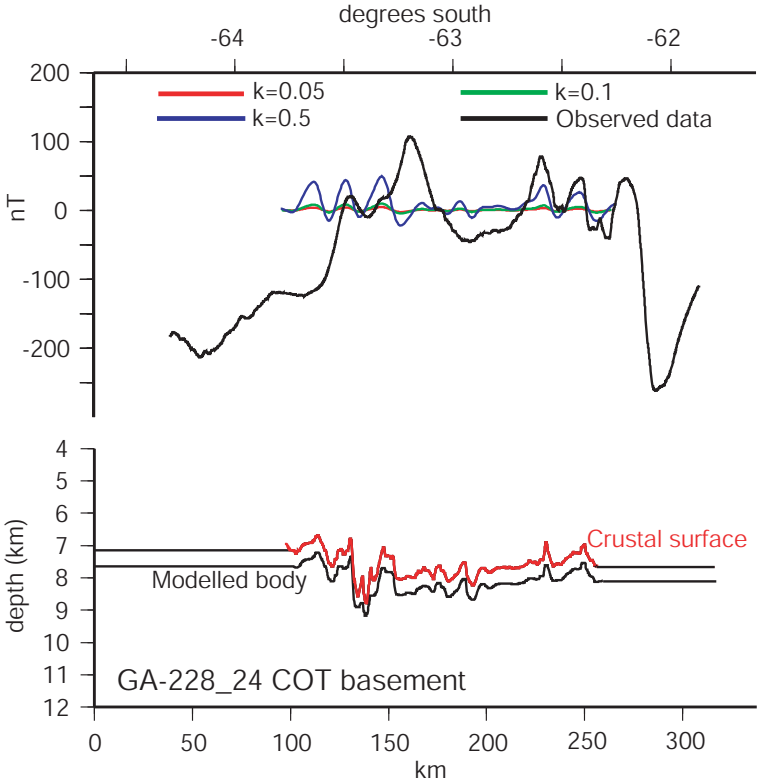

Figure 5.13: Modelled induced magnetisation anomalies and observed magnetic anomalies. Model geometry from basement depth of the continent-ocean transition zone, as interpreted from MCS data on line GA-228_24. Three values of magnetic susceptibility (k) were modelled to assess the sensitivity of the induced magnetisation to k.

lies associated with topographic variations represent a negligible component of the measured total magnetisation, for *constant susceptibility and source layer thickness*. However, the correlation of basement topographic highs with observed positive anomalies on Line GA-228_24 indicates that induced magnetisation components of the total magnetisation may be important for transition zone crust and/or altered oceanic crust in isolated instances.

5.3 Interpretation and Discussion

5.3.1 Magnetic Anomaly Compilation and Correlation

Figure 5.14 shows a compilation of open file, GA-228, GA-229, and JNOC magnetic anomaly data from 105°E and 140°E. The observed magnetic anomalies are correlated to modelled anomalies based on the spreading rate model in Figure 5.10. The variation in modelled and observed spreading rates (i.e. based on anomaly identification) since breakup is also illustrated graphically in Figure 5.16 for a number of profiles across the margin.

Figure 5.16 clearly illustrates the ultra-slow spreading rates prior to anomaly 18 time. In ∼40 My, less than 250 km of oceanic crust was created between the SEIR and Antarctica. The AAB, accordingly, was narrow (relative to its present-day width) for over 40 My following breakup. The close temporal correlation of the distinct change in spreading rates across the SEIR and the initial collision of Greater India with the Eurasian plate has been noted by previous workers, this major tectonic event may have been a catalyst for changes in spreading rate along strike of the spreading ridge system encircling the Antarctic continent.

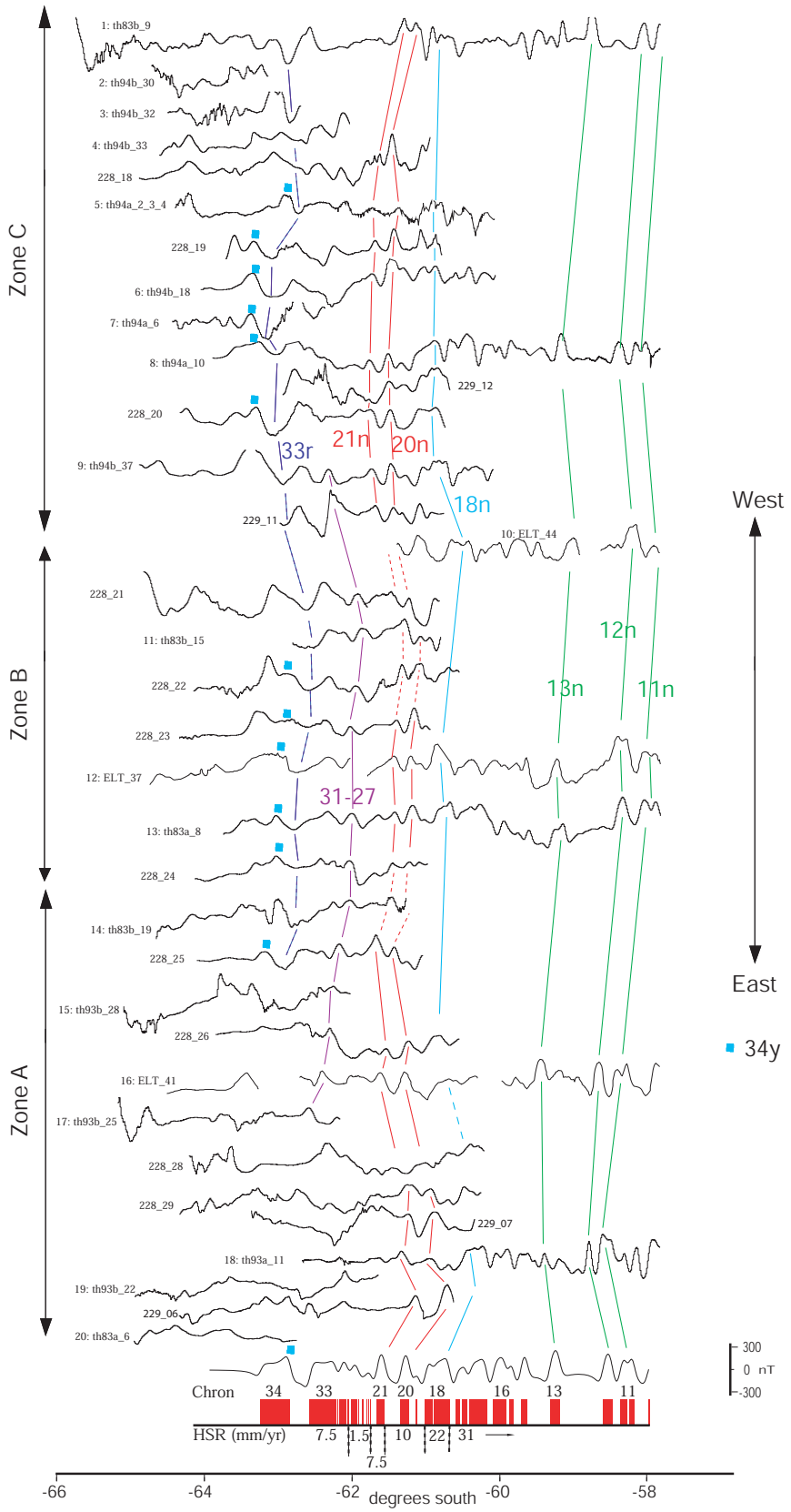
Zone C
Zone B
Zone A
1: th83b_9
2: th94b_30
3: th94b_32
4: th94b_33
228_18
5: th94a_2_3_4
228_19
6: th94b_18
7: th94a_6
8: th94a_10
229_12
228_20
33r
21n
20n
9: th94b_37
18n
229_11
10: ELT_44
228_21
11: th83b_15
12n
228_22
13n
11n
228_23
12: ELT_37
31-27
13: th83a_8
228_24
14: th83b_19
228_25
15: th93b_28
228_26
16: ELT_41
17: th93b_25
228_28
228_29
229_07
18: th93a_11
19: th93b_22
229_06
20: th83a_6
West
East
34y
300
0 nT
-300
Chron
34
33
21
20
18
16
13
11
HSR (mm/yr)
7.5
1.5
10
22
31
7.5
-66
-64
-62
degrees south
-60
-58

Figure 5.14: (*Previous page*) All GA-228, GA-229, JNOC, and Eltanin magnetic anomaly profiles across the Wilkes land margin correlated to a modelled profile. Anomaly correlations are less distinct in the eastern sector of the AAB (Zone *A* of Weissel & Hayes [1972]). Numerical identifiers for each profile correspond to location of profile in Figure 5.15.

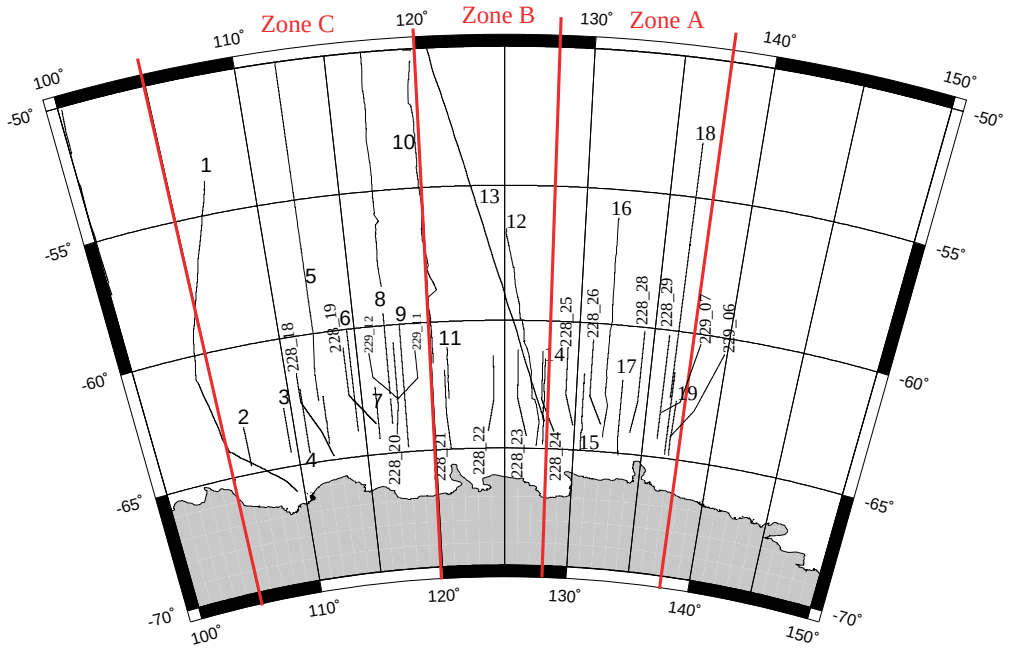

Figure 5.15: Location of GA-228, GA-229, JNOC, and Eltanin survey lines across the Wilkes land margin shown as profiles in Figure 5.14. Zones A, B and C are after Weissel & Hayes [1972] and are defined by zones of distinct morphologic, seismologic, and magnetic anomaly character at the SEIR.

The most strike continuous anomaly sequences are 11-12-13, 16-17, 18, and 19-20-21, these anomalies typically correlate very well along the margin (in all zones) and with the modelled profile for the variable spreading rate model illustrated (Figure 5.14). The anomaly sequence associated with oceanic crust emplaced between breakup and anomaly 21 time is significantly more enigmatic. The positive anomaly correlated with polarity reversals 27-31 in Figure 5.14 is continuous only in the central Wilkes Land margin sector from ~117-130°E. Landward of this peak, the negative anomaly associated with the reverse polarity interval of Chron 33 (i.e. 33r) is continuous along the width of the margin west of ~130°E, although the wavelength and amplitude of the anomaly is variable. The final anomaly identified as possibly of seafloor spreading origin is anomaly 34 (observed anomaly *A*).

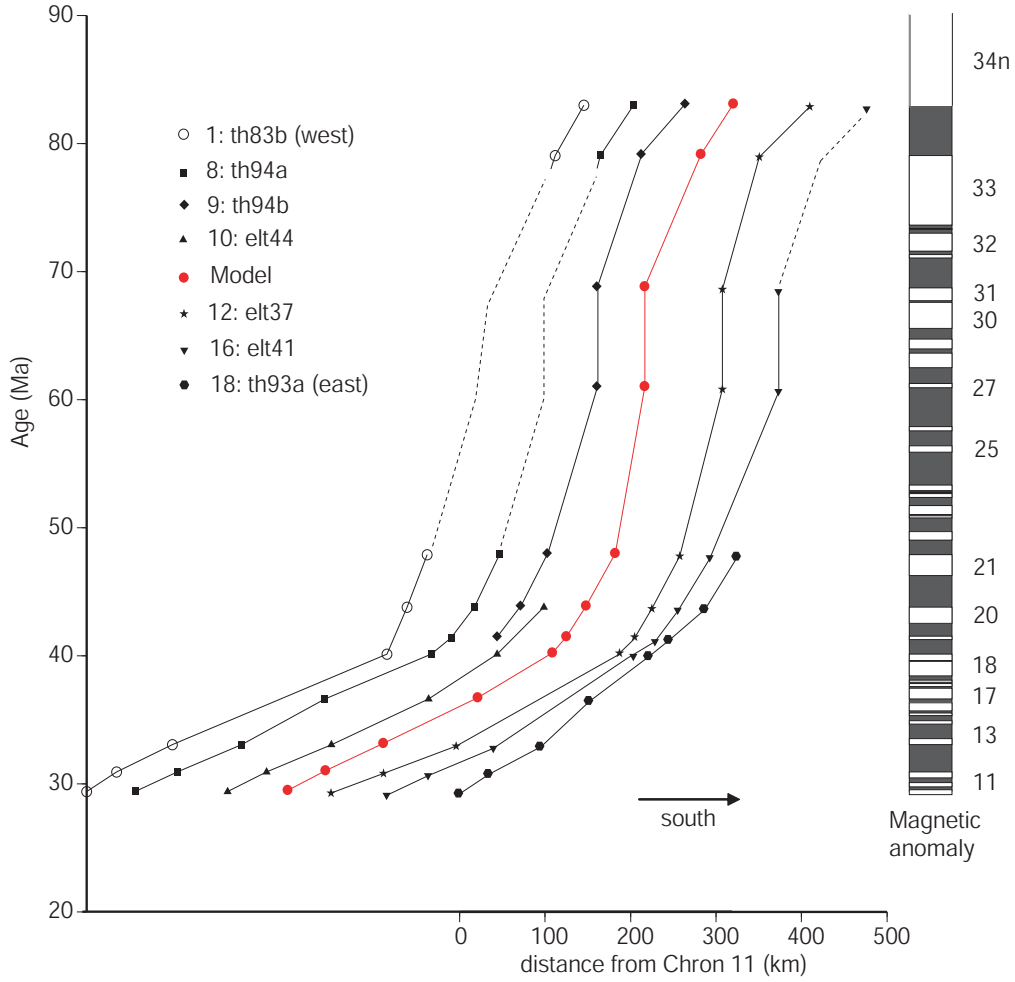

Figure 5.16: Distance of well correlated magnetic anomalies as a function of time for six observed magnetic anomaly profiles from the Wilkes Land margin (located in Figure 5.15). Profiles are normalised to anomaly 11. The almost identical trends of the modelled distance-age profile (solid circles) relative to observed trends indicates the applicability of the spreading rate model. Note that normal polarity periods are denoted by black blocks in this figure.

The location of confidently correlated magnetic anomalies on the Wilkes Land margin are shown in Figure 5.17 along with the extent of the Continent-Ocean Transition Zone (COTZ) interpreted from seismic reflection data (Chapter 4, Figure 4.23). Anomaly 34y, where it is identified in the western and central Wilkes Land sector of the AAB is located within the COTZ. The seaward edge of the COTZ off east Wilkes Land and the Adelie Rift Block (ARB) extends as far north as the Chron 21 lineation. This indicates that the earliest oceanic crust seaward of the ARB was emplaced during the Middle Eocene (~45 Ma), ~35-40 My later than in the central AAB. The onset of seafloor spreading

between the ARB and the conjugate southeastern Australian margin correlates to the end of ultra-slow spreading based on the spreading rate model presented here.

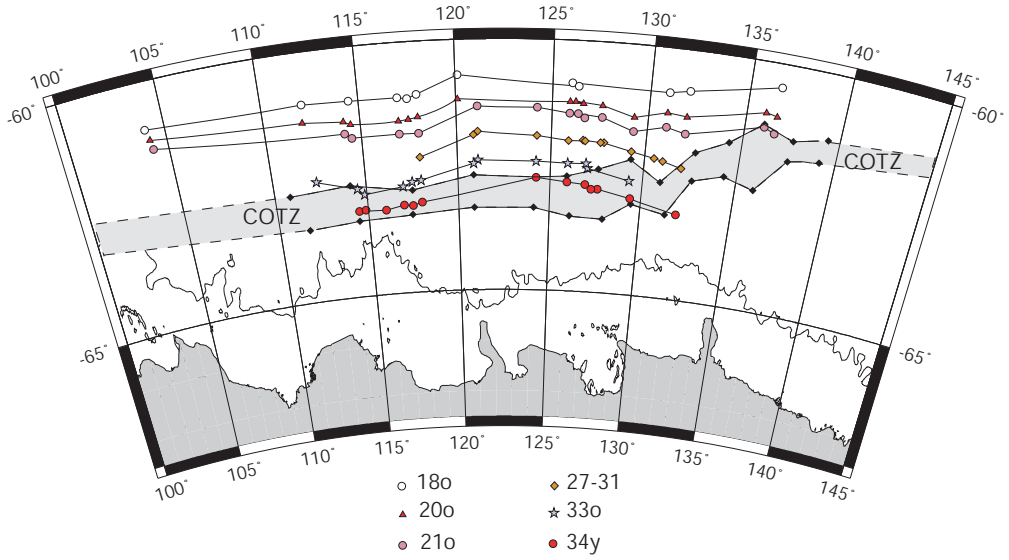

Figure 5.17: Correlatable magnetic anomaly lineations for the Wilkes Land margin and the continent-ocean transition zone (COT) as interpreted from seismic reflection data (Figure 4.23).

Anomaly '34' exhibits variable form across the margin, hence it is difficult to confidently identify it as a seafloor spreading anomaly. If it is not an anomaly associated with emplacement of oceanic crust, it is likely associated with either a regional magmatic pulse or exhumed upper mantle peridotites, which recorded the TRM of Chron 34n, prior to final breakup. An anomaly of similar form and relative location (i.e. landward of 33r) is also observed on the southern Australian margin (e.g. Veevers [1987] and Tikku & Cande [1999]).

In the central Wilkes Land sector of the AAB, anomaly 34 is most consistently formed and the fit of the modelled anomaly 34 with the observed anomaly is best. Seismic reflection data at the approximate latitude of this anomaly indicate a transition-zone not typical of continental or oceanic crust. However, given the modelled spreading rates of ~7.5 mm/yr and the subsequent hiatus in spreading, typical oceanic crust acoustic character should not be entirely expected.

The absence of correlatable magnetic anomalies over the ARB is further evidence that it comprises stretched continental crust, as suggested in Chapter 4. The magnetic anomaly pattern from the conjugate sector of the southern Australian margin is also interpreted to be devoid of anomalies older than anomaly 20 (Figure 5.18).

The more extensively studied southern Australian margin exhibits a very similar

magnetic anomaly pattern to the Wilkes Land margin, a complete discussion of these data is provided by Weissel & Hayes [1972], Veevers [1986], Veevers *et al.* [1990], and Tikku & Cande [1999]. Figure 5.19 illustrates the similarities in the anomaly pattern on the conjugate margins. Despite the greater data density from the southern Australian margin, the origin of anomaly 34 is still not conclusively established.

Figure 5.18: Interpretation of magnetic anomaly data on the southern Australian margin from Veevers *et al.* [1990]. The oldest anomaly sequence identified in the central southern Australian margin (30-34) is not evident east of ~132°E. This termination of the magnetic anomaly sequence remains, however, more than 250 km west of the Spencer fracture zone, indicating that extended continental crust is likely to abut the eastern extent of the oldest oceanic crust in the central sector of the margin.

5.3.2 Magnetic Anomaly Variability

As outlined above the magnetic anomaly sequence recorded in oceanic crust emplaced between breakup and the Middle Eocene is far from ideal. It is generally poorly repeated on profiles separated by more than a few 10s of kilometres. The variation in form along strike indicates that either this oceanic crust did not acquire strong TRM during emplacement or processes have acted to alter the original TRM since emplacement.

As oceanic crust basalt ages it is altered such that its magnetisation becomes substantially reduced [Kent & Gee, 1994]. The process of maghemitisation of titanomagnetite on the seafloor occurs throughout Layer 2A [Smith & Banerjee, 1986], generally within a few million years of extrusion. As a result, the amplitude of linear magnetic anomalies falls by about an order of magnitude from the central anomaly over an active spreading centre to older lineations over oxidised seafloor [Dunlop, 1995]. The correlation of

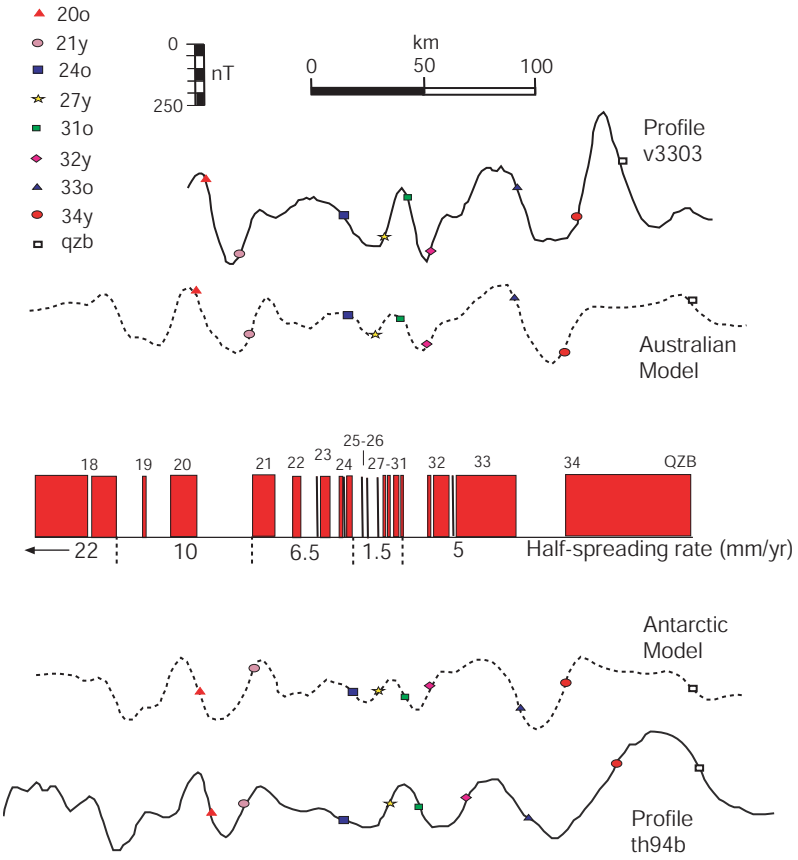

Figure 5.19: Spreading rate model of Tikku & Cande [1999] and profiles from the Wilkes and GAB margins. Synthetic magnetic profiles created using the following input parameters: top of magnetic source layer depth of 5.5 km, source layer thickness of 0.5 km, remanent inclination and declination of -74° and 0° respectively, and a 3 km Gaussian filter. Note that profile th94b is the same as th94b_37 in Figure 5.14.

anomalies older than a few million years in all ocean basins indicates that some memory of the primary TRM is retained during this alteration.

Remanent magnetisation that remains following alteration is known as Chemical Remanent Magnetisation (CRM) (e.g. Özdemir & Dunlop [1985]). CRM is phase-coupled to TRM (i.e. retains the direction of the TRM during alteration/oxidation) for fine-grained rocks only, and this explains the survival of linear magnetic anomalies [Özdemir & Dunlop, 1985; Dunlop, 1995]. Clearly then, for oceanic crust to retain an accurate geomagnetic record it must be sufficiently fine-grained.

Although young oceanic crust is typically accompanied by large-amplitude, linear magnetic anomalies, there are examples of young oceanic crust that is not. They include the northeast Pacific Ocean (e.g. Davis & Riddihough [1982], the northern Juan de Fuca Ridge (e.g. Davis & Lister [1977], and the Guaymas Basin in the Gulf of California (e.g.

Larson *et al.* [1972]). In addition to the absence of interpretable magnetic anomalies, each of these areas is overlain by sediments up to 1 km thick [Levi & Riddhough, 1986]. Larson *et al.* [1972] suggested a causal relationship between the sediment cover and the low-amplitude of observed magnetic anomalies.

Vogt *et al.* [1970] suggested that magmas crystallising under sediment will not form extrusive pillow lavas, but will cool more slowly and comprise larger grain-size and correspondingly lower TRM and CRM intensities. However, Levi & Riddhough [1986] suggest that primary cause of low-amplitude magnetic anomalies is pervasive hydrothermal alteration, which is encouraged by the blanketing of sediments over very young oceanic crust. Faults and contraction fractures typically provide pathways for sea water to interact with hot, young oceanic crust at spreading centres and encourage cooling (e.g. Lister [1972]). Sea water and magmatic fluids interact to create hydrothermal fluids that circulate and, in the absence of extensive sediment cover, vent directly into overlying cold sea water. Levi & Riddhough [1986] define this as an *"open"* system. In contrast, if there is extensive sediment cover at a spreading centre the hydrothermal circulation system is not open, and this is defined by Levi & Riddhough [1986] as a *"closed"* system.

In a closed system, hydrothermal fluids have a comparatively long residence time within the basalt, and cool more slowly while they thermally and chemically equilibrate with the basalt and overlying sediment Levi & Riddhough [1986]. This results in pervasive alteration and leaching of iron-oxides, and therefore diminishes the amplitude of lineated magnetic anomalies. Clearly, a closed system must allow sea water interaction with hot, young basalt and magmatic fluids while also preventing open circulation of these fluids.

The lack of continuity of lineated magnetic anomalies on the Wilkes Land margin is interpreted to indicate a closed system of hydrothermal circulation, at the SEIR, from breakup to the Middle Eocene. Due to the very slow spreading rates during this interval, the basin separating Australia and Antarctica would have been relatively narrow for a period of 10s of My. If sediment flux was sufficient during this interval of slow spreading, young oceanic crust, and possibly even the spreading centre itself, could have been capped by detrital sediments from the adjacent continents. Hydrothermal alteration of oceanic crust in the AAB from breakup to the Middle Eocene may, therefore, contribute to the discontinuity in lineated magnetic anomalies and the associated difficulties in interpreting the observed anomalies.

5.4 Summary

The ultra-slow early spreading rates modelled here (Figure 5.14) and the associated likely hydrothermal alteration, explains, at least in part, the variability in the observed anomaly

sequence 34-21. On the strength of magnetic evidence alone a breakup age of ~90Ma is indicated for the central sector of the Wilkes Land margin. However, uncertainty in the correlation of the observed anomaly *A* to modelled anomaly 34 prevents this being conclusively determined from magnetic anomaly data alone. The absence of the anomaly sequence 34-21 off eastern Wilkes Land, within the ARB, indicates that breakup, whenever it did initiate, was not synchronous along the extent of the margin.

Chapter 6

Gravity, Flexure and Backstripping

6.1 Gravity

6.1.1 Introduction

Observations of the Earth's gravitational field provide an important means of investigating the structure of the crust and lithosphere. Gravity observations are sensitive to both static mass distribution and dynamic processes. Gravity data interpretation suffers, however, from problems of non-uniqueness. The ambiguity of gravity interpretations can be reduced by considering independent geophysical and geological information in conjunction with gravity data. Most commonly, seismic data are used to provide constraints on model geometry and physical properties.

Two approaches to gravity interpretation of gravity data are the forward and inverse modelling methods. Inverse gravity modelling calculates body parameters directly from the observed anomaly, without requiring rigourous external constraints on source geometries. Forward modelling techniques require the definition of source geometries and properties, from which gravity anomalies can be calculated and compared to observed data.

Gravity data were acquired coincident with all GA-228 MCS survey lines using a *LaCoste and Romberg* air-sea gravimeter. A sample interval of 1 s was maintained throughout surveying. Cross-coupling corrections were calculated from beam position, beam slope, and cross and long accelerometers that were also logged using a 1 s sample rate. Drift corrections were applied based on ties to land gravity base stations in Cape Town, South Africa, and Hobart, Australia. Eötvös corrections, accounting for the vector addition of gravity meter's velocity and the Earth's rotational velocity, were applied according to,

$$E = 7.503\,V\,cos\theta\,sin\nu + 0.004154\,V^2$$

where E is in mGal, V is speed in knots, θ is latitude, and ν is the heading.

The satellite derived free air gravity field of Sandwell & Smith [1997] has been utilised to extend line data where necessary. No Bouguer Anomaly (BA) data is available for the onshore Wilkes Land margin, or indeed for much of the Antarctic continent. Accordingly, gravity models were terminated at the Antarctic coast and compared to FAA data only.

Traditionally, gravity modelling of continental margins has utilised seismic data to constrain a model geometry comprising water, sedimentary, crustal and mantle bodies. These bodies are assigned average density values based on available geophysical data (e.g. refraction velocity, stacking velocity, and well-log data). Models have typically been created assuming either Airy or flexural isostatic conditions. Models created without consideration of isostatic balance that comprise bodies of varying densities and geometry are referred to herein as *object-oriented*. Object-oriented models attempt to represent the current state of a margin and provide information on the applicability of the defined density distribution only. These models rarely represent a state of stable equilibrium and therefore implicitly argue against the theory of isostasy.

Forward modelling techniques were employed extensively throughout this study, however, inverse modelling of specific gravity anomalies was also completed to aid final interpretation. Gravity models were constrained by Multi-Channel Seismic (MCS) data, and refraction data where available. The unsurveyed margin portion, extending from the southern termination of GA-228 and GA-229 survey lines to the Antarctic coast, was modelled using extrapolated source geometries constrained with other data where possible as outlined in Chapter 4. Two-dimensional gravity methods form the basis of interpretation for this study due to the nature of the MCS data distribution (approximately parallel line data separated by up to 90km). Three-dimensional methods are investigated also, but provide for more qualitative interpretation only.

6.1.2 Parameterisation

Initial model parameters were chosen following the method of Cochran [1981]. Using a reference column through a mid-ocean ridge crest (defined as a 5 km thick crust under 2.5 km of water, underlain by 1,333°C mantle) Cochran [1981] demonstrated that the crustal parameters required to provide an internally consistent, isostatically balanced system (assuming a linear thermal gradient) for a lithospheric thickness of 125 km, were as summarised in Table 6.2. These parameters provided a defensible starting point for forward modelling, however, parameters were varied in accord with standard forward modelling practice.

Crustal thickness is poorly constrained by seismic and gravity studies for the Antarctic continent as a whole, however, where data does allow this parameter to be tested,

mantle density at 0°C (ρ_m)	3330 kg/m^3
crustal density at 0°C (ρ_c)	2800 kg/m^3
water density (ρ_w)	1030 kg/m^3
initial crustal thickness (T_c)	31.2 km
coefficient of thermal expansion	3.4×10^{-5}°C^{-1}
asthenospheric temperature	1,333°C
thermal diffusivity	0.008 cm^2/s
thermal conductivity	0.0075 cal/deg cm s

Table 6.1: Crustal parameters demonstrated by Cochran [1981] to provide an isostatically balanced system with a reference column through a mid-ocean ridge crest.

values of 30-40 km have been determined for the East Antarctic craton [Bentley, 1991]. Accordingly a range of values of 35±5 km were tested through the modelling process. It can be shown that the modelled gravity anomaly is relatively insensitive to initial crustal thickness (where crustal and mantle density are held constant) for a range of initial values, accordingly it is only possible to assess the accuracy of the initial crustal thickness value where seismic reflection and refraction data image the *Moho* discontinuity. Where large sediment accumulations occur, a lower limit of crustal thickness can be determined by establishing the minimum initial crustal thickness that requires a *Moho* depth shallower than basement depth to maintain isostatic equilibrium. For lines off west Wilkes Land, where sediment thickness is greatest, GA-228_18 to GA-228_21, a minimum initial crustal thickness of ∼35 km is necessary to ensure the modelled *Moho* remains deeper than the top of basement.

As the density of seawater is well known (1030 kg/m^3), the remaining input parameter to any gravity model is the sediment density; this varies primarily as a function of porosity and grain composition. The porosity is controlled by diagenetic processes, depth of burial, and compaction. For gravity modelling, sediments can either be decompacted and modelled with a correspondingly lower density, or considered in their compacted state and modelled with a higher density.

Seismic velocity (*P-wave* or interval) is known to correlate to density in a predictable fashion (e.g. Hamilton [1976], Hamilton & Bachman [1982]). Empirical relationships, calibrated with well-log data, provide a means of estimating density from interval velocities (determined through moveout correction of reflectors in MCS data or from refractor velocities in wide-angle data) for different marine environments and sediment compositions. Broadly, increased seismic velocity corresponds to an increase in density (Figure

6.1a). However, seismic velocity is also a function of grain-size (Figure 6.1b). The predictions of Hamilton [1976] have been confirmed to be very accurate by well-log sediment density data (e.g. Jarrard *et al.* [1989]).

Figure 6.1: Seismic or sound velocity is related to both a) density, and b) grain size for continental shelf and slope sediments. Figure from Hamilton & Bachman [1982].

Velocity-density relationships must be applied with some caution on the Wilkes Land margin, however, as the composition of sediments is inferred almost entirely from MCS data and very little well data is available to confirm interpreted lithologies. It is reasonable to assume that post-rift sediments are almost entirely siliceous (clastic near margin grading to pelagic in the abyssal plain). Due to the relatively high latitude of Antarctica since rifting, it is unlikely that there are significant carbonate reef platforms or salt layers.

The range of observed interval velocities for the post-rift sediment sequence on the Wilkes Land margin is 1700-3600 m/s (Figure 6.2) this corresponds to a density range of ~1600-2400 kg/m^3. Typically only the very upper layers exhibit interval velocities less than 2000 m/s. This full range of inferred sediment density values was tested during the modelling procedure, however, examination of interval velocity profiles indicate a *mean* sediment density of between 2100 and 2350 kg/m^3 is most applicable across and along the margin. The sensitivity to variations in sediment, crustal and mantle density, and initial crustal thickness is examined to ensure a procedure robust to reasonable levels of variation.

6.1.3 Gravity Anomaly Computation

Two-Dimensional Modelling

The line integral method of Talwani *et al.* [1959] is used to calculate gravity anomalies of two-dimensional bodies throughout this thesis. In this method, the contributions of

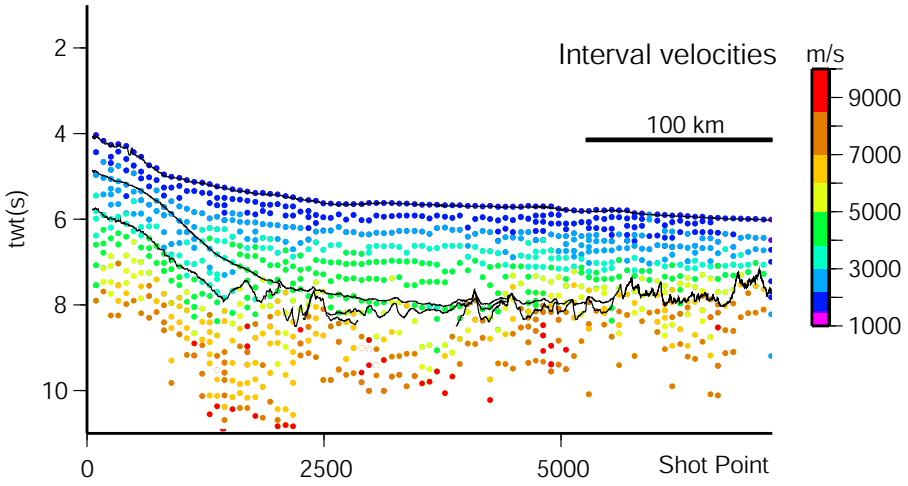

Figure 6.2: Interval velocities, converted from original seismic stacking velocities using Dix's equation, for Line GA-228_24. Base of the post rift sequence, the Eocene unconformity and the water bottom as interpreted in MCS data are superimposed (black solid lines).

a number of thin, horizontal layers, that extend infinitely in the positive-x direction, are summed to calculate the gravity anomaly of an arbitrary polygon (Figure 6.3). The gravity anomaly, Δg, of any single layer or interface, in the x,z coordinate system at point P is described by the equation,

$$\Delta g = 2G\Delta\rho(-[x_1 sin\, i + z_1 cos\, i][sin\, i\, log\frac{r_2}{r_1} + cos\, i(\phi_2 - \phi_1)] + z_2\phi_2 - z_1\phi_1)$$

where G is the universal gravitational constant, $\Delta\rho$ is the density contrast across the interface, and x_1, x_2, z_1, z_2, r_1, r_2, ϕ_1 and ϕ_2 are shown in Figure 6.3.

As the gravity field is sensitive to lateral density contrasts, the gradient of the interface between two elements is significant. For the case of $i = 0$ in Figure 6.3, no lateral density contrast exists between layers BB' and CC', and no gravity anomaly results. The wavelength of a gravity anomaly, however, is primarily controlled by the depth to a causative source body. The field strength associated with a wavenumber component (k) of the measured gravity decreases by a factor of e^{-kh}, where h is the height above the density interface. Hence, the higher frequency field components diminish as the height of observation increases. Therefore, the gravity anomaly associated with the *Moho*/crust interface has a much longer wavelength relative to anomalies associated with anomalous masses of identical dimensions closer to the surface (or level of measurement).

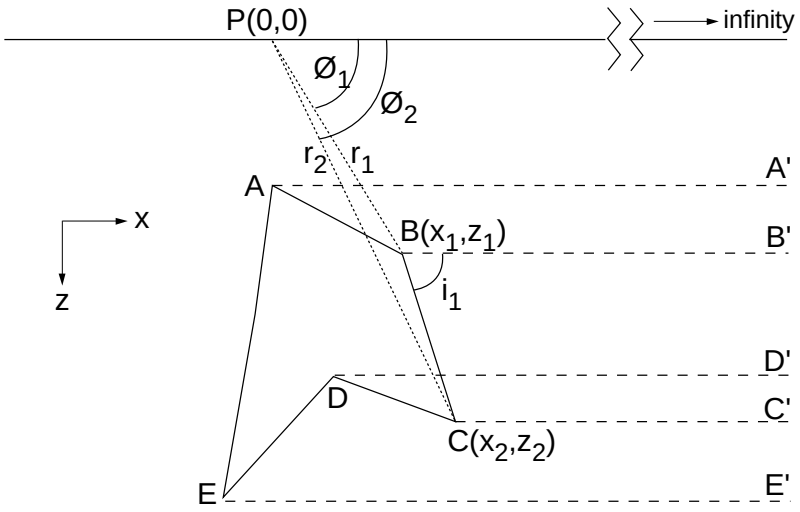

Figure 6.3: Geometry of an arbitrary polygon and the method of Talwani *et al.* [1959] for two-dimensional gravity modelling.

Three-Dimensional Modelling

Direct methods of calculating gravity anomalies associated with three-dimensional bodies are computationally intensive and time consuming [Parker, 1972]. Therefore, the method of Parker [1972] for the rapid calculation of potential anomalies is utilised here to calculate the gravity anomaly associated with density contrasts across three-dimensional surfaces, in this way bodies are simulated by two or more surfaces. Parker [1972] demonstrates that for the gravity anomaly, Δg,

$$\mathcal{F}[\Delta g] \quad = \quad -2\pi G e^{-|k|z_0} \sum_{n=1}^{\infty} \frac{(|k|)^{n-1}}{n!} \mathcal{F}[\Delta\rho(z_1^n - z_2^n)] \tag{6.1}$$

where $\mathcal{F}[\ ]$ represents the Fourier transform of the enclosed variable, G is the universal gravitational constant, k is the wavenumber and $\Delta\rho$ is the density contrast across the surface. The gravity anomaly is calculated at some surface, $z = z_0$, where z is depth, and the upper and lower surfaces of the body of anomalous mass are at depths of $z = z_1$ and $z = z_2$ respectively (Figure 6.4). Although the Fourier transform comprises infinite terms of Taylor's expansion series, terms for n>4 are of negligible magnitudes and are disregarded in gravity anomaly calculation.

6.1.4 Data

The marine satellite derived gravity field of Sandwell & Smith [1997] is routinely used in geophysical studies. However, special consideration must be given to the use of these data at high latitudes because, i) shiptrack data is sparse, providing less possibilities

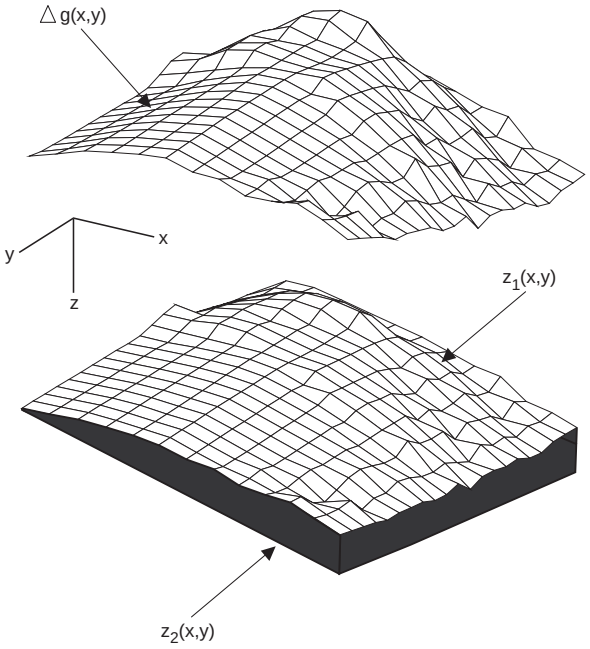

Figure 6.4: Three-dimensional calculation of the gravity anomaly for a layer bounded by z_1 and z_2, based on the Fourier transform methods of rapid calculation of potential field data [Parker, 1972].

for calibration with measured data, and ii) the perennial coverage of the ocean (at polar latitudes) with ice. Complex radar echoes from sea ice confuse trackers onboard altimeter satellites and produce noisy height estimates [McAdoo & Laxon, 1996].

McAdoo & Laxon [1997] derived a high-resolution gravity grid for the poorly charted and ice covered oceanic sector of West Antarctica, from 145-360°E. They incorporated ERS-1 altimetry data, which has a more steeply inclined orbit relative to Geosat and is therefore capable of observing to higher latitudes, in their grid. McAdoo & Laxon [1997] utilised the full 20 Hz ERS-1 wave-form (WAP) data set rather than the ocean product (OPR) data set. This allowed the data to be reprocessed and the height noise significantly reduced [Laxon & McAdoo, 1994]. However, no equivalent data is available for the Wilkes Land sector of East Antarctica.

Comparison of free-air satellite derived gravity anomaly data with GA-228 shiptrack data illustrates the close similarity of the two fields (Figure 6.5a). The close correlation of shiptrack and satellite derived free-air anomaly (FAA) data decreases at higher latitudes (Figure 6.5b). Data acquired by the *R/V S.P. Lee* (survey L184) extends as far south as 66°S, at these latitudes shorter wavelength anomalies observed in shiptrack data are not observed in satellite derived data. This is a function of the problems associated with high latitude satellite altimetry data and the complexities associated with sea ice, as outlined

above. The extents of ice during the austral winter and summer, as shown in Figure 6.6, illustrate that even during times of minimum ice extent, much of the positive peak of the edge-effect anomaly remains ice covered.

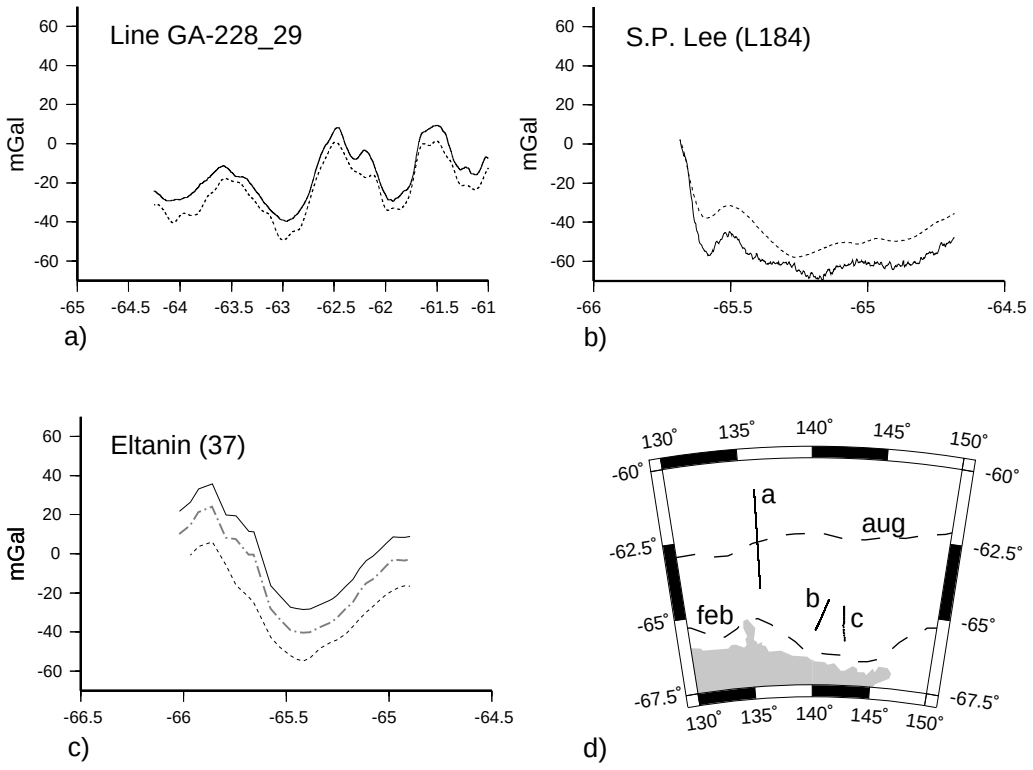

Figure 6.5: Profile comparisons of shiptrack observed (solid) and satellite derived (dashed) free air gravity anomaly data off the Wilkes Land margin for, a) GA-228 survey data, b) *R/V S.P. Lee* survey L184 data, c) *R/V Eltanin* survey 37 data (grey dashed line is shiptrack measured data following correction as discussed in text), and d) Location of profiles for a, b and c, and the August (austral winter) and February (austral summer) ice extents (from R. Larter, BAS).

The most striking feature of Figure 6.5a is the shift between satellite derived and shiptrack data of 5-10 mGal. Comparison of satellite derived FAA data with shiptrack data from survey of L184 [Childs & Stagg, 1987] exhibits the converse relationship (Figure 6.5b). Further confusion is added by the fact that McAdoo & Laxon [1997] demonstrated that L184 shiptrack gravity anomaly data is offset by $\sim$+30 mGal relative to their high-resolution grid; thus, data that is negatively offset relative to satellite derived data on the Wilkes Land margin is positively offset relative to the high-resolution satellite derived data on the West Antarctic margin. Earlier surveys by the *R/V Eltanin* (1968-1972) measured gravity anomaly data that, similarly to the GA-228 and GA-229 data, is shifted positively relative to the satellite derived FAA data (Figure 6.5c). However, the Generic

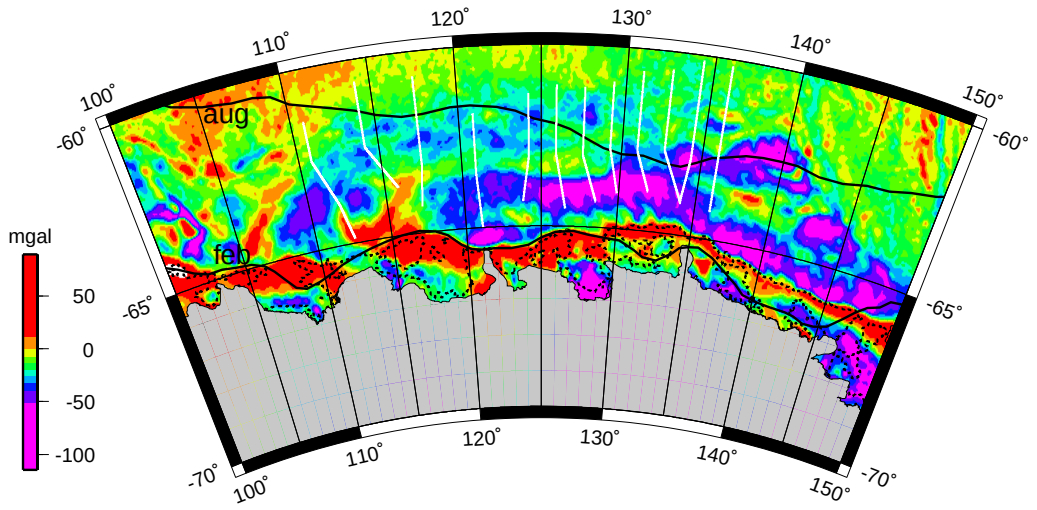

Figure 6.6: August (winter) and February (summer) ice extents (from R. Larter, BAS) for the Wilkes Land margin in solid black. Dashed black represents the 500 m bathymetric contour (GEBCO 1m), and white lines are GA-228 survey lines from 18 (west) to 29 (east). The 500 m contour correlates to the location of the steepest gradient of the edge-effect positive anomaly and also to the minimum (February) ice extent also. Gravity data from Sandwell & Smith [1997].

Mapping Tools (GMT[1]) default (version 3.4) correction file[2] provides corrections for many of the *R/V Eltanin* data, which decrease the magnitude of the positive shift relative to satellite FAA data (Figure 6.5c).

As no tie-line exists between the GA-228 survey lines there are no internal cross over errors, therefore, external cross over error analysis provides the only means of assessing the accuracy of gravity data acquired during the GA-228 survey. Figure 6.7a illustrates the location of shiptrack gravity data for the Wilkes Land margin, a total of 940 external cross over errors were determined between all datasets, the mean value of which was 0.07 mGal with a standard deviation of 11.58. Figure 6.7b illustrates their distribution. Figures 6.7c-f illustrate the external cross over error distribution between groups of surveys (e.g. all *USNS Eltanin* survey data) and all other data. Predictably (given the offsets relative to satellite FAA data) the *USNS Eltanin* and *R/V S.P. Lee* data are respectively positively and negatively shifted relative to the mean for all external cross over errors. *USNS Eltanin* data is corrected where possible. Only 47 cross over errors

[1]http://www.soest.hawaii.edu/gmt

[2]The GMT database contains open-file marine geophysical data. This data can be extracted in 'raw' or 'corrected' format, however, details of the correction are not provided, likely they are associated with different theoretical gravity formulae used in data reduction and referencing to the Potsdam network rather than to the IGSN71 network of base stations.

were determined for GA-228 gravity data, the mean of these errors is 0.93 mGal with a standard deviation of 12.72.

The JNOC survey dataset represents the closest analogue to the GA-228 survey in terms of navigation (i.e. both are GPS controlled) and exhibits a similar mean external cross over error and standard deviation. By examining internal cross over errors for the JNOC cruises we can therefore make some inferences about the level of accuracy achieved by survey GA-228. Internal cross over error analysis of the JNOC cruises of 1983, 1993, and 1994 indicates that mean errors are less than 0.47 mGal for each survey and standard deviations range from 2.06 to 3.65. These low standard deviations, relative to external cross over errors, indicates that the data acquired in each of these surveys is of high quality. A similar reduction in standard deviation could be expected for GA-228 internal cross over errors, were they to exist, and accordingly we can infer an accuracy of better than ± 5 mGal in GA-228 gravity data.

Long Wavelength Analysis and Removal

Gravity models created throughout this study include upper mantle and shallower bodies only, therefore gravity anomalies of very long wavelengths are not modelled. Measured gravity data, however, comprises both the shorter wavelength signals due to crustal density anomalies and longer wavelengths due to density anomalies within the mantle and the curvature of the geoid. If long wavelength anomalies contribute unequally across the study area then it is necessary to remove these from observed data to allow direct comparison with modelled gravity anomalies. Utilising the geopotential coefficient model of Rapp & Pavlis [1990] it is possible to isolate gravity anomaly data of any given waveband by using the simple (and approximate) relationship between spherical harmonic degree and order (of the coefficient model) and gravity signal wavelength by

$$\lambda \;=\; 360 \times \frac{111}{n} \tag{6.2}$$

where λ is wavelength in km, and n is the spherical harmonic degree and order.

The threshold value over which all greater wavelengths are removed is ultimately a subjective choice. The gravity field for a number of degree and order values equivalent to wavelengths from ~5000-2000 km are shown in Figure 6.8. The magnitude of the long wavelength components illustrated do not exceed 25 mGal, but are almost entirely negative. The negative regional FAA reflects the negative depth anomalies associated with the ~2000 km wide Australia-Antarctica Depression (AAD), which extends at least 900 km from the ridge crest.

Hayes & Conolly [1972] suggested that the AAD and observed depth anomalies are associated with a downwelling convective current in the asthenosphere. To remove the deep,

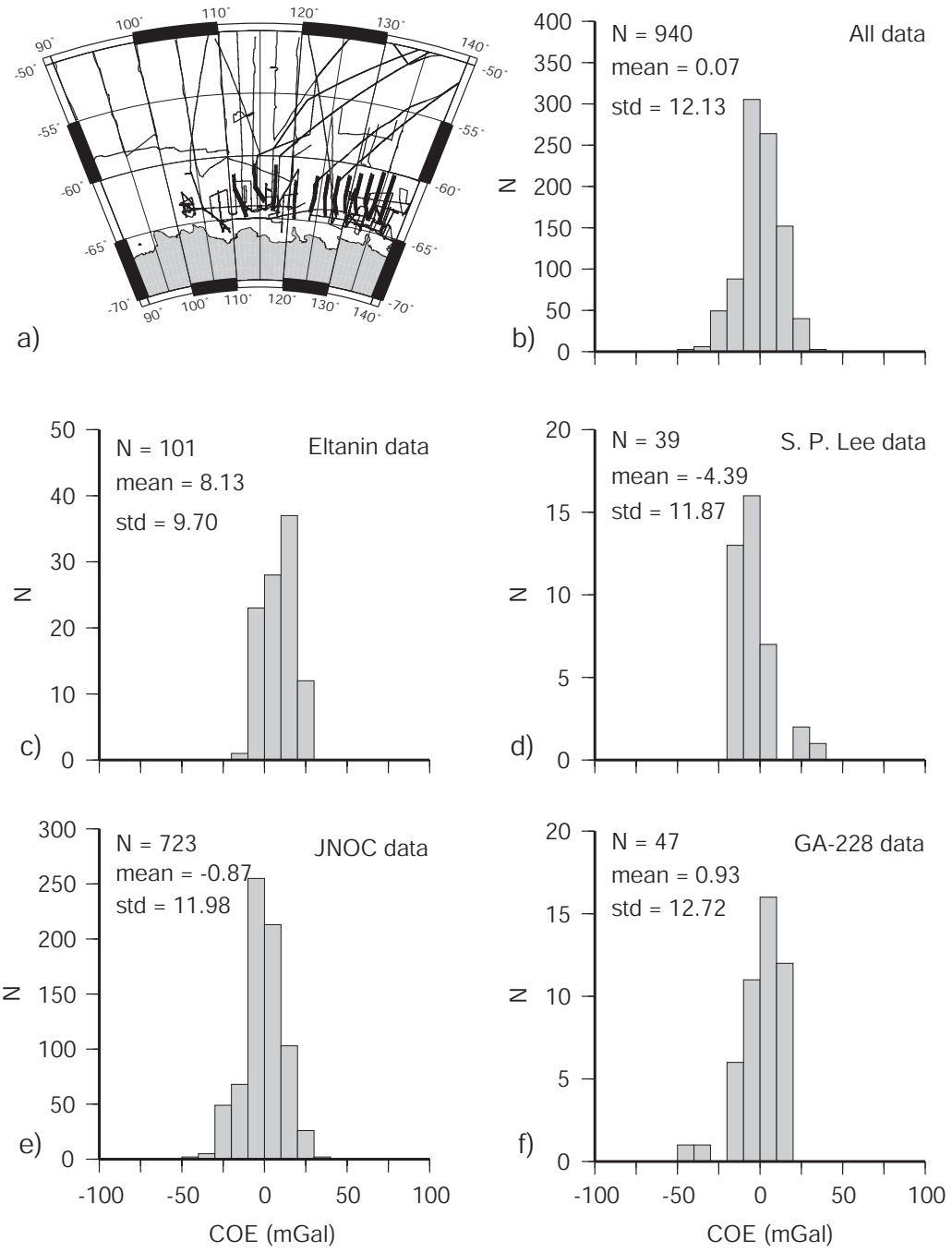

Figure 6.7: External cross over error analysis of shiptrack gravity data for the Wilkes Land margin. a) Shiptrack plot of all open access, JNOC and GA-228 (bold) gravity data. Distribution of cross over error magnitudes for b) all data, c) Eltanin data (after correction where possible), d) USGS S.P. Lee data, e) Japanese National Oil Company (JNOC) data, and f) Geoscience Australia survey GA-228.

asthenospheric contribution to the regional negative gravity field, wavelengths greater than ∼3333 km ($n = 12$) were subtracted from the total field satellite derived FAA data. All subsequent analysis and comparisons of observed gravity data (shiptrack and satellite derived), throughout this study, have had components equal and greater to degree and order 12 removed.

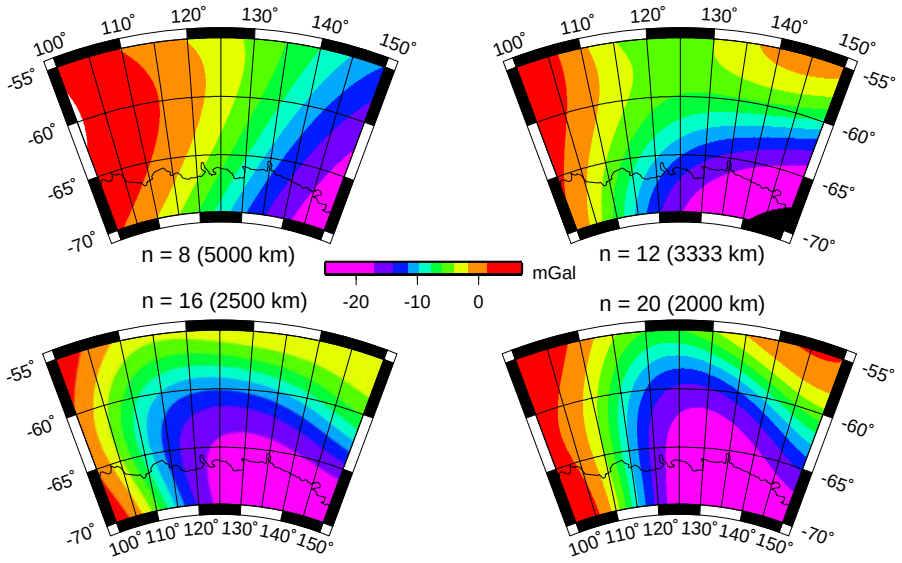

Figure 6.8: Comparison of the long wavelength gravity field [Rapp & Pavlis, 1990] in the Wilkes Land margin region, for four different degree and order values, n. Approximate minimum included wavelengths are bracketed. The long wavelength fields are almost entirely negative for the extent of the Wilkes Land margin.

Wilkes Land Edge Effect Gravity Anomaly

A number of features of the edge effect anomaly, as imaged in the satellite derived FAA gravity data, are worthy of note prior to quantitative analysis and modelling. One of the most prominent features of the marine free-air gravity field (e.g. Figures 6.6 and 6.9b) is the *edge effect* observed at the continental margin. This anomaly typically consists of a gravity high over the shelf break and a low over the continental slope/rise. This high-low 'couple' is observed along much of the Wilkes Land margin. The edge effect high exceeds 60 mGal in the eastern sector only and the low is typically no more negative than -40 mGal. North-south profiles extracted from the satellite FAA field (Figure 6.10) illustrate the variation in the edge effect anomaly along the margin.

In the central sector the edge effect anomaly is relatively consistent in form and magnitude. To the west and east, however, significant departures from this form are evident. In the western sector, at ∼112°, the edge effect high is shifted abruptly southwards by

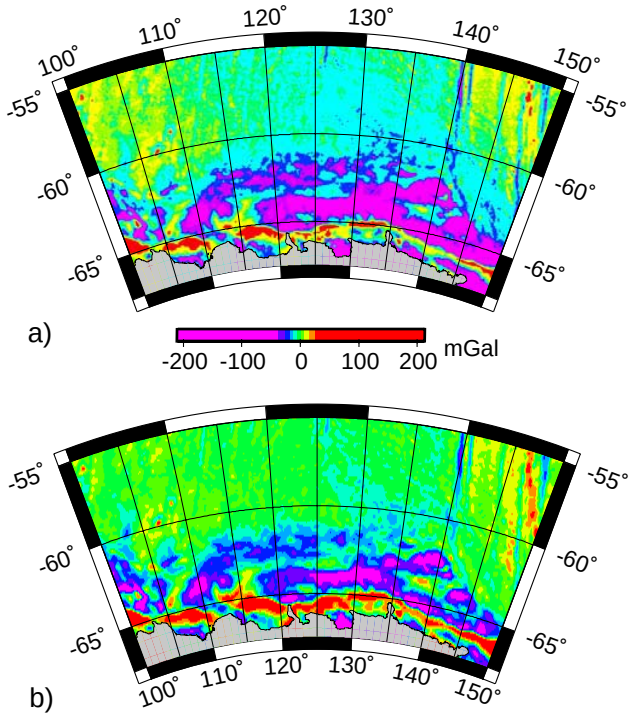

Figure 6.9: Comparison of a) total satellite derived gravity anomaly field of Sandwell & Smith [1997], and b) residual gravity field after subtracting the long wavelength gravity field to degree and order $n = 12$ (i.e. wavelengths ~3333 km).

more than 100 km. This edge effect discontinuity occurs at the prominent Budd Coast headland, formed by the Law Dome. The physiography of this margin sector is unusual, it is characterised by a very narrow continental shelf and an absence of a clear shelf-break. The absence of a shelf break explains the discontinuity in the edge effect high.

The outer continental rise sector of the Budd Coast Basin (BCB), as defined in Chapter 4, broadly correlates to the east-west positive FAA at ~62.5°S, from ~115-130°E (Figure 6.11). This indicates that the basin sediments are, at least in part, uncompensated.

To the east, between ~132-142°E, the relatively broad edge effect low is replaced by an *outer high* and the low is split into two limbs encircling this anomalous high. This anomaly was discussed in Chapters 4 and 5 due to its coincidence with anomalous seismic reflection and magnetic anomaly data. The eastern sector of the Wilkes Land margin is characterised by much thinner sediment loads, decreasing to less than 1 km in some areas.

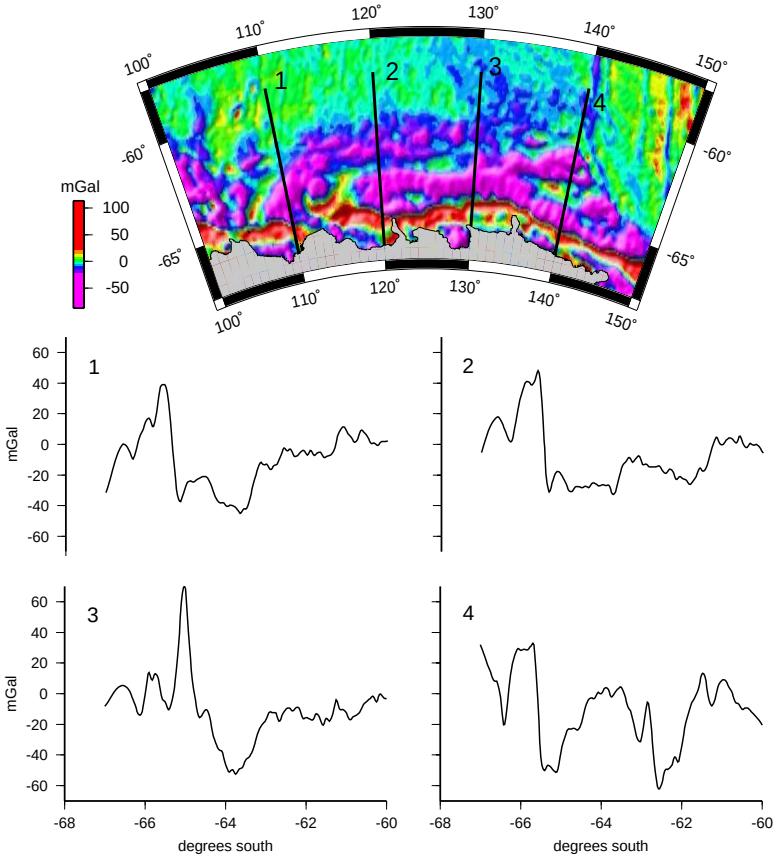

Figure 6.10: Four north-south profiles extracted from satellite derived free air gravity anomaly data, located as per black solid lines on map above. The edge effect anomaly is best developed in the central sector (profile 3) between 122-132°E.

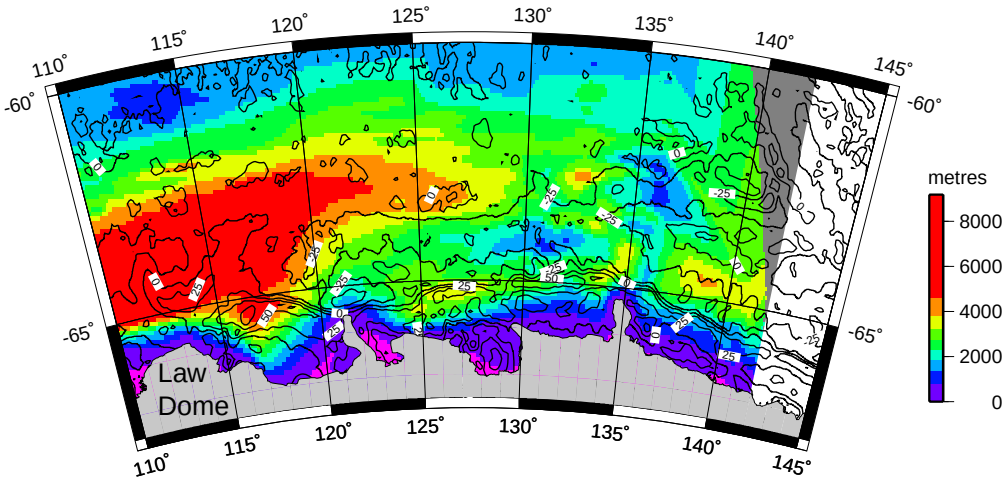

Figure 6.11: Total sediment isopach overlain by satellite derived FAA contours [Sandwell & Smith, 1997]. The edge effect low is deflected by the thick sediments off the western sector of the Wilkes Land margin. The correlation between sediment thickness and positive gravity anomalies indicates that the sediments are, at least in part, uncompensated.

6.2 Backstripping, Flexure and Process-Oriented Modelling

6.2.1 Backstripping and Flexure

Backstripping is a method developed by Watts & Ryan [1976] to "correct" a stratigraphic sequence for the disturbing effects of sediment and water loading, and hence isolate the unknown tectonic driving forces responsible for the rift basin subsidence. By applying this technique Watts & Ryan [1976] were able to determine the depth at which basement would be in the absence of the driving loads of water and sediments (i.e. the *tectonic subsidence*). Sawyer [1985] defined the *Total Tectonic Subsidence* (TTS) as the difference between the pre-rifting continental crust elevation and the present, sediment unloaded or backstripped basement depth.

To determine the TTS we consider the deflection of an elastic plate in response to the loading effect of a sediment layer (S) and the loading effect of water due changes in sea level (Δ_{sl}), Figure 6.12. The general equation for the deflection of an elastic plate (Equation 1.1), therefore, becomes

$$D\frac{d^4w}{dx^4} + (\rho_m - \rho_{infill})gw = (\rho_s - \rho_w)gS + \rho_w g\Delta_{sl} \tag{6.3}$$

where D is the flexural rigidity (Equation 1.2), w is the deflection of the plate (i.e. flexure), ρ_m and ρ_{infill} are the densities of the mantle and the material that infills the deflection respectively, ρ_s is the average density of the sediment load, and ρ_w is the density of water. Solving this equation using Fourier transforms provides,

$$\begin{aligned} \hat{W}[Dk^4 + (\rho_m - \rho_{infill})g] &= (\rho_s - \rho_w)g\hat{S} + \rho_w g\hat{\Delta_{SL}} \\ \hat{W} &= \phi\left[\hat{S}\frac{(\rho_s - \rho_w)}{(\rho_m - \rho_{infill})} + \hat{\Delta_{sl}}\frac{\rho_w}{(\rho_m - \rho_{infill})}\right] \end{aligned} \tag{6.4}$$

where the hat above an upper-case variable denotes the Fourier transform of the lower case variable, k is wavenumber, and ϕ is the flexural parameter,

$$\phi = \left[1 + \frac{Dk^4}{(\rho_m - \rho_{infill})g}\right]^{-1} \tag{6.5}$$

For the case of Airy isostasy (i.e. D=0), $\phi = 0$, and the solution to Equation 6.4 reduces to,

$$w = S\left[\frac{(\rho_s - \rho_w)}{(\rho_m - \rho_{infill})}\right] + \Delta_{sl}\left[\frac{\rho_w}{(\rho_m - \rho_{infill})}\right] \tag{6.6}$$

Figure 6.12 illustrates that a sedimentary layer (S) may be considered as the sum of a load (y) and its flexure (w), i.e. $S = y + w$. We also see that the TTS (Y) is the sum of the load and water depth, i.e. $Y = y + W_d$. Therefore, by setting $\rho_{infill} = \rho_w$, the

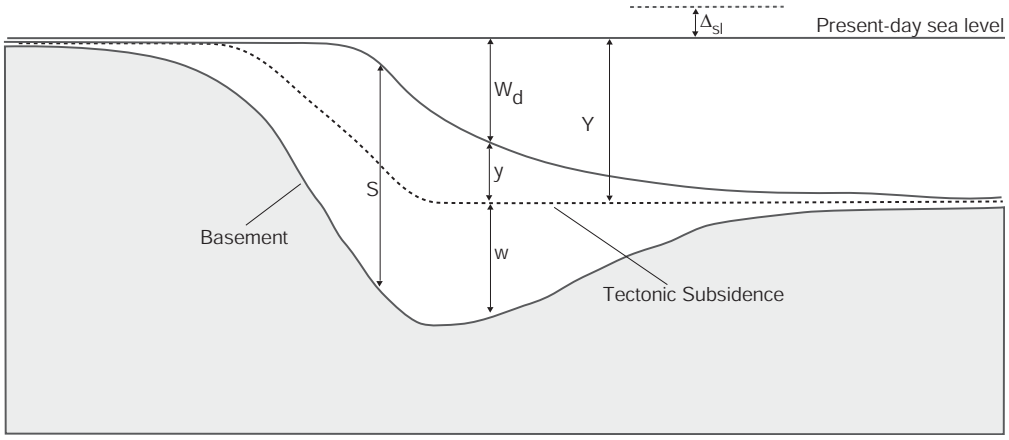

Figure 6.12: Schematic representation of the backstripping process. A sedimentary layer of thickness S can be considered as the sum of a load, y, and its flexure, w. The total tectonic subsidence (TTS), $Y = y + W_d$, is shown as a dashed line.

TTS for Airy isostasy ($D = 0$) is given by,

$$\begin{aligned} Y &= S - w + W_d \\ &= S - \left[S \left(\frac{(\rho_s - \rho_w)}{(\rho_m - \rho_w)} \right) + \Delta_{sl} \left(\frac{\rho_w}{(\rho_m - \rho_w)} \right) \right] + W_d \end{aligned} \tag{6.7}$$

The TTS for the flexural case is, following the logic above, given by,

$$Y = S - \mathcal{F}^{-}1 \left[\phi \hat{S} \left(\frac{(\rho_s - \rho_w)}{(\rho_m - \rho_w)} \right) + \hat{\Delta_{SL}} \left(\frac{\rho_w}{(\rho_m - \rho_w)} \right) \right] + W_d \tag{6.8}$$

where $\mathcal{F}^{-}1$ represents the inverse Fourier transform.

6.2.2 Stretching Factor (β) and Rifted Crust Structure

Combining the backstripping process with kinematic rift models (e.g. McKenzie [1978]) allows a quantitative estimation of crustal thinning in rift basins. Crustal structure and the stretching factor (β) can be determined from the backstripped basement (TTS) by assuming a state of isostasy during rifting.

For Airy isostatic compensation during rifting, subsidence is compensated locally by crustal thinning, and conversely uplift is compensated by crustal thickening. Assuming Airy isostasy during rifting implies a zero-strength lithosphere. Strength, or layers of increased strength, within the lithosphere introduce a flexural component to the compensation of a rift basin.

Dynamic modelling of Braun & Beaumont [1989], using a finite element model with a depth dependent rheology, showed that thinning or *necking* occurs preferentially at the depth of the lithospheric strength maxima. Kooi *et al.* [1992] define the *depth of*

necking as a surface which, in the absence of gravity or buoyancy forces, would not move vertically during extension. For a given depth of necking (Z_{neck}) and stretching factor (β), Weissel & Karner [1989] showed that the kinematic rift basin depth (S_t), as shown in Figure 6.13, is given by

$$S_t = (1 - \frac{1}{\beta})Z_{neck} \tag{6.9}$$

and that the $Moho$ occurs at a depth of T_c/β below S_t, where T_c is the initial, zero-elevation, crustal thickness.

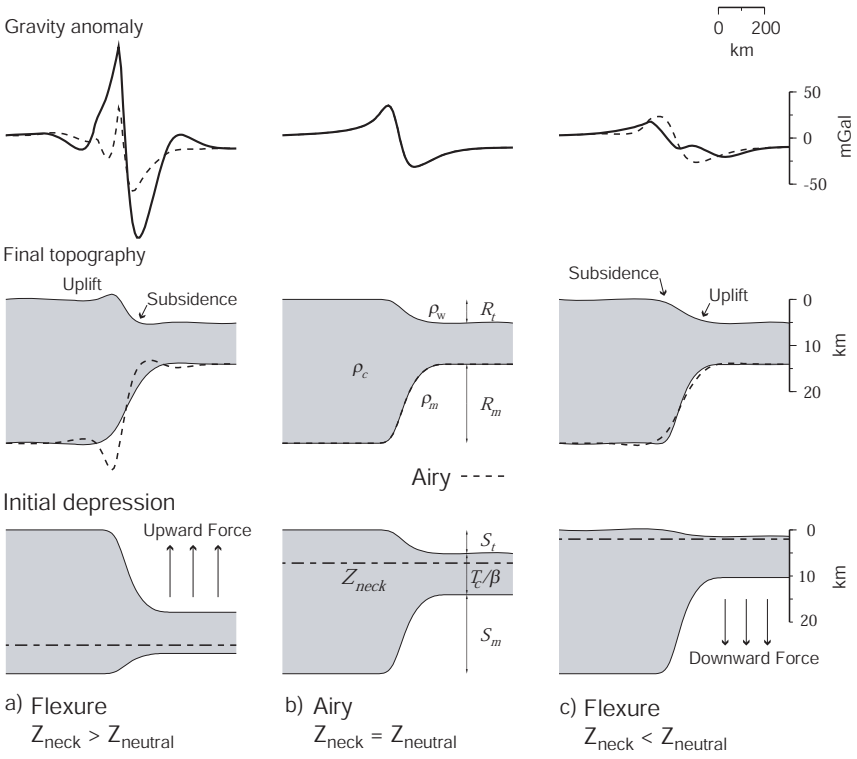

Figure 6.13: Schematic illustration of the effect of including a depth of necking, Z_{neck}, in rift modelling. The forces associated with an a) oversized, and c) undersized basin, and their effects on the initial and final rift topography and gravity anomaly are illustrated. b) shows the Airy or $Z_{neck} = Z_{neutral}$ solution for comparison. Reproduced from Watts [2001] after Watts & Stewart [1998].

The isostatic inequilibrium associated with the initial, kinematic basin depth causes vertical forces which act to restore isostatic equilibrium. The balance of upward and downward forces, q_{net}, associated with the replacement of crust by mantle and air/water respectively, is given by (for a water filled basin),

$$q_{net} = [S_m(\rho_m - \rho_c) + S_t(\rho_w - \rho_c)]g \tag{6.10}$$

where ρ_m, ρ_c, and ρ_w are the densities of the mantle, crust and water respectively. The final basin depth (R_t) and *Moho* upwarp (R_m) is controlled by the distribution of q_{net} and the strength of the lithosphere during rifting.

For any given combination of crust, mantle, and infill density, and initial crustal thickness, there exists a unique Z_{neck} for which $q_{net} = 0$, we call this $Z_{neutral}$. For $Z_{neck} = Z_{neutral}$, the basin geometry is equivalent to that predicted by Airy compensation. For $\rho_c = 2800\,kg/m^3$, $\rho_m = 3300\,kg/m^3$, $\rho_w = 1030\,kg/m^3$, and $T_c = 35\,km$, $Z_{neutral} =\sim 7.7$ km. Weissel & Karner [1989] demonstrated that for $Z_{neck} < Z_{neutral}$ a shallow basin with increased *Moho* relief forms, and conversely for $Z_{neck} > Z_{neutral}$ a deep basin with subdued *Moho* relief forms (Figure 6.13).

Watts & Stewart [1998] directly related the TTS to β, accounting for both Z_{neck} and a finite syn-rift strength (Te_{rift}),

$$\beta^{-1} = \frac{q_{net}(x) - [Y - Z_{neck}](x)\,\psi(x)}{Z_{neck}\,\psi(x) + q_0} \tag{6.11}$$

where

$$\psi(x) = Dk^4 + (\rho_m - \rho_w)g$$

Equation 6.11 allows the β distribution to be determined directly from the backstrip, taking into account the possibility of strength during rifting. Once β is determined, it is a simple matter to compute the $Moho$ configuration [Watts & Stewart, 1998].

6.2.3 Process-Oriented Modelling

The observed gravity anomaly at a continental margin can be considered as the result of all dynamic and geological processes that have shaped it through time. These include rifting, volcanism, sedimentation, and magmatic underplating [Watts & Fairhead, 1999]. The 'Process-oriented' method models the gravitational contribution of individual geological processes, with an aim of better understanding the causes of edge-effect variations. This method contrasts with object-oriented modelling, where the density structure that best explains the observed gravity anomaly is determined.

Object-oriented modelling is useful in determining the physical properties of the lithosphere, however, the non-uniqueness of any model is amplified by the sensitivity to user input. Object-oriented methods also provide little insight into the effect that geological processes may play in the evolution of a margin. The process-oriented method is a powerful forward modelling technique as it allows the long term mechanical properties of the lithosphere to be constrained, by considering the geological processes that have shaped the margin through time. Additionally, the direct methods by which the process-oriented

method models the gravity anomalies, using defined formative processes, helps to address the problems of non-uniqueness inherent to gravity modelling.

Process-oriented modelling describes a three-stage process (Figure 6.14) that is particularly applicable in rifted continental margin environments where spectral techniques are incapable of extracting T_e estimates due to large sedimentary accumulations. The foremost and most basic assumption of this technique is that prior to rifting there existed a crust of uniform average thickness, T_c, that was stretched during rifting to create a subsided and water filled, rift basin.

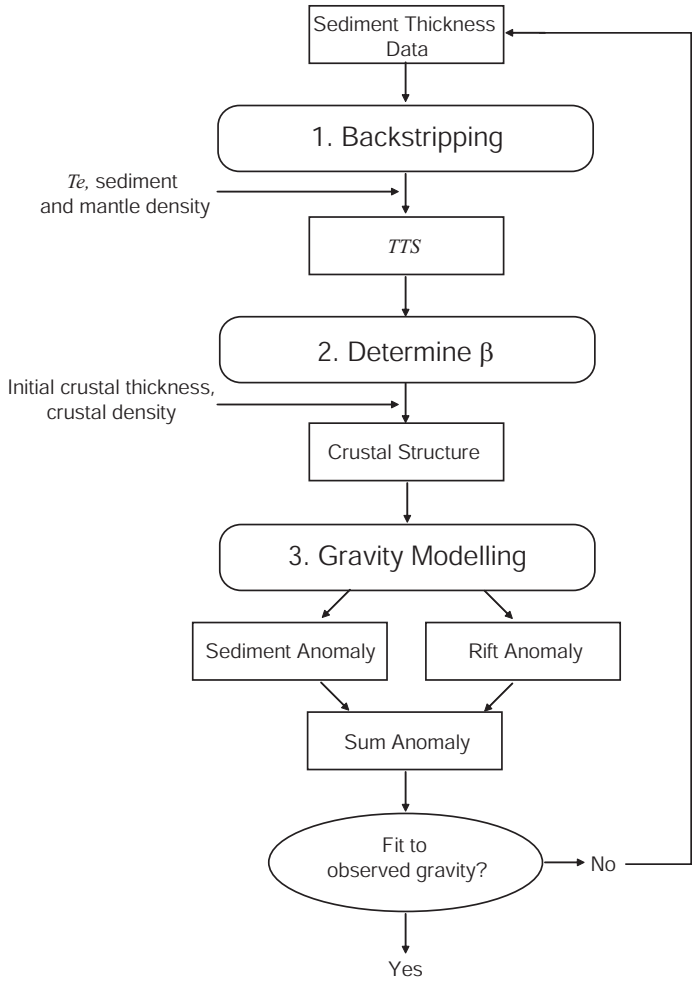

Figure 6.14: Flow chart of the three stages involved with process-oriented modelling.

The first stage of the process-oriented method involves backstripping sediments within the rift basin to determine the *TTS*. The second stage requires the determination of the stretching factor (β), assuming either Airy or flexural isostasy during rifting. The third stage involves the calculation of gravity anomalies that can be summed and compared to the observed gravity anomaly. The model gravity anomaly is considered to be the sum

of the gravity effects of all the processes operating at the margin. The three-stages of the process-oriented method are iterated until an optimal fit between modelled and observed gravity anomalies is achieved.

The third stage of the process-oriented method applied here models the competing gravity effects of rifting and sedimentation. Hence, the gravity anomalies associated with rifting, the *rift anomaly*, and sedimentation, the *sediment anomaly*, are calculated independently and summed to create the *sum anomaly*.

The rift anomaly (Figure 6.15a) is the anomaly associated with the changes in crustal thickness resulting from the rifting process, without the disturbing effect of sediment loading. It comprises the negative contribution of water replacing crust ($\rho_w - \rho_c$) and the positive contribution of mantle replacing crust ($\rho_m - \rho_c$). The depth of the basin is defined by the TTS surface and the depth to the *Moho* by the β factor distribution determined in stage 2. The anomaly is characterised by a landward high, over the seaward edge of unstretched crust, and a flanking low, over the stretched crust. The geometry of this anomaly represents the greater wavelength of the positive mantle anomaly due to its greater depth.

The sediment anomaly (Figure 6.15b) is the anomaly associated with sedimentation within the rift basin and its compensation. It comprises a positive component due to the replacement of water by denser sediments (i.e. $\rho_s - \rho_w$) and negative components due to their compensation, which occurs at the basement (i.e. $\rho_s - \rho_c$) and at the *Moho* (i.e. $\rho_c - \rho_m$). As the compensation occurs at greater depths than the sediment load, the wavelengths of the corresponding gravity anomalies (flexure and *Moho* flexure anomalies in Figure 6.15b) are greater relative to that of the sediment load. Hence, the sedimentation anomaly comprises a single high with flanking, lower amplitude, lows.

The sum anomaly (6.15d) is simply the sum of the rift and sediment anomalies. This is because the sum anomaly is a result of mass additions (or subtractions) to the original, uniform thickness crust and the gravity effect of these anomalies have been calculated *in situ*. The sum anomaly represents the gravity contribution of the crustal thickness changes associated with a dynamic rifting process, and the subsequent modification of the rift structure by sedimentation. The addition of the sediment anomaly to the rift anomaly shifts the positive peak oceanward over the new prograded shelf break. The relative importance of the component anomalies depends upon the thickness and geometry of the sedimentary sequence and on the T_e structure.

The form of the sum anomaly can differ significantly for low and high T_e margins. Figure 6.16 illustrates two simple margin models with different T_e structures. The "weak" margin is characterised by a double edge effect anomaly, comprising two relatively lower amplitude and shorter wavelength positive anomalies over the original and new shelf

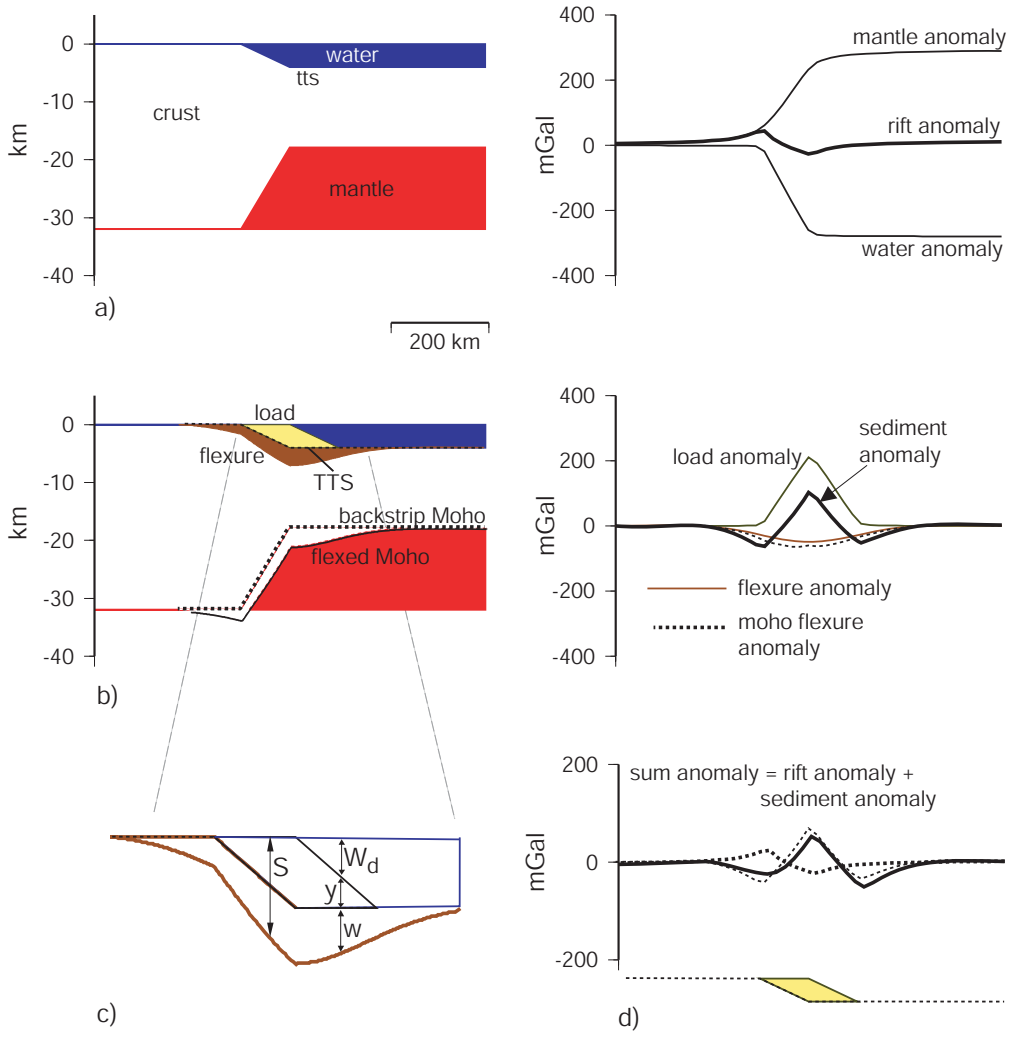

Figure 6.15: Schematic representation of important components and principles of process oriented gravity modelling. a) Original rift margin structure and associated rift anomaly. b) Present day margin structure, loaded with flexurally compensated sediments, and the sediment anomaly. The Total Tectonic Subsidence (TTS), determined from backstripping, is the crucial surface for defining load and flexure in the process-oriented method. c) Detailed section of sediment sequence and the relationship between load and flexure. d) Sum gravity anomaly (solid black) and component rift and sediment anomalies (dashed black).

breaks. Whereas the "strong" margin exhibits the more typical single edge effect anomaly, of greater amplitude and wavelength, with the peak amplitude reached over the locus of the thickest sediments [Watts & Marr, 1995]. The terms strong and weak here are not meant to characterise the actual margin strengths, which requires knowledge of the maximum stresses required to cause failure. Rather, the terms are used to describe the

lithosphere's ability to support long term loads. In the case of the strong margin, much of the load is supported by lithospheric strength. In contrast, the load at a weak margin is primarily supported by the underlying fluid substratum [Watts & Marr, 1995].

The above simple examples demonstrate that the form of the edge effect anomaly is a strong function of the strength of the underlying lithosphere. Although the gravity signal of the original margin structure is modified by sediment loading for both the weak and strong cases, the strength of the lithosphere determines the form of this modification [Watts & Marr, 1995].

Figure 6.16: Simple models of a) *weak*, low T_e, and b) *strong*, high T_e - margins and their associated process oriented, sum free air gravity anomalies. A marked difference in the modelled gravity anomaly is observed for these two models, indicating a strong dependence of the gravity signal on T_e.

6.2.4 Isostatic Anomalies

Residual gravity anomalies that remain after subtracting the isostatically modelled gravity field from the observed field are labelled *Isostatic Anomalies* (IA). If Airy isostasy is

assumed in modelling, then the term Airy isostatic anomaly is used. If regional isostatic compensation is assumed in modelling, then the residual anomalies are labelled flexural isostatic anomalies.

If geometries and properties of a model are perfectly constrained, but isostatic anomalies remain, it indicates that a load is somehow "undercompensated" or "overcompensated" in the sense that there is a deficiency or excess of mass involved in its compensation [Stewart, 1998]. If Airy isostatic anomalies remain it may indicate that loads are supported by the flexural strength of the lithosphere so that compensating masses may be offset from the load, however, integration of such isostatic anomalies over the region of compensation should tend to zero. Two further explanations of both Airy and flexural isostatic anomalies are.

1. A load may not have been present or absent for a sufficient period to allow a region to achieve isostatic equilibrium, accordingly isostatic gravity anomalies will be measured over the region. For example, areas subject to Pleistocene glaciation not completely adjusted to the removal of ice loads (e.g. Walcott [1973]).

2. The presence of density anomalies within the lithosphere, even if compensated, can also cause isostatic anomalies (Figure 6.17). A mass excess within the crust may be completely locally compensated, however, if there is no associated topographic expression then neither the mass or its compensation is accounted for in an isostatic model. Hence, an isostatic anomaly exists despite perfect isostatic balance within the lithosphere.

The process-oriented method allows isostatic anomalies to be computed that account for flexural compensation, accordingly we take isostatic anomalies to represent density anomalies or departures from the assumed isostatic regime. Density anomalies in the post-rift sedimentary sequence are likely to be directly resolved by changes in reflection character and/or by zones of anomalous seismic velocity. In the absence of such observations it is reasonable to assume that inferred density anomalies are intra- or sub-crustal. Typically, the wavelength of an isostatic anomaly will indicate whether it is likely that the causative source is at crustal or mantle levels. The process-oriented method, therefore, allows the density structure of the crust to be interrogated without the interfering effects of other geological processes (e.g. rifting, sediment loading).

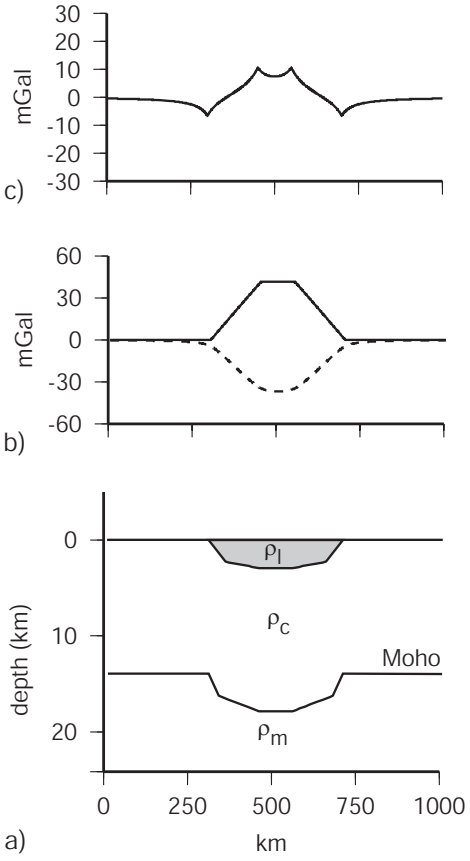

Figure 6.17: a) A mass anomaly (ρ_l) within the crust (ρ_c), that is perfectly locally compensated at the crust/mantle (ρ_m) boundary. b) the free-air anomalies associated with the mass anomaly (solid) and its compensation (dashed). c) The isostatic anomaly that exists in this situation despite perfect local isostatic compensation.

6.3 2-Dimensional Gravity Modelling on the Wilkes Land Margin

6.3.1 Airy Isostatic Models

Classic Airy Modelling

The conceptually simplest gravity model utilised in margin studies is the *"classic-Airy"* model which considers the observed basin topography to be supported by crustal thickness variations. The crustal thinning required to Airy compensate a basin is calculated, assuming some initial, zero-elevation crustal thickness (T_c), from the observed water depth (T_w). This is achieved by mass balancing the base of an unstretched crustal column with a water, stretched-crust, and mantle column (Figure 6.18). That is,

$$\rho_c T_c = \rho_w T_w + \rho_c t_c + \rho_m T_m \tag{6.12}$$

Where ρ_w, ρ_c and ρ_m are the densities of water, crust and mantle respectively. Solving this for either T_m or t_c allows the *Moho* geometry to be defined, e.g.

$$T_m = T_w \frac{\rho_c - \rho_w}{\rho_m - \rho_c} \tag{6.13}$$

The gravity effect of the topography is calculated, using a density contrast of $\rho_w - \rho_c$, for the water filled rift basin. The gravity effect of the compensation is calculated assuming a density contrast of $\rho_m - \rho_c$. These competing gravity contributions are summed to calculate the classic-Airy gravity anomaly.

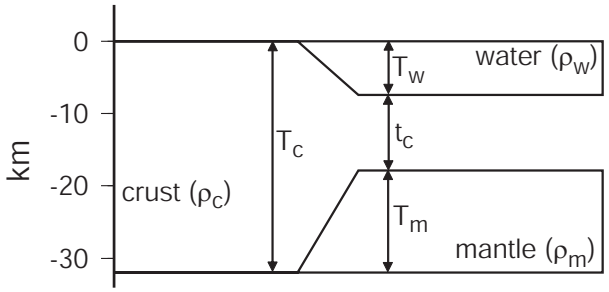

Figure 6.18: Schematic representation of parameters important in determining the crustal structure for a rift basin of depth T_w.

As this type of model makes no corrections for the effects of sedimentation on the total gravity field, it is more likely to yield close fits to observed data for regions of low sediment thickness. The difference between the observed FAA and the gravity effect of the topography and its Airy-type compensation is the Airy isostatic anomaly, as discussed previously.

The Airy isostatic anomaly was used by early workers as a means of identifying the COB location in a number of rift margin basins, [Rabinowitz & LaBrecque, 1977; Talwani & Eldholm, 1973], although it was subsequently demonstrated that the outer

high observed in Airy isostatic anomaly profiles, interpreted to represent the COB, could be explained by considering flexural compensation of sediment loads [Karner & Watts, 1982].

Classic-Airy models were created for survey lines GA-228_18 to GA-228_29 and GA-229_06 using MCS derived bathymetry supplemented by GEBCO 1 minute bathymetry data between the Antarctic coast and the survey line terminations. The models for selected lines and their calculated gravity fields are plotted and compared to the satellite and shiptrack gravity fields in Figures 6.19 and 6.20. The location of the edge effect anomaly is correctly located in the modelled sections. However, the fit between the observed edge effect low and corresponding section of the modelled profile is poor. In general, the long wavelength positive gradient observed seaward of the edge effect low is matched by the modelled profiles, however, the shorter wavelength components included in observed data are not simulated in these simple models.

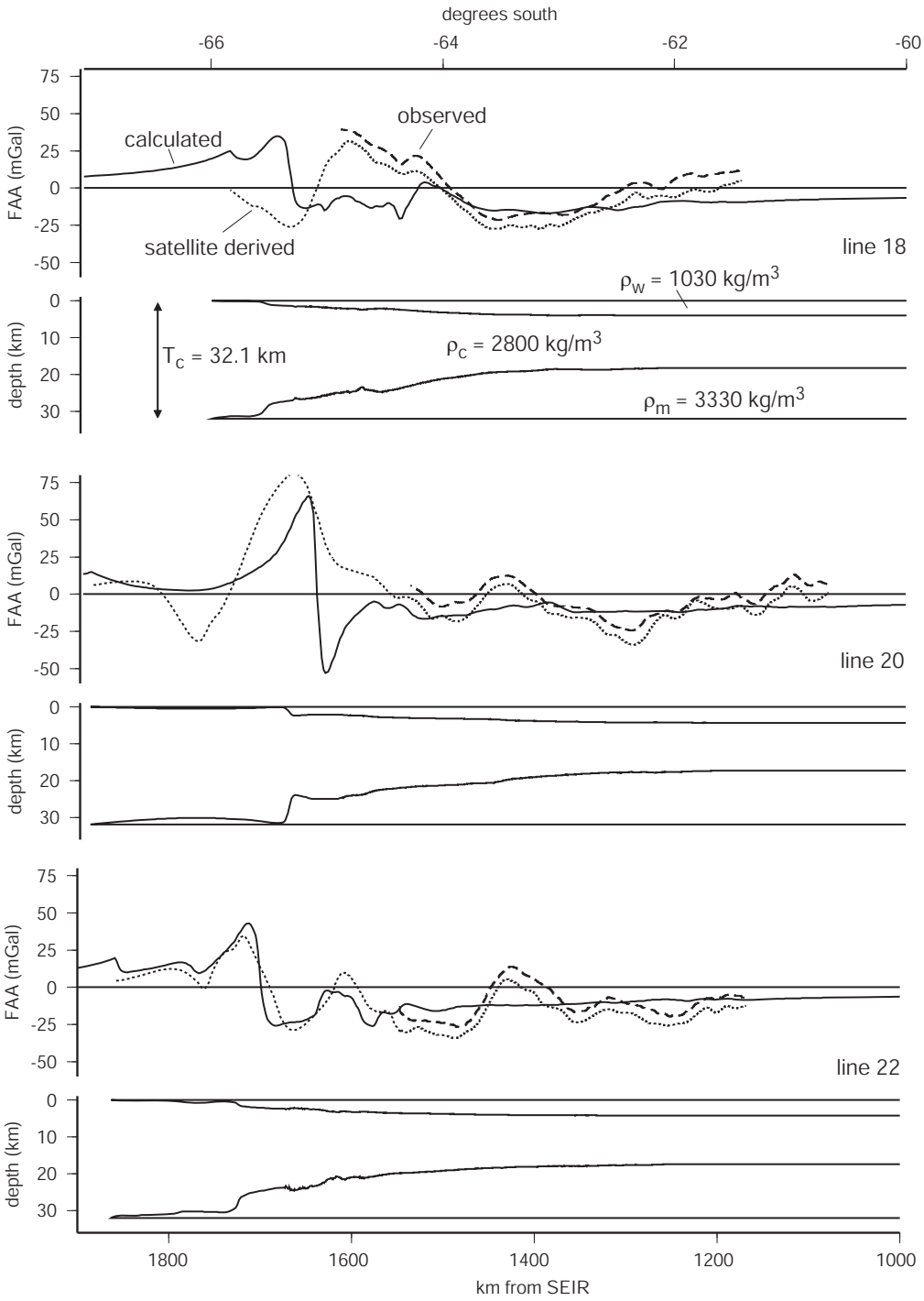

Figure 6.19: Classic Airy isostatic gravity models for survey lines GA-228_18, GA-228_20 and GA-228_22, and corresponding modelled free air gravity anomalies (solid black) compared to observed free air gravity (dashed black) and satellite derived (dotted black) free air gravity from Sandwell & Smith [1997].

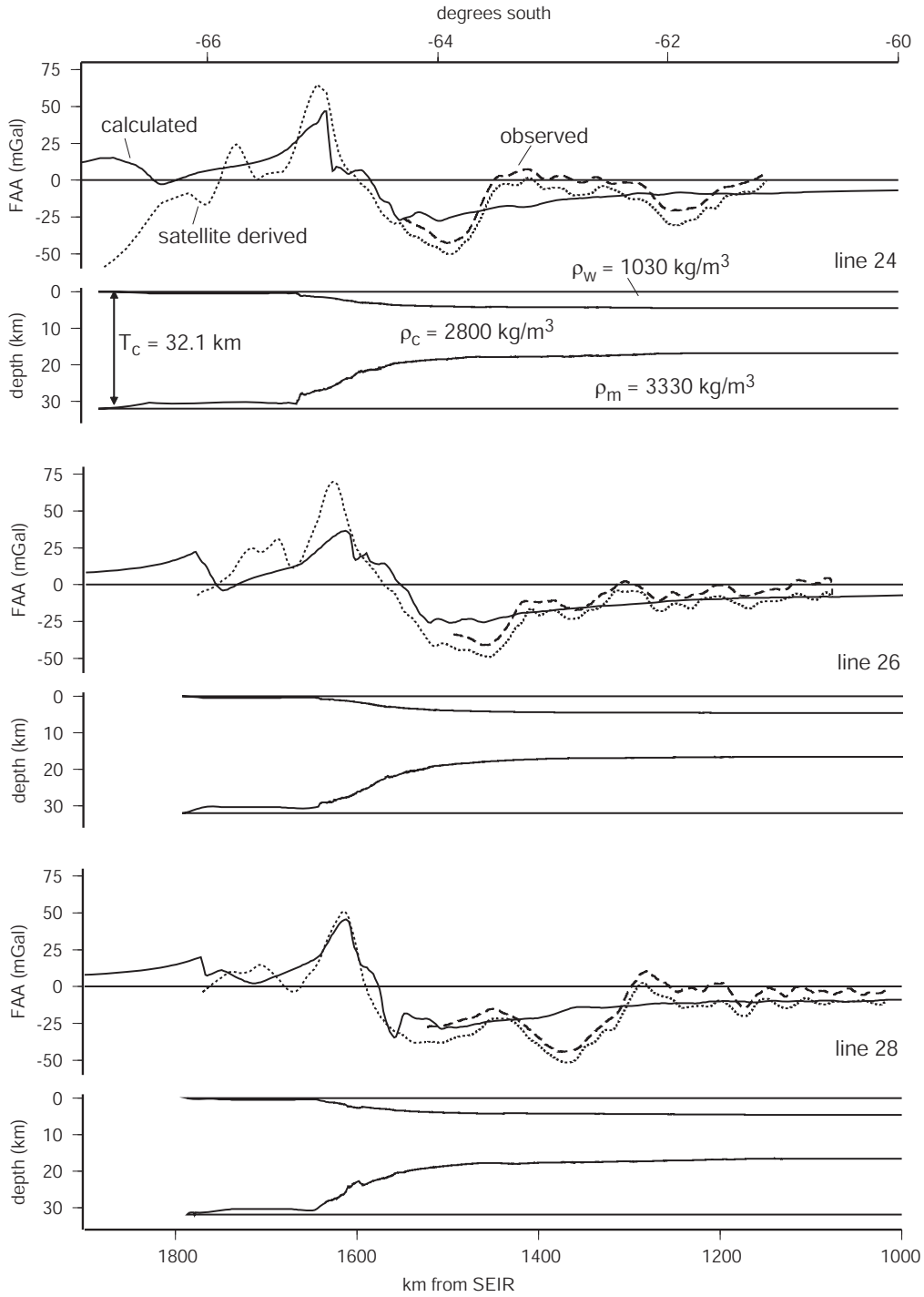

Figure 6.20: Classic Airy isostatic gravity models for survey lines GA-228_24, GA-228_26 and GA-228_28, and corresponding modelled free air gravity anomalies (solid black) compared to observed free air gravity (dashed black) and satellite derived (dotted black) free air gravity from Sandwell & Smith [1997].

Sediment Corrected Airy Modelling

The classic-Airy model can be adjusted to incorporate sediment thickness data where available. This process essentially provides a simple sediment correction by adding a third model body that is assumed to be replacing crust and completely locally compensated (Figure 6.21). Similarly to the classic-Airy approach, the depth to *Moho* can be calculated to maintain a state of Airy isostatic balance by considering

$$\rho_c T_c = \rho_w T_w + \rho_s t_s + \rho_c t_c + \rho_m T_m \tag{6.14}$$

where variables are as for Equation 6.12 and ρ_s and t_s are the density and thickness of sediment respectively. Solving this for either T_m or t_c allows the *Moho* geometry to be defined by

$$T_m = \frac{A(\rho_c - \rho_w) + t_s(\rho_w - \rho_s)}{\rho_m - \rho_c} \tag{6.15}$$

where $A = T_w + t_s$ (Figure 6.21).

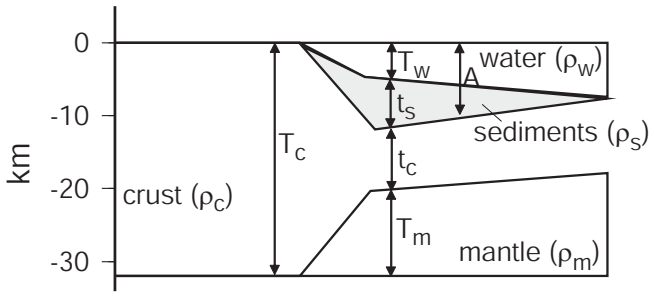

Figure 6.21: Schematic representation of parameters important in determining the crustal structure for a rift basin of depth T_w with a sedimentary section of thickness t_s.

The gravity calculations required for the sediment corrected Airy model are as for the classic-Airy model, with a further negative contribution associated with the sediment body ($\rho_s - \rho_c$). Sediment corrected Airy models were created for survey lines GA-228_18 to GA-228_29 and GA-229_07 using the same procedure as for the classic-Airy case, however, a sediment body defined by depth converted MCS data was included.

In general, the addition of an Airy compensated sediment body does not improve the fit between the calculated and observed FAA relative to the classic-Airy models (Figure 6.22). In each of the sediment corrected Airy model profiles the amplitude of the edge effect anomaly is decreased relative to the classic-Airy models (except for Line GA-228_18. The biggest misfit between calculated and measured gravity anomalies is observed on line GA-228_18, where the locus of thickest sediments corresponds to a large amplitude positive FAA. The classic and sediment corrected Airy models both predict a negative anomaly at this location, this indicates that the sedimentary sequence, at least in part, is not Airy or locally compensated.

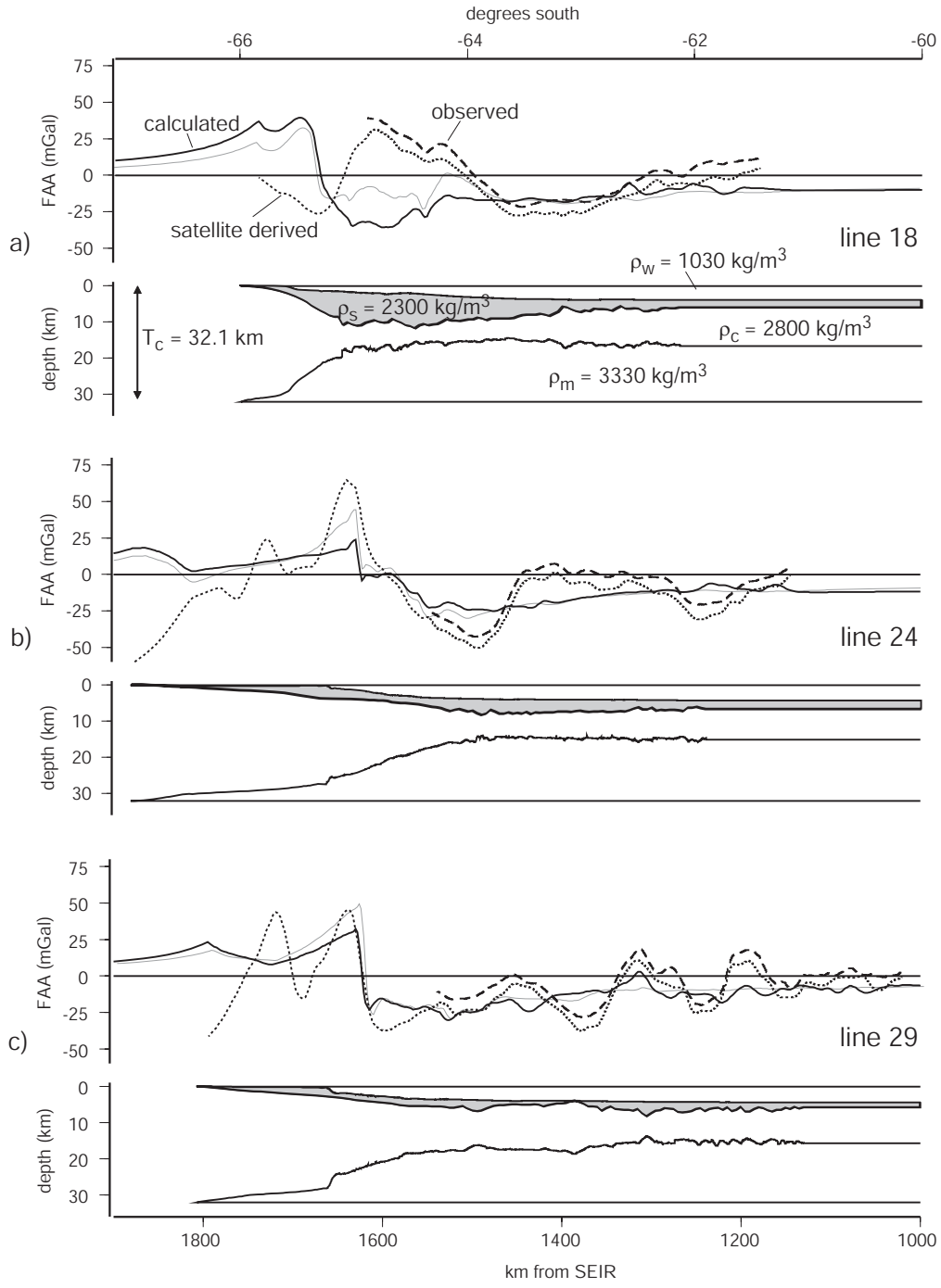

Figure 6.22: Sediment corrected Airy isostatic gravity models for survey lines GA-228_18, GA-228_24 and GA-228_29, sediment bodies are shaded grey. Corresponding free air gravity anomalies (solid black), shiptrack (dashed black) and satellite (dotted black) derived free air gravity data are shown above the modelled crustal section. The classic-Airy calculated anomaly profile is illustrated for comparison as a thin, grey line.

Summary of Airy Modelling

Results of classic-Airy modelling indicate that the broad trends of the observed gravity field are controlled by basin topography and its compensation. The results of the sediment corrected Airy models indicate that it is unlikely that sediments are locally compensated, and that flexural compensation of the sediment load is important at the Wilkes Land margin. This is particularly evident for west Wilkes Land, where large misfits between calculated and observed FAA correlate to the locus of the thickest sediments along the Wilkes Land margin.

6.3.2 Two-Dimensional Process Oriented Modelling

Introduction

The correlation of large positive free air gravity anomalies and the locus of thickest sediments off west Wilkes Land is taken to indicate that the sediment load is flexurally compensated, implying a finite crustal strength. Process oriented modelling is used here to investigate the flexural strength of the crust and its relationship with observed gravity anomalies.

Initial process oriented modelling was conducted utilising a single backstrip (i.e. backstripping the entire sediment thickness in a single step), with non varying T_e values in stage 1. Airy compensation was assumed in determining stretching factors and rifted crustal structure in stage 2 (i.e. no strength during rifting). This makes the implicit assumption that during rifting (i.e. heating and stretching) the lithosphere is massively weakened and local compensation is applicable, and that as the thermal anomaly decays (e.g. McKenzie [1978]) the lithosphere regains strength such that sediment loading may be supported by flexure of the lithosphere. Kusznir & Park [1987] demonstrated that the geothermal gradient exerts the strongest control on lithospheric strength and that a decreasing thermal perturbation correlated to increasing lithospheric strength, which provides support for this assumption in stage 2.

The process-oriented method is illustrated for line GA-228_21 using a constant T_e of 15 km in Figure 6.23. Each of the component anomalies associated with the rift and sediment anomalies are shown before summing and comparison with the observed signal. The procedure is as for the synthetic example above.

Modelling is repeated for a range of T_e estimates to determine the T_e that provides the best fit between calculated and observed gravity anomalies. Specific observed anomalies may be best fit by different T_e models. This is demonstrated in Figure 6.24 where a star marks regions of best fit on different calculated profiles. Some sections are equally well fit by almost all T_e values, and others again are not well fit by any of the calculated

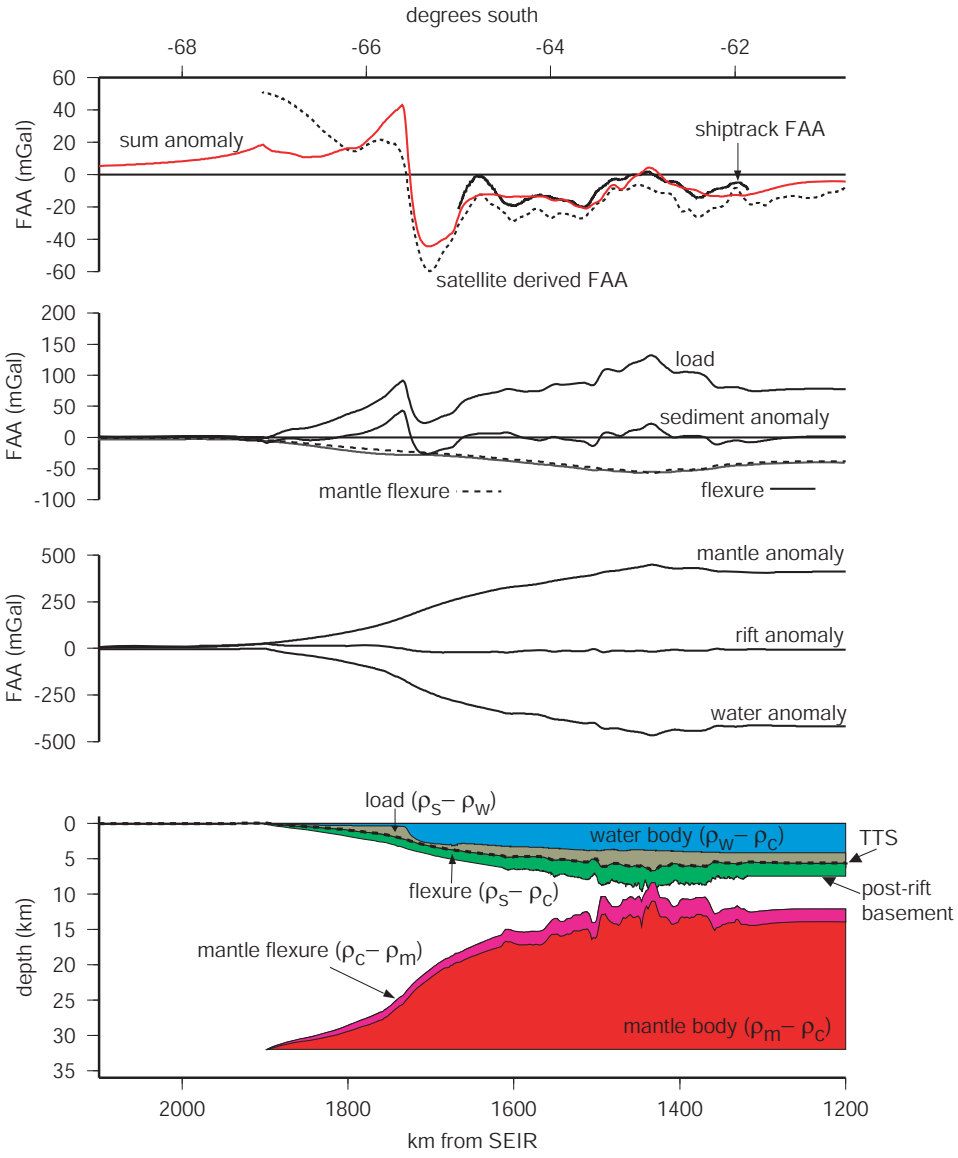

Figure 6.23: The process oriented method demonstrated for line GA-228_21 using a T_e of 15 km.

profiles. These relationships provide information regarding spatial variation in T_e. Spatial variation can be important in defining along margin segmentation (e.g. Watts & Stewart [1998]) or inferring the location of the COB (e.g. Watts [1988]).

A more quantitative way of assessing the fit of calculated and observed anomalies is to calculate and analyse the flexural isostatic anomaly. Where the flexural isostatic anomaly is defined as the *difference* between the calculated and observed anomalies as outlined previously. Sections of low and high isostatic anomaly indicate good and poor fit between calculated and observed data respectively. Hence, the standard deviation (SD) or root mean square (RMS) of the flexural isostatic anomaly profiles is another means of

determining the best fitting calculated T_e profile.

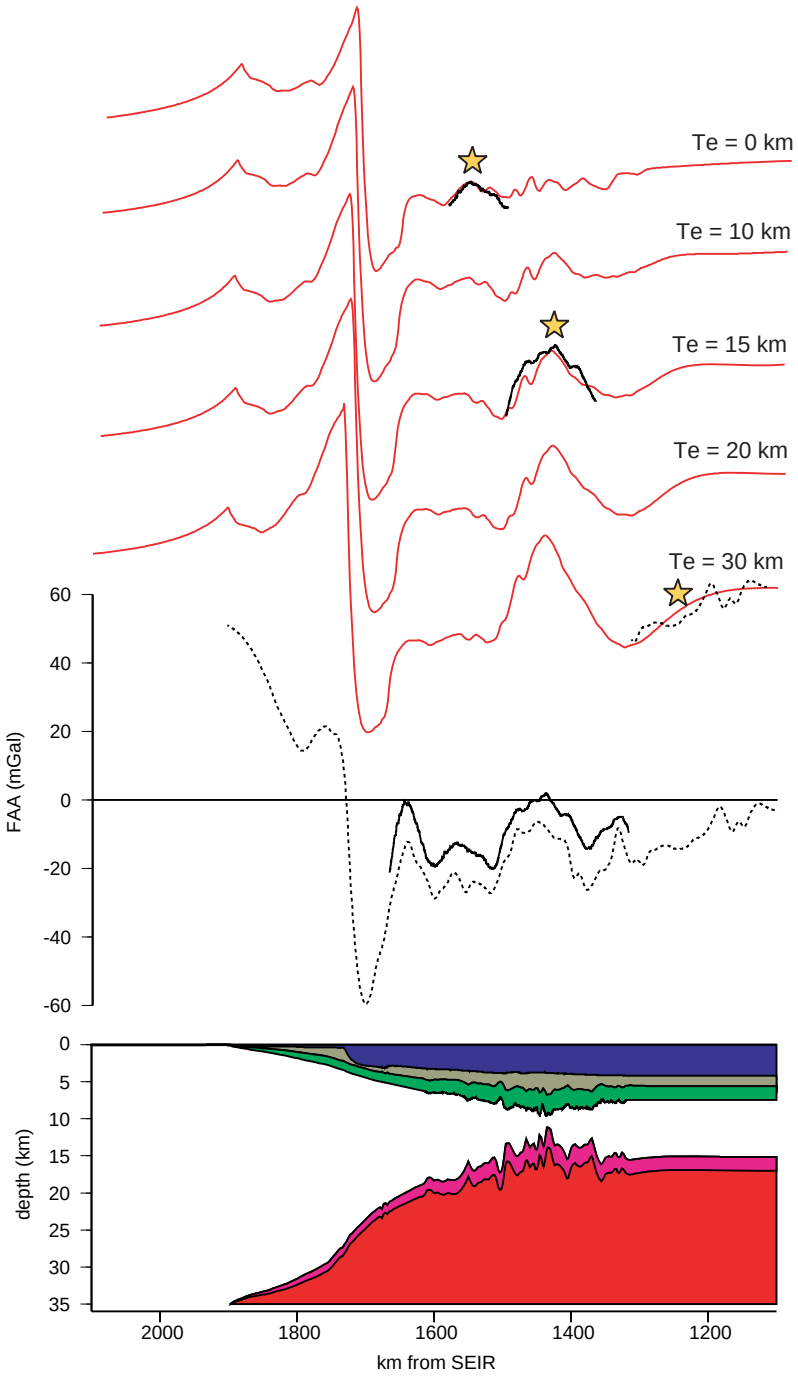

Figure 6.24: Comparison of observed FAA data to modelled profiles for a range of T_e values. Specific sections of observed data are best fit by different T_e models as marked by a yellow star, the observed data is overlain the modelled to emphasise these correlations (shiptrack = solid, satellite derived = dashed).

Sensitivity Analysis

An analysis of the sensitivity to variations in model parameters, namely ρ_s, ρ_c, ρ_m, T_c and T_e was undertaken. Figure 6.25 illustrates the variation in the RMS of the flexural isostatic anomaly for varying model parameters for lines GA-228_18 and GA-228_29. Lines GA-228_18 and GA-228_29 are subjected to the greatest and smallest magnitudes of sediment loading respectively, and are therefore representative of the extremes of model sensitivity.

Figure 6.25 demonstrates the greater sensitivity to parameter variation for line GA-228_18 models relative to line GA-228_29. Plots of RMS as a function of ρ_c, ρ_s, ρ_m and T_c illustrate that the model is relatively insensitive to variation in these parameters for $\rho_c < 2900kg/m^3$. Except for the case of a low density mantle ($\rho_m < 3200kg/m^3$) where the limit of sensitivity for crustal density is $\rho_c = 2800kg/m^3$. This indicates an upper bound on crustal density of 2800-2900 kg/m^3. The sensitivity of the model, for $\rho_c < 2900kg/m^3$ is much higher for variation in T_e relative to density or T_c variation. Although this is more profound for line GA-228_18 it is still evident for line GA-228_29. This indicates that models are more sensitive to parameter variation for greater sediment thicknesses, however, the greater relative sensitivity to T_e variation is evident for the range of sediment thicknesses observed along the Wilkes Land margin.

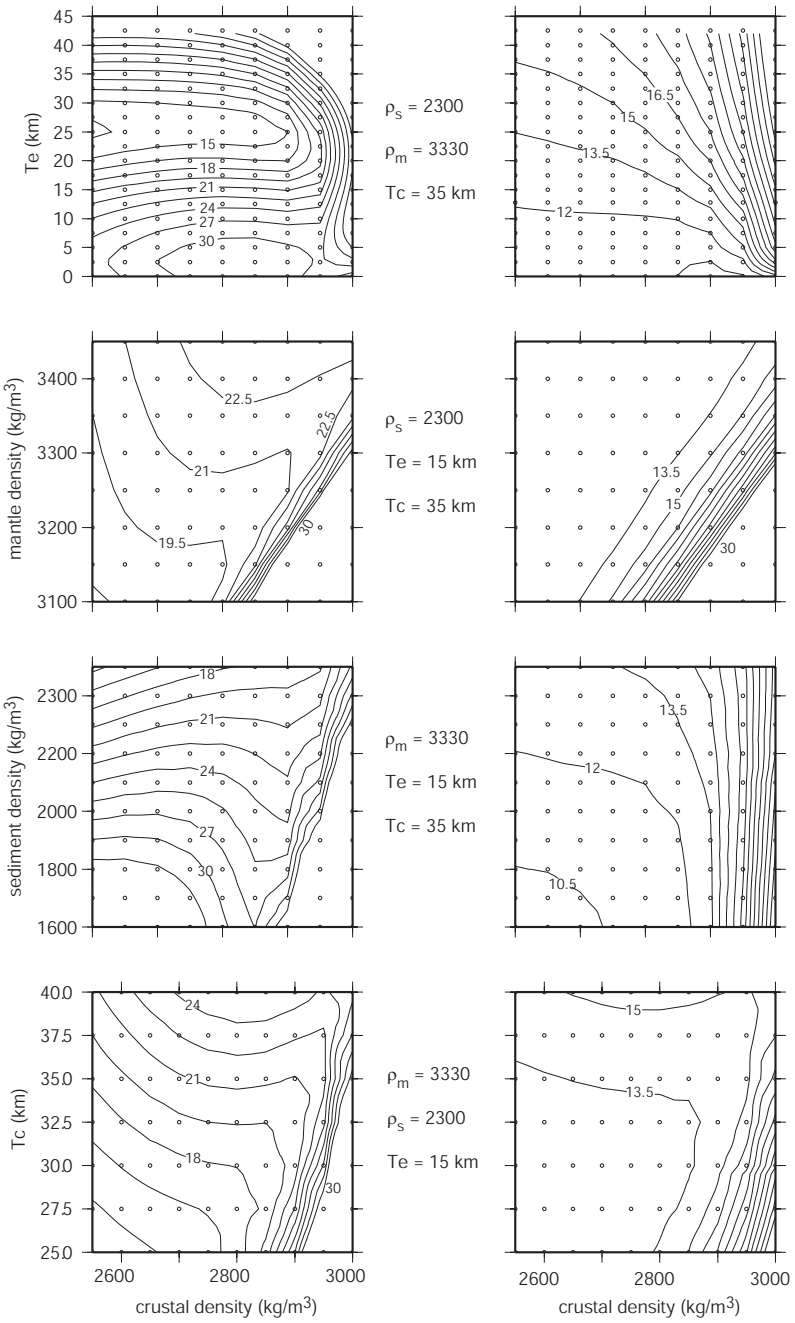

Figure 6.25: Sensitivity of isostatic anomaly to model parameters for lines GA-228_18 and GA-228_29 (left and right panels respectively) as a function of crustal density (ρ_c). Contour interval is 1.5 mGal and RMS values of greater than 30 mGal are excluded. The RMS of the flexural isostatic anomaly is more sensitive to variation in T_e relative to other model parameters (for $\rho_c < 2900\,kg/m^3$). Mantle, crustal, and sediment density denoted by ρ_m, ρ_c, and ρ_s respectively, all in units of kg/m^3.

Modelling

Utilising the parameters constrained via the initial modelling and sensitivity analysis (Table 6.2) process-oriented modelling was completed for lines GA-228_18 to GA-228_29 and GA-229_06. The depth converted MCS reflectors and their landward extrapolations (as detailed in Chapter 4) were used to constrain model geometries. A range of T_e and crustal thickness values were tested for each line and RMS values calculated for each associated isostatic anomaly profile to assess the fit with the observed gravity data. Figures 6.26 to 6.32 shows for each line the model created with T_e=15 km and calculated profiles, for a range of T_e values, compared to the shiptrack and satellite free air gravity. The greatest sensitivity to T_e is on the western lines, and specifically over the greatest sediment thicknesses associated with the Budd Coast Basin. The calculated profiles for lines GA-228_27 to GA-228_29 are similar for all T_e values tested, this is not surprising given that the T_e is extracted by analysing load induced flexure. Where the crust has not been significantly loaded (sediment thickness of these eastern-most lines rarely exceeds 2 km) the backstrip is relatively insensitive to T_e.

Parameter	**Range and Units**
Initial crustal thickness, T_c	29 - 35 km
Crustal density, ρ_c	2800 kg/m^3
Sediment density,ρ_s	2300 kg/m^3
Mantle density, ρ_m	3330 kg/m^3
Water density, ρ_w	1030 kg/m^3

Table 6.2: Parameters utilised in process oriented modelling.

The initial crustal thickness parameter, T_c, was varied to comply with two simple principles. Firstly, the T_c must be great enough such that the *TTS* surface remains shallower than the modelled *Moho* surface, i.e. there are no negative β values. Regions where the present day basement is at great depth or the sea floor is anomalously deep require greater values of T_c as a significant shallowing of the *Moho* is necessary to compensate for deep, water filled basins. Secondly, that the modelled flexed *Moho* depth correlates with any *Moho* velocities extracted from refraction data and also to the depth of inferred *Moho* reflections from MCS data. Less confidence can be placed in *Moho* depths indicated by MCS reflections as the conversion of these from time to depth could introduce errors of up to several km due to poor constraints on velocity models, used for depth conversion, at greater depth. The refraction and reflection inferred *Moho* horizons are overlain on the models in Figures 6.26 to 6.32. A summary of the characteristic features

of models from the western, central and eastern Wilkes Land margin sectors, and their associated gravity anomalies follows.

Figures are constructed as follows: Models constrained by MCS data (lower panels), which include mantle (red), water (blue), sediment load (olive), crustal flexure (green) and *Moho* flexure (purple) bodies. MCS inferred *Moho* depths are indicated by thick blue lines, sonobuoy (SB) inferred mantle velocity refractor depths are indicated by a thick black line over the width that the sonobuoy recorded. Calculated gravity anomalies for a range of T_e values (red = 0 km to blue = 45 km) are compared to shiptrack (black solid) and satellite derived (black dashed) gravity anomaly data (middle panels). The isostatic anomaly (IA) for each T_e estimate is calculated for the length of shiptrack constrained data (upper panels). The RMS of the isostatic anomaly is plotted as a function of T_e (inset graphs), this provides an indication of the fit between calculated and observed anomalies.

West Wilkes Land

Lines GA-228_18 to GA-228_22 (Figures 6.26 to 6.28):

The observed edge effect anomaly is distorted off west Wilkes Land due to the lack of a distinct shelf break and the presence of uncompensated sediment banks as noted previously. This explains the poor fit between the modelled and satellite derived edge effect anomalies for Line GA-228_18. The poor fit between modelled and satellite derived edge effect anomalies on Lines GA-228_19 and GA-228_20 is more likely a function of uncertainties in sediment thickness and bathymetry, and poor quality satellite derived FAA data (due to the perpetual ice coverage of the continental shelf in this region). The edge effect is better modelled on Lines GA-228_21 and GA-228_22, however, the modelled edge effect is insensitive to T_e for these lines so no inferences regarding T_e are possible.

Broadly, models of Lines GA-228_19, GA-228_20 and GA-228_22 are relatively insensitive to variations in T_e, as demonstrated by the lack of clear minima in the RMS v T_e plots. However, for Line GA-228_19, models for higher T_e estimates (30-45 km) predict a positive anomaly over the locus of thickest sediments that simulates the peak amplitude and negative gradient flank of the broad positive observed anomaly. Seaward of this, the peak-trough-peak at ~62°S is almost perfectly matched by the T_e=0 km profile, indicating the presence of a T_e discontinuity at approximately this location.

Lines GA-228_18 and GA-228_21 are for more sensitive to T_e variations, as demonstrated by the RMS v T_e plots, and the observed data are well fit by calculated anomalies relative to other lines. A wide (>200 km), positive anomaly, with a peak amplitude of ~60 mGal, is located at the southern end of Line GA-228_18, over the locus of thickest

sediments. Calculated anomalies are very sensitive to T_e variation in this region. Low T_e estimates predict no anomaly, whereas for $T_e = 45$ km the calculated anomaly exhibits a peak amplitude ∼30 mGal greater than the observed anomaly. For $T_e = 30$ km, however, the calculated anomaly is almost identical to the observed anomaly in both shape and amplitude, and there is a clear minima in the RMS for this T_e. This high sensitivity to T_e and good fit between observed and calculated anomalies indicates that flexural compensation is important in this region and that the lithosphere is characterised by $T_e = 30$ km.

A clear minima in the RMS is evident for $T_e = 15$ km for models of Line GA-228_21. However, variations in T_e can be inferred across the margin. Seaward of the edge effect low, three distinct positive anomalies, of varying amplitude and width, are evident in observed data. The first (most landward) of these peaks is relatively narrow (∼50 km) and has an amplitude of almost 20 mGal, calculated profiles fail to predict this anomaly for any T_e estimate. The next distinct observed anomaly comprises a smaller peak amplitude of ∼10 mGal and a width of ∼75 km, this anomaly is matched very well by the $T_e = 0$ km modelled profile, which predicts both the amplitude and width very closely. Higher T_e profiles exhibit no predicted anomalies in this section. Further seaward is the broadest (∼120 km) and largest amplitude (>25 mGal) of the three anomalies. The observed anomaly is only fit in amplitude and width by the $T_e = 15$ km modelled profile, lower and higher T_e values lead to under and over estimations of amplitude respectively.

Crustal thickness is not constrained by seismic data in this region. The only interpreted *Moho* reflections occur on Line GA-228_22, where a laterally non-continuous reflector is observed beneath the outer continental rise at a depth of ∼15 km. For an initial crustal thickness (T_c) of 32 km, the depth of the modelled flexed *Moho* occurs within 1 km of the interpreted *Moho* reflector depth. Lines to the west of GA-228_22 are modelled with a $T_c = 35$ km, a lower T_c requires mantle compensation to occur at a shallower depth than basement, which violates the modelling principles outlined previously.

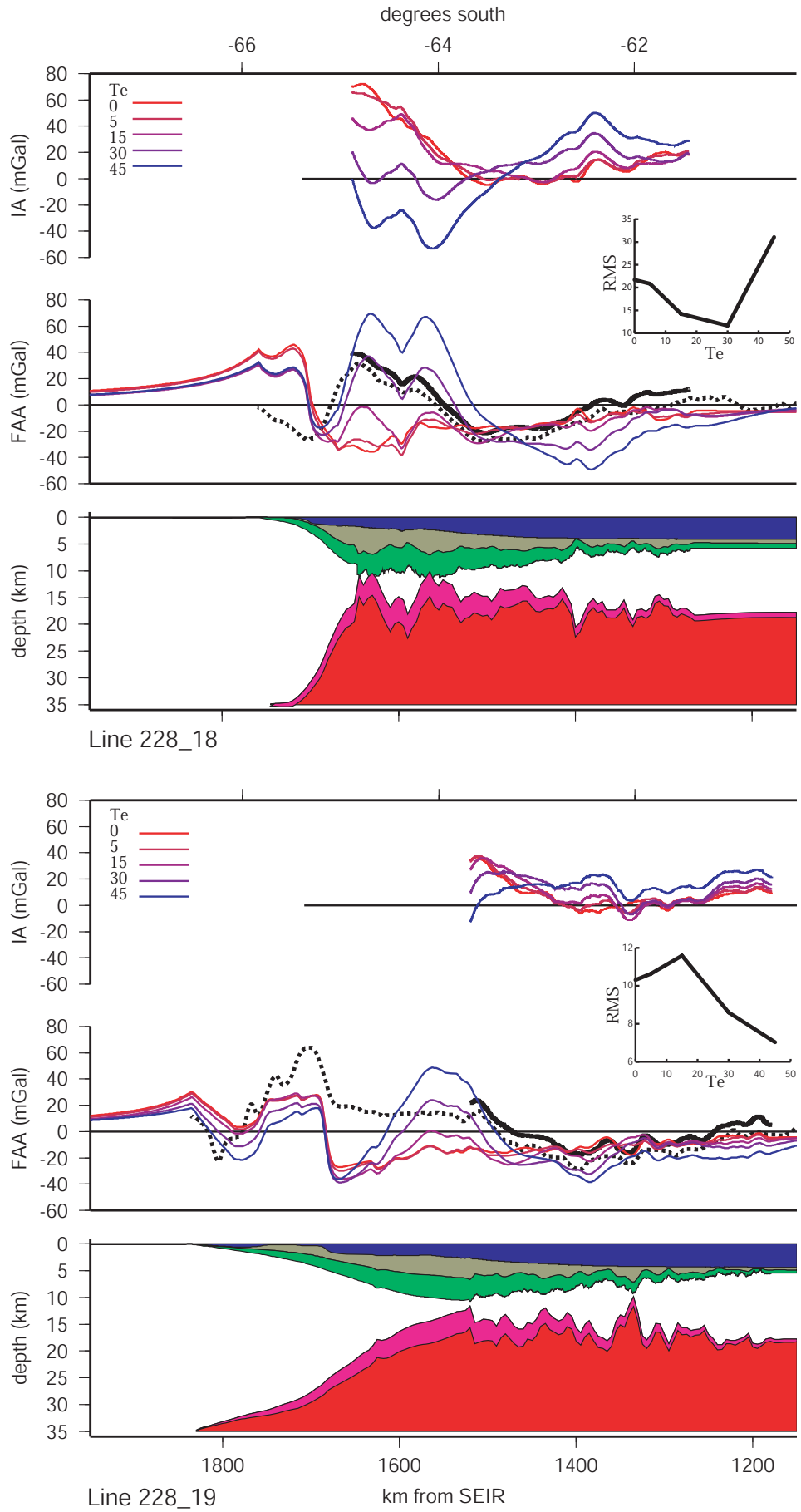
degrees south
-66
-64
-62
IA (mGal)
FAA (mGal)
depth (km)
Te
0
5
15
30
45
RMS
Te
Line 228_18
Line 228_19
1800
1600
1400
1200
km from SEIR

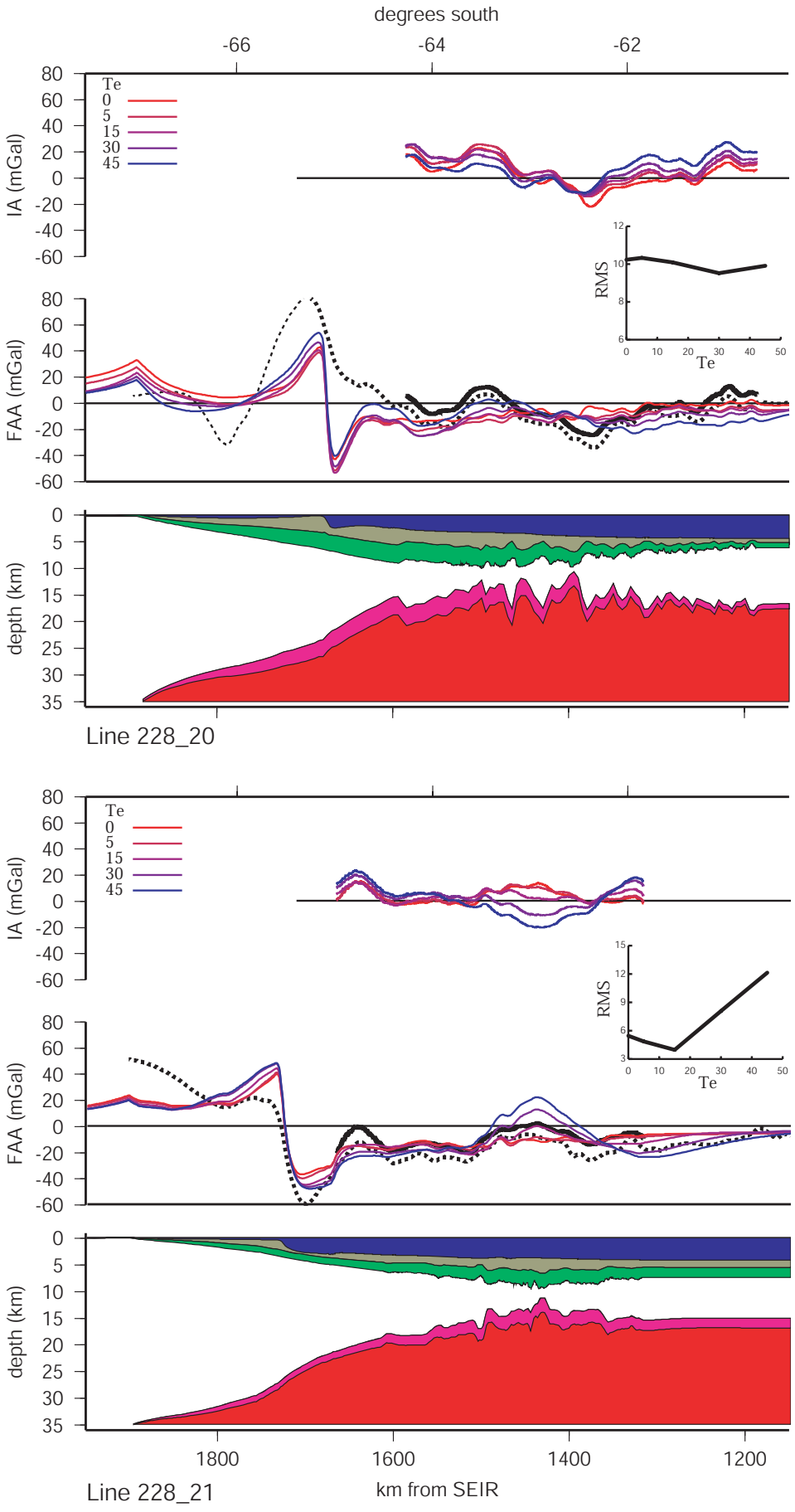

Figure 6.27: Lines GA-228_20 and GA-228_21 process-oriented modelling.

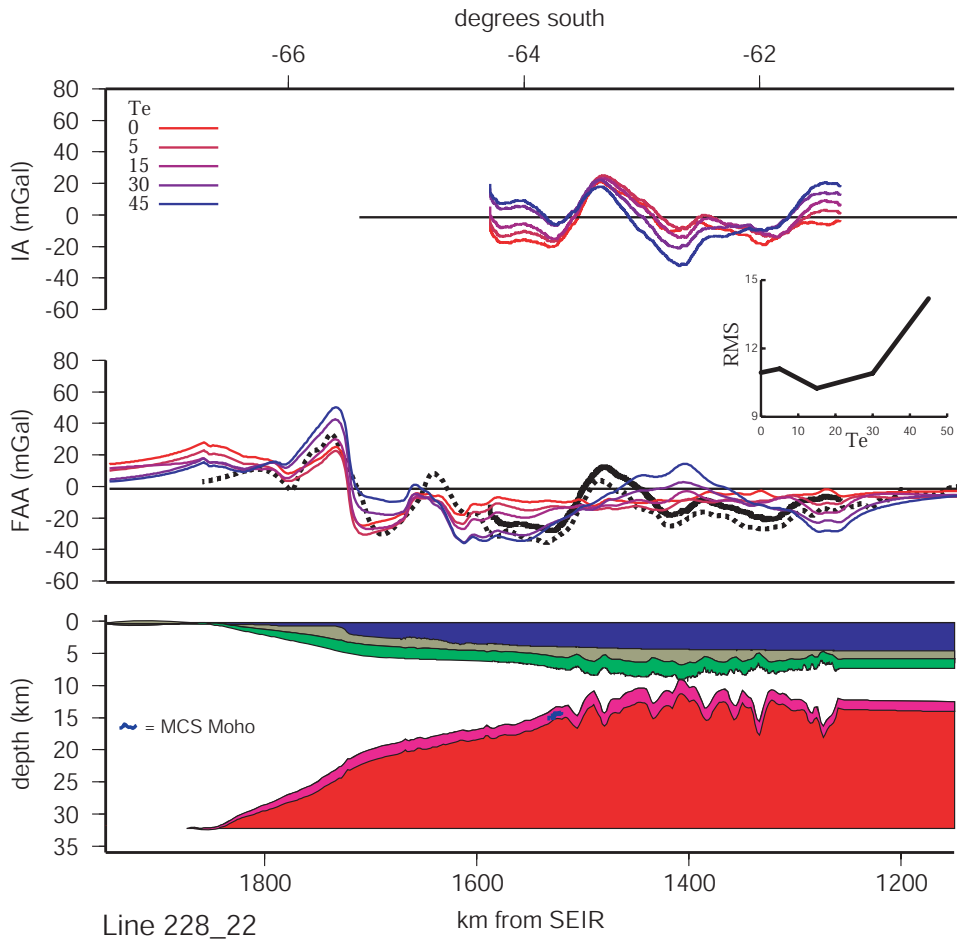

Figure 6.28: Line GA-228_22 process-oriented modelling.

Central Wilkes Land

Lines GA-228_23 to GA-228_26 (Figures 6.29 to 6.30):

The edge effect anomaly is characterised by a consistent amplitude and wavelength high-low couple in central Wilkes Land relative to the western and eastern sectors. Although not traversed by GA-228 and GA-229 shiptracks, some constraint on sediment thickness was provided by data from the *S. P. Lee* L184 survey data. The satellite derived edge effect anomaly is well simulated by calculated anomalies for each of the models from this margin sector. However, the peak positive amplitudes are only modelled for Line GA-228_23. This may be a function of incorrect assumptions regarding sediment thickness or uncertainties in the satellite derived FAA data. The edge effect is ubiquitously best modelled using high T_e estimates.

Broadly, the T_e = 30 km models provide the best simulation of observed anomalies in this sector. The fit of the observed positive anomalies seaward of the edge effect

low on Lines GA-228_23 and GA-228_24 is very sensitive to T_e, providing a high level of confidence in the inference of a high T_e. Additionally, the RMS v T_e plots exhibit clear minima for $T_e = 30$ km for all lines except Line GA-228_26, for which models are relatively insensitive to T_e.

The flexural isostatic anomaly profiles for Lines GA-228_23, GA-228_25 and GA-228_26 are characterised by a positive anomalies at the location of greatest crustal thinning. The origin of these anomalies is discussed further in Chapter 7.

Crustal structure and *Moho* depth is better constrained by seismic data for this sector relative to the western margin sector. *Moho* reflections are interpreted in seismic reflection data from all lines in this sector except Line GA-228_23. Although of limited lateral extent, their depths correlate to the depth of the modelled flexed *Moho* for $T_c = 31$ km.

Mantle velocities were also modelled from two sonobuoy stations in this sector on Lines GA-228_25 and GA-228_26. On Line GA-228_25, modelled sonobuoy data indicates a *Moho* depth of ∼12.5 km, which correlates almost exactly with the depth of both the seismic reflection interpreted *Moho* and the modelled flexed *Moho*. This further supports that $T_c = 31$ km for this margin sector. The sonobuoy modelled *Moho* depth for Line GA-228_26 correlates to the flexed *Moho* depth at its landward extent, however, the sonobuoy is located in a region of high *Moho* gradient according to Airy isostasy. The depth of the sonobuoy inferred *Moho* may be predicted too deep due to a dipping refractor, or alternatively the compensation may not be entirely local in this region. The misfit between modelled and observed gravity anomalies in this region would be improved if the mantle peak implied by Airy isostasy, but not supported by the limited seismic data, was not actually present.

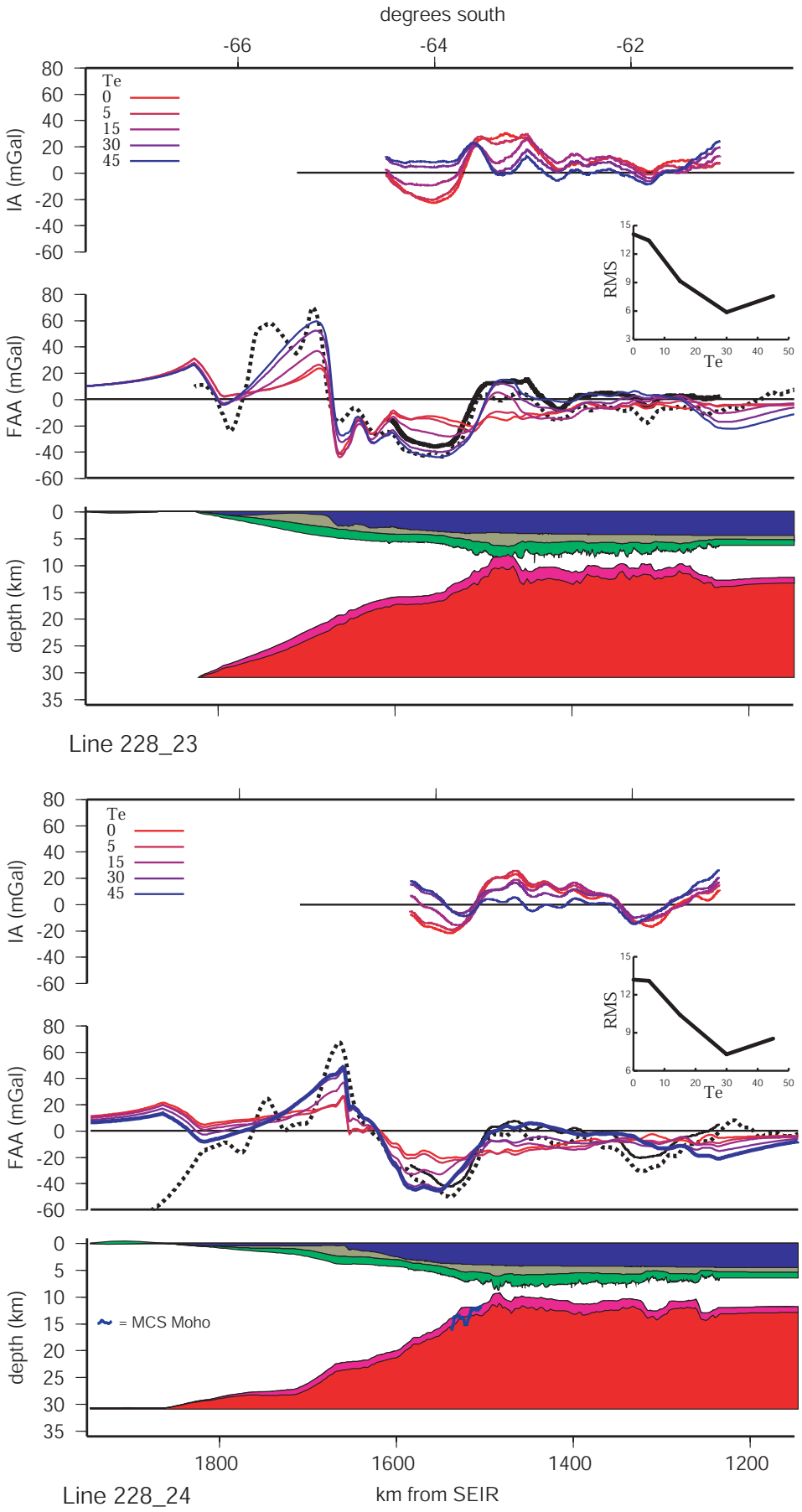

Figure 6.29: Lines GA-228_23 and GA-228_24 process-oriented modelling.

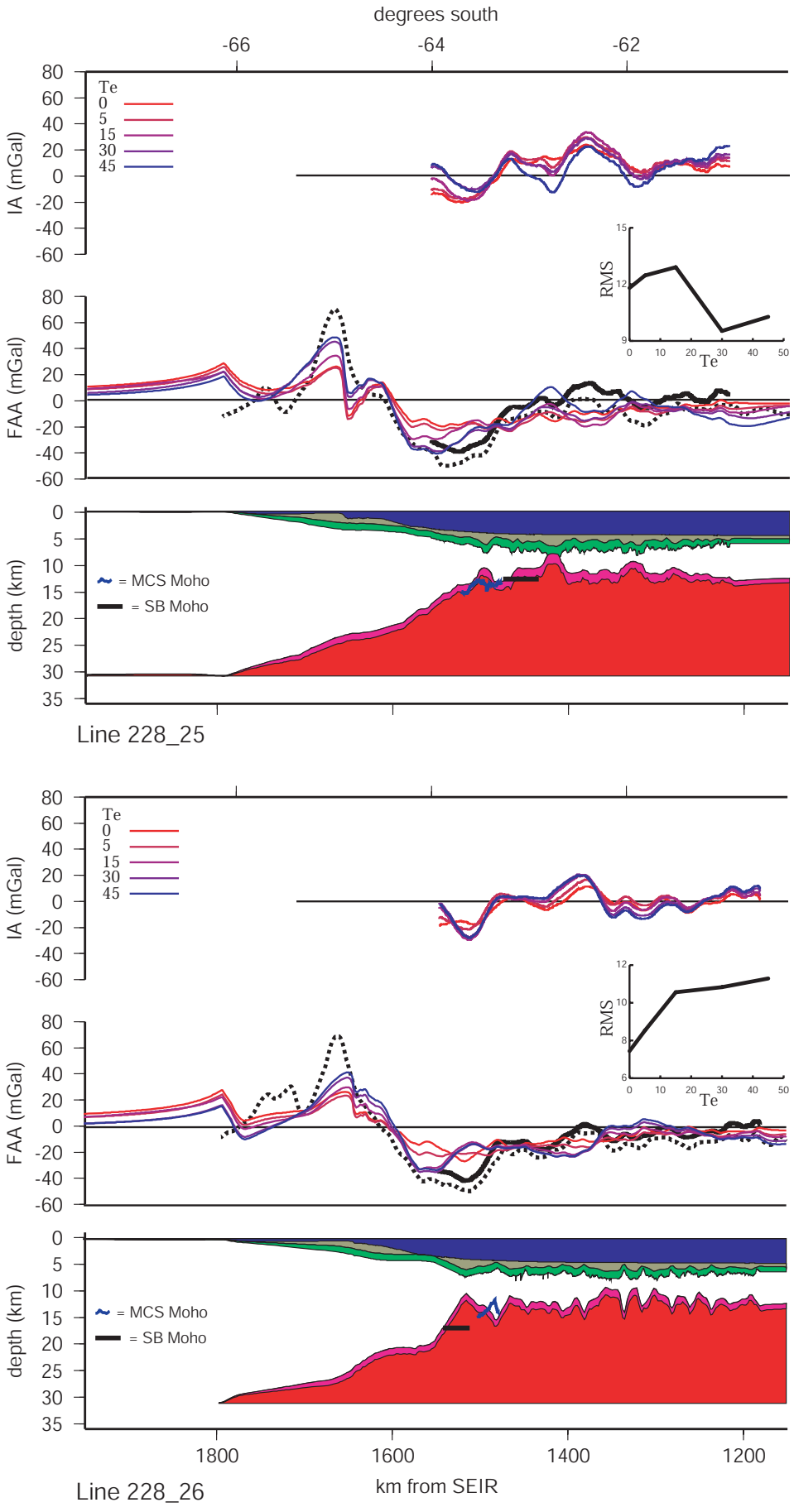

Figure 6.30: Lines GA-228_25 and GA-228_26 process-oriented modelling.

Eastern Wilkes Land

Lines GA-228_27 to GA-228_29 (Figures 6.31 to 6.32):

A relatively consistent edge effect anomaly extends along the margin in the eastern sector. The satellite derived edge effect anomaly is best simulated by models for T_e estimates of 30-45 km, particularly along the landward projections of Lines GA-228_27 and GA-228_28, which both exhibit T_e sensitivity in the region of the edge effect.

Calculated anomalies (for the shiptrack data constrained portion of the model) are relatively insensitive to T_e for Lines GA-228_27 and GA-228_28. The calculated anomalies, however, do account for most of the observed anomalies. Similarly to lines from the central sector, a positive isostatic anomaly is observed on Line GA-228_28 just seaward of the point of greatest crustal thinning.

A greater sensitivity to T_e is evident for models of Line GA-228_29, however, it is difficult to infer which T_e provides for the best fit between calculated and observed anomalies. This is primarily due to large amplitude basement topography and a relatively thin sediment cover. The positive anomaly immediately seaward of the edge effect low on this line is best modelled for a high T_e. However, the observed positive anomaly further seaward (at $\sim$62.5-62°S), which correlates to a basement high, is poorly simulated for high T_e. This poor fit is a result of the negative gravity effect of a deepening $Moho$ to compensate for the basement high. If the basement high is not locally compensated then the observed anomaly is well simulated by the high T_e calculated anomaly. Additionally, the seismic reflection interpreted $Moho$ correlates well for most of this line with the modelled flexed $Moho$, however, it does not predict a crustal thickening associated with this basement high.

The correlation between seismic constraints on $Moho$ depth and the modelled flexed $Moho$ is excellent in this margin sector for T_c = 29 to 30 km. The sonobuoy derived $Moho$ depth over oceanic crust on Lines GA-228_27 and GA-228_29 correlates very closely to the modelled flexed $Moho$ depths. The seismic reflection interpreted $Moho$ on Line GA-228_27 correlates closely to the depth of the modelled flexed $Moho$, except for at the point of maximum crustal thinning where the model predicts a mantle peak that is not observed in seismic data. This may indicate that the corresponding basement feature is not locally compensated, this would account for the negative isostatic anomaly that is associated with the elevated $Moho$. The geometry of the modelled flexed $Moho$ and the seismic reflection interpreted $Moho$ on Line GA-228_28 is remarkable, providing a high level of confidence in the assumed T_c and the assumption of Airy isostasy during rifting.

One exception in this margin sector, to the generally close correlation between the depth of the modelled flexed $Moho$ and the seismic reflection inferred $Moho$, occurs on

Line GA-228_29. The basement high at ~62.5°S corresponds to a modelled increase in crustal thickness, however, the interpreted *Moho* reflections do not deepen beneath this basement feature. This misfit in modelled and observed *Moho* depth and the positive isostatic anomaly that correlates to this feature may indicate non-local compensation.

Adélie Rift Block

Line GA-229_06 (Figure 6.32):

The satellite derived edge effect high is modelled equally well for all T_e estimates for this line, however, the edge effect low is poorly modelled. A positive anomaly seaward of the edge effect low correlates to the point of maximum crustal thinning interpreted from seismic reflection data. Seaward of this anomaly, over the basement high interpreted as the western edge of the Adélie Rift Block, a broad negative gravity anomaly is observed. The calculated anomaly is very sensitive to T_e in this region. This broad negative is very well simulated by the calculated anomaly profile for T_e = 45 km. However, similarly to Line GA-228_29 this is largely due to the negative gravity effect of crustal thickening associated with the basement high. There is no constraint on $Moho$ depth from sonobuoy data and only a very limited seismic reflection interpreted $Moho$ reflection for this line. Hence, it is difficult to assess whether the best fit for the high T_e model is actually representative of a rigid lithosphere, or simply an artifact of the assumption that basement features on all scales are locally compensated. A T_c of 30 km was assumed for this line.

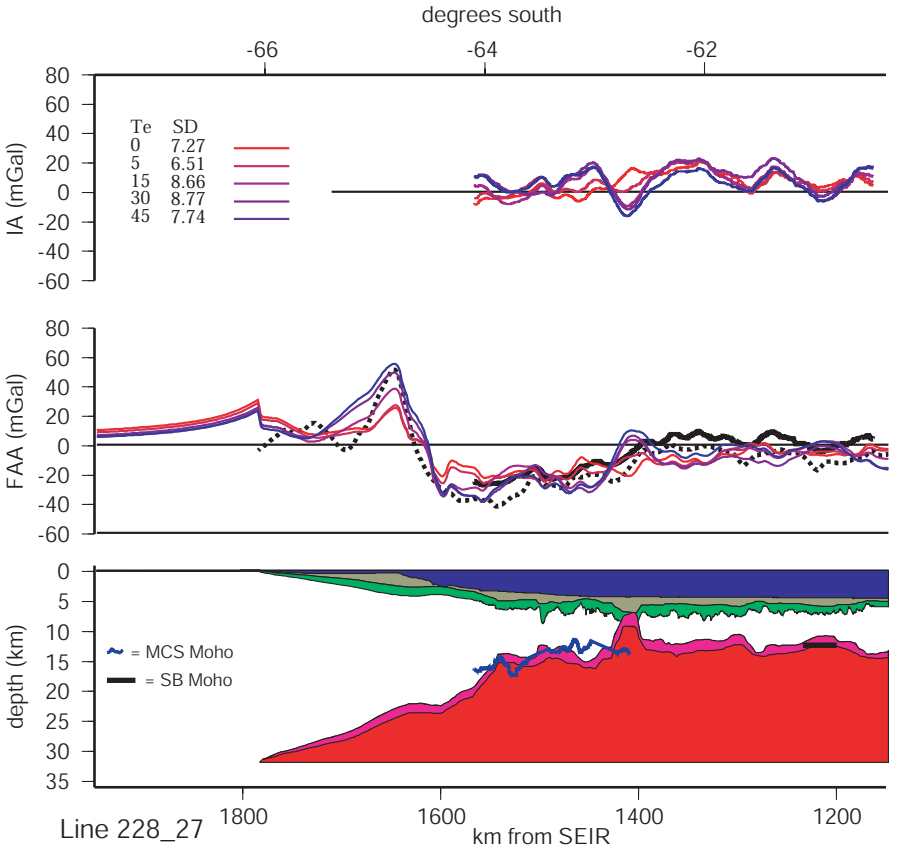

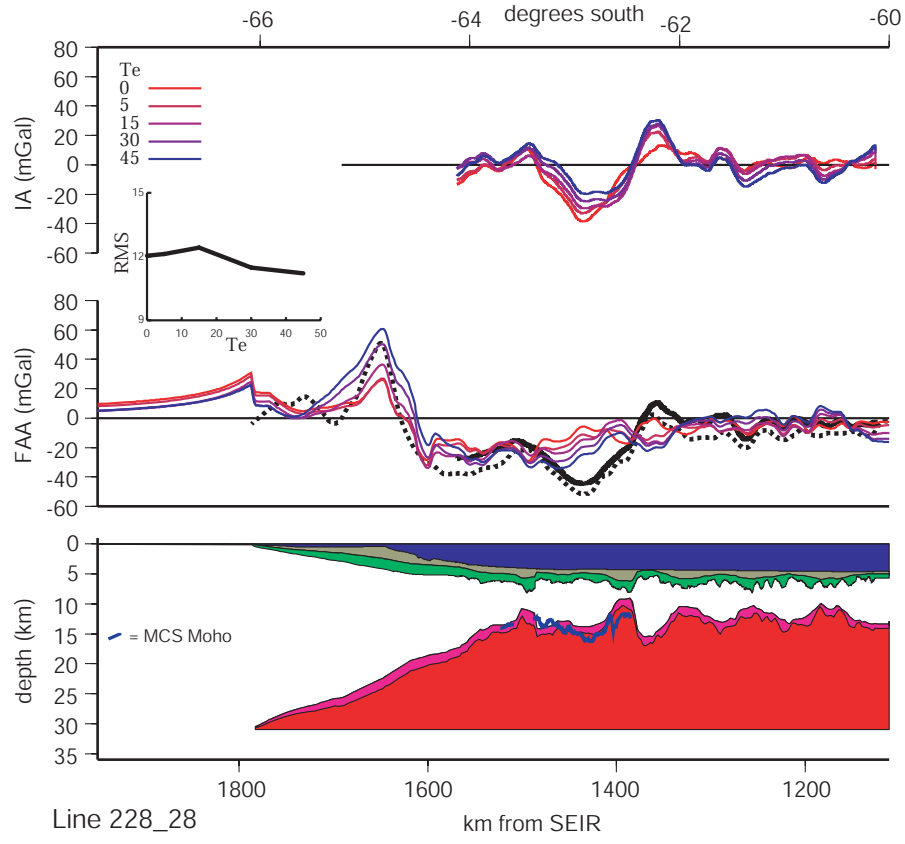

Figure 6.31: Lines GA-228_27 and GA-228_28 process-oriented modelling.

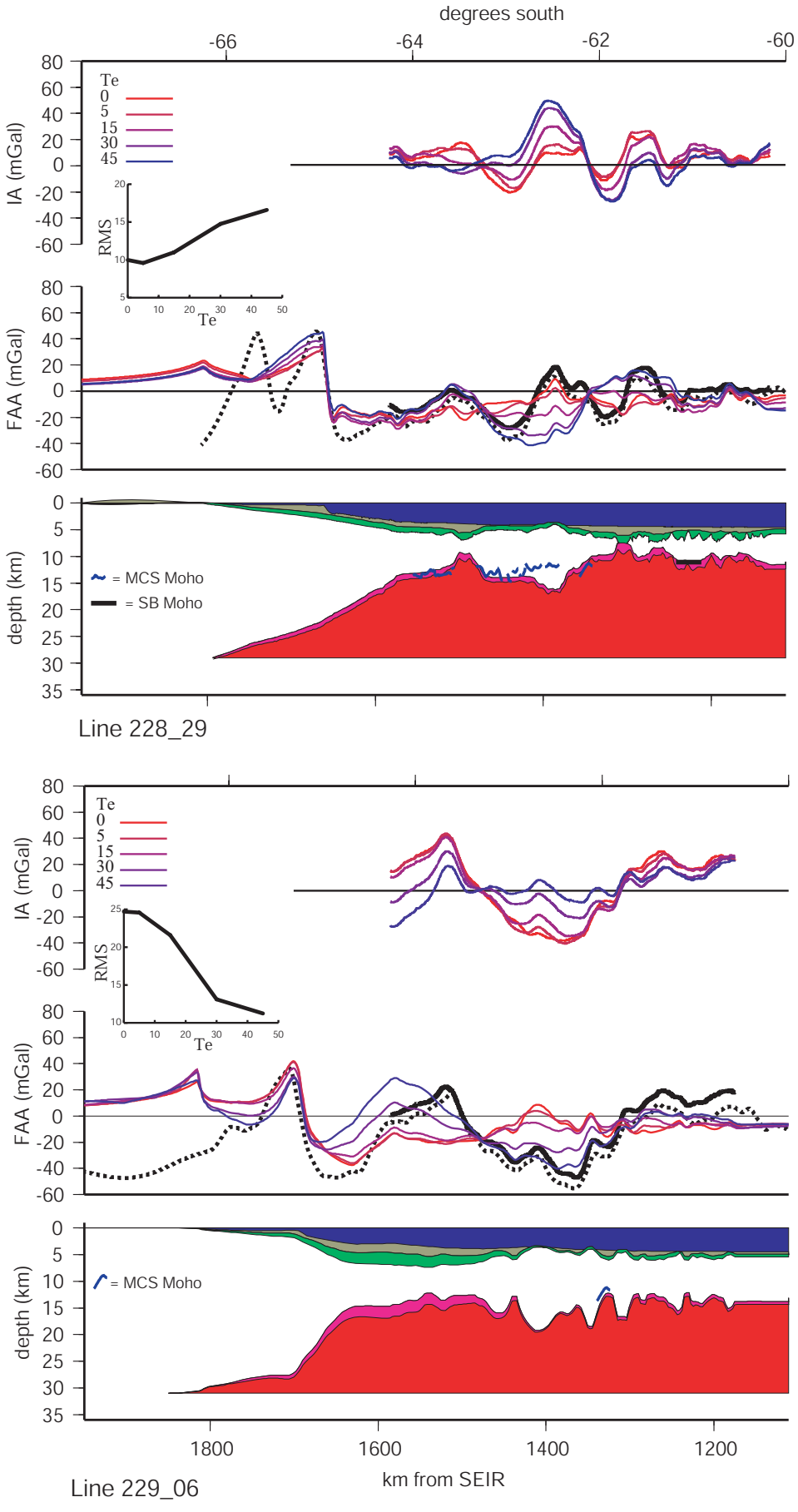

Figure 6.32: Lines GA-228_29 and GA-229_06 process-oriented modelling.

6.3.3 Strength During Rifting

The initial modelling detailed above assumed Airy isostasy during rifting, i.e. stretching factors were determined in stage 2 assuming local compensation. We now test the effect of incorporating strength during rifting (Te_{rift}) and a depth of necking (Z_{neck}) in the determination of stretching factors in stage 2 of process-oriented modelling. As outlined in section 6.2.2, Te_{rift} and the depth of Z_{neck} controls the rift crustal structure, and hence effects the rift and sediment anomalies in process oriented modelling.

Whereas Z_{neck} describes the depth to the strength maxima, Te_{rift} defines the 'strength' of the lithosphere during rifting. This strength controls the distribution of restoring forces associated with kinematic isostatic inequilibrium. For $Te_{rift} = 0$ km, the crust does not resist the restoring forces and the observed gravity anomaly is identical to the Airy case regardless of Z_{neck}. If there is strength during rifting (i.e. $Te_{rift} > 0$), then the basin geometry is modified by flexure.

Process oriented modelling was repeated for each of the survey lines on the Wilkes Land margin utilising strength during rifting. A range of parameters were tested during this process to assess if the fit between calculated and observed gravity anomaly profiles could be improved by the introduction of strength during rifting. It is clear, however, that no combination of model parameters would produce improved results by incorporating strength during rifting. The modelled gravity anomaly profiles for a range of T_e, Z_{neck} and Te_{rift} values for line GA-228_25 are illustrated in Figure 6.33. We see that the $Te_{rift} = 0\,km$ is identical for all depths of Z_{neck} tested, as predicted by the theory. A Z_{neck} depth of less than ~7.2 km predicts a subdued edge effect and a large positive anomaly over the deepest section of the rift basin due to an elevated *Moho*. For $Z_{neck} = 7.2\,km$ the modelled anomaly profile does not vary with Te_{rift} due to the equal magnitude upward and downward restoring forces. For Z_{neck} $7.2\,km$ the predicted amplitudes and wavelengths of the edge effect high and low anomalies are greatly increased. There is also a poor correlation between refraction and MCS reflection inferred *Moho* depths and the flexed *Moho* determined for models incorporating Z_{neck} and Te_{rift}.

These tests incorporating strength during rifting and depth of necking indicate that the Antarctic-Australia breakup is more likely to have occurred under Airy state isostatic balance, and that there was no specific zone of lithospheric strength that mechanically resisted the rifting process. This is somewhat surprising given the geological evidence that suggests a relatively low geotherm during breakup (e.g. lack of evidence of volcanism, low magma discharge rates associated with slow seafloor spreading, low strain rates associated slow extension).

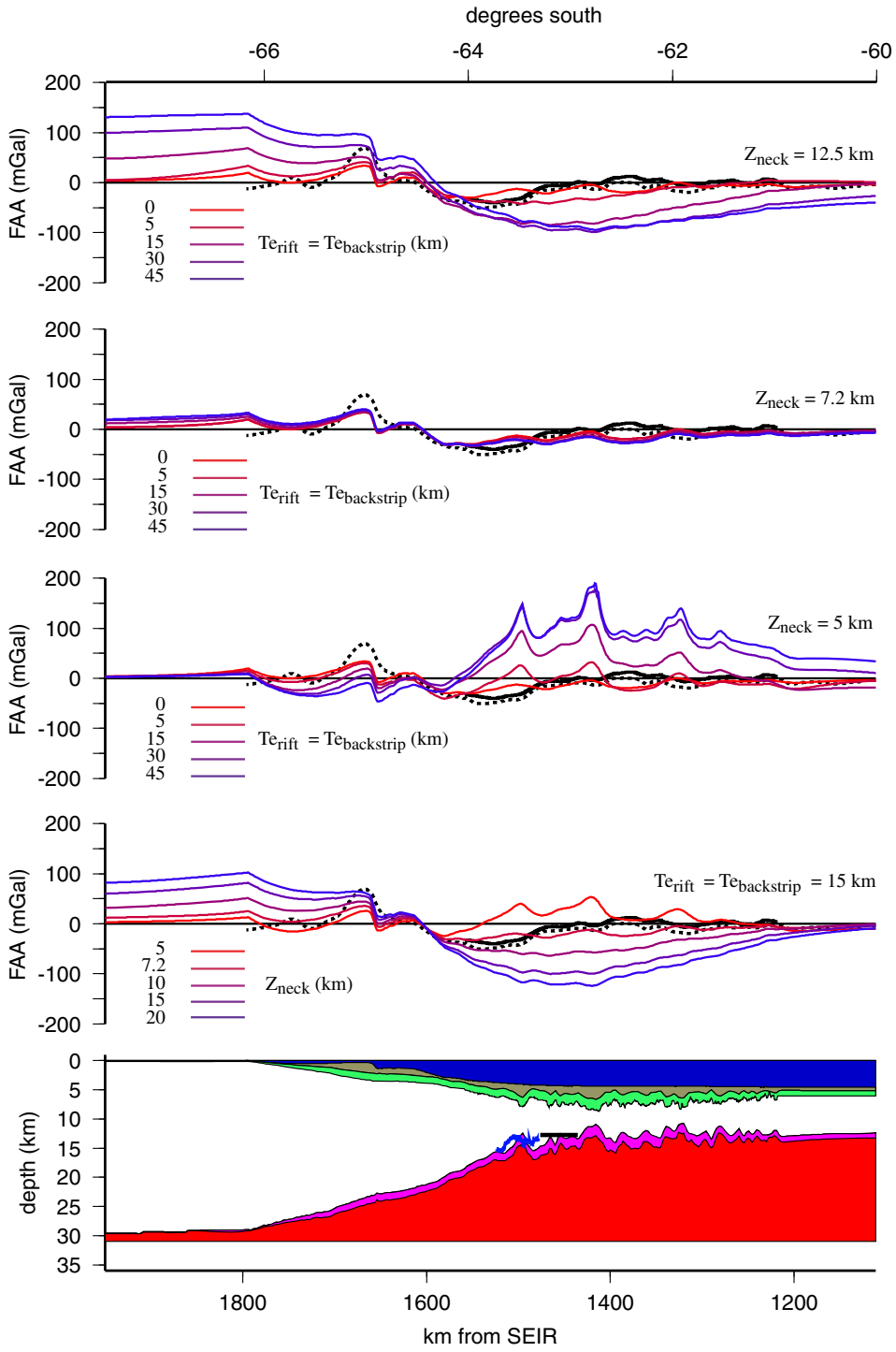

Figure 6.33: Demonstration of the effect of incorporating strength during rifting for line GA-228_25.

6.3.4 Multi-Layer Backstripping

Until this point, sediment loads have been backstripped in one step. However, typically seismic stratigraphy allows any sedimentary sequence to be divided into distinct strati-

graphic units. In many margin environments well-log and core data can then be used to constrain the physical properties of each unit. It is possible to test temporal variations in T_e by backstripping individual stratigraphic units, and summing the subsidence due to each layer to determine the *TTS*. By backstripping layers individually it is also possible to use different sediment density parameters for each layer. Multi-layer backstripping produces a significantly different *TTS* only if T_e changes are introduced for each layer backstrip and if the depositional geometry varies for each or some of the individual units backstripped.

The crust may respond to post-rift cooling, associated with the increased distance to the spreading centre, by increasing in strength and accordingly T_e as in oceanic crust (e.g. Watts [1978]). Alternatively, sediment blanketing during thermal subsidence may result in a reduction in lithospheric strength, as suggested by Beaumont *et al.* [1982]. Hence, sediments may be loaded on crust that comprises a T_e that varies with time since rifting.

The only regionally correlatable stratigraphic horizons, for which age estimates are constrained, on the Wilkes Land margin are the *Turonian* and *Eocene* unconformities, as outlined in Chapter 4. The sedimentary sequence is, therefore, most logically divided, for backstripping purposes, into two units by the *Eocene* unconformity. Two-layer backstripping and process oriented modelling was undertaken for each of the Wilkes Land seismic transects to test whether varying the backstrip T_e and/or the densities of the two units improved the fit of calculated and observed anomalies.

Process-oriented modelling utilising a two-layer backstrip provides negligible improvement in the fit between calculated and observed gravity anomalies. A range of T_e estimates and sediment densities were tested for each backstrip and the calculated gravity anomaly compared to observed data. Results did not suggest any systematic variation in T_e between the time of loading of Sequence 1 and Sequence 2 (where Sequences 1 and 2 are as defined in Chapter 4). Additionally, no systematic spatial variation in T_e was evident from backstripping with a spatially varying T_e. Initial variable T_e functions tested were based on inferred T_e structure from single-layer backstrip process-oriented modelling. Additionally, T_e functions which followed the depth to oceanic isotherms from 150-600°C were tested, as studies of flexure in the oceans demonstrate that T_e follows the depth to the 450°C [Watts, 1978].

These results do not directly indicate that T_e has not changed through time or that the density of the two sediment layers is equal, it simply indicates that the *average* values assumed in the single backstrip case were representative of the average margin T_e and sediment density, and that as a result the *TTS* is not significantly different for a one- or two-layer backstrip. Another significant factor controlling the similar results from

the two approaches is the sediment load distribution, on most lines the thickness of the Sequence 1 is much greater than the Sequence 2 thickness. Hence, the sediment load driven subsidence of Sequence 1 contributes most strongly to the total sediment driven subsidence, and the TTS is not significantly altered by backstripping Sequence 2 with a different T_e. Also due to the greater average thickness of Sequence 1, the best fitting average T_e for a single-layer backstrip will be approximately equal to the best fit T_e for Sequence 1 in the multi-layer backstrip.

The consequences of calculating the gravity anomaly associated with each loading step for the multi-layer backstrip were also investigated. This requires the calculation of many more individual sediment anomaly components and therefore allows greater flexibility with regards to the density of individual loading events and water/sediment/crustal replacements. Again the differences were negligible, primarily as the overall geometry is not altered significantly (for the same reasons as outlined for the multi-layer backstrip). Also, the density differences can only be varied intuitively, and therefore are difficult to alter significantly without violating the simplicity of the process oriented method by introducing arbitrary density anomalies.

6.3.5 Two-Dimensional Modelling Summary

The models illustrated here represent simplified geological models that include a limited number of bodies and uniform density contrasts. These models have been constructed utilising knowledge of the processes that have shaped the margin through time, but no attempt has been made to find by "trial and error" the number of bodies of variable density that will best fit the observed gravity anomaly. Two-dimensional process-oriented models account for a significant component of the observed gravity anomaly and provide insights into the structure and strength distribution of the Wilkes Land margin.

A relatively consistent spatial trend of crustal strength variations is indicated, these are summarised in Table 6.3 and illustrated in Figure 6.34. Although across margin variation in T_e can be inferred, there is little evidence for along margin segmentation of T_e. The edge effect anomaly is best fit by models of higher T_e ($\sim$30 km) for all lines in central and east Wilkes Land, indicating that the relatively unstretched continental crust has either retained strength during the rifting process or regained strength since rifting. The poor fit between calculated and observed edge effect anomalies and the relative insensitivity to T_e variation on western Wilkes Land models (lines GA-228_18 to GA-228_20) makes it difficult to determine if the T_e is systematically lower relative to the east as inferred on lines GA-228_21 and GA-228_22.

Tests incorporating strength during rifting do not support the maintenance of crustal

rigidity during rifting. Therefore the high T_e estimates of ~30 km inferred for much of the Wilkes Land margin are interpreted to indicate that rigidity or strength has been recovered over time since rifting. It is also evident that the greater thickness of Sequence 1 sediments results in a T_e estimate from backstripping that is representative of margin strength some 30-40 Ma after rifting. Multi-layer backstrips are, therefore, relatively insensitive to temporal T_e variations.

Zones of low T_e are inferred on a number of lines. This is interpreted to indicate that sections of continental and/or transitional crust have been weakened significantly by the rifting process and failed to regain strength since rifting. The consistency of these zones along the margin supports the interpretation of a zone of weakened transitional crust, defined on the basis of flexural rigidity, interleaving continental and oceanic crust.

Although the most oceanward sections of observed data are generally most poorly fit by calculated anomalies, the gradients observed are simulated most accurately by modelled data for higher T_e values (15-30 km). The inferred oceanward increase in T_e is representative of the transition to oceanic crust which is known to exhibit a simple relationship of increasing T_e and increasing age of the lithosphere at the time of loading [Watts, 1978].

Table 6.3 also summarises the T_c inferred for each line, although these initial average crustal thicknesses are approximate only, they indicate a distinct trend of decreasing crustal thickness from west to east. Although there are no independent constraints on *Moho* depth for western Wilkes Land, the thick sedimentary sequences observed require a compensation depth of at least 35 km to prevent rift models inferring that there was significant amount of mantle material shallower than the water bottom of the initial rift basin. *Moho* depth is better constrained for east Wilkes Land where MCS and sonobuoy refraction data provide an independent indication of depth on a number of lines. If initial crustal thickness is held at 35 km for east Wilkes Land, then there is a poor correlation between the modelled and observed/inferred *Moho* depths. The correlation is improved if initial crustal thickness is reduced to between 29 and 32 km. More seismic refraction data is required to confirm this trend, however, it seems clear that there is a distinct change in the depth of compensation and the initial, pre-rift crustal thickness between east and west Wilkes Land.

Line	T_e **at shelf break (km)**	**low** T_e **zone***	**Oceanward increasing** T_e	T_c **(km)**
18	-	200, 100	yes	35
19	-	280, 100	-	35
20	-	-	yes	35
21	15	135, 100	yes	35
22	15	-	no	32
23	30	no	-	31
24	30	-	yes	31
25	30	-	-	31
26	30	240, 120	yes	31-32
27	30	120, 100	-	32
28	30	250, 200	no	31
29	-	-	no	29
229_06	-	-	no	31

*Distance from shelf break (km), width (km)

Table 6.3: Summary of interpreted T_e structure and T_c based on process-oriented modelling results.

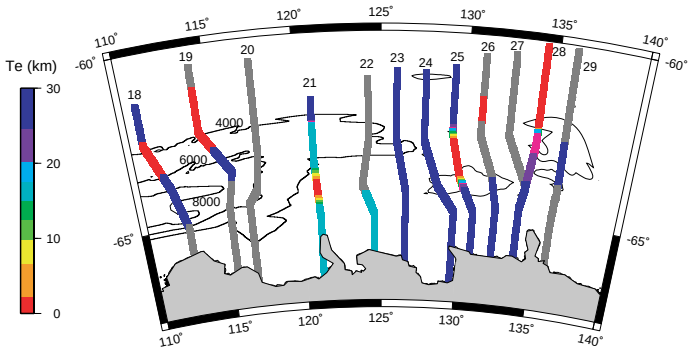

Figure 6.34: Inferred T_e for each survey transect plotted over sediment thickness contours. A relatively consistent trend of T_e distribution is exhibited northward from the margin, however, it is difficult to confidently infer east-west segmentation of crustal strength or rigidity.

The greatest sensitivity to T_e is exhibited by lines west of GA-228_24. Although lines east of GA-228_24 exhibit lower sensitivity to variation in T_e, the RMS of the flexural isostatic anomalies for these lines is significantly lower than for free air gravity anomaly data. This indicates that even if process-oriented modelling does not allow the crustal

rigidity distribution to be uniquely determined, it remains a useful means of further reducing free air anomaly data in a geologically rigourous manner that is not overly sensitive to user input. The isostatic anomaly profiles exhibit a number of features that correlate between survey lines, further gravity modelling using seismic and magnetic data constraints may provide insight to the origin, geometry, depth and physical properties of the causative features of these isostatic anomalies.

6.4 3-Dimensional Gravity Modelling on the Wilkes Land Margin

6.4.1 Introduction

Three-dimensional (3D) modelling, in general, offers some advantages over two-dimensional (2D) modelling. Typically in 2D models, bodies are assumed to extend infinitely out of plane. No such assumptions are made in 3D modelling. This may be significant in regions of rapid lateral change of bathymetry, sediment thickness, basement depth, or crustal thickness. However, for the Wilkes Land margin the sediment isopach is not truly 3D, but rather a gridded series of widely spaced, parallel line data. Hence, it is difficult to assess the accuracy of 3D process-oriented modelling as there exist large uncertainties in the along margin variation in sediment thickness. However, analyses of 3D flexural isostatic anomalies provides a useful tool for qualitative interpretation.

6.4.2 Airy Isostatic Model

As for the 2D case, the conceptually and computationally simplest type of 3D isostatic anomaly is the classic-Airy isostatic anomaly. The GEBCO 1M data [IOC *et al.*, 2003] is the most extensive bathymetric data compilation that is not supplemented by satellite derived bathymetry estimates for the Wilkes Land margin, and, therefore, is used as the basis of the 3D classic-Airy model.

The modelling methodology is identical to the 2D classic-Airy model considered previously. The calculated gravity anomaly is simply the sum of the anomalies resulting from the replacement of crust by water and mantle, where the model geometry is constrained by the present-day bathymetry and its Airy-type compensation. The 3D calculations were carried out in the Fourier domain as outlined previously, accordingly care was taken to ensure that the input grids extended far enough in every direction such that spurious edge effects associated with tapering of data were not superimposed on data in the region of interest. The Airy isostatic anomaly was calculated by subtracting the calculated gravity anomaly data from the satellite derived free air gravity grid of Sandwell & Smith

[1997].

The calculated classic-Airy model FAA, satellite derived FAA, and Airy isostatic anomaly maps are shown in Figure 6.35. The amplitude of the edge effect anomaly is significantly reduced in the isostatic anomaly map, particularly in the central Wilkes Land area, relative to the satellite derived free air data. There is a large amplitude positive isostatic anomaly situated off the west Wilkes Land margin between ∼112°E and ∼120°E, this anomaly correlates to the location of uncompensated sediment banks and the thick sediments of the Budd Coast Basin. Similarly to the 2D case, the classic-Airy model does not predict the complexity of observed gravity anomalies, and large isostatic anomalies remain oceanward of the edge effect low.

6.4.3 3D Process Oriented Modelling

Three-dimensional process-oriented modelling is identical in methodology to 2D process-oriented modelling, except that it is carried out using a sediment thickness grid rather than a sediment thickness profile. Hence, any errors introduced in the creation of the 3D sediment thickness grids, associated with the large line spacing and lack of data from the upper continental rise to the continental shelf, are propagated through the backstripping and gravity modelling process. Uncertainty in the sediment thickness grid introduces the largest source of unconstrainable error. Despite this obvious limitation, there is still significant benefit in calculating 3D flexural isostatic anomalies as they provide a means of quantitative and qualitative interpretation of the crustal structure of the Wilkes Land margin.

Three-dimensional modelling was undertaken using a single backstrip of the post-rift sediment thickness grid (Chapter 4) assuming a range of constant T_e values. Densities of water, sediment, crust and mantle are as for 2D modelling (Table 6.2). An initial crustal thickness of 35 km was assumed. However, tests indicate that the isostatic anomaly is relatively insensitive to variation of this parameter.

Figure 6.36 illustrates the rift, sediment and sum anomalies calculated for $T_e = 30$ km, compared to satellite derived FAA data. The right hand panels in Figure 6.36 show profiles extracted through the corresponding grid, along line GA-228_25, compared to the 2D solution obtained earlier using the line integral method. The profiles extracted compare almost exactly to the 2D profiles illustrating the assumptions of loads and bodies of infinite lateral extent in the 2D modelling introduced only negligible error. The slight differences that are apparent result from the resampling of the 2D data during gridding. Data spacing along the 2D profiles is ∼0.05 km, whereas the 3D grid spacing is 5 minutes (∼9 km in the north-south plane and between ∼4 to 4.5 km in the east-west plane). It

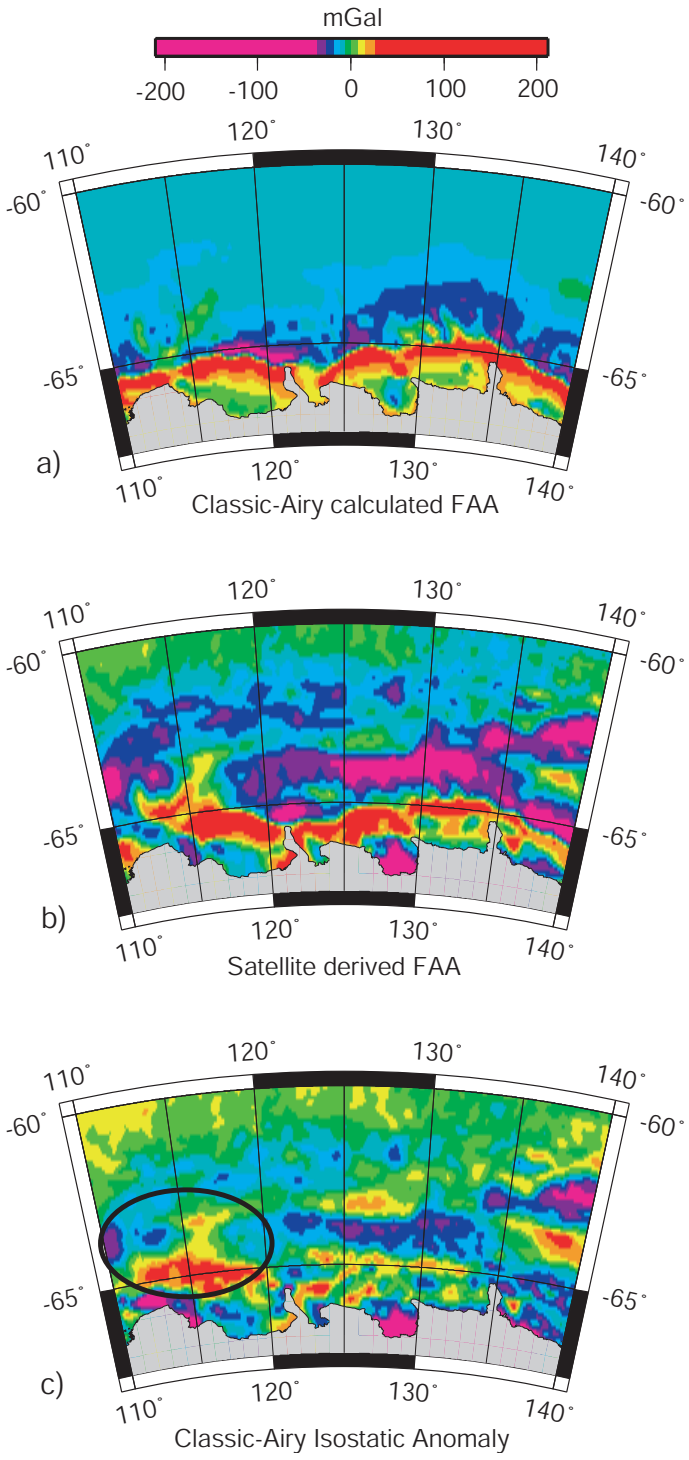

Figure 6.35: a) Classic-Airy model FAA. b) Satellite derived FAA from Sandwell & Smith [1997]. c) Classic-Airy isostatic anomalies for the Wilkes Land margin, the edge effect anomaly has been decreased in amplitude, however, large amplitude isostatic anomalies remain oceanward of the edge effect low. The Budd Coast Basin is circled in (c).

is necessary to alias the data during resampling to some degree due to the asymmetry in the north-south (∼0.05 km shot point spacing) and east-west (∼90 km line separation) data spacing. If gridding is completed using the maximum north-south data resolution then spurious interpolations are introduced in the east-west direction.

Flexural isostatic anomaly grids for T_e=0,5,10,20,30 and 45 km were created by subtracting the calculated sum anomalies from the satellite derived FAA. Flexural isostatic anomaly maps for T_e=0,5,10,20,30 and 45 km are displayed in Figure 6.37, some isostatic anomalies are common to each isostatic anomaly map indicating an insensitivity to T_e. The anomaly associated with the Adélie Rift Block (132-140°E) and the large positive amplitude anomaly off the west Wilkes Land margin are examples of isostatic anomalies that are not reduced more efficiently by any particular T_e. It must be noted that both these areas of large amplitude isostatic anomalies are outside the extents of MCS data, hence the errors are possibly related to insufficient data constraints. The positive isostatic anomaly off West Wilkes Land is located immediately landward of the southern extents of lines GA-228_19 and GA-228_20, where large sediment accumulations are observed. If the assumed landward extrapolations of these sediments are inaccurate then errors are introduced and isostatic anomalies result.

Isostatic anomalies within the areas directly constrained by MCS data are most effectively reduced for higher T_e estimates (30-45 km). The positive isostatic anomalies along ∼65°S are associated with misfit between calculated and observed edge effect anomalies. These isostatic anomalies are most reduced for high T_e. The isostatic anomalies outlined in Figure 6.37 are interpreted to represent flexurally compensated sediments of the BCB. These anomalies are relatively large for low T_e (0-10 km), however, they are effectively reduced for higher T_e estimates. Therefore, 3D modelling results accord with those of 2D modelling and indicate that the Wilkes Land margin is, in general, characterised by a high (for a rifted margin) T_e. The results of 3D modelling do not indicate any along margin segmentation of T_e.

The correlation between thick sediments and high T_e indicates that there is not necessarily a positive correlation between zones of weakened lithosphere and large scale sediment accumulation. This positive correlation has been suggested by Beaumont *et al.* [1982] and demonstrated for the northeast U.S. margin by Wyer [2003].

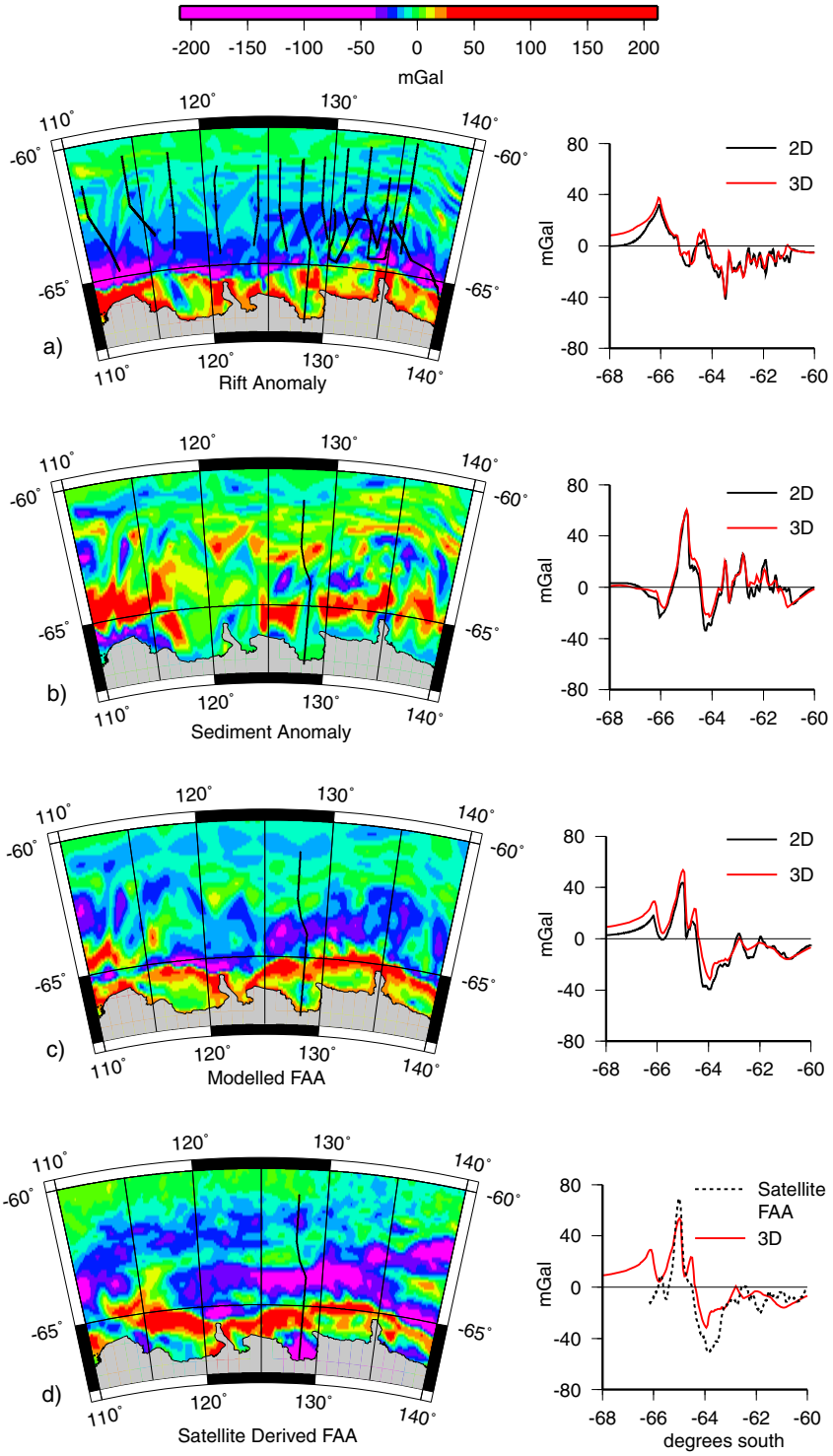

Figure 6.36: Gravity anomaly maps of the process oriented, T_e=30 km, a) rift anomaly, b) sediment anomaly, c) sum modelled free air anomaly, and d) the satellite derived free air gravity anomaly data. Right hand panels show profiles extracted through the associated grid (red) along line GA-228_25 compared to the 2D line integral solutions (black). Profile location is plotted on each map (black solid line) and the location of MCS data is plotted on the rift anomaly map.

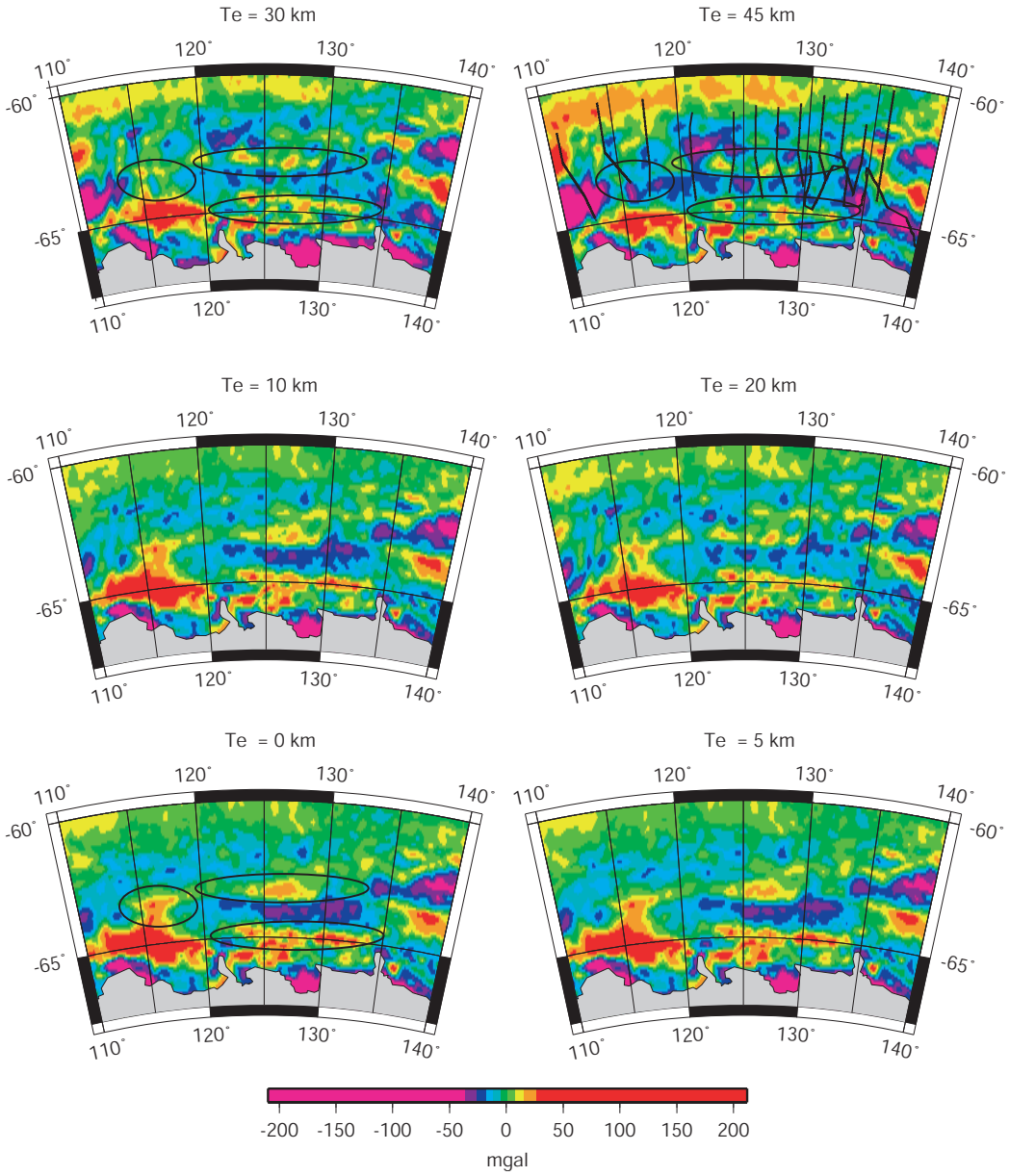

Figure 6.37: Isostatic anomaly maps for T_e as labelled. The amplitude of isostatic anomalies associated with the Budd Coast Basin (BCB) and the edge effect (as outlined for T_e =0,30 and 45 km) are most effectively reduced for the high T_e estimates. MCS line data locations are overlain on the T_e=45 km isostatic anomaly map.

6.4.4 Spectral Analysis

Computing the power spectra of the satellite derived FAA and isostatic anomaly data provides another technique of analysing gravity anomalies. By transforming the space domain anomaly data into the frequency domain (i.e. Fourier transform), power spectra can be analysed as a function of frequency or wavelength. Power spectra illustrate the wavelengths at which the greatest power or energy (spectral peaks) of a signal are associated. The differences in power spectra can be interpreted in terms of the applicability of T_e estimates and the fit between calculated and observed anomalies.

As no data is available for onshore Wilkes Land it is necessary to restrict the spectral analysis to the offshore region only. The southern limit of data included in spectral analyses can be considered as the Antarctic coastline or the extent of sea ice due to uncertainty in satellite derived free air gravity anomaly data over ice covered regions (section 6.1.4), both possibilities were tested.

Figure 6.38 illustrates the three-dimensional power spectra of the satellite derived FAA, classic-Airy isostatic anomaly, and flexural isostatic anomalies for T_e=0, 15 and 30 km. The spectra were calculated for both the entire offshore region (i.e. limited by the coastline) and also for the region offshore of the austral summer ice extents. The correlation between the shelf break, edge effect high and sea ice extent is significant with regards to inclusion in spectral analyses. The coastline limited power spectrum of free air anomaly data shows peak amplitudes at wavelengths of ∼300 and 500 km, the ice extent limited spectrum illustrates peaks at identical wavelengths, however, the amplitude of the ∼300 km peak is reduced by more than half. As the ice limited spectrum effectively excludes input from the edge effect high the ∼300 km peak can be correlated with the edge effect high.

The spectra for the coastline limited analyses indicate that power associated with the edge effect high is reduced in both the classic-Airy and flexural isostatic anomalies from ∼38 to ∼20 mGal^2. The greater amplitude and longer wavelength power peak observed in the FAA spectrum is reduced most efficiently in the classic-Airy isostatic anomaly, from >40 to <10 mGal^2, however, this peak is also reduced by more that half in the flexural isostatic anomaly spectra. This peak is interpreted to correlate to power associated with the edge effect low. The spectra created using the sea ice extent as the basis of data exclusion suggest that the edge effect low power is effectively reduced in both the classic-Airy and flexural isostatic anomalies.

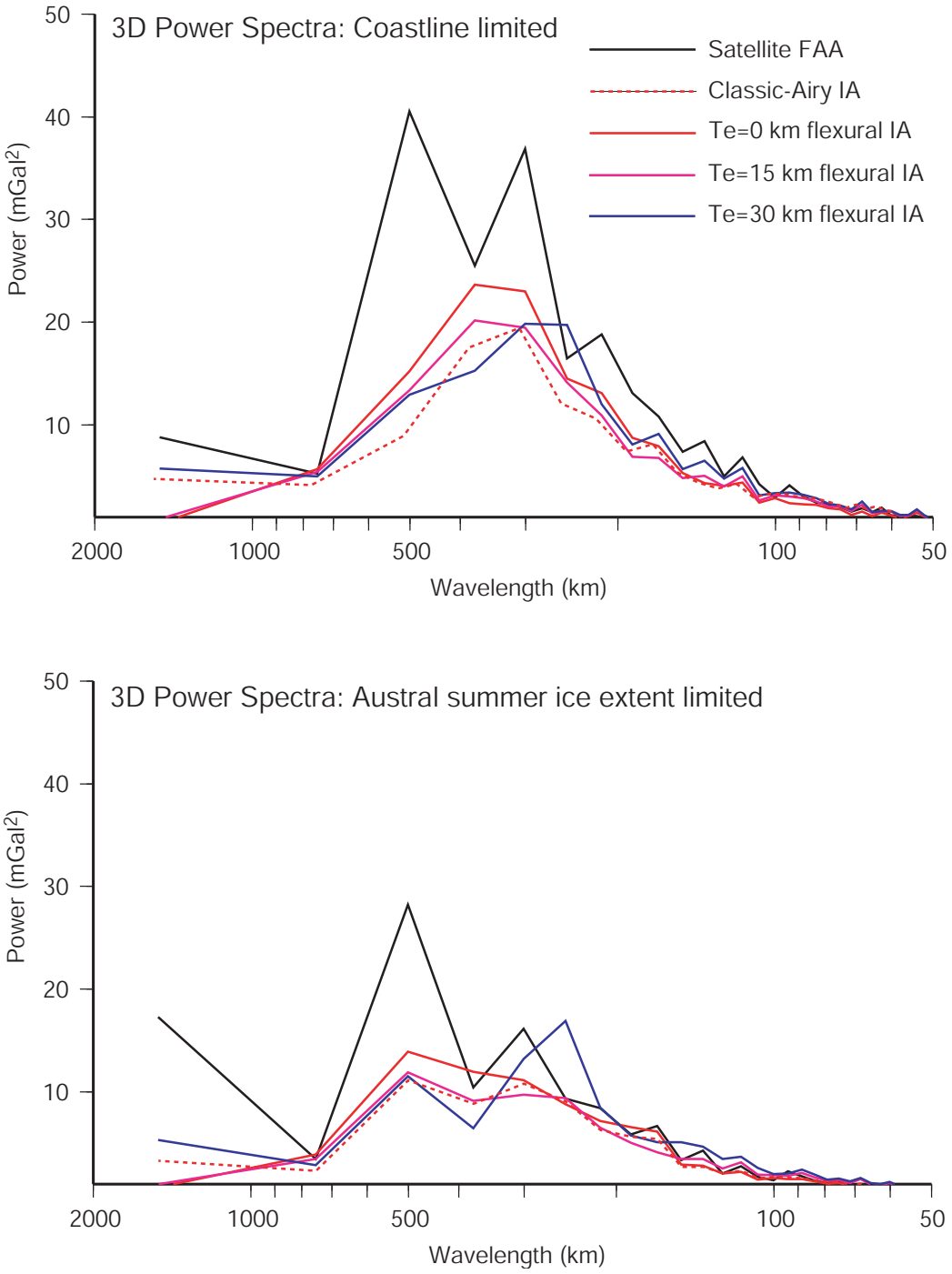

Figure 6.38: Three dimensional (3D) power spectra of satellite free air anomaly (FAA), Airy and flexural isostatic anomaly (IA) data for a) coastline limited analyses, and b) Austral summer sea ice extent limited analyses. Long wavelength power associated with the edge effect anomaly is significantly reduced in IA data relative FAA data.

6.5 Summary

Despite the limitations of gravity data and the extent of seismic reflection data on the Wilkes Land margin, 2D and 3D process-oriented gravity modelling provides important results. The T_e structure of the margin has been, for the first time, estimated and constrained via modelling. The high T_e inferred for most of the margin contrasts with other rift margins, which are typically characterised by low T_e. Crustal structure has been constrained and the variation in stretching factor across and along the margin can now be determined. The close correlation between modelled and seismic data inferred $Moho$ depths, and the results of incorporating syn-rift strength and a depth of necking, broadly validate the assumption of Airy isostasy in determining crustal structure.

The results presented here further demonstrate the ability of process-oriented modelling to constrain the gravity anomaly contributions of individual geological processes in a continental margin environment. This, in turn, allows density anomalies and breakdowns in isostatic assumptions to be investigated without the interfering effects of other geological processes.

Chapter 7

Discussion

7.1 Introduction

This chapter comprises four main sections. The first two sections address key issues that arise from the studies undertaken in previous chapters. In the first section, one of the main aims of this chapter and thesis is addressed, namely, the integration of the results of interpretation and modelling of the seismic reflection and refraction, magnetic and gravity data. The interpretation of these data has led to a number of questions with regard to the location of the COB and the nature of the COT. Here we use combined magnetic and gravity modelling to infer serpentinised peridotites associated with exhumed mantle within the COT.

In the second section we summarise the subsidence history of the margin. Following backstripping, the pattern of crustal thinning can be inferred. Oceanic crust is observed to occur at anomalously great depth off the Wilkes Land margin, even once adjusted for the thick sediment load associated with Tertiary glaciation. The effect of ice-induced subsidence is also discussed with regards to alteration of the continental shelf, and possibly continental rise, morphology.

The third section comprises a study of the conjugate margin structure. A fundamental question of rift studies is to determine whether conjugate margins can be classified as symmetrical or asymmetrical with regard to crustal thinning patterns, width of extended crust, volcanism, subsidence history, segmentation, and long-term thermo-mechanical properties. Process-oriented gravity modelling is undertaken on the southern Australian margin to allow comparison with interpretation of the Wilkes Land margin.

The strength of extended continental crust is discussed in the fourth section of this chapter. The permanent mechanical alteration of continental crust and the transient changes in the geotherm associated with rifting alter the YSE of the extended continental crust and, therefore, potentially its T_e structure.

7.2 Mantle Exhumation in the Continent-Ocean Transition Zone

The existence of serpentinised mantle peridotites in the Continent-Ocean Transition (COT) zone at the West Iberian rifted margin has been established through dredging and drilling (e.g. Boillot *et al.* [1980], Pinheiro *et al.* [1996]). Seismic refraction data have also been used to constrain the presence and extent of serpentinised peridotite (e.g. Dean *et al.* [2000]). Serpentinised peridotites have also been interpreted within the COT zone of the southwest Greenland (e.g. Chian & Louden [1994]). Figure 7.1, a schematic cross-section through the south-west Greenland margin, illustrates the suggested mode of occurrence of serpentinised mantle within the COT zone. At this margin, serpentinised mantle is interpreted beneath thinned continental crust and as top basement where total crustal separation has occurred [Pérez-Gussinyé *et al.*, 2001].

Figure 7.1: Cross-section through the south-west Greenland margin illustrating the presence of serpentinised peridotites within the COT zone. Figure from Pérez-Gussinyé *et al.* [2001], after Chian & Louden [1994].

A basement ridge complex, interpreted as a combination of serpentinised peridotites and mafic rock associated with mantle upwelling, has also been identified off the Great Australian Bight (GAB) margin of southern Australia [Sayers *et al.*, 2001]. However, the interpretation of this basement ridge, which is only based on seismic character and gravity and magnetic modelling, is yet to be tested by drilling or seismic refraction.

Minshull *et al.* [1998], Dean *et al.* [2000] and other workers suggest that serpentinisation is facilitated if there are readily available pathways for seawater to reach the upper mantle, and if the upper mantle is cool. These conditions are commonly satisfied at fracture zones on slow spreading ridges, in COT zones, and at the axes of extinct rifts. However, in each of these environments Minshull *et al.* [1998] observe that serpentinisation sufficient to significantly lower the seismic velocity and density of mantle peridotites

does not penetrate beyond ~5 km into the crust. The slow spreading (<10 mm/yr HSR) and inferred low-temperature (as evidenced by a lack of volcanic rocks and the great depth of the AAB oceanic crust) breakup of Australia and Antarctica, therefore, makes the Wilkes Land margin a likely location for the occurrence of serpentinised peridotites.

A number of basement highs, characterised by a relatively transparent internal acoustic character, were identified in seismic reflection data from the COT zone off the Wilkes Land margin (as discussed in Chapter 4). Some of these basement highs protrude through the post-rift sediments and have a bathymetric expression off east Wilkes Land and Terre Adélie, where they correlate to positive free air gravity anomalies.

In-situ, but altered, peridotite blocks have been dredged from one of the basement highs that forms a seamount at the seaward extent of the Adélie Rift Block (ARB) (Seamount B, Figures 4.24 and 4.25). Geochemical analyses of these dredged peridotite samples indicate the seamount comprises upper-mantle peridotites that have a fertile, sub-continental mantle origin [Yuasa *et al.*, 1997].

Sediment-covered basement features in central and eastern Wilkes Land, similar to the seamounts dredged in the ARB, correlate to Flexural Isostatic Anomalies (FIA), and in some cases, magnetic anomalies also. Forward modelling and inversion of FIA and forward modelling of magnetic anomalies was undertaken to constrain the geometry and physical properties of the possible sources of these anomalies and determine if exhumed and potentially serpentinised mantle peridotites could be inferred outside of the ARB.

The density and seismic velocity, and magnetic susceptibility, of mantle peridotites varies with degree of serpentinisation (e.g. Horen *et al.* [1996], Oufi & Cannat [2002]). The relationship between density and degree of serpentinisation being far more systematic than variations in magnetic susceptibility. Table 7.1 summarises the density and seismic (P wave) velocity of variably serpentinised peridotite samples recovered from ophiolites. The density and seismic velocity of peridotites decreases systematically as the degree of serpentinisation increases.

% serpentinisation	ρ (kg/m^3)	V_p (m/s)
3	3260	7759
15	3200	7346
35	3030	6744
45	2930	6355
75	2710	5864

Table 7.1: Relationship between degree of serpentinisation, density, and seismic velocity. After Horen *et al.* [1996].

The magnetic susceptibility (k) of serpentinised peridotites does not linearly correlate to degree of serpentinisation [Oufi & Cannat, 2002]. Instead, k remains subdued in partially serpentinised peridotites and then increases rapidly as a threshold degree of ~75% alteration is reached. This is related to the formation of magnetite during the serpentinisation process. A wide range of k and Königsberger ratios (Q) were determined by Oufi & Cannat [2002] based on the analysis of samples from ODP drilling. A k range of 0.01 to 0.15 is demonstrated and a Q range from 0 to 10. The grain size distribution and serpentinite micro-structure controls the importance of remanent magnetisation, for larger grain-size the contribution of remanence after alteration is decreased [Dunlop, 1995; Oufi & Cannat, 2002].

Figure 7.2 illustrates the spatial correlation on Line GA-228_22 of a COT zone basement high, a FIA, and a large amplitude magnetic anomaly that occurs on the 'anomaly 34y' lineation (see Figure 5.14). The FIA and observed magnetic anomalies are well fit by the calculated anomalies for the two-dimensional body illustrated, constrained by the depth to basement interpreted from depth converted seismic reflection data. A positive density contrast of 300 kg/m^3 (equivalent to an absolute density of 3100 kg/m^3 as the FIA was calculated assuming a crustal density of 2800 kg/m^3). A density of ~3100 kg/m^3 correlates to a serpentinisation of ~25%. A magnetic susceptibility of 0.1 SI units was assumed in modelling. The calculated magnetic anomalies are assumed to be due to induction in the present-day geomagnetic field only (i.e. very low Königsberger ratio). Ambient magnetic field properties assumed in modelling are as for the present day Wilkes Land margin, i.e. field strength = 66,000 nT, inclination = -80°, and declination = -3° [IAGA, 2000].

The base of the body illustrated in Figure 7.2 does not correlate with the depth to the flexed $Moho$ from process-oriented modelling. By lowering the density of the body and increasing its thickness these surfaces can be forced to correlate more closely without altering the quality of fit between calculated and observed anomalies. However, as there is no constraint on depth to $Moho$ in the COT zone and we infer higher density basement in the COT, the depth to the flexed $Moho$ calculated assuming a crustal density of 2800 kg/m^3 is likely too deep. Therefore, this apparent 'misfit' is not corrected here. Without further constraint on depth to $Moho$ it was considered arbitrary to alter density or thickness of bodies to conform to a flexed $Moho$ calculated assuming Airy isostasy.

A similar spatial correlation of FIA and magnetic anomalies, and rugged COT zone topography, occurs close to the point of maximum crustal thinning on Line GA-228_23 (Figure 7.3). The geometry of the bodies required for calculated gravity anomalies to fit the FIA correlate closely to the basement surface and flank a shallow point in the modelled flexed $Moho$. Densities of 3120 and 3100 kg/m^3 were assumed for the two bodies, again

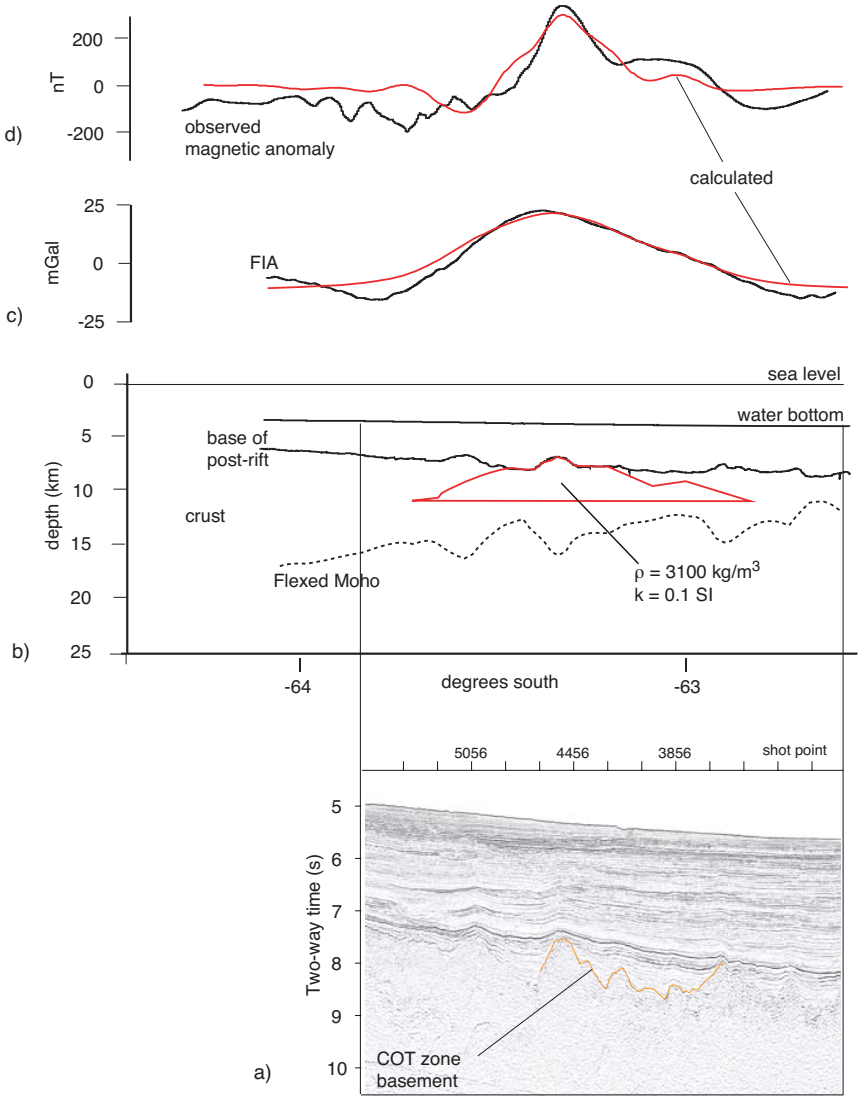

Figure 7.2: a) Seismic reflection data from Line GA-228_22. b) Crustal structure from process-oriented modelling (dashed black) and modelled body geometry (red) with density (ρ) and magnetic susceptibility (k) as labelled. c) FIA and calculated gravity anomaly for body in (b). d) Observed magnetic anomalies compared to calculated anomalies assuming induction only for the body in (b).

suggesting ~25% serpentinisation of exhumed peridotites. The geometry of these bodies do not provide a calculated magnetic anomaly that accurately fits the observed magnetic anomaly. However, slight variations of the body geometries assumed in the gravity model, with an upper surface still constrained by the basement depth, provides for an accurate fit between calculated and observed anomalies assuming magnetic susceptibilities of 0.09 and 0.04 SI. The magnetic sources required to predict calculated anomalies of similar magnitude to observed anomalies, assuming induction only, are of much greater thickness

(∼2 km) than the typical thickness of layer 2 oceanic crust.

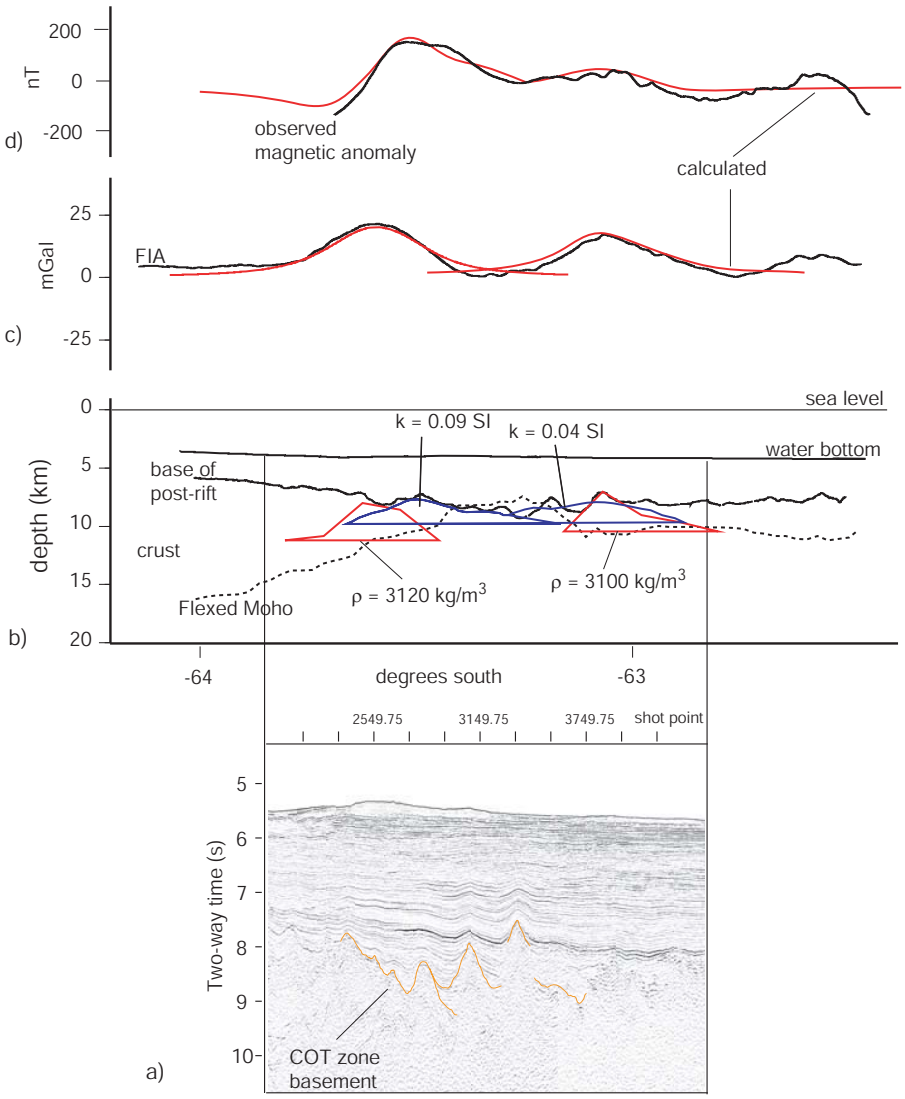

Figure 7.3: a) Seismic reflection data from Line GA-228_23. b) Crustal structure from process-oriented modelling (dashed black) and modelled body geometries for gravity (red) and magnetic (blue) modelling with density (ρ) and magnetic susceptibility (k) as labelled. c) FIA and calculated gravity anomaly for red bodies in (b). d) Observed magnetic anomalies compared to calculated anomalies assuming induction only for blue bodies in (b).

Figure 7.4 illustrates the coincidence of an interpreted zone of COT zone crust and a positive FIA for Line GA-228_26. Forward modelling of the FIA indicates the presence of a relatively broad mass excess in the upper crust with a density of 3100 kg/m^3. Again, this is interpreted to indicate the presence of serpentinised peridotites associated with exhumation of the upper mantle within the COT zone. The magnetic anomaly pattern

for this line is very complex landward of 62.5°S (see Figure 5.14). The FIA at this location does not occur on the lineation of 'anomaly 34y', rather it occurs within the COT zone interpreted from seismic reflection data. Results from modelling of Line GA-228_27 are very similar (Figure 7.5). There is no spatial correlation of magnetic and FIA, but a mass excess correlated to the basement surface, with a density of 3050 kg/m^3, is inferred from gravity modelling.

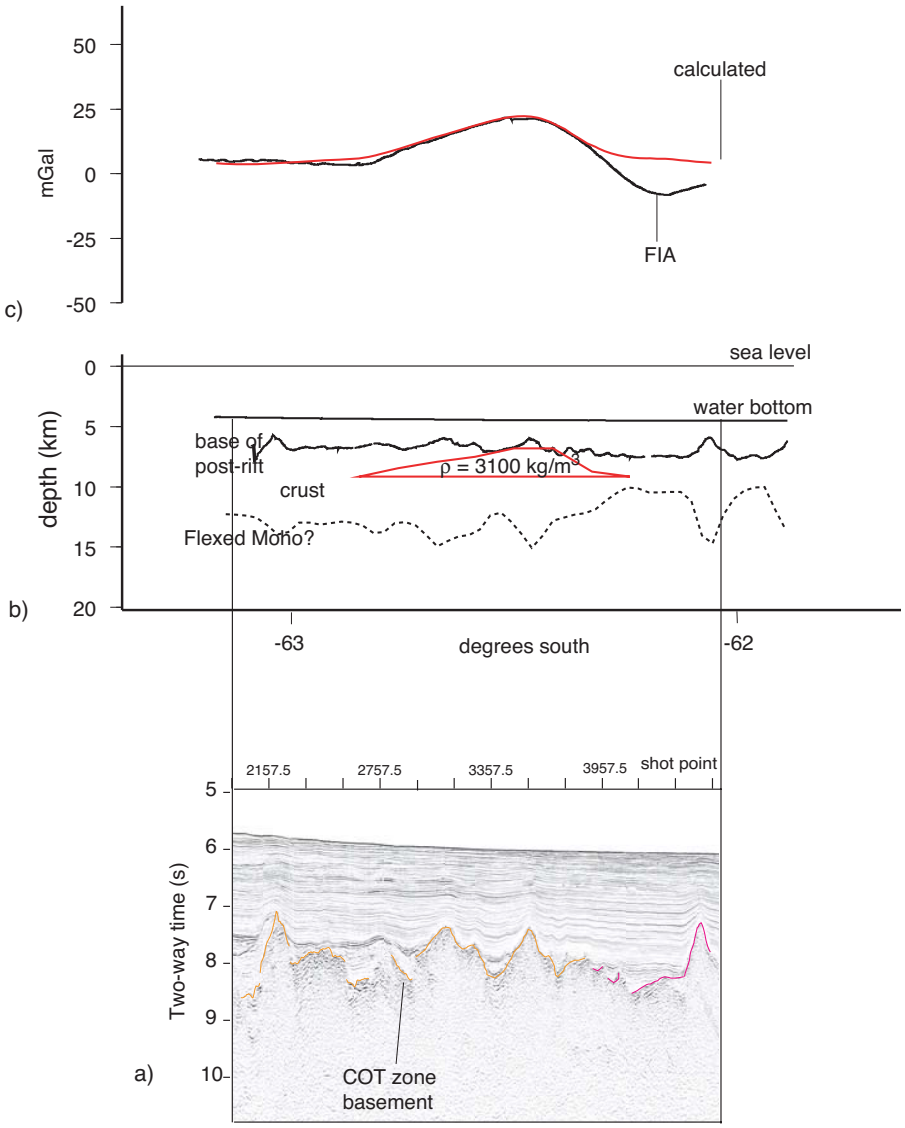

Figure 7.4: a) Seismic reflection data from Line GA-228_26. b) Crustal structure from process-oriented modelling (dashed black) and modelled body geometry (red) with density (ρ) as labelled. c) FIA and calculated gravity anomaly for body in (b).

A FIA occurs over the basement high located at the seaward limit of the interpreted COT zone for Line GA-228_29 (Figure 7.6). No observed magnetic anomalies correlate

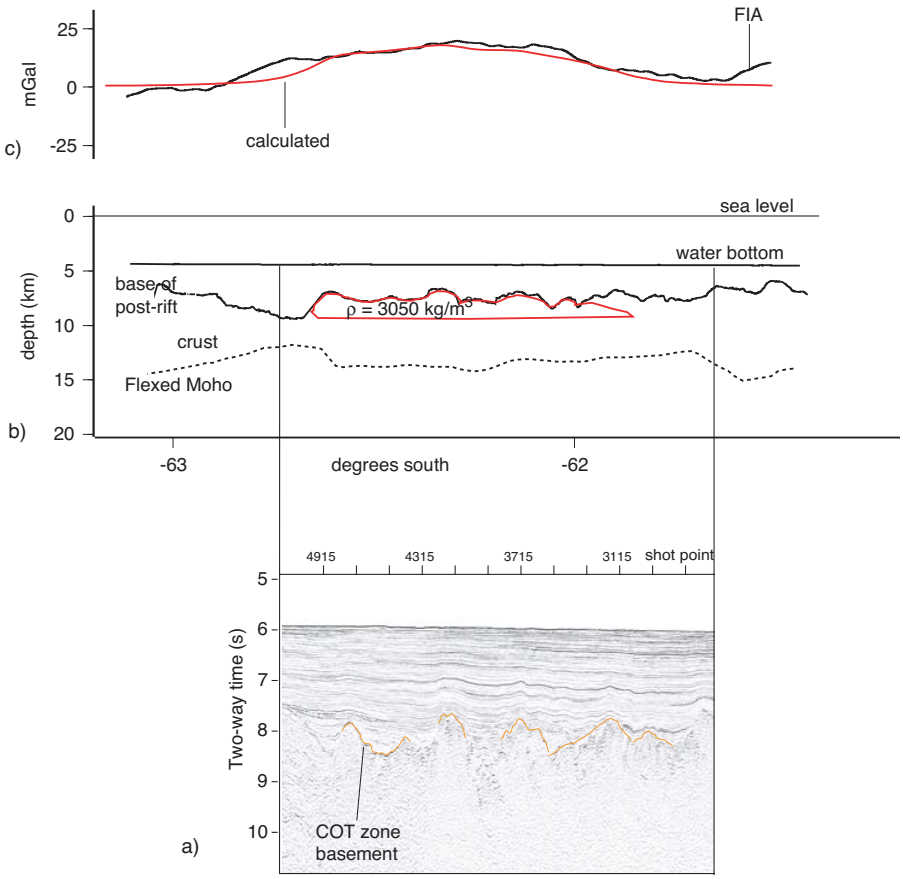

Figure 7.5: a) Seismic reflection data from Line GA-228_27. b) Crustal structure from process-oriented modelling (dashed black) and modelled body geometry (red) with density (ρ) as labelled. c) FIA and calculated gravity anomaly for body in (b).

to this basement high and FIA. Forward modelling, constrained by the geometry of the basement high, indicates a density for this feature of 3100 kg/m^3.

The consistency of the spatial correlation of positive FIA and basement features within the COT zone, which modelling indicates have a density of ~3100 kg/m^3, indicates the presence of serpentinised upper-mantle peridotites. This has already been established for the ARB off the eastern Wilkes Land margin, however, these results indicate their presence along margin from the ARB. The serpentinised, peridotite ridges occur both at the landward (e.g. Lines GA-228_22 and GA-228_23) and seaward extents (e.g. Line GA-228_29) of the COT zone. Despite variation in the geometry of the interpreted COT zones and ridges, the gross structure is similar to the schematic section from the south-west Greenland margin discussed above (Figure 7.1).

Coincident magnetic and gravity modelling indicates that magnetic anomalies that occur on the 'anomaly 34y' lineation (Figure 5.14) are likely not associated with *normal*

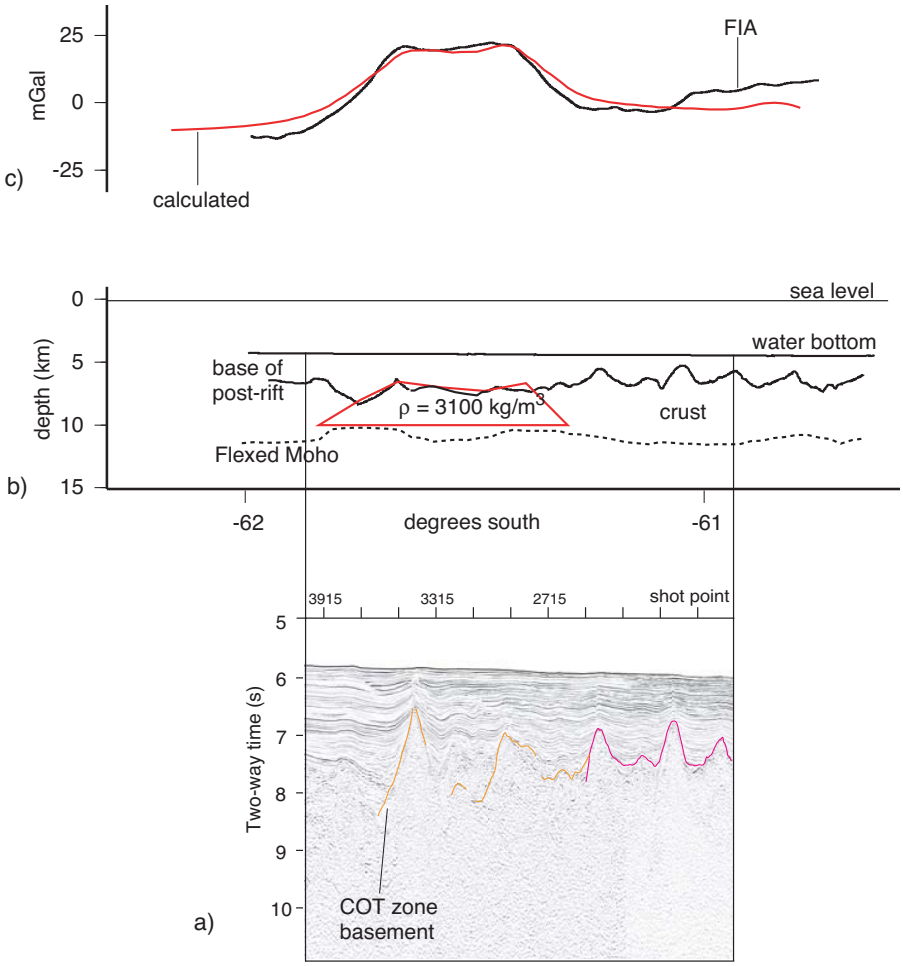

Figure 7.6: a) Seismic reflection data from Line GA-228_29. b) Crustal structure from process-oriented modelling (dashed black) and modelled body geometry (red) with density (ρ) as labelled. c) FIA and calculated gravity anomaly for body in (b).

oceanic crust. It was demonstrated in Chapter 5 that the observed magnetic anomalies did not correlate to basement topography for a constant thickness magnetic source layer. However, it is clear from the modelling undertaken here that there is a strong correlation between basement topography and the observed magnetic anomalies for a non-constant thickness source body. The additional correlation with positive FIA provides for greater confidence in reinterpreting the magnetic anomalies previously identified as anomaly 34y to be associated with serpentinised upper-mantle peridotites, exhumed during continental extension. The observed magnetic lineation is likely a function of the approximately contemporaneous exhumation of upper mantle segments along the Wilkes Land margin.

The massive extension and rupture of the upper- and lower-crust is indicated by the presence of exhumed, altered mantle at the base of the post-rift sediments for much of the

COT zone off the Wilkes Land margin. As outlined previously, many of the factors considered important in allowing mantle serpentinisation and exhumation at rifted margins occur at the Wilkes Land margin. Namely, low extension rates and low mantle temperatures, which both contribute to low melt generation, a key factor in allowing mantle exhumation [Pérez-Gussinyé *et al.*, 2001]. Figure 7.7 illustrates the temporal evolution for a 'West Iberia type' margin and the mode of mantle hydration and serpentinisation suggested by Pérez-Gussinyé *et al.* [2001]. However, a décollement surface at the crust-mantle boundary (CMB), similar to that suggested by Pérez-Gussinyé *et al.* [2001] (for which there is evidence in seismic reflection and refraction data at the Iberian margin [e.g. Krawczyk *et al.* [1996]]), is not apparent in seismic data from the Wilkes Land margin. This indicates that mantle exhumation may occur due to crustal separation without full-crust penetrating detachment surfaces.

Figure 7.7: Schematic representation of the temporal evolution at a central rift zone for a 'West Iberia Type' margin. For stretching factors of 4 or greater the whole crust is brittle and crust-cutting faults allow hydration and serpentinisation of the upper mantle. A similar mechanism is interpreted at the Wilkes Land margin, however, no evidence of major detachment or décollement surfaces are evident in seismic reflection data from the Wilkes Land margin. Figure from Pérez-Gussinyé *et al.* [2001].

Further investigation with wide-angle seismic refraction techniques are required to determine if the COT zone inferred here shares the same characteristic velocity structure as observed off the Iberian margin. However, the presence of exhumed mantle peridotites at the Wilkes Land margin can be interpreted on the basis of seismic reflection data interpretation and, gravity and magnetic modelling.

These results provide further support to the suggestions of Tikku & Cande [1999] and Sayers *et al.* [2001] that 'anomaly 34y' and its interpreted lineation (e.g. Figures 5.10 and 5.14) is not a seafloor spreading anomaly as it overlies extended continental crust

and exhumed upper-mantle lithosphere. This has a number of important implications for the breakup history of Australia and East Antarctica. Due to the lack of a confidently identifiable magnetic anomaly sequence prior to the Eocene, and the recognition that 'anomaly 34y' may not be a seafloor spreading anomaly, it is very difficult to constrain the timing of the onset of seafloor spreading between Antarctica and Australia. Additionally, it is apparent that a boundary between continental and oceanic crust is not present at the Wilkes Land margin, arguably a COB should therefore be defined at the boundary between exhumed continental lithosphere mantle and oceanic crust. Although the COB can be defined in this fashion, determination of a stretching factor (β) within the COT has little meaning as a total absence of continental crust is inferred within this zone.

The re-interpretation of the genesis of 'anomaly 34y' does not, however, require the interpreted COT zone to be re-assessed. This is because it was originally defined herein (Figure 4.23) as the zone interleaving crust of clear continental and oceanic affinity. The presence of exhumed mantle, interpreted to represent continental lithosphere, does not constitute unequivocal continental crust, therefore, the interpreted COT zone is robust to the results of the above modelling.

7.3 Extension and Subsidence at the Wilkes Land margin

7.3.1 Extension and Crustal Thinning

Thermal contraction, following heating of the lithosphere, and crustal thinning associated with erosion have been demonstrated to contribute to subsidence at rifted margins (e.g. Sleep [1971]). However, lateral extension of the crust and upper-mantle is now believed to be the primary causative process responsible for the creation of rift-type basins in passive margin settings. McKenzie [1978] developed a model in which extension is responsible for both the thermal anomaly and crustal thinning necessary for a sedimentary basin to form (as discussed in Chapter 1). McKenzie [1978] defined the ratio of initial to extended crustal and lithospheric-mantle thickness as the stretching factor (β). In this uniform stretching model, there exists a unique subsidence history for any given value of β. Accordingly, defining β at rifted margins has important consequences for understanding the subsidence history and margin evolution.

The McKenzie [1978] model, however, does not account for lateral heat conduction or lithospheric flexure associated with syn- and post-rift processes, and assumes instantaneous rifting. These processes were demonstrated to alter the theoretical subsidence and evolution of a basin beyond the simple controls that the degree of stretching imparts (e.g. Steckler & Watts [1981], Watts *et al.* [1982], Cochran [1983]).

Modelling by Cochran [1983] demonstrated that incorporating a finite rift interval in concert with the effects of lateral heat conduction and lithospheric flexure predicted markedly different subsidence and uplift histories relative to the uniform stretching model of McKenzie [1978]. Specifically, Cochran [1983] predicted that post-rift subsidence could be as much as 25% less than predicted by the method of McKenzie [1978] for a rift interval of 20 Ma.

The subsidence history at rifted margins is usually constrained by backstripping sedimentary sequences, observed in core and well-log data, in conjunction with palaeontological data that provides information on water depth through time (e.g. Steckler & Watts [1978]). By comparing backstripped curves of tectonic subsidence through time with theoretical curves based on the models of, for example, McKenzie [1978] and Cochran [1983], it is possible to deduce information on basin forming mechanisms. However, as no well data is available on the Wilkes Land margin, this is not possible here.

Stewart *et al.* [2000] used *pseudo-well* analyses, to supplement data from a single well, to investigate the subsidence history and palaeowater depths at the Namibian rift margin. Pseudo-wells can be 'created' at any point where the sediment thickness is constrained, and can be flexurally or Airy backstripped if a sediment thickness profile or grid is available. In this way each seismic-stratigraphic unit is backstripped and the cumulative backstrip compared to theoretical subsidence plots to infer palaeowater depths.

The tectonic subsidence can be calculated for only three points at the Wilkes Land margin, as there are age constraints on only two seismic-stratigraphic sequences. Therefore, the resulting tectonic subsidence 'curve' is poorly defined (Figure 7.8). Figure 7.8 compares the cumulative backstrip and TTS, for two pseudo-wells on Line GA-228_23, to theoretical curves of tectonic subsidence based on the model of Cochran [1983]. An initial crustal thickness of 31 km, a rift age of 100 Ma, and a rift duration of 15 Ma were assumed in the calculation of the theoretical tectonic subsidence curves, based on subsidence curves inferred from wells on the southern Australian margin (e.g. Hegarty *et al.* [1988]). The difference between the cumulative backstrip and the theoretical subsidence curve can be inferred to represent palaeowater depths. For the margin region constrained by seismic reflection data, pseudo-well analyses indicate that the water depth has exceeded 1.5 km since at least 83 Ma.

Although the subsidence history can not be constrained in detail, the TTS is constrained from backstripping. Studies of TTS are advantaged relative to studies of crustal thinning as they involve no assumption about initial crustal thickness. Henning *et al.* [2004] use variations in TTS depth to infer the presence and thickness of serpentinised mantle in the COT zone off west Iberia. In their study, local compensation of sediments is assumed. Additionally, complete alteration to serpentinite is assumed for the zone of

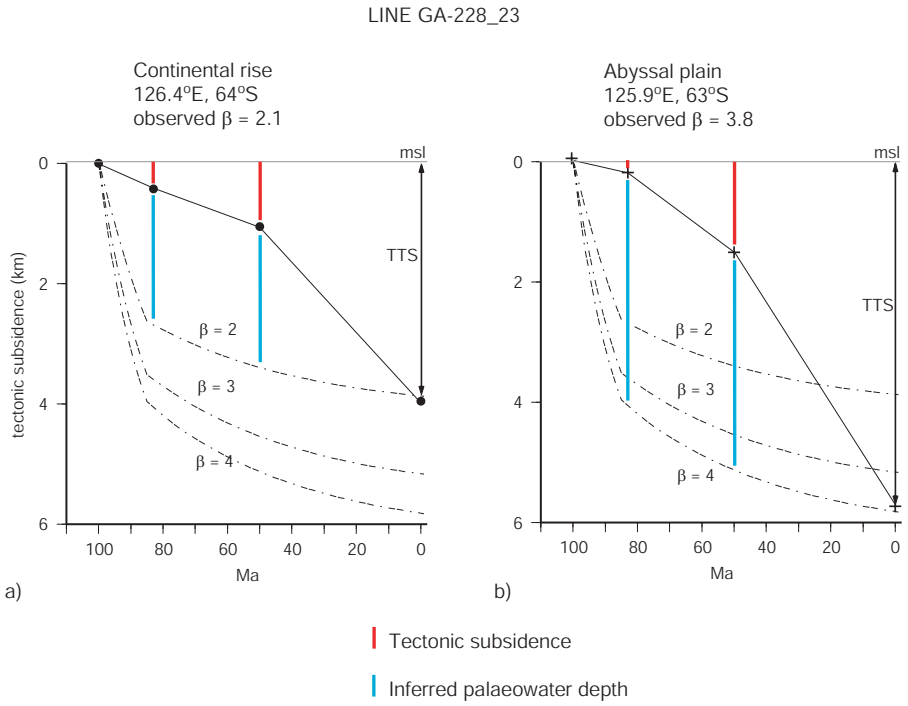

Figure 7.8: The difference between the cumulative backstrip curve (solid) and the theoretical subsidence curve (dashed) provide an estimate of palaeowater depth for two pseudo-wells on Line GA-228_23. The observed β values are taken from the gravity model crustal structure for this line and correlate very closely to the theoretical subsidence predicted by the model of Cochran [1983].

altered mantle (i.e. a density of 2550 kg/m^3). Despite these limitations, they find a correlation between TTS and the presence of serpentinised peridotites determined from drilling, dredging, and seismic refraction experiments. Analysis of the TTS off Wilkes Land do not show any clear correlation between TTS and the COT zone. Given the lack of seismic refraction data to independently constrain the extent of exhumed mantle and the degree to which it has been serpentinised, it is not possibly to quantitatively analyse the TTS data with regard to possible thicknesses of serpentinised mantle.

In addition to the importance in understanding basin evolution, the β distribution at rifted margins is one of the most useful parameters by which dynamic models of rifting can be constrained (e.g. Bassi [1991], Bassi [1995], Pérez-Gussinyé *et al.* [2001]). Whether or not lithospheric necking occurs and the degree to which conjugate margins are symmetrical is a strong function of the crustal thinning pattern (e.g. Buck *et al.* [1999]). Additionally, estimates of β are integral to inferring strain rate during rifting at ancient passive margins, a parameter believed to strongly influence the final width of extended continental crust (e.g. Bassi [1995]). Pérez-Gussinyé *et al.* [2001] also demonstrate that

β is a critical factor in the serpentinisation of the upper-mantle during rifting.

The pattern of thinning at the Wilkes Land margin has been investigated by using the crustal structure parameters determined from process oriented modelling (i.e. TTS and initial crustal thickness), which were demonstrated to correlate closely to the independent crustal structure data available (i.e. seismic reflection and sonobuoy refraction inferred $Moho$ depths). Figure 7.9 plots β as a function of distance from the landward or inner limit of the COT zone (herein referred to as the Continent-Transition Boundary [CTB]), as defined from seismic reflection data interpretation (Figure 4.23). The dashed lines beyond the inner limit of the COT zone show the β distribution as far as the outer limit of the COT zone. It is not clear, however, that β has any physical meaning in a COT zone where top basement comprises, in part, exhumed mantle peridotite and there is a complete absence of continental crust. Evidence from the West Iberian margin suggests that there is a gradation in the vertical seismic velocity in the COT zone, rather than a sharp change associated with a continental or oceanic lithosphere crust-mantle boundary [Dean *et al.*, 2000]. This further suggests that the determination of β within the COT zone is of limited value.

Bathymetry profiles for each β profile are included to allow any relationships with the present-day margin morphology to be assessed. The 13 GA-228 and GA-229 lines are divided into western, central, and eastern sectors for analysis in Figure 7.9. Although this is partly undertaken to improve the clarity of the images, these regions are also distinct in terms of free air gravity anomaly patterns, post-rift sediment distribution and, more importantly, inferred initial crustal thickness as outlined in Chapter 6.

The greatest amount of crustal extension in the western margin sector is inferred for Lines GA-228_18 and GA-228_19. However, there are no independent constraints on crustal thickness for this sector and the greatest sediment thickness is also observed. Due to the large sediment thickness a deep basement is observed and, therefore, a large degree of crustal thinning is required to compensate for this. Therefore, large β values are inferred, however, if a greater initial crustal thickness value was assumed (i.e. >35 km) the points of maximum necking would not be as radically thinned.

The pattern of crustal thinning for Lines GA-228_20 to GA-228_26 are very similar. A total width of extended continental crust of ~350 km is observed, and the distance from the shelf-break to the inner limit of the COT is ~150-200 km. The β increases approximately linearly from unity at the coast, to ~2.5 at 100 km landward of the CTB. A sharp increase in β occurs towards the CTB, and maximum values of ~5 are reached at or just landward of the CTB.

The pattern of crustal thinning in the eastern Wilkes Land and Terre Adélie margin sector is far more variable. Lines GA-228_27 and GA-228_28 exhibit a relatively similar

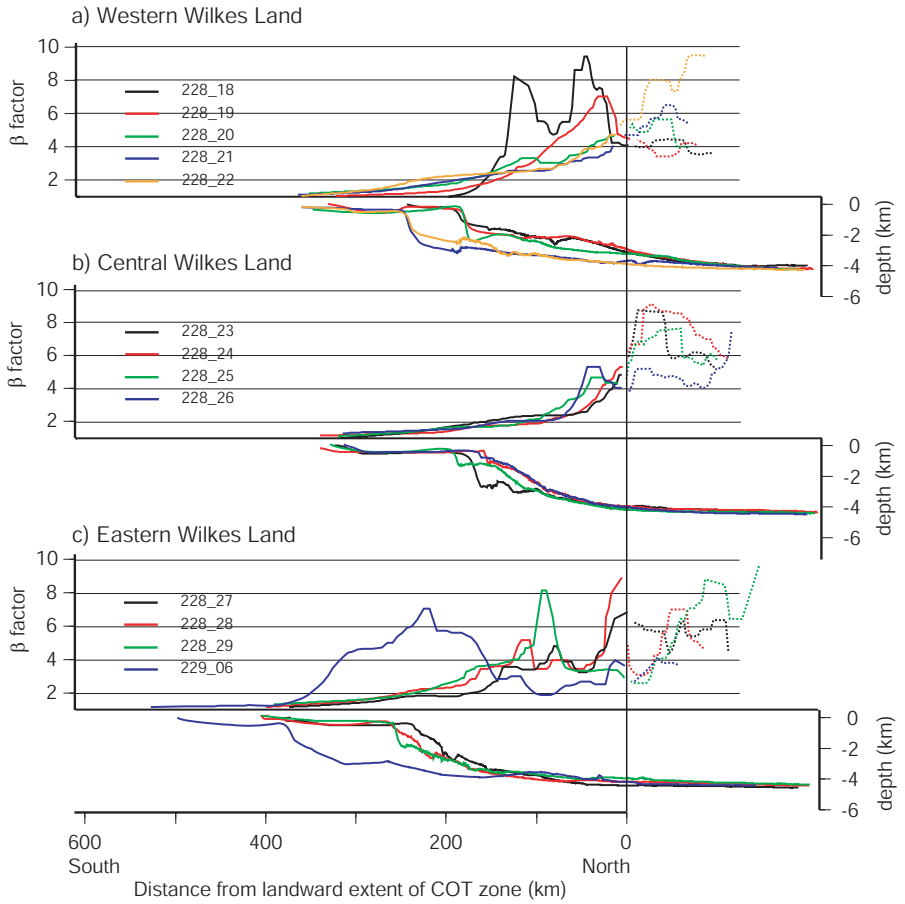

Figure 7.9: Degree of crustal stretching (β) as a function of distance from the inner limit of the COT zone (Figure 4.23) a) western, b) central, and c) eastern Wilkes Land. Bathymetry data are illustrated in the lower panels beneath the β profiles.

pattern to central Wilkes Land transects, except that peak β values exceed 6 and 8 on these lines respectively. Both these lines also indicate a zone of increased crustal thinning ($\beta > 4$) at ~100 km landward of the CTB. The peak β on Line GA-228_29 (~8) occurs coincident with this zone of increased crustal thinning, not at the CTB. The total width of extended continental crust for Lines GA-228_27 to GA-228_29 is almost 400 km, and the shelf-break to CTB distance is 225-275 km.

The β distribution for Line GA-229_06, across the ARB, is markedly different relative to the transects from margin sectors to the west. The total width of extended continental crust on this line is over 500 km, and the shelf-break to CTB separation is almost 400 km. The width of crust characterised by $\beta > 4$, almost 200 km, is also much greater than in other margin sectors. The region of maximum β occurs more than 150 km landward of the inferred CTB. A $\beta < 4$ characterises the limit of extended continental crust, lower than for all other lines except GA-228_29. This indicates that the point of eventual

crustal rupture for eastern most Wilkes Land and Terre Adélie occurred seaward of the point of maximum crustal extension.

Figure 7.10 compares the β distribution inferred for the central Wilkes Land margin (Line GA-228_24) with the inferred β results of backstripping, gravity modelling and crustal restoration studies at other passive, rift-type margins. Results from the margins of South Africa, Nova Scotia, Gabon, eastern U.S.A., Brazil (Campos Basin), Goban Spur, Carolina, and Valencia Trough (western Mediterranean) are included from a compilation by Watts & Fairhead [1997]. Results from the Otway Basin are after the published wide-angle refraction data of Finlayson *et al.* [1998]. Results from West Iberia are courtesy of T. Cunha (unpubl., Uni. of Oxford), and results from the Great Australia Bight (GAB) margin are from this study.

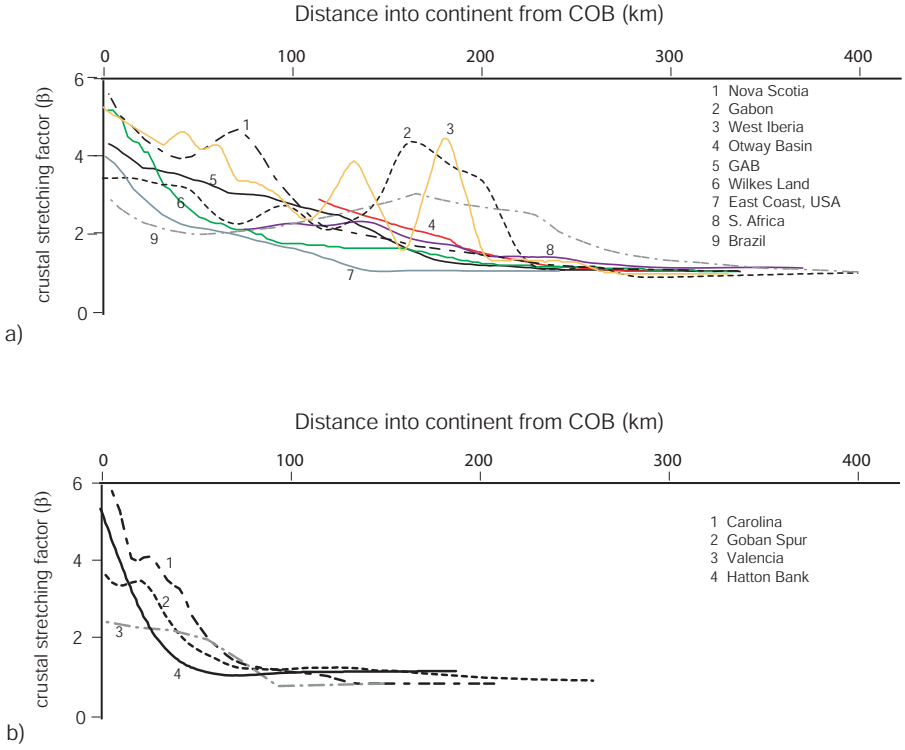

Figure 7.10: Comparison of crustal extension, as determined from a variety of methods, as a function of distance from the COB. a) Rifts where extended crust occurs up to and beyond 200 km landward of the COB, and b) narrow rifts where extension is focused within 100 km of the COB. The results from West Iberia and Gabon indicate that the locus of extension can occur at large distances from the point of eventual crustal rupture.

The results in Figure 7.10 are broadly divided on the basis of width of extended crust. The crustal thinning pattern from Wilkes Land is clearly more comparable to the patterns observed for the wider rift margins. The results from the West Iberia, Nova

Scotia, and Gabon margins indicate that crustal thinning is not confined to the region of the COB, but can occur up to 150-200 km landward of the COB. These results are similar to the observed crustal thinning pattern for eastern Wilkes Land and Terre Adélie.

The two examples of conjugate margin pairs included in Figure 7.10 (i.e. Brazil-Gabon and West Iberia-Nova Scotia) are all wider rifts that exhibit non-uniform stretching. The reasons for the large variations in crustal thinning patterns at rifted margins are not well understood. As outlined in Chapter 1, rift margin evolution is a complex function of the geotherm, rheology, lithospheric strength, extension and strain rates, and thermal processes.

Modelling (e.g. Bassi [1991], Bassi [1995], Buck *et al.* [1999]) and geological observations (e.g. Taylor *et al.* [1995], Pérez-Gussinyé *et al.* [2001]) indicate that wider rifts, with variable loci of extension, and a broad COT zone are associated with lower strain rates, which allow greater heat loss and, therefore, rheological hardening during rifting and a corresponding increase in strength. Whereas, narrow rift margins are associated with rapid extension, high strain rates, and, therefore, less heat loss and a greater propensity for melt generation and magmatism. Davis & Kusznir [2002], however, demonstrate that there is a continuum of rifted margin widths from ∼50 km to almost 500 km. This emphasises that the large number of factors involved in controlling rift margin formation can interact over a wide range and produce the great variety of rifted margin styles and structures observed.

7.3.2 Oceanic Crust Depth Anomalies

The rate and magnitude of oceanic crust subsidence does not depend on extension, as for rifted continental crust, but rather on thermal contraction and, therefore, time since emplacement or age (e.g. Sclater & Francheteau [1970]). Therefore, where the age of oceanic crust is constrained, normally by the correlation of magnetic anomalies with the geomagnetic reversal time scale, its depth can be relatively accurately predicted.

Parsons & Sclater [1977] demonstrated a linear relationship between the depth to oceanic crust and $\sqrt{t}$, where t is the age of the oceanic crust, which applies for $t < 60$ Ma. They showed that for older crust that this relationship breaks down, and that depth decays exponentially with age toward a constant asymptotic value. Parsons & Sclater [1977] predict oceanic crust to subside according to the following relationship for $0 < t < 60$ Ma,

$$D_t = 2500 + 350\sqrt{t} \tag{7.1}$$

and for $t > 60$ Ma,

$$D_t = 6400 - 3200e^{(\frac{-t}{62.8})} \tag{7.2}$$

Where D_t (metres) is the depth of oceanic crust at time t. The data used by Parsons & Sclater [1977] to derive these relationships were taken from the Atlantic and north Pacific Oceans only. However, Marty & Cazenave [1989] demonstrated that data from almost all oceanic plates are characterised by similar trends for young oceanic crust. In contrast to Parsons & Sclater [1977], they suggest that there is no asymptotic flattening and that oceanic crust continues to subside proportional to $\sqrt{t}$ indefinitely. Using an algorithm to remove small-scale consructional features on oceanic crust, Hillier & Watts [2005], however, confirm the plate-like subsidence of oceanic crust and asymptotic flattening in general accord with Parsons & Sclater [1977].

Where oceanic crust is sediment loaded it will have subsided to a greater depth than predicted by Equations 7.1 and 7.2. Therefore, to compare observed and predicted oceanic crust depths it is necessary to backstrip sediments to determine the depth to which the crust would have subsided in the absence of sediments. The difference in the observed (backstripped where sediment loaded) and predicted depth of oceanic crust is termed a *depth anomaly*.

Figure 7.11 compares the observed and predicted depths of oceanic crust for western, central and eastern Wilkes Land as a function of crust age. The observed depths are based on the anomaly identifications summarised in Figure 5.14. Predicted depths are calculated for both Equations 7.1 (curve 1) and 7.2 (curve 2), the depths predicted by these two equations do not diverge until after ~60 Ma. A third predicted depth curve is plotted based on Equation 7.2, with a constant shift of -600 m added (curve 3).

Figure 7.11 illustrates a consistent trend of deeper than predicted oceanic crust for the extent of the Wilkes Land margin. The only data points which do not conform to this trend are for Chron 33r aged crust on Line GA-228_20 and for Chron 20 and 21 aged crust on Line GA-229_06. The spurious result for Line GA-228_20 is likely associated with greater error due to the large sediment accumulation and uncertainty in identifying anomaly 33r on this line, it is possible that basement comprises transition zone rather than oceanic crust at this location. The correlation between the predicted depths for curves 1 and 2 and the observed depth for Chrons 20 and 21 on Line GA-229_06 may indicate that the ARB represents the eastern extent of anomalously deep oceanic crust. However, there is insufficient data to confidently infer this.

The magnitude of depth anomalies range from 200-800 m. There is no clear correlation between the age of the oceanic crust and the magnitude of the depth anomaly. Predicted depth curve 3, shifted -600 m relative to curve 2, provides the best fit to observed depths. This indicates that the depth anomalies are likely associated with a greater depth of zero-age crust at the SEIR relative to the Atlantic mid-ocean ridge and the Pacific spreading ridge system.

Figure 7.12 illustrates the distribution and magnitude of inferred depth anomalies off the Wilkes Land margin. There is no clear correlation between latitude and/or longitude and the magnitude of the inferred depth anomalies. However, the greatest magnitude anomalies are observed from ~120-136°E.

The results of this study, with regards the magnitude and approximate lateral extent, accord with previous interpretations of depth anomalies in the AAB associated with the Australia-Antarctica Discordance (AAD). The cause of the great depth of oceanic crust associated with the AAD has not been determined absolutely. Hayes & Conolly [1972] suggested that the observed depth anomalies are associated with a downwelling convective current in the asthenosphere. This interpretation was later supported by other workers (e.g.

Gurnis *et al.* [1998] suggest that the great depth of the AAD is associated with the Mesozoic subduction of Pacific ocean crust beneath the eastern margin of Australia. Geochemical data supports the notion of distinct mantle sources east and west of the AAD (Figure 2.16). This is cited by Gurnis *et al.* [1998] as evidence of the intersection at depth of the present-day SEIR and the ancient subduction zone which is plunging westwards.

Although the origin of the AAD remains enigmatic, the evidence for oceanic crust at anomalously great depths is well established. The results of this study provide some of the first regional estimates of the depth of unloaded oceanic crust along the extent of the Wilkes Land margin. With further improvements in dating of the oceanic crust and definition of the three-dimensional sediment distribution, it will be possible to better constrain the spatial and temporal extents of the AAD.

7.3.3 Ice Loading and Flexure

In addition to subsidence associated with the extension of continental crust and the cooling of oceanic crust, and sediment loading, high latitude margins are subject to load induced (e.g. glaciers and ice-sheets) subsidence and uplift. The East Antarctic Ice Sheet (EAIS) covers almost all of East Antarctica. Ice thicknesses of up to 4500 m occur locally and an average of 2500 m is observed for East Antarctica. The EAIS is isostatically supported almost entirely by the continental lithosphere of East Antarctica.

The flexural compensation of the EAIS explains, in part, the great depth of the continental shelf of Antarctica (e.g. ten Brink *et al.* [1995]). Although the ice sheet does not directly load the continental shelf (except during glacial maxima), the flexural response of the lithosphere results in a deepened continental shelf. Kagami [1995] suggested that the flexural response may extend beyond the continental shelf and manifest itself as crustal

upwarping beneath the continental rise (Figure 7.13).

A domed or upwarped basement has been observed in seismic reflection data off eastern Wilkes Land in a number of studies (e.g. Eittreim & Smith [1987], Tanahashi *et al.* [1987]). The landward extents of Lines GA-228_23 and GA-228_24 exhibit an upwarp of the *tur* unconformity that correlates to the doming identified in other studies. Kagami [1995] suggests that the region that is now upwarped originally subsided to a greater depth and was characterised by normal faults and seaward increasing subsidence. He suggested that the weight of the ice sheet was the main factor that contributed to an adjustment in the basement structure and resulted in upwarping.

A simple two-dimensional model, as illustrated in Figure 7.14, demonstrates that the upwarped structure observed in seismic reflection data is not associated with flexure due to ice sheet loading. Three-dimensional models were also tested, however, as the thickness of the EAIS does not vary rapidly laterally, the results are almost identical to two-dimensional models. A range of T_e estimates were tested and a spatially varying T_e model, varying from 100 km inland to 30 km at the margin, was also tested.

The model comprises a 3000 m thick ice sheet that terminates at the inner-limit of a 100 km wide continental shelf. This thickness of ice is representative of the ice-thickness for most of the EAIS in the Wilkes Land region. Ice sheet induced flexure deepens the inner limit of the continental shelf by ∼200-400 m depending on the T_e assumed in modelling. Whether or not a landward dipping continental shelf results is a function of the depth assumed for the shelf break. Although the downwarping of the continental shelf is as much as 400 m, the magnitude of the flexural bulge is less than 50 m for all T_e estimates tested. Therefore, it is unlikely that the 1-2 km of doming that is observed on the Wilkes Land margin is associated with ice sheet development in the Tertiary.

Three-dimensional flexural modelling of the Antarctic lithosphere, due to the load of the EAIS, was also carried out. The results of this modelling indicate that due to the long wavelength represented by the load of the EAIS, it is effectively locally compensated. Accordingly, there is very little difference in the modelled flexure predicted for a wide range of T_e estimates. The results proximal to the margins of Antarctica, where variations in flexure occur with changes in T_e, are almost identical to the simple two-dimensional model detailed above.

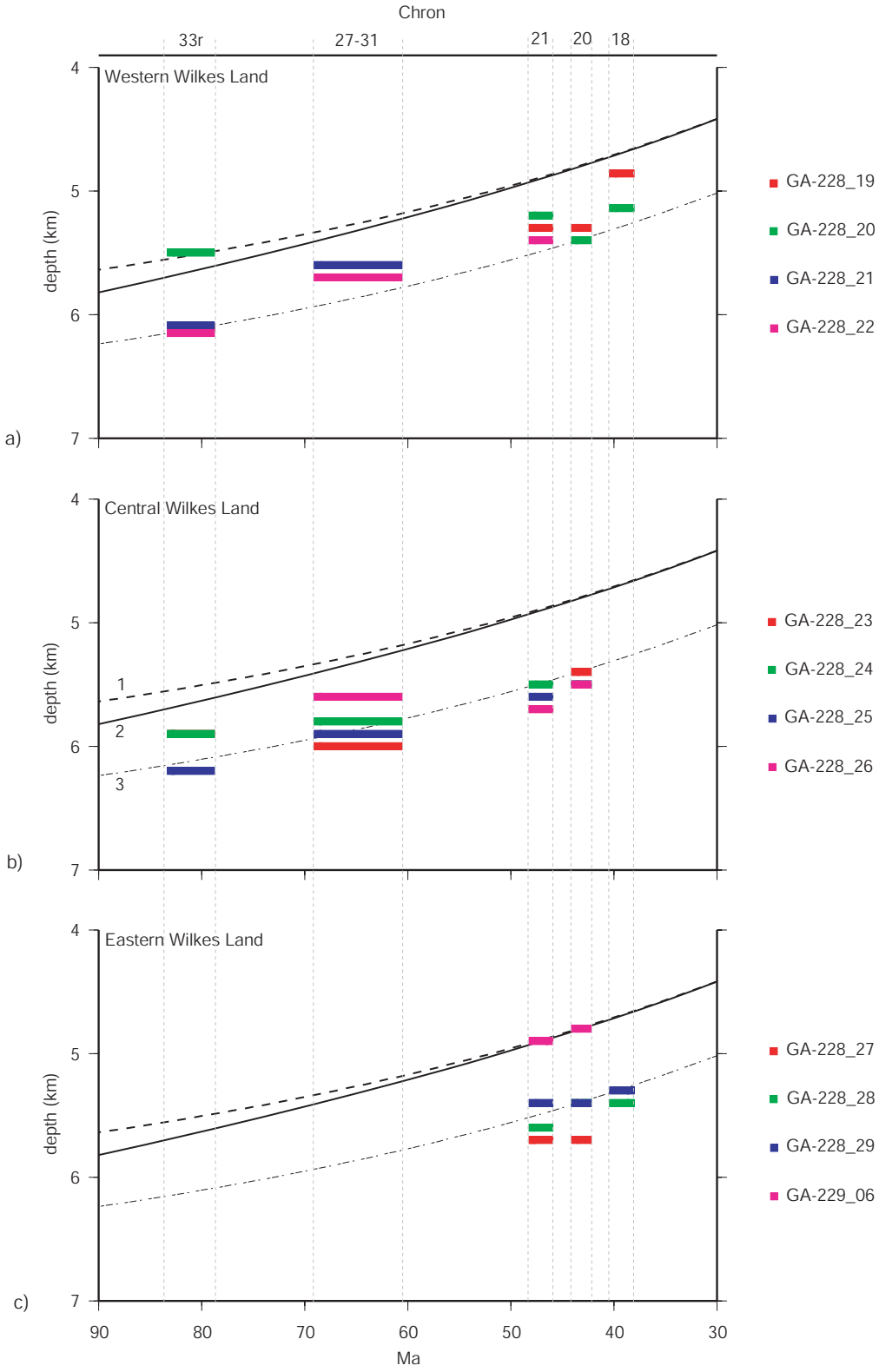

Figure 7.11: Comparison of predicted and backstripped depths of top of oceanic crust layer 2 for a) western, b) central, and c) eastern Wilkes Land. The predicted depth curves are based on Parsons & Sclater [1977] for $0 < t <\sim 70$ Ma (curve 1) and for $t >\sim 70$ Ma (curve 2), where t is the age of oceanic crust. Curve 3 is for $t >\sim 70$ Ma shifted by -600 m, this curve provides a better fit to the observed depths.

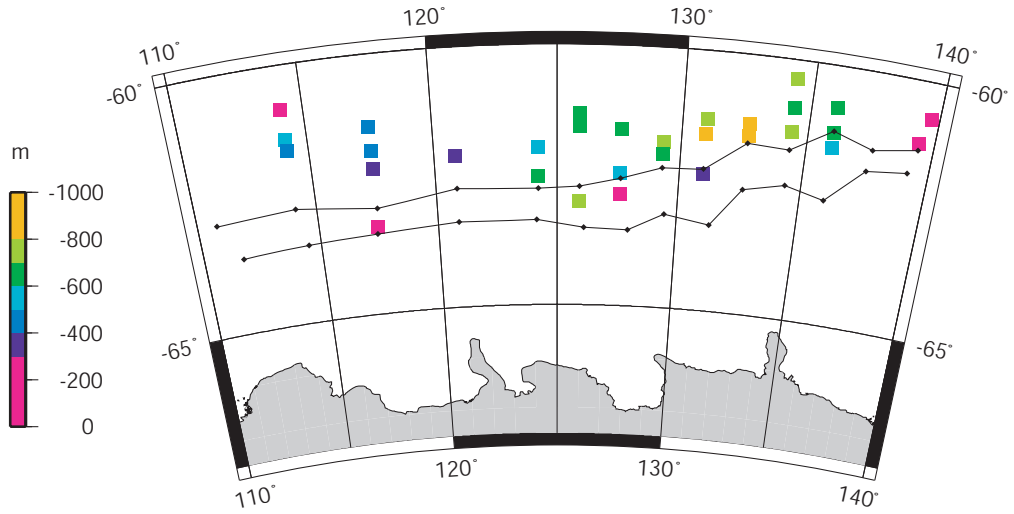

Figure 7.12: Depth anomalies calculated using the theoretical subsidence of Parsons & Sclater [1977] and the backstripped depth of oceanic crust observed on GA-228 and GA-229 survey lines. There is no spatial correlation of depth anomaly magnitude. The COT zone interpreted from MCS data (Figure 4.23) is shown (black solid lines).

Figure 7.13: The Kagami [1995] schematic model for upward arched basement at the Wilkes Land margin. Kagami [1995] attributed the uparched basement to the flexural compensation of ice sheet loading. OC = oceanic crust, M = mantle.

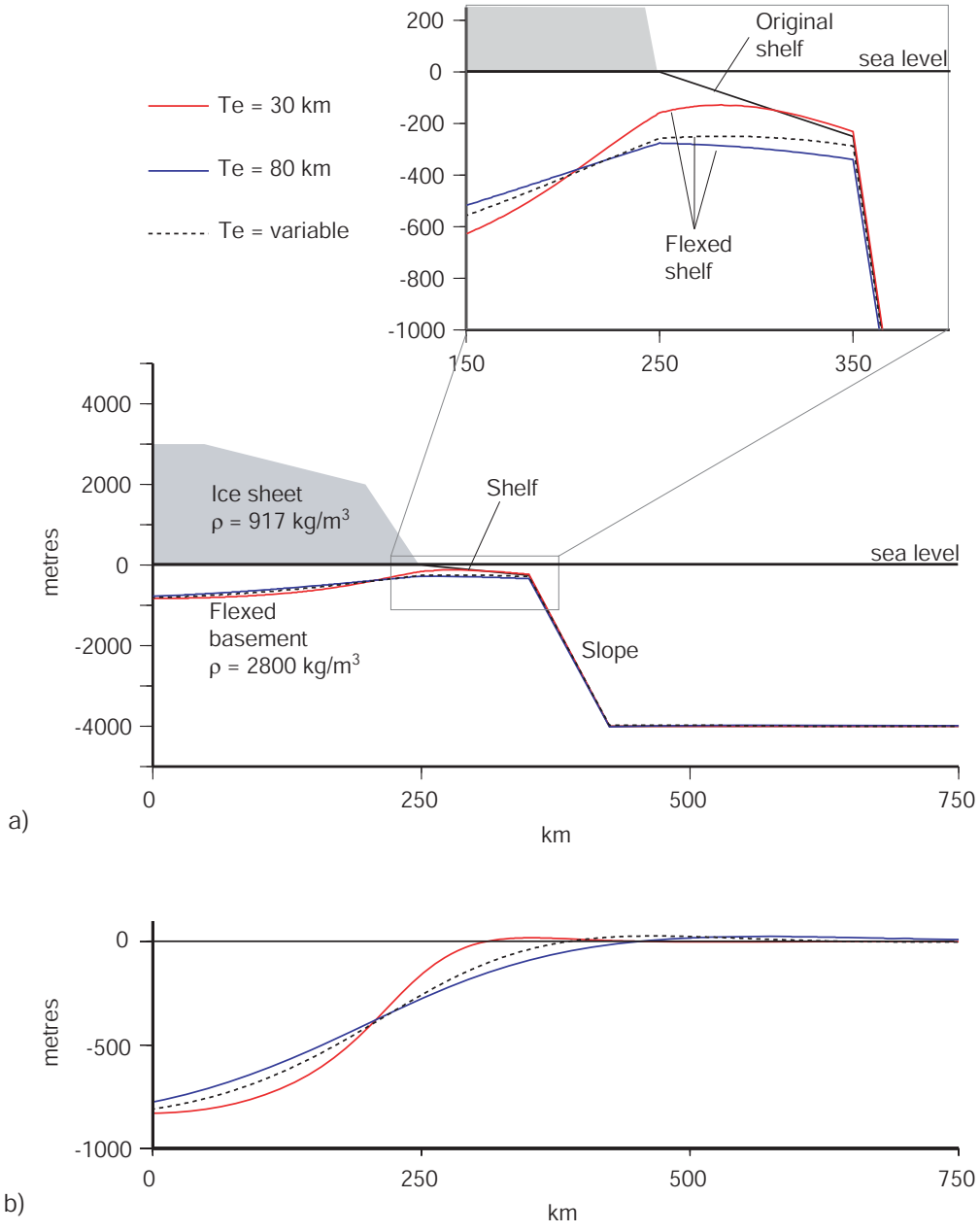

Figure 7.14: a) Model of ice sheet induced flexure and its modifying effect on a simplified margin morphology. The inset figure demonstrates the minor contribution of ice sheet loading to the great depth of the Antarctic continental shelf, except for the inner shelf. b) The flexure associated with the ice sheet load illustrated in (a), the amplitude of the flexural bulge does not exceed 50 m.

7.4 Conjugate Margin Structure

7.4.1 Regional Setting

Australia is a low elevation, stable continental mass where active volcanoes are absent and large earthquakes rare. The majority of the land mass comprises the Australian Precambrian Shield (e.g. Ludbrook [1980]). The Shield is a composite of blocks that became stable during the Proterozoic and have not been subjected to major tectonism since (Figure 7.15). The oldest rocks occur within the Pilbara and Yilgarn Blocks of Western Australia. The *Tasman Line* (e.g. Murray *et al.* [1989]) broadly divides the western terrane of Precambrian blocks from the Phanerozoic fold belt systems of eastern Australia [Direen & Crawford, 2003]. The southern margin of Australia comprises a number of distinct blocks, from the Yilgarn Block in the west to structurally complex Cambrian terranes of western Tasmania in the east (e.g. Meffre *et al.* [2000]).

Figure 7.15: Major structural elements of Australia, from Ludbrook [1980]. The Tasman Line represents the structural boundary between the Australian Precambrian Shield to the west and the Phanerozoic fold belt systems to the east.

The basins of the southern margin are largely a product of protracted extension throughout eastern Gondwana from the Jurassic to the Cretaceous, which led to the development of the Southern Rift System (SRS) [Willcox & Stagg, 1990]. The extension resulted in the final breakup of what are now the Australian and Antarctic Plates in the Late Cretaceous, as discussed previously. The SRS, comprising the Great Australian Bight (GAB), Otway, and Sorell Basins, extends for more than 4000 km, from the Naturaliste Plateau in the west to the South Tasman Rise (STR) in the southeast (Figure 7.16). The Bass Strait region represents a major splay of the SRS that separates the continental crust of the Australian mainland and Tasmania.

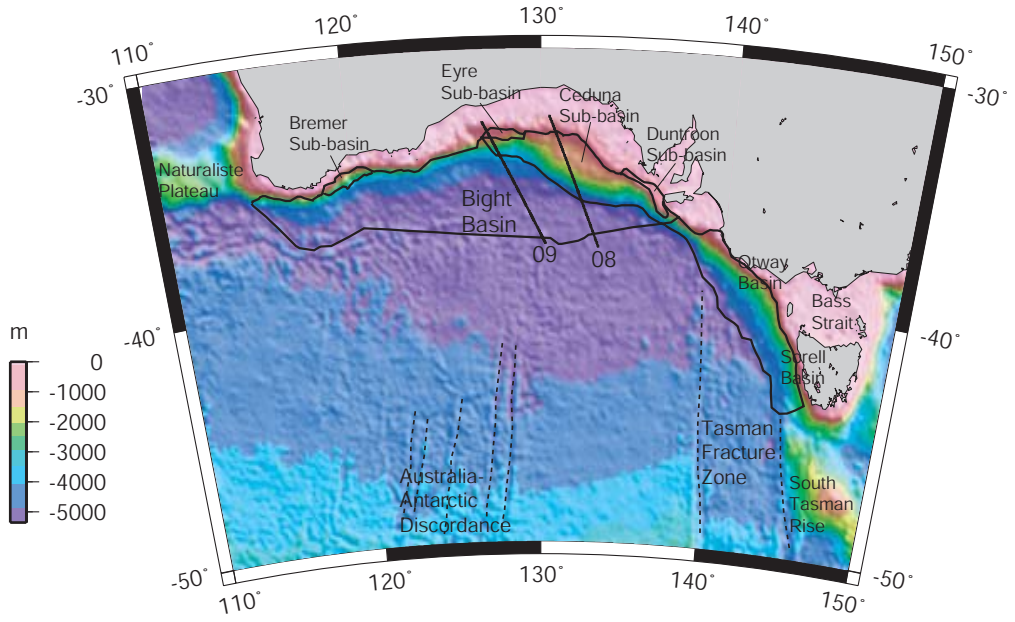

Figure 7.16: Location of the Bight Basin (with component sub-basins), Otway Basin, and Sorell Basin, which together form the Southern Rift System (SRS). Transects 08 and 09 are the location of seismic reflection profiles illustrated in Figure 7.17.

The GAB basin, or Bight Basin [Totterdell *et al.*, 2000], is the most areally significant of the SRS basins, extending from the southwest tip of Australia to ∼140°E. The Bight Basin contains five main depocentres; they are, from west to east, the Bremer, Recherche, Eyre, Ceduna, and Duntroon sub-basins [Totterdell & Bradshaw, 2004]. The Bight Basin underlies the continental shelf and slope, including two bathymetric terraces, in water depths ranging from 200 to over 4000 m. The largest and thickest depocentre, the Ceduna Sub-basin, comprises a sedimentary sequence of >15 km thickness [Totterdell *et al.*, 2000]. The breakup unconformity within the Bight Basin is interpreted as the approximately Turonian aged base of the Tiger Super-Sequence [Totterdell *et al.*, 2000].

To the east of the Bight Basin are the Otway and Sorell Basins, which are located in

a region where continental separation failed to continue eastward but was instead offset to the south by the Tasman Fracture System west of Tasmania [Moore *et al.*, 2000]. The breakup unconformity within the Otway and Sorell basins was interpreted as the top of the Sherbrook Group (∼64 Ma) by Moore *et al.* [2000].

The STR occurs ∼200 km south of Tasmania approximately along strike of the Tasman Fracture System from the Sorell Basin. It consists of a triangular core of Palaeozoic basement, flanked by basins containing up to 6 km of sediments Stagg *et al.* [1999]. Willcox *et al.* [1989] correlated the seismic sequences in these basins, on the basis of seismic character, to the Otway Basin. They inferred that the STR may have been conjugate to the Otway Basin prior to the Late Cretaceous.

Sediment Distribution

The SRS, particularly the Bight Basin, is characterised by very thin Cainozoic sediments. Because of the arid climate and low elevation of most of southern Australia, the SRS has been sediment starved throughout the Tertiary. Even the great thickness of sediments in the Ceduna Sub-basin was deposited almost entirely throughout the Jurassic and Cretaceous. Figure 7.17 illustrates the thickness of seismic-stratigraphic units, based on the interpretation of Totterdell *et al.* [2000], for two profiles across the GAB margin.

Both transects are characterised by very thin Tertiary sequences, of less than 1000 m. However, the thickness of Cretaceous sediments on Lines 08 and 09 is markedly different. Line 08, which traverses the Ceduna Terrace and Sub-basin, is characterised by a thick (up to 6000 m) Turonian to Santonian (syn-rift?) sequence, and a similarly thick Santonian to Tertiary, lower post-rift sequence. A hiatus in sedimentation is inferred for most the Palaeocene and the erosional upper surface of the lower post-rift sequence is unconformably overlain by the basal units of the Eocene and younger upper post-rift sediments. In contrast, the maximum syn- and post-rift sediment thickness on Line 08 is less than 2000 m.

Figure 7.18 illustrates the total sediment isopach for the Bight Basin [Totterdell & Krassay, 2003]. The great thickness of sediments in the Ceduna Sub-basin is evident, however, a large proportion of this is pre- and syn-rift. No regional post-rift sediment thickness grid is available for the entire Bight Basin due to data limitations.

The great thickness of sediments within Ceduna Sub-basin is attributed to deposition by high sediment flux, delta progradation [Totterdell *et al.*, 2000; Totterdell & Bradshaw, 2004]. Basins outside of this region received relatively low sediment input throughout the Late Cretaceous. Since the Early Tertiary the entire Bight Basin and the Otway basin have been sediment starved, although sedimentation continues in the Sorell Basin

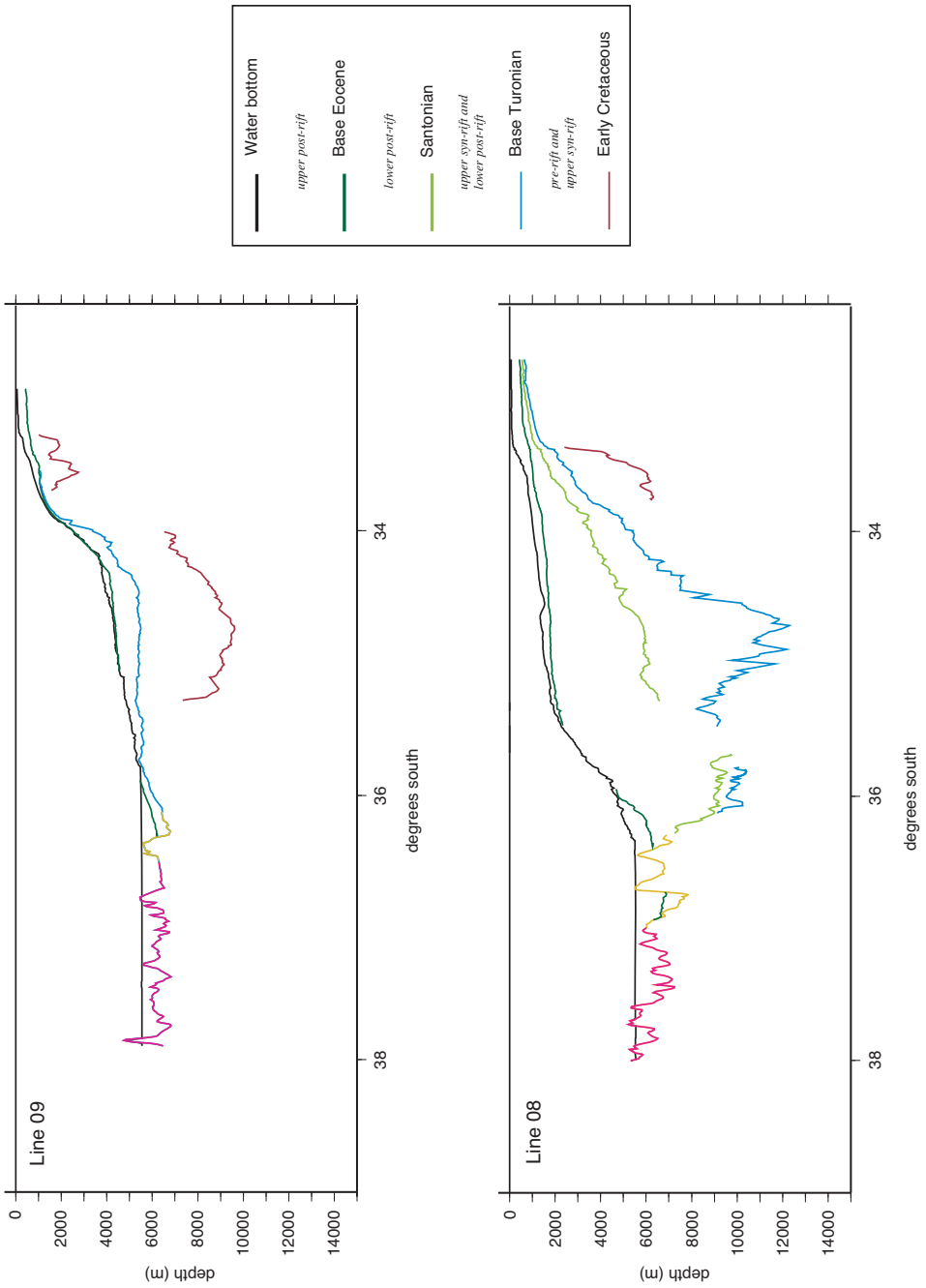

Figure 7.17: Seismic-stratigraphy from Totterdell *et al.* [2000] for two seismic reflection profiles across the Bight Basin, as located in Figure 7.16. Profile 08 traverses the Ceduna Sub-basin, whereas profile 09 is located to the west and is characterised by a much thinner sedimentary sequence.

off western Tasmania.

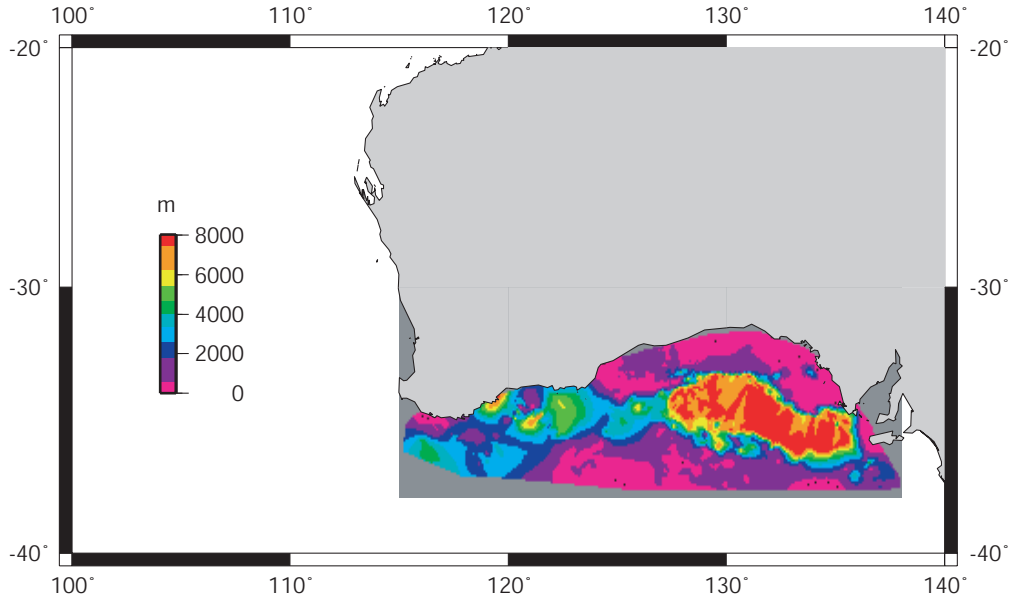

Figure 7.18: Total sediment isopach (including pre-, syn- and post-rift sediments) for the Bight Basin of the southern Australian margin. The Ceduna Sub-basin is the locus of thickest sediments. Data from Geoscience Australia [Totterdell & Krassay, 2003], resolution is nominally ∼3 minute.

Crustal Structure

Constraints on crustal structure and thickness for the Australian continent and its margins are sparse. However, Collins *et al.* [2003] estimate that ∼73% of onshore continental Australia is characterised by a crustal thickness of 35-41 km using seismic refraction data. Data from the onshore sector of the southern Australian margin is particularly sparse. Figure 7.19 illustrates velocity depth curves from the Yilgarn Block of southwest Australia, and from Tasmania. A shallower depth to *Moho* is inferred for Tasmania relative to the far west of Australia. Crustal thickness estimates for the southern margin vary along-strike from 30-35 km (e.g. Collins *et al.* [2003], Brown *et al.* [2003]).

Figure 7.19: Velocity-depth curves for the Yilgarn Block (southwest Australia) and Tasmania (see Figure 7.15 for location of the blocks). Grey shading marks the range of *Moho* depths for each location. After Collins *et al.* [2003].

Estimates of *Moho* depth offshore of the southern Australian margin are based on sonobuoy refraction and seismic reflection data only. Ocean Bottom Seismometer (OBS) data exists for a small portion of the Otway Basin margin only. Figure 7.20 shows the location of sonobuoy data, where *Moho* velocities have been interpreted, from Geoscience Australia Survey 199 [Sayers *et al.*, 2001] and *Vema* Cruise 33 [Talwani *et al.*, 1978]. The depth to the sea floor and *Moho* are summarised for each of these sonobuoy locations in Table 7.2.

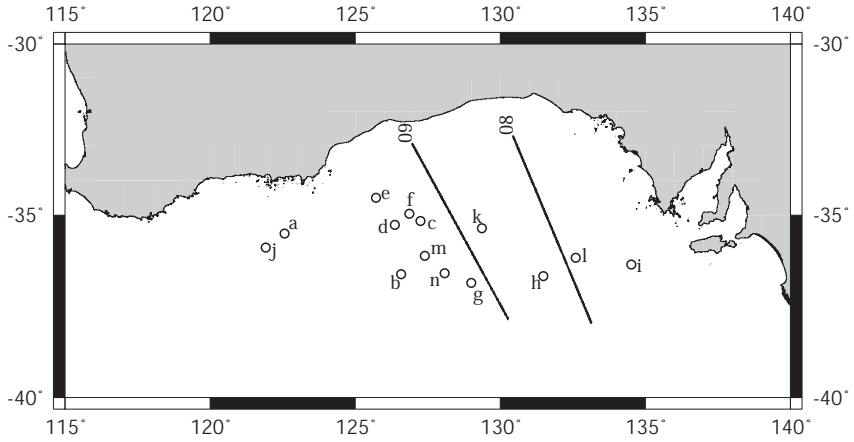

Figure 7.20: Sonobuoy locations for the Bight Basin (circles), with labels referring to Table 7.2. Profiles 08 and 09 are as illustrated in Figure 7.17.

7.4.2 Process-Oriented Modelling

Two-dimensional process-oriented modelling was undertaken for profiles 08 and 09 across the Bight Basin. Three-dimensional modelling was also conducted, on both the total sediment thickness and on sediment thickness grids adjusted to exclude pre- and syn-rift sediments. The applied methodology and parameters were identical to that outlined in Chapter 6, unless specifically stated otherwise (i.e. densities etc. as per Table 6.2).

Two-Dimensional Process Oriented Modelling

Figures 7.21 and 7.22 illustrate the results of process-oriented modelling for Lines 09 and 08 respectively. An initial, zero-elevation, crustal thickness (T_c) was selected such that the depth the flexed *Moho* was broadly in accord with the depth to *Moho* interpreted from off-line sonobuoys projected onto the 08 and 09 profiles. As the calculated gravity is relatively insensitive to T_c, this is the only constraint available.

Modelling on Line 09 is not sensitive to T_e as there is only a very thin post-rift sedimentary sequence in this region. The results are not altered by including the syn-

SB	cruise	station	long.	lat.	wb (km)	*Moho* (km)
a	*Vema* 33	6	122.57	-35.52	4.69	13.5
b	*Vema* 33	8	126.59	-36.65	5.59	12.0
c	*Vema* 33	11	127.25	-35.16	5.0	14.4
d	*Vema* 33	12	126.37	-35.27	5.05	13.0
e	*Vema* 33	13	125.72	-34.50	4.03	13.8
f	*Vema* 33	15	126.86	-34.95	4.57	16.7
g	*Vema* 33	16	129.00	-36.89	5.61	11.2
h	*Vema* 33	19	131.48	-36.71	5.61	11.7
i	*Vema* 33	21	134.52	-36.39	5.0	15.6
j	*Vema* 33	27	121.91	-35.91	5.05	13.0
k	*Vema* 33	36	-35.37	129.36	5.03	15.8
l	*Vema* 33	40	132.60	-36.20	5.03	15.8
m	GA 199	2	127.40	-36.15	5.5	15.7
n	GA 199	5	128.08	-36.62	5.5	14.1

Table 7.2: Sonobuoy (SB) data which have recorded mantle velocities in the Bight Basin, southern Australia, as located in Figure 7.20. wb = water bottom.

rift sediments (Tiger Supersequence Totterdell *et al.* [2000]), along with the post-rift sediments, in modelling. The edge effect high is well simulated by the calculated profiles for all T_e estimates tested. However, the magnitude of the edge effect low is not reached for any T_e estimate. The positive seaward gradient exhibited by the observed data is simulated by the calculated profiles, however, inferring the T_e via process-oriented modelling is not possible for this line.

Although T_e can not be constrained for Line 09 due to a lack of sediment loading since rifting, the number of sonobuoy stations where mantle velocities have been interpreted in the vicinity (within ∼100 km) of this line allow T_c to be constrained. For $T_c > 31$ km the flexed *Moho* is almost ubiquitously deeper than the sonobuoy inferred *Moho* depths. For $T_c = 31$ km, the modelled flexed *Moho* depth occurs within the range of *Moho* depths inferred from sonobuoys.

Survey 199 Line 08 is much more sensitive to T_e variation in process-oriented modelling. This is primarily because of the greater sediment thickness relative to Line 09 to the west. Due to the relatively shallow submarine extension of the Ceduna Terrace, there are effectively two edge effect anomalies across this line, one at the shelf break proper, and another further seaward at the change in slope across the terrace at ∼35°S. The large magnitude positive anomaly that correlates with the change in slope of the terrace

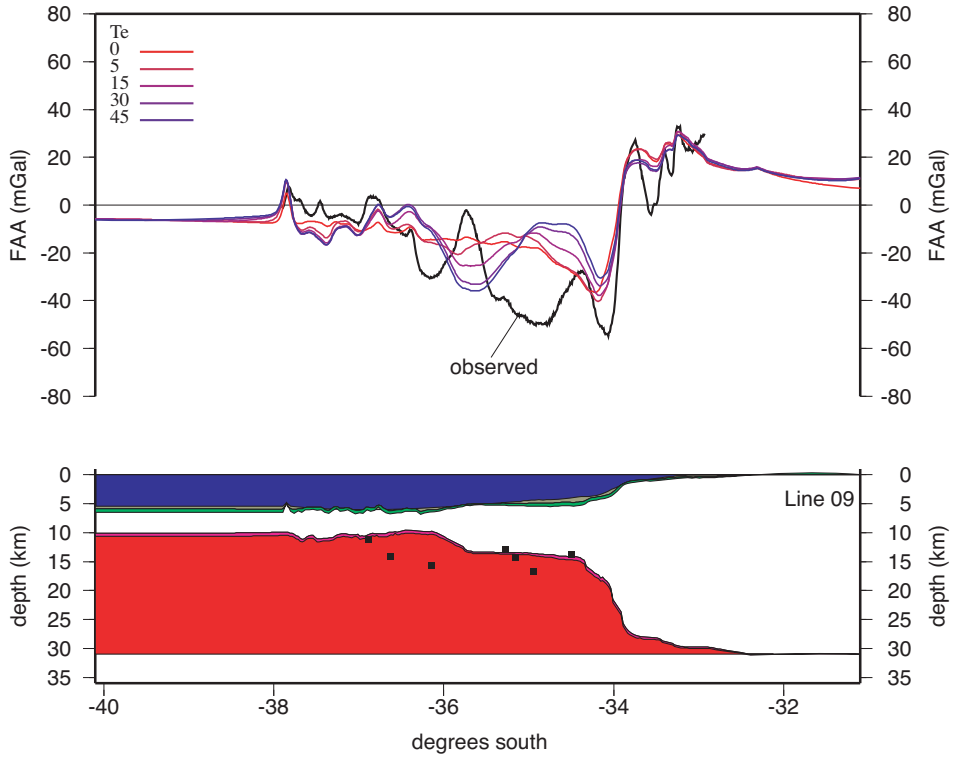

Figure 7.21: Process-oriented modelling for GA survey Line 09, as located in Figure 7.20. Black squares indicate the depth to *Moho* inferred from sonobuoy data projected laterally onto this section. Observed data is shiptrack measured gravity. Crustal section is for $T_e = 15$ km.

is also coincident with the locus of thickest sediments on this line.

Modelling with low T_e ($\leq$10 km) under-estimates the magnitude of the positive anomaly over the thickest sediments and over-estimates the magnitude of the edge effect high. Conversely, for high T_e ($\geq$30 km) the edge effect high is under-estimated and the high over the thickest sediments is over-estimated (along with the low seaward of this high). However, for T_e=15 km a good fit is achieved between calculated and observed anomalies. The shape and amplitude of the observed anomalies are almost perfectly simulated by the calculated profile. This indicates that the lithosphere underlying this region of the Bight Basin is characterised by T_e=15 km.

Although the T_e can be well-constrained for Line 09, it is more difficult to determine T_c due to the lack of seismic refraction and/or reflection data that images the *Moho* in this region. A slightly higher T_c of 33 km was assumed in modelling of this line, however, it is not possible to confidently infer T_c more accurately than by the range of $31 < T_c < 35$ km. The T_c does not exert a strong influence on the calculated gravity anomaly profile, however, the determination of crustal stretching factors is strongly dependent upon the

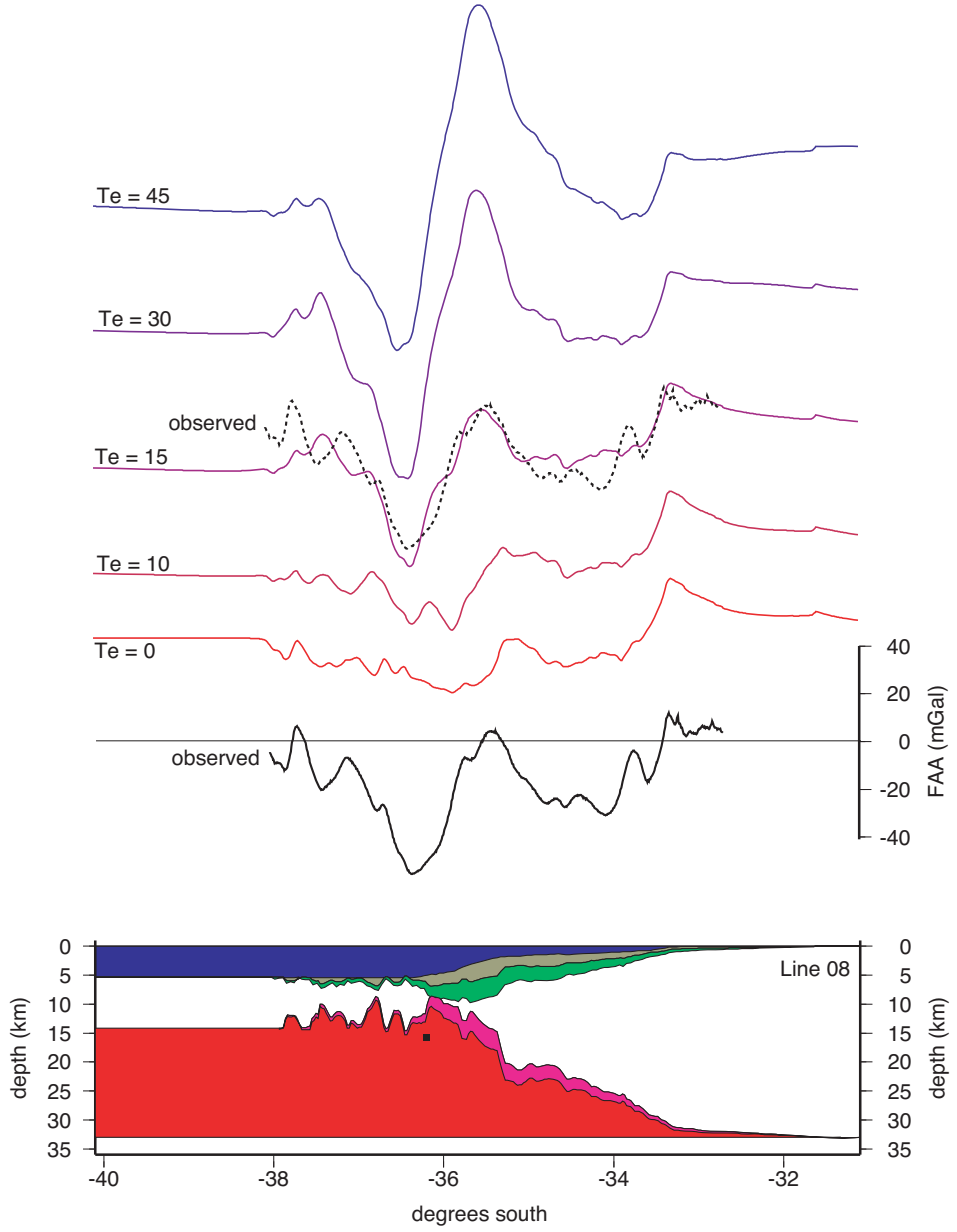

Figure 7.22: Process-oriented modelling for GA survey Line 08, as located in Figure 7.20. Black square indicates the depth to *Moho* inferred from sonobuoy data projected laterally onto this section. Observed data is shiptrack measured gravity. The calculated anomaly profile for T_e=15 km accurately simulates all features of the observed data. Crustal section is for $T_e = 15$ km.

assumed T_c.

Three-Dimensional Process Oriented Modelling

Three-dimensional gravity modelling was undertaken. The classic-Airy model isostatic anomaly was calculated for the entire southern Australian margin region using GEBCO 1 minute bathymetry [IOC *et al.*, 2003]. However, process-oriented modelling was conducted for the Bight Basin region of the margin only, as a sediment thickness grid is not available beyond this region.

Figure 7.23 shows the satellite derived free air gravity field [Sandwell & Smith, 1997] for the southern Australian margin[1], the classic-Airy modelled free air gravity field, and the classic-Airy isostatic anomaly. The free air field is characterised by a continuous, but relatively subdued, edge effect high and a broad, large amplitude edge effect low. The classic-Airy model simulates the broad character of the observed free air gravity field, however, it fails to predict the full extent of the observed edge effect low and some small sections of the edge effect high (e.g. 115-125°E).

The Ceduna Terrace region correlates to a positive free air anomaly in the classic-Airy model, however, the observed field is largely negative, except for the seaward edge of the Terrace. The classic-Airy isostatic anomaly map illustrates that although a large amount of the observed free air gravity field can be explained by the Airy compensation of the water filled basin, there is sufficient complexity such that a simple Airy model, which does not account for the presence of sediments, is inadequate.

Three-dimensional process-oriented modelling was undertaken for the Bight Basin. However, although the total sediment thickness is known for this region, the relative thickness of pre-, syn- and post-rift sediment is not constrained. Analysis of survey 199 Line 08 illustrated that in the Ceduna Sub-basin, the locus of thickest sediments in the Bight Basin, the pre- and syn-rift sediments comprised up to half of the total sediment thickness. Backstripping and gravity modelling of the total sediment thickness is, therefore, clearly not comparable to the methodology adopted for the Wilkes Land margin where only post-rift sediments were considered.

Process-oriented modelling was initially conducted using the total sediment isopach, clipped to a maximum thickness equivalent to the maximum observed post-rift sediment thickness (∼8000 m) (case 1). This is obviously an over-estimation of the *average* post-rift sediment thickness. Therefore, modelling was subsequently undertaken assuming a ratio of 1:1 for pre- and syn-rift, and post-rift sediment thickness (i.e. half the total sediment thickness was assumed to be post-rift) (case 2). Figure 7.24 illustrates flexural isostatic anomaly maps of the Bight Basin region, for three T_e estimates, for both

[1] After removal of wavelengths greater than ∼3333 km ($n = 12$) according to the geopotential coefficient model of Rapp & Pavlis [1990]

sediment thickness cases considered.

For T_e=0 km, the results for sediment thickness cases 1 and 2 are very similar. Neither are fully devoid of the residual edge effect low, and both almost entirely account for the edge effect high. For higher T_e the results for cases 1 and 2 diverge further. The differences are most evident in the region of the Ceduna Sub-basin and the thickest sediments. Larger isostatic anomalies are associated with the greater sediment thickness of case 1. The differences are substantial for T_e=30 km, a large amplitude negative anomaly occurs in the region of the Ceduna Sub-basin for both cases, however, the amplitude and size of the anomaly is much greater for case 1. Lower T_e models clearly more accurately simulate the observed gravity data.

Although in general a low T_e ($\sim$15 km) is inferred for the Bight Basin region, specific regions are best fit by higher and lower T_e estimates. For example, the positive linear FIA off the south-west margin sector is effectively reduced by different T_e estimates in different lateral segments. Circled areas in Figure 7.24 illustrate that the margin may be segmented to some degree with regards to T_e structure. To confirm this, a detailed knowledge of the thickness of post-rift sediments is required for the entire Bight Basin region.

Spectral analyses of flexural isostatic anomalies and the satellite derived FAA (Figure 7.25) confirm that the Bight Basin region is characterised by low T_e ($\leq$15 km). Two distinct peaks are evident in the FAA power spectrum, at wavelengths of $\sim$400 and 650 km, which reach amplitudes 50 and 90 mGal^2 respectively. These peaks are reduced in the power spectra of the flexural isostatic anomalies for sediment thickness case 1 for T_e=0 and 15 km, however, for T_e=30 km the peaks are of greater magnitude relative to the FAA spectrum. This indicates that for the maximum possible post-rift sediment thickness in the Bight Basin region, the $T_e << 30$ km. For sediment thickness case 2, the peaks in the flexural isostatic anomaly power spectra are reduced relative to the FAA spectrum for T_e=0, 15 and 30 km. However, the longer wavelength peak amplitude of the T_e=0 and 15 km power spectra is less than half that of the T_e=30 km spectrum. This indicates that even for the minimum likely post-rift sediment thickness, a $T_e < 30$ km best characterises the Bight Basin.

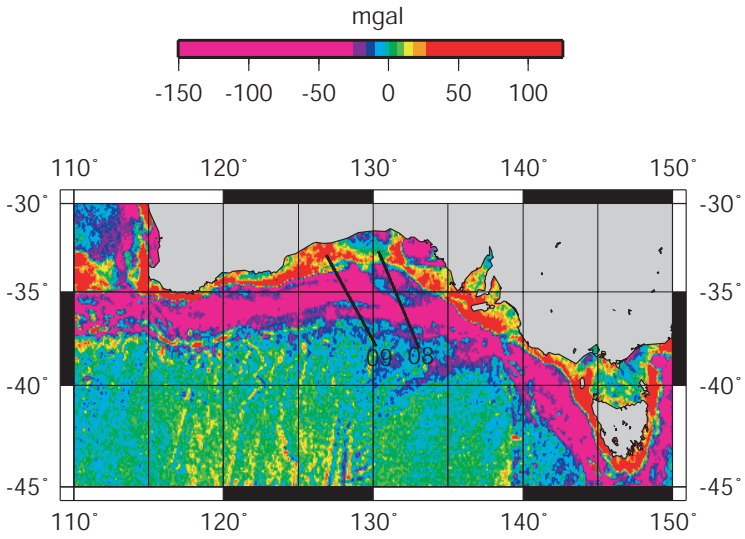

a) Observed free air anomaly

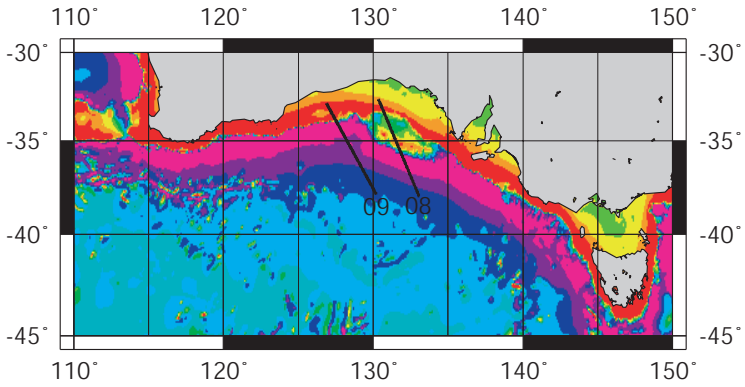

b) Classic-Airy modelled free air anomaly

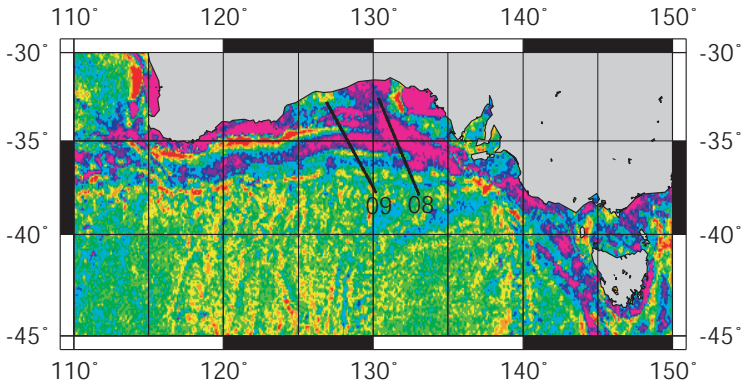

c) Classic-Airy model isostatic anomaly

Figure 7.23: a) Satellite derived free air anomaly map of the southern Australian margin [Sandwell & Smith, 1997]. b) Classic-Airy modelled free air anomaly map based on GEBCO 1 minute bathymetry [IOC *et al.*, 2003]. c) Classic-Airy isostatic anomaly map, which illustrates the failure of the classic-Airy model to predict the large amplitude edge effect low.

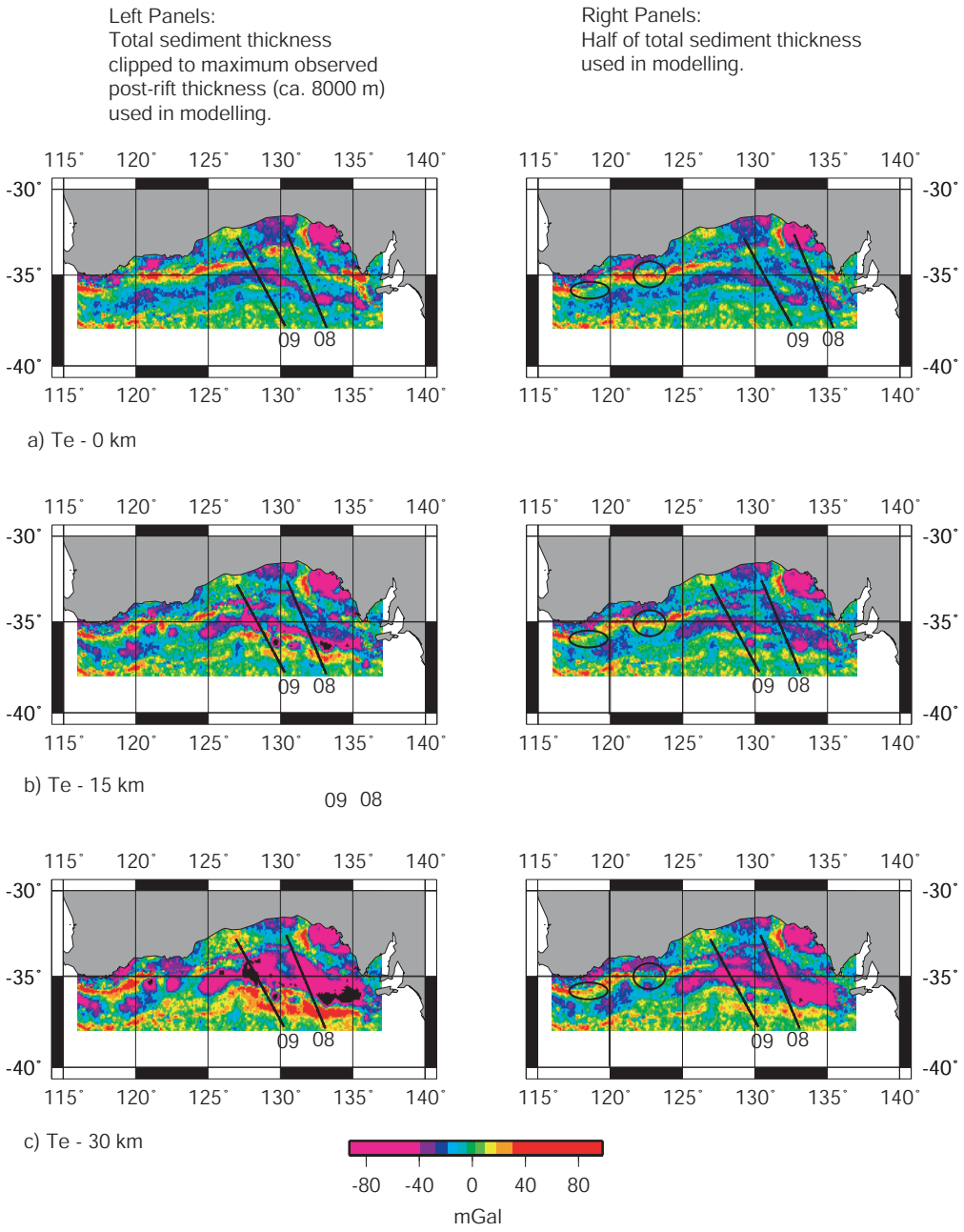

Figure 7.24: Flexural isostatic anomaly maps of the Bight Basin region for a) T_e=0 km, b) T_e=15 km, and c) T_e=30 km. Left panels were calculated assuming the maximum possible post-rift sediment thickness. Right panels were calculated assuming that half of the total sediment thickness comprises post-rift sediments, a more realistic assumption. The broad trends for both cases are similar.

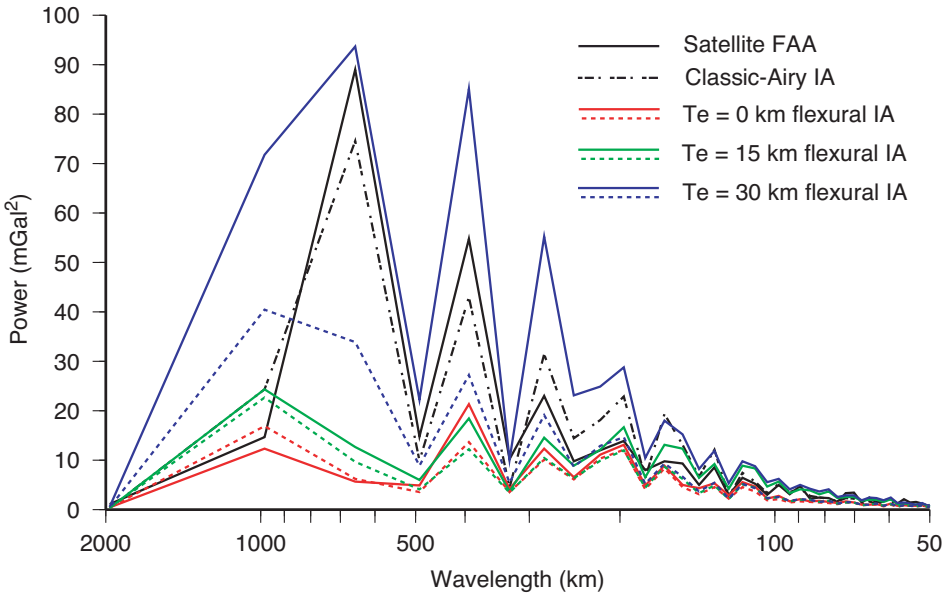

Figure 7.25: Spectral analyses of free air anomaly and isostatic anomaly data for the Bight Basin region. Solid and dashed flexural isostatic anomaly (IA) spectra are of data in the left and right panels of Figure 7.24 respectively. Power peaks are observed in the satellite derived free air anomaly (FAA) spectrum at ~400 and 650 km, these are effectively reduced for flexural IA spectra for low T_e estimates ($\leq$15 km).

7.4.3 Conjugate Margin Comparisons

Figure 7.26 illustrates the present-day bathymetry of the southern Australian and Wilkes Land margins reconstructed to Chron 18o (~40 Ma), using the rotation pole of Royer & Rollet [1997]. A tighter closure is not attempted as older anomaly lineations are, in general, poorly defined. The major differences in the conjugate margin morphology primarily reflect the disparate environments dominant on each continent throughout the Tertiary. The rugged and very deep continental shelf of Wilkes Land, for instance, is a function of extensive glacial erosion and flexural downwarping associated with the East Antarctic Ice Sheet.

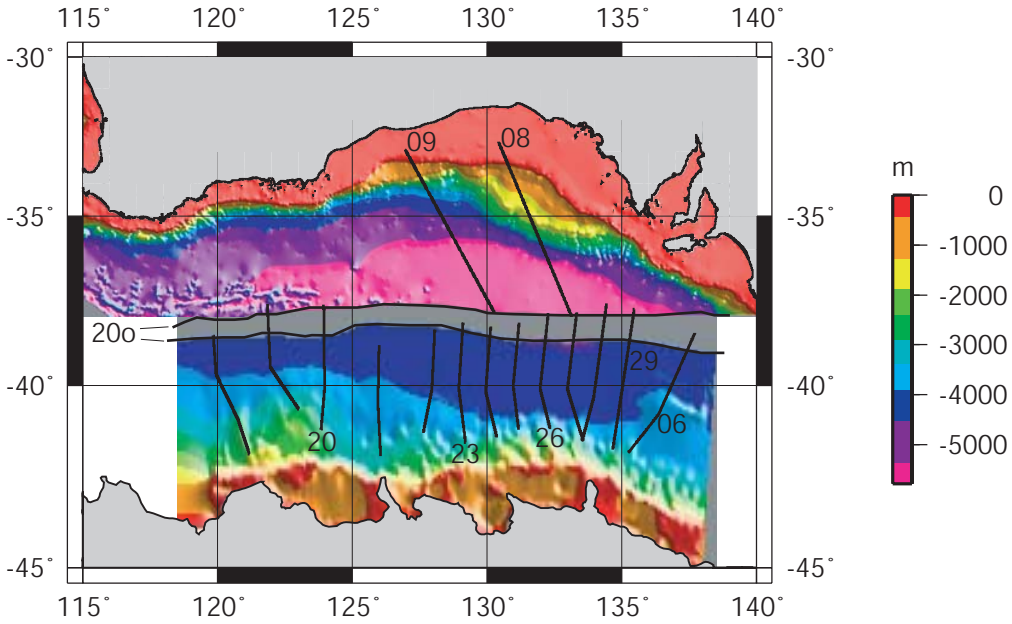

Figure 7.26: Bathymetry of the Wilkes Land and southern Australian margins reconstructed to Chron 18o (~40 Ma) and clipped at Chron 20o (~44 Ma). Reconstruction is based on the rotation pole of Royer & Rollet [1997] (rotation pole: 14.32°N, 31.75°E, and rotation angle: 23.77°).

The abyssal plain of the southern Australian margin occurs at a much greater depth (~1000 m) relative to the Wilkes Land margin. To determine whether this is a function of crustal structure or sediment thickness, and to assess the symmetry of this conjugate margin pair, conjugate profiles of bathymetry, sediment thickness, TTS, crustal structure, and inferred crustal thinning, also clipped to anomaly 20, are compared in Figure 7.27. Comparisons of the FAA and magnetic anomaly profiles are illustrated in Figure 7.28. We see in Figure 7.26 that survey 199 Lines 08 and 09, across the Bight Basin, are approximately conjugate to Lines from GA-228_22 to GA-228_27 on the Wilkes Land

margin.

The difference in abyssal plain bathymetry is, in part, explained by the thinner Tertiary sedimentary sequence on the southern Australian margin Figure 7.27a. Although the bathymetry is deeper on the southern Australian margin, the basement depth is, in general, comparable with or shallower than the sediment loaded basement of the Wilkes Land margin. Comparing the backstripped basement surfaces (i.e. the TTS) in Figure 7.27b, illustrates that the sediment corrected basement depths are comparable across Lines GA-228_22/GA-228_23 and 09. However, the TTS on Lines GA-228_26/GA-228_27 is some 1500 m shallower than the conjugate Line 08. The large calculated TTS may have contributed to the greater thickness of syn-rift and post-rift sediments observed in the region of the Ceduna Sub-basin by allowing greater accommodation space during early rift stages.

Due to the lack of constraints on $Moho$ depth on the southern Australian margin it is difficult to determine the accuracy of the calculated crustal stretching factor (β) profiles (Figure 7.27c). Therefore, establishing whether or not the pattern of extension is symmetrical across the conjugate margin sectors is difficult. Broadly, extension increases relatively linearly towards the COT across Lines GA-228_22/GA-228_23 and 09, whereas across Lines GA-228_26/GA-228_27 and 08 a sharp increase in β is observed close to the COT.

The free air anomaly pattern across this conjugate margin pair is not symmetric as illustrated in Figure 7.28a. The edge effect anomaly is subdued on the southern Australian margin relative to the Wilkes Land margin. Although both margins are characterised by almost entirely negative free air anomalies, the pattern of anomalies is not symmetric. However, this is primarily a function of the differences in the sediment distribution and morphology of the opposing margins.

The inconsistent patterns of magnetic anomaly lineations have been discussed in detail for the Wilkes Land margin in Chapter 5. Similar problems in identification of anomalies older than Chron 21 occur on the southern Australian margin (e.g. Veevers [1986], Tikku & Cande [1999]). There is very poor correlation in the magnetic anomaly pattern between Lines GA-228_26/GA-228_27 and 08 (Figure 7.28b). However, the correlation between Lines GA-228_22/GA-228_23 and their symmetry with Line 09 is improved.

In particular, the large amplitude positive magnetic anomaly at the landward extent of Lines GA-228_22/GA-228_23, attributed to upper mantle peridotite ridges, is mirrored at a similar distance landward from anomaly 20 on Line 09. This magnetic anomaly corresponds to a positive free air gravity anomaly (Figure 7.27d) and the location of the basement ridge interpreted by Sayers *et al.* [2001] as a serpentinised peridotite ridge. This symmetry indicates that the magnetic anomaly lineations previously attributed to

Chrons 22 [Weissel & Hayes, 1972] and 34 [Cande & Mutter, 1982] likely have a common origin, but one that is not associated with *normal* seafloor spreading.

The results of this study suggest that the southern Australian and Wilkes Land margins are broadly symmetrical. The total width of extended continental crust at each margin is comparable, as are the basement depths when corrected for sedimentation. This suggests that this conjugate margin pair formed in a similar way to the Iberian non-volcanic rifted margin; that is, via largely pure-shear deformation at the lithosphere scale [Brun & Beslier, 1996]. Additionally, there is no substantial evidence for upper-crustal detachment surfaces and/or lithosphere-penetrating shear zones as predicted by simple shear models which predict asymmetric rifting (e.g. Wernicke [1985]). The inferred widespread presence of upper mantle peridotites in the COT zone, of the Wilkes Land and southern Australian margins, is also analogous to the rifted Iberian margin.

This conjugate margin pair was previously interpreted as asymmetric and the product of a mixed-mode simple and pure shear extension mechanism by Etheridge *et al.* [1989] and Lister *et al.* [1991]. They interpreted the southern Australian margin as an 'upper plate' margin and the opposing Wilkes Land margin as a 'lower plate' margin. This interpretation was questioned by Sayers *et al.* [2001] on the basis of the structure of the Great Australian Bight margin of southern Australia. The additional constraints provided here, through modelling and interpretation of data from the Wilkes Land margin, supports the reassessment of Sayers *et al.* [2001] that this conjugate margin pair is most appropriately considered as the product of lithosphere-scale pure shear.

Figure 7.27(next page): Comparison of a range of observed and derived parameters for the central Wilkes Land and Bight Basin conjugate margins. Seaward ends of profiles are truncated at anomaly 20. Line labels for (b)-(d) are as in (a). Total tectonic subsidence (TTS), crustal structure and β in (b) to (d) are calculated assuming a T_e of 30 km for the Wilkes Land transects and 15 km for the Bight Basin transects. Blue circles in (b) are the expected depth of Chron 20 ($\sim$43 Ma) aged oceanic crust based on Parsons & Sclater [1977]. The boxed regions in (c) outlines the COT zone.

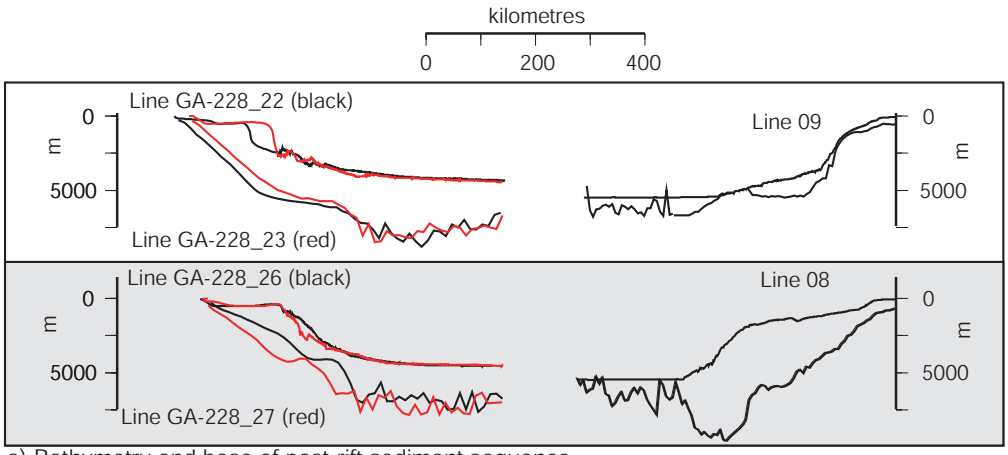

a) Bathymetry and base of post-rift sediment sequence

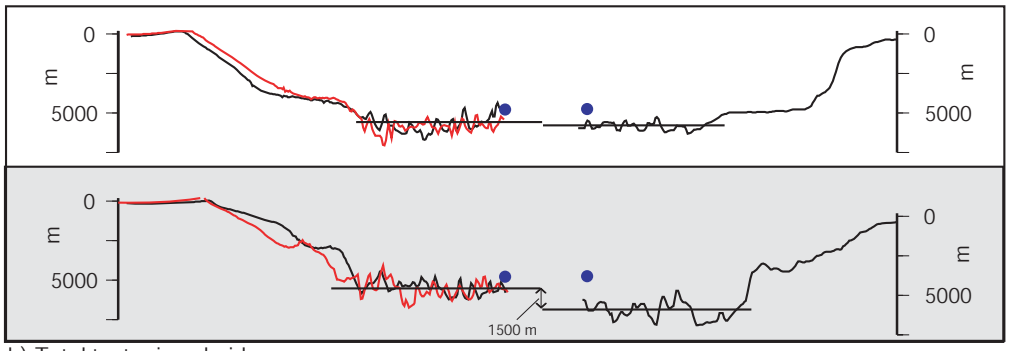

b) Total tectonic subsidence

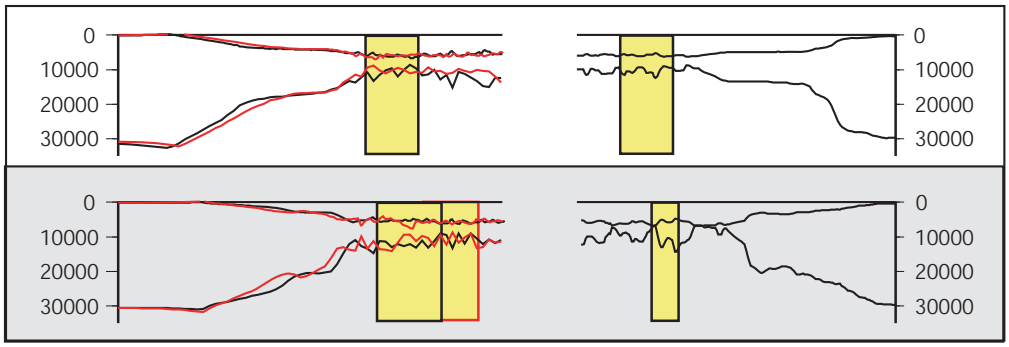

c) Crustal structure after rifting assuming Airy isostatic compensation

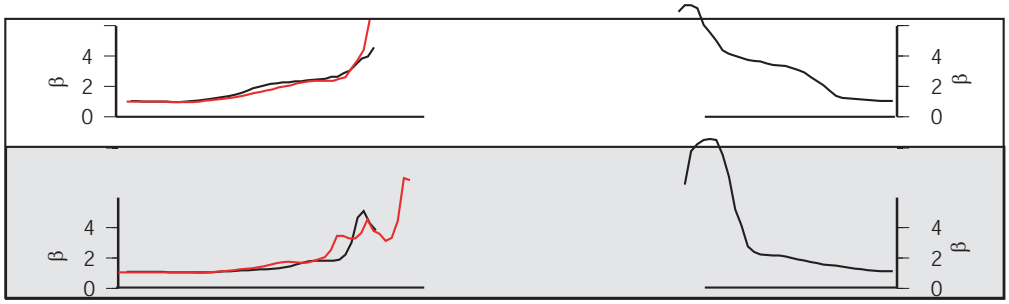

d) Crustal stretching factor (β) to the inner limit of the COT

Figure 7.27: Caption on previous page.

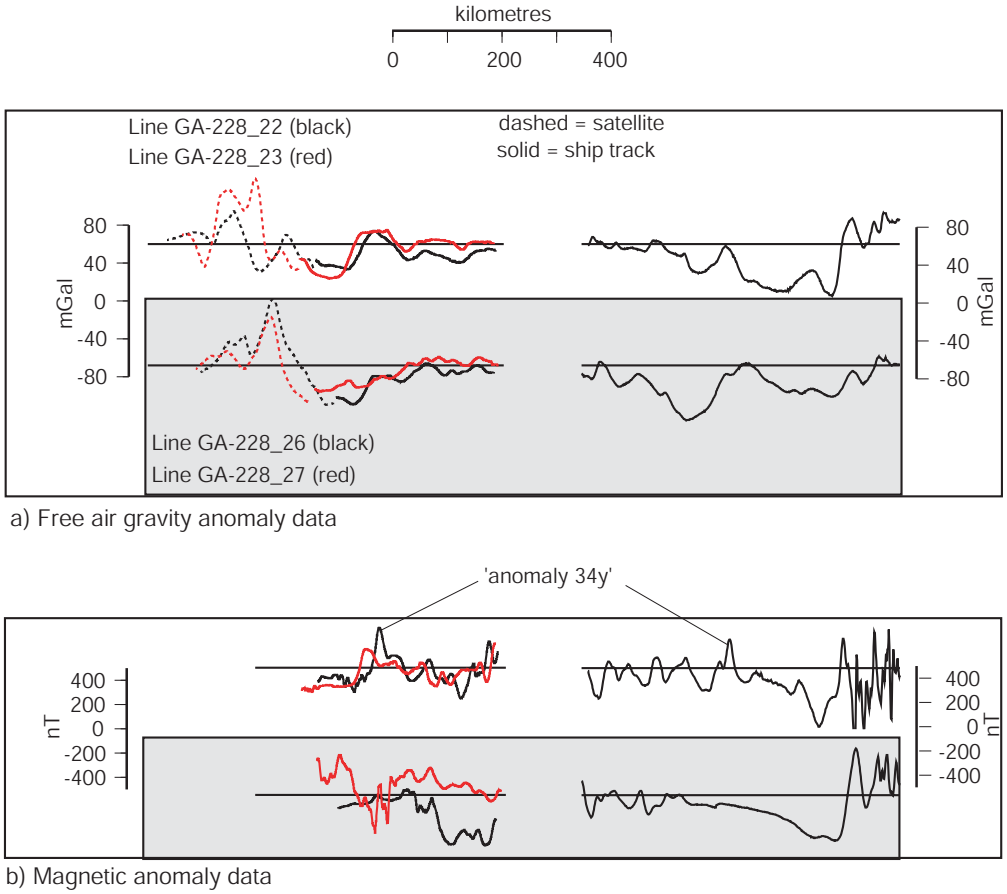

Figure 7.28: Comparison of a) FAA, and b) magnetic anomaly data across the central Wilkes Land and Bight Basin conjugate margins. Seaward ends of profiles are truncated at anomaly 20. Line labels for (b) are as in (a).

7.5 Strength of Extended Continental Lithosphere

Rifted continental crust is permanently mechanically altered by extensional thinning. A rifted margin comprises not only altered continental crust, but also relatively unaltered continental crust and oceanic crust. Despite the apparent complexity of lithospheric structure at rifted margins, a single T_e estimate, that provides the best overall description of observed flexural behaviour, is normally reported in T_e studies. These T_e estimates typically being based on gravity modelling of the edge effect anomaly or comparison of observed and theoretical flexural subsidence.

Previous estimates of T_e at rifted margins vary widely. They range, for example, from a low of 5-10 km for the Valencia Trough [Watts & Torné, 1992] and Baltimore Canyon Trough [Watts, 1988] to a high of 40-60 km for the West Greenland margin [Keen & Dehler, 1997]. These single T_e estimates at rifted margins represent, however, the *average* response of the lithosphere to sediment loading. They do not refer to a particular crustal type or time since rifting. These estimates may be biased downwards relative to their present day rigidity if lithospheric rigidity was very low during syn-rift and early post-rift sedimentation.

It is, therefore, difficult to use these data to constrain the T_e structure of stretched continental crust and determine whether or not it is able to recover strength with time. However, it is difficult to constrain T_e for discrete time intervals and therefore assess any possible bias in T_e estimates at rifted margins. The difficulty in constraining discrete T_e estimates is primarily a function of relatively continuous sedimentation, that occurs at almost all continental margins, within the developing rift basin from the onset of subsidence to the present-day. Only where discrete loading events can be identified and timed can estimates of the T_e of the lithosphere during a discrete interval be constrained.

The Amazon Cone is one example of a discrete sediment load where constraints exist on both the magnitude of the sediment load and timing of deposition. ODP results (e.g. Damuth [1975]) indicate a mid- to late-Miocence (8-12 Ma) age for the Cone. This load, therefore, occurs on a rifted margin that formed some 140 Ma previously during the opeing of the central Atlantic Ocean [Rabinowitz & LaBreque, 1979]. Cochran [1973] estimated that $T_e = 31.1$ km in the region of the Amazon Cone.

A second and similar example of a large sediment load that was deposited in a discrete interval are the sedimentary basins of the Bay of Bengal, India. Although rifting initiated during the Jurassic, large amounts of the observed sediment thickness have been deposited since the Eocene, due to uplift within the Himalayas [Krishna *et al.*, 2000]. Gravity modelling by Krishna *et al.* [2000] suggests that $T_e = 30$ km in the Krishna-Godavari Basin region of the Bay of Bengal.

A further example of a discrete loading event on rifted continental lithosphere where T_e has been estimated is the West Taiwan Basin. Lin & Watts [2002] demonstrated that T_e = 13 km in this region on the basis of flexural and gravity modelling of the orogenic loading, associated with the development of the basin, on the rifted lithosphere of the South China Sea. They relate this T_e estimate to the rigidity of the rifted margin lithosphere ∼23-51 Ma after rifting.

Process-oriented modelling on the Wilkes Land and Bight Basin margins indicates that they are characterised by a different average T_e. Whereas an average T_e of 30 km most effectively reduces the magnitude of flexural isostatic anomalies for the Wilkes Land margin, an average T_e of ∼15 km is inferred from modelling at the Southern Australian margin.

The southern Australian-Wilkes Land conjugate margin pair are unique in that they have almost opposite sedimentation or loading histories, i.e. the southern Australian margin has been sediment starved throughout the Tertiary while areas of the Wilkes Land margin were subject to very large sediment loads. The low T_e inferred for the southern Australian margin, therefore, indicates that immediately following rifting and through the Late Cretaceous, the lithosphere was relatively weak. However, the high T_e inferred for the Wilkes Land margin indicates that the lithosphere was relatively strong by the mid-Tertiary when the major loading event on this margin occurred. The asymmetry of the southern Australian and Wilkes Land margins, in terms of inferred T_e, may therefore not reflect absolute difference in T_e, rather it demonstrates that the T_e has increased through time.

The examples of the Amazon Cone, the Bay of Bengal, the Taiwan foreland, and the Wilkes Land-southern Australian margins suggest that continental lithosphere does regain strength with time following rifting. Figure 7.29 illustrates the relationship of increasing T_e with increasing time elapsed between rifting and load emplacement. A similarly crude positive correlation between T_e and the age of the lithosphere at time of loading has been established for the continents (e.g. Burov & Diament [1995]). This result accords with the numerical modelling of Burov & Poliakov [1995]. They suggest that lithospheric rigidity initially decreases during rifting but regains strength during the post-rift interval. However, it has proved difficult to assign a single isotherm that describes the rigidity-time relationship as is possible for oceanic lithosphere.

The results compiled here (Figure 7.29) accord approximately with the 450°C isotherm, however, a paucity of data prevents this relationship being defined absolutely. The 450°C isotherm best describes the T_e evolution of oceanic crust, where $T_e = 3\sqrt{t}$ and t is My. This suggests that there may be a thermal control on T_e in continents and at rifted continental margins, but that other factors (such as post-rift sedimentation, geotherm during

rifting, strain rates, and rheology) may also play an important role.

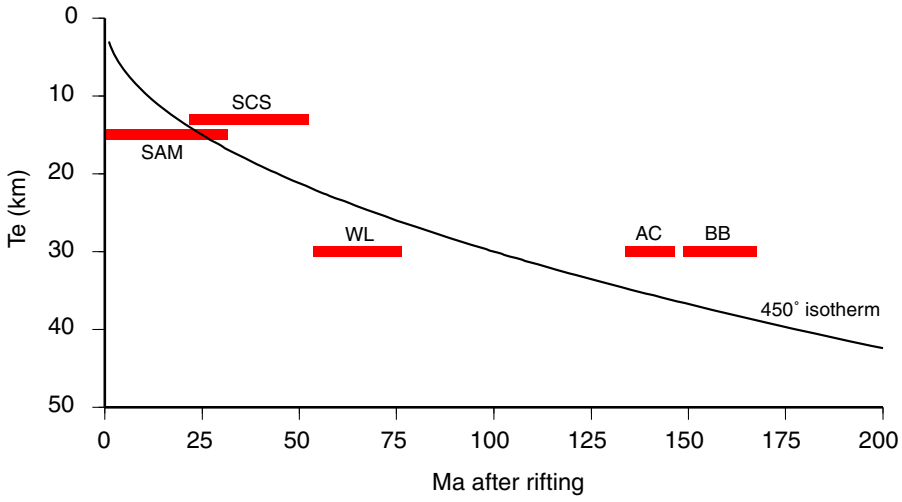

Figure 7.29: Plot of T_e as a function of elapsed time between rifting and load emplacement for discrete loads on rifted continental margin lithosphere. AC = Amazon Cone, BB = Bay of Bengal, SAM = Southern Australian Margin, SCS = South China Sea, WL = Wilkes Land. See text for references.

It has been suggested that sediment blanketing at continental margins contributes to lithospheric weakening and, therefore, a long-term reduction in T_e. The suggested processes by which this occur include (after Wyer [2003]):

1. Increasing the mean crustal temperature through insulation (e.g. Steckler & Ten Brink [1986]).

2. Increasing the depth to the *Moho* and, therefore, increasing the temperature at the base of the crust (e.g. Lavier & Steckler [1997]).

3. Reducing the lithostatic pressure at brittle depths in the yield strength envelope (e.g. Steckler & Ten Brink [1986]).

The results of Lavier & Steckler [1997] demonstrate that a sediment thickness of 3-5 km is sufficient to reduce T_e significantly. However, Karner [1991] illustrates that only if sedimentation rates are unrealistically high during the rift or early post-rift phase of basin development may T_e be reduced to near zero values by sediment blanketing. Even then, during subsequent cooling, he predicts that T_e will increase with time and that sediment blanketing alone can not cause T_e to remain low for long (>50 Ma) periods of time. Additionally, a clear correlation of high T_e (~30 km) off west Wilkes Land and the thick sediments of the Budd Coast Basin is indicated in this study. Therefore, the occurrence of thick sediments does not ubiquitously correlate to a low T_e.

Whether some rifted margins maintain or regain strength during and after rifting, while others remain weak, has not been firmly established. However, evidence from this

study suggests that the lithosphere does regain strength following rifting, and that low T_e estimates at other margins are biased by analytical methodology. It is possible, however, that the complex interaction of the controlling parameters (e.g. geotherm, rheology, etc.) and post-rift sedimentation could contribute to the wide range of T_e estimates at different rift margins.

Chapter 8

Conclusions and Future Work

8.1 Conclusions

8.1.1 Introduction

The aim of this study has been to present the data acquired during surveys GA-228 and GA-229, and, where appropriate, interpretations and modelling results of these data. This chapter aims to summarise the main results of this work, and suggest possible areas of further research.

The strength of this study is its utilisation of all available data for the Wilkes Land margin, and the application of both process- and object-oriented modelling methods. In Chapter 4, interpretation of deep-penetrating seismic reflection data provide for the first regional seismic stratigraphic summary for this Antarctic margin sector. Magnetic anomaly compilation, modelling and interpretation was undertaken in Chapter 5 to further constrain the breakup age of Antarctica and southern Australia. Due to a number of factors, however, magnetic lineations in the AAB are poorly formed and difficult to interpret for oceanic crust older than ∼48 Ma (Chron 21o). The interpreted and depth converted seismic reflection data provide the key input to process-oriented gravity modelling in Chapter 6. Process-oriented modelling was undertaken to constrain the individual gravity contributions of different geological processes at this rifted continental margin. The process-oriented gravity modelling results have also allowed the long-term rigidity of the Wilkes Land margin lithosphere to be inferred. Chapter 7 integrates the results of the preceding chapters and demonstrates that the geophysical characteristics of the COT zone off Wilkes Land are consistent with the presence of exhumed and partially serpentinised upper-mantle peridotites as top basement. The subsidence history of the margin is also inferred as far as possible in Chapter 7. Finally, a comparison between the conjugate Wilkes Land and southern Australian margins is carried out in Chapter 7.

8.1.2 Conclusions

The primary and most important results of this study are summarised here in conclusion to this thesis.

• Seismic reflection data indicate the presence of up to 5 s TWT (∼8-9 km) of post-rift sediments on the Wilkes Land margin. These sediments are divided into two major sequences by a regional unconformity, interpreted to be Eocene aged (∼50 Ma), on the basis of comparison with seismic reflection data from the southern Australian margin.

1. The younger of the two major post-rift sequences (Sequence 1) comprises a much greater thickness relative to the older Sequence 2. This is interpreted to represent the high sediment fluxes associated with the period of polythermal glaciation from ∼34-9 Ma.

2. The asymmetric distribution of Sequence 1 sediments indicates that deep-marine processes were important in lateral, along-margin sediment transport. A west to east direction of movement is inferred by the sediment distribution. This direction is opposite to the present-day marginal currents along the continental slope and rise.

3. Seismic reflection data also indicate a zone of anomalous crust between unequivocal continental and oceanic crust. This interpreted Continent-Ocean Transition (COT) zone is typically <100 km wide, and its inner-limit located ∼150-200 km from the shelf break.

4. A seaward excursion of ∼200 km is observed in the COT zone off east Wilkes Land and Terre Adélie. This is based on the identification of stretched continental crust beneath a region of anomalously shallow bathymetry characterised by a number of seamounts at its seaward edge. This region is interpreted to represent a sunken marginal plateau or a microcontinental block. 5. As the Wilkes Land margin is characterised by a diffuse COT zone, and a lack of volcanic rocks and evidence of magmatic influence during rifting, it can be classified as non-volcanic.

• Interpretation and modelling of magnetic anomaly data demonstrates a complex pattern of seafloor spreading anomalies.

1. A lineation previously associated with Chron 34 (the Cretaceous Long Normal Quiet period) is interpreted to overlie the COT zone interpreted from seismic reflection data.

2. Accurately constraining the breakup age of Antarctica and Australia on the basis of seafloor spreading anomaly identification is not possible due to the ambiguity in the magnetic anomaly lineation patterns.

3. That breakup was not synchronous along the margin is demonstrated by the interpretation of magnetic anomaly data in concert with interpretation of seismic reflection data. The earliest seafloor spreading anomaly seaward of the Adélie Rift Block is anomaly 21. This indicates that east Wilkes Land is characterised by a Tertiary breakup age, whereas, central and west Wilkes Land is interpreted to have rifted from southern

Australia during the Late Cretaceous.

4. Seafloor spreading rates are interpreted to vary between 1.5 and 10 mm/yr HSR prior to Chron 18 time (∼38-40 Ma), when normal seafloor spreading rates (20-35 mm/yr) begin.

• Process-oriented gravity modelling reveals that the Wilkes Land margin lithosphere was characterised by a relatively high T_e (∼30 km) during the loading of sediments associated with polythermal glaciation from ∼34-9 Ma.

• Two-dimensional modelling of coincident flexural isostatic anomalies and magnetic anomalies indicate the presence of high density (∼3100 kg/m^3) and susceptibility (0.05-0.1 SI units) source, which is spatially correlated to basement ridge structures within the COT zone. This is interpreted to indicate the presence of partially serpentinised (∼25%) upper-mantle peridotites, which were exhumed during extension prior to the initiation of seafloor spreading. A number of magnetic anomalies that occur on the 'anomaly 34y' lineation are unlikely to be associated with seafloor spreading anomalies, and therefore do not necessarily represent isochrons.

• The pattern of crustal thinning across the central Wilkes Land margin is broadly similar to other passive rift margins from around the world. However, the great width of highly extended crust associated with the microcontinental block off Terre Adélie is unusual in that the locus of greatest extension occurs ∼200 km landward of the point of eventual breakup.

• Depth anomalies are evident for backstripped oceanic crust along the Wilkes Land margin. The magnitude of the depth anomalies varies from 200-800 m. The greatest magnitude depth anomalies are observed to the south and south-east of the present day location of the AAD. The continuity of the depth anomalies to the oldest likely oceanic crust indicates that the cause of the great depth of the AAD is long-lived.

• The conjugate southern Australian margin is characterised by a much thinner Tertiary sediment thickness relative to the Wilkes Land margin. However, large thicknesses of sediment are observed in seismic reflection data from the Ceduna Sub-basin.

1. Two-dimensional process-oriented modelling indicates a T_e of 15 km for the region of the Ceduna Sub-basin.

2. Three-dimensional process-oriented modelling also supports the notion of a low ($\leq$15 km) for the Bight Basin region of the southern Australian margin, conjugate to Wilkes Land.

3. This apparent asymmetry in T_e is interpreted to represent the strengthening of the rifted lithosphere through time. The southern Australian margin was largely loaded in the Late Cretaceous and Early Tertiary, whereas the Wilkes Land margin was loaded from ∼34-9 Ma, some 50 to 70 Ma after rifting. As process-oriented modelling reveals

the T_e at the time of loading, the results from the Wilkes Land and southern Australian margins suggest that the rifted lithosphere was weak initially following rifting, but has regained strength through time.

4. Despite the apparent asymmetry in T_e structure, the Wilkes Land and southern Australian margins are broadly symmetric with regards to width of extended continental crust and inferred crustal structure. Depth anomalies are evident from oceanic crust on both margins, supporting the notion that the cause of the great depth of oceanic crust is imparted at the spreading ridge.

8.1.3 Future Work

An essential requirement in improving the understanding of the breakup of Australia and Antarctica is the acquisition of wide-angle refraction data along both margins. The limited constraints on crustal thinning and initial crustal thickness do not allow the ambiguity of gravity models to be reduced to the extent that would be possible if the $Moho$ structure was known from refraction surveying. Also, wide-angle data will allow the velocity structure of the margin to be determined, and the presence of a COT zone and serpentinised mantle rocks within the basement confirmed.

Additionally, a seismic reflection transect that ties the north-south profiles of surveys GA-228 and GA-229 would allow the seismic stratigraphy to be characterised in greater detail. If this was completed in conjunction with a well-placed drilling survey, it would be possible to constrain the ages of the major horizons evident in seismic reflection data. This would also allow constraints on the subsidence history of the margin, which as yet can only be inferred from comparison with the southern Australian margin or through entirely theoretical studies.

A detailed MCS survey off west Wilkes Land would be beneficial as this would allow the three-dimensional geometry of the thick sequence of sediment waves to be constrained. This may be important in understanding the palaeocirculation patterns off East Antarctica.

The acquisition of further magnetic data will allow some improvement in the identification of seafloor spreading anomaly lineations. However, given the complex patterns evident in available data, it is unlikely that magnetic anomaly data will ever allow the unambiguous definition of breakup age and the location of a COB.

Finally, the acquisition of onshore geophysical data, namely seismic refraction, gravity, and magnetic anomaly data, in the Wilkes Land sector of East Antarctica will allow more complete comparison with the conjugate Australian margin. The lack of comprehensive onshore datasets is a problem almost unique to Antarctica.

Despite the obvious need for further data in Wilkes Land, and East Antarctica in general, it is unlikely that a marine geophysical survey on the magnitude of surveys GA-228 and GA-229 will be repeated for several decades. The only likely means of acquiring well and core data from the Wilkes Land margin is through a successful application to the IOPD program. Although site selection will require further surveying, primarily an along-margin tie line, a number of potentially optimal sites for drilling can be identified in GA-228 and GA-229 data.

The lower slope of the central Wilkes Land margin, e.g. landward extents of Lines GA-228_24 and GA-228_25, provides an appealing drilling target. The relatively thin post-rift sequence there and the identification of a number of distinct unconformities would allow the full post-rift stratigraphy to be sampled and described.

Basement highs identified off east Wilkes Land and within the Adélie Rift Block (ARB) also provide drilling targets as they occur under relatively small amounts of post-rift sediments and are of somewhat equivocal composition. The broad high on Line GA-229_06 would also potentially provide greater constraints on the subsidence of the ARB and the final stages of breakup between Australia and Antarctica.

Bibliography

Airy, G. B. 1855. On the computation of the effect of the attraction of the mountain masses, as disturbing the apparent astronomical latitude of stations in geodetic surveys. *Phil. Trans. Roy. Soc. Lond.*, **145**, 101–104.

Alley, R. B., Blankenship, D. D., Rooney, S. T., & Bentley, C. R. 1989. Sedimentation beneath ice shelves - the view from ice stream B. *Marine Geology*, **85**, 101–120.

Anderson, J. B. 1991. The Antarctic Continental Shelf: Results from Marine Geological and Geophysical Investigations. *Pages 285–326 of:* Tingey, R. J. (ed), *The Geology of Antarctica*. Clarendon Press, Oxford.

Bamber, J. L., Vaughan, D. G., & Joughin, I. 2000. Widespread Compled Flow in the interior of the Antarctic Ice Sheet. *Science*, **287**, 1248–1250.

Barker, P. F., Dalziel, I. W. D., & Storey, B. C. 1991. Tectonic development of the Scotia Arc region. *Pages 215–244 of:* Tingey, R. J. (ed), *The Geology of Antarctica*. Clarendon Press, Oxford.

Barnes, P. W. 1987. Morphologic Studies of the Wilkes Land Continental Shelf, Antarctica-Glacial and Base to Iceberg Effects. *Pages 175–194 of:* Eittreim, S. L., & Hampton, M. A. (eds), *The Antarctic Continental Margin Geology and Geophysics of Offshore Wilkes Land*. Houston, Texas, USA: Circum-Pacific Council for Energy and Mineral resources.

Barrett, P. J. 1991. The Devonian to Triassic Beacon Supergroup of the Transantarctic Mountains and correlative in other parts of Antractica. *Pages 120–152 of:* Tingey, R. J. (ed), *The geology of Antarctica. Oxford Monographs on Geology and Geophysics*. Clarendon Press.

Bassetto, M., Alkmim, F. F., Szatmari, P., & Mohriak, W. U. 2000. The Oceanic Segment of the Southern Brazilian Margin: Morpho-Structural Domains and Their Tectonic Significance. *Pages 235–260 of:* Mohriank, W., & Talwani, M. (eds), *Atlantic Rifts and Continental Margins*. AGU.

Bassi, G. 1991. Factors controlling the style of continental rifting from numerical modelling. *Earth and Planetary Science Letters*, **105**, 430–452.

Bassi, G. 1995. Relative importance of strain rate for the mode of continental extension. *Geophysical Journal International*, **122**, 195–210.

Beaumont, C., Keen, C. E., & Boutilier, R. 1982. On the evolution of rifted continental margins: comparison of models and observations for the Nova Scotian margin. *Geophysical Journal of the Royal Astronomical Society*, **70**, 667–715.

Behn, M. D., & Lin, J. 2000. Segmentation in gravity and magnetic anomalies along the U.S. East Coast passive margin: Implications for incipient strucure of the oceanic lithosphere. *Journal of Geophysical Research*, **105(B11)**, 25,769–25,790.

Bentley, C. R. 1974. Crustal structure of Antarctica. *Tectonophysics*, **20**, 229–240.

Bentley, C. R. 1983. Crustal Structure of Antarctica from Geophysical Evidence-A Review. *Pages 491–497 of:* Oliver, R. L., James, P. R., & Jago, J. B. (eds), *Antarctic Earth Science*. Australian Academy of Science, Canberra.

Bentley, C. R. 1987. Antarctic ice streams; a review. *Journal of Geophysical Research*, **92**, 8843–8858.

Bentley, C. R. 1991. Configuration and Structure of the Subglacial Crust. *Pages 335–358 of:* Tingey, R. J. (ed), *The Geology of Antarctica*. Clarendon Press, Oxford.

Bentley, C. R., & Clough, J. W. 1972. Antarctic subglacial structure from seismic refraction measurements. *Pages 683–692 of:* Adie, R. J. (ed), *Antarctic geology and geophysics*. Universitetsforlaget.

Bindoff, N. L., Rosenberg, M. A., & Warner, M. J. 2000. On the circulation and water masses over the Antarctic continental slope and rise between 80 and 150°E. *Deep-Sea Research II*, **47(12-13)**, 2299–2326.

Blanchard, D. P., Rhodes, J. M., Dungan, M. A., Rodgers, K. V., Donaldson, C. H., Brannon, J. C., Jacobs, J. W., & Gibson, E. K. 1976. The Chemistry and Petrology of Basalts From Leg 137 of the Deep-Sea Drilling Project. *Journal of Geophysical Research*, **81(23)**, 4231–4247.

Boeuf, M. G., & Doust, H. 1975. Structure and development of the southern margin of Australia. *APEA Journal*, **15(1)**, 33–43.

Boillot, G., Grimaud, S., Mauffret, A., Mougenot, D., Kornprobst, J., Mergoil-Daniel, J., & Torrent, G. 1980. Ocean-continent boundary off the Iberian margin: A serpentinite diapir west of the Galicia Bank. *Earth and Planetary Science Letters*, **48**, 23–34.

Bown, J. W., & White, R. S. 1994. Variation with spreading rate of oceanic crustal thickness and geochemistry. *Earth and Planetary Science Letters*, **121**, 435–449.

Bown, J. W., & White, R. S. 1995. Effect of finite extension rate on melt generation at rifted continental margins. *Journal of Geophysical Research*, **100**, 18,011–18,029.

Bratt, S. R., & Purdy, G. M. 1984. Structure and variability of oceanic crust on the flanks of the East Pacific Rise between 11° and 13°N. *Journal of Geophysical Research*, **89**, 6111–6125.

Braun, J., & Beaumont, C. 1989. A physical explanation of the relation between flank uplifts and the breakup unconformity at rifted continental margins. *Geology*, **17**, 760–764.

Brown, B. J., Müller, R. D., Struckmeyer, H. I. M., Stagg, H. M. J., & Symonds, P. A. 2003. Formation and evolution of Australian passive margins: implications for locating the boundary between continental and oceanic crust. *Pages 223–244 of:* Hillis, R. R., & Müller, R. D. (eds), *Evolution and Dynamics of the Australian Plate. Geological Society of Australia Special Publication 22 and Geological Society of America Special Paper 372.*

Brun, J. P., & Beslier, M. O. 1996. Mantle exhumation at passive margins. *Earth and Planetary Science Letters*, **142**, 161–173.

Buck, W. R., Lavier, L. L., & Poliakov, A. N. B. 1999. How to make a rift wide. *Philosophical Transactions of the Royal Society of London*, **357**, 671–693.

Burov, E. B., & Diament, M. 1995. The effective elastic thickness (Te) of continental lithosphere: What does it really mean? *Journal of Geophysical Research*, **100(B3)**, 3905–3927.

Burov, E. B., & Poliakov, A. 1995. Erosion and rheology controls on synrift and postrift evolution: Verifying old and new ideas using a fully coupled numerical model. *Journal of Geophysical Research*, **100(B3)**, 16,461–16,481.

Cande, S. C., & Kent, D. V. 1995. Revised calibration of the geomagnetic polarity timescale for the Late Cretaceous and Cenozoic. *Journal of Geophysical Research*, **100:B4**, 6093–6095.

Cande, S. C., & Mutter, J. C. 1982. A revised identification of the oldest sea-floor spreading anomalies between Australia and Antarctica. *Earth and Planetary Science Letters*, **58**, 151–160.

Cande, S. C., & Stock, J. M. 2004. Cenozoic reconstructions of the Australia-New Zealand-South Pacific sector of Antarctica. *Pages 5–18 of:* Exon, N., Kennett, J. P., & Malone, M. (eds), *The Cenozoic Southern Ocean: Tectonics, Sedimentation and Climate Change Between Australia and Antarctica: Geophysical Monograph Series (151).* AGU.

Chalmers, J. A., & Pulvertaft, T. C. R. 2001. Development of the continental margins of the Labrador Sea - a review. *Pages 77–106 of:* Wilson, R. C. L., Whitmarsh, R. B., Taylor, B., & Froitzheim, N. (eds), *Continental Margins: A Comparison of Evidence from Land and Sea. Special Publication 187.* London: Geological Society London.

Chian, C., & Louden, K. E. 1994. The continent-ocean transition across the southwest Greenland margin. *Journal of Geophysical Research*, **99**, 9117–9135.

Childs, J.R., & Stagg, H. M. J. 1987. The Deep Crustal Structure of the Wilkes Land Continental Margin. *Pages 90–99 of:* Eittreim, S. L., & Hampton, M. A. (eds), *The Antarctic Continental Margin Geology and Geophysics of Offshore Wilkes Land.* Houston, Texas, USA: Circum-Pacific Council for Energy and Mineral resources.

Cochran, J. R. 1973. Gravity and magnetic investigations in the Guiana Basin, Western Equitorial Atlantic. *Geol. Soc. Am. Bull.*, **84**, 3249–3268.

Cochran, J. R. 1981. Simple models of diffuse extension and the pre-seafloor spreading development of the continental margin of the Northeastern Gulf of Aden. *Pages 155–165 of: Proceedings 26^{t}h International Geological Congress, Geology of continental margins sumposium*. Oceanol. Acta.

Cochran, J. R. 1983. Effects of finite rifting times on the development of sedimentary basins. *Earth and Planetary Science Letters*, **66**, 289–302.

Cochran, J. R., & Martinez, F. 1988. Evidence from the northern Red Sea on the transition from continental to oceanic rifting. *Tectonphysics*, **153**, 25–53.

Coffin, M. F., & Eldholm, O. 1994. Large igneous provinces: Crustal structure, dimensions and external consequences. *Review of Geophysics*, **32**, 1–36.

Cogley, G. J. 1984. Deglacial hypsometry of Antarctica. *Earth and Planetary Science Letters*, **67(3)**, 284–296.

Coleman, P. J., Michael, P. J., & Mutter, J. C. 1982. The origin of the Naturaliste Plateau, SE Indian Ocean; implications from dredged basalts. *Journal of the Geological Society of Australia*, **29**, 457–468.

Collier, J. S., Henstock, T. J., Pierce, T. J., & Watts, A. B. 1998. A detailed geophysical study in the Canary Basin (eastern Atlantic): Implications for the internal structure of 130 Ma oceanic crust. *Geophysical Journal International*, **135**, 943–963.

Collins, C. D. N., Drummond, B. J., & Nicoll, M. G. 2003. Crustal thickness patterns in the Australian Continent. *Pages 121–128 of:* Hillis, R. R., & Müller, R. D. (eds), *Evolution and Dynamics of the Australian Plate. Geological Society of Australia Special Publication 22 and Geological Society of America Special Paper 372*.

Colwell, J. B., Stagg, H. M. J., Direen, N. G., Bernadel, G., & Borissova, I. in press. The structure of the continental margin off Wilkes Land and Terre Adelie, East Antarctica. *In:* Futterer, D. (ed), *Antarctic Contributions to Global Earth Science, Proceedings 9th International Symposium on Antarctic Earth Sciences, Potsdam*.

Cooper, A. K., & O'Brien, P. in press. Leg 188 Synthesis: Transitions in the Glacial History of the Prydz Bay Region, East Antarctica, from ODP Drilling. *Chap. 1 of:* Cooper, A. K., O'Brien, P. E., & Richter, C. (eds), *Proceedings of the Ocean Drilling Program, Scientific Results Volume 188*.

Cooper, A. K., Davey, F. J., & Behrendt, J. C. 1987. Seismic stratigraphy and structure of the Victoria Land Basin, Western Ross Sea, Antarctica. *Pages 27–76 of:* Cooper, A. K., & Davey, F. J. (eds), *The Antarctic Continental Margin: Geology and Geophysics of the Western Ross Sea*. Houston, Texas, USA: Circum-Pacific Council for Energy and Mineral resources.

Cox, K. G. 1988. The Karoo Province. *Pages 239–271 of:* MacDougall, J. D. (ed), *Continental flood basalts*. Kluwer Academic Publishers.

Cox, K. G., Macdonald, R., & Hornung, G. 1967. Geochemical and petrographic provinces in the Karoo basalts of southern Africa. *American Mineralogist*, **52(9,10)**, 1451–1474.

Dalziel, I. W. D. 1992. Antarctica; a tale of two supercontinents. *Annual Review of Earth and Planetary Science Letters*, **20**, 501–526.

Dalziel, I. W. D, & Elliot, D. H. 1982. West Antarctica: problem child of Gondwana. *Tectonics*, **1**, 3–19.

Damuth, J. E. 1975. Echo character of the western equatorial Atlantic floor and its relationship to the dispersal and distribution of terrigenous sediments. *Marine Geology*, **18**, 17–45.

Damuth, J. E. 1979. Migrating sediment waves created by turbidity currents in the northern South China Basin. *Geology*, **7**, 520–523.

Davis, E. E., & Lister, C. R. B. 1977. Tectonic structures on the Juan de Fuca Ridge. *Geological Society of America Bulletin*, **88**, 346–363.

Davis, E. E., & Riddihough, R. P. 1982. The Winona Basin: Structure and tectonics. *Canadian Journal of Earth Sciences*, **19**, 767–788.

Davis, M., & Kusznir, N. 2002. Are buoyancy forces important during the formation of rifted margins. *Geophsical Journal International*, **149**, 524–533.

De Charpal, O., Guennoc, P., Montadert, L., & Roberts, D. G. 1978. Rifting, crustal attenuation and subsidence in the Bay of Biscay. *Nature*, **275**, 706–711.

De Conto, R. M., & Pollard, D. 2003. A coupled climate-ice-sheet modeling approach to the Early Cenozoic history of the Antarctic ice sheet. *Palaeogeography, Palaeoclimatology, Palaeoecology*, **198(1-2)**, 39–52.

De Santis, L., Brancolini, G., & Donda, F. 2003. Seismo-stratigraphic analysis of the Wilkes Land continental margin (East Antarctica): influence of glacially driven processes on the Cenozoic deposition. *Deep-Sea Research II*, **50(8-9)**, 1563–1594.

Dean, S. M., Minshull, T. A., Whitmarsh, R. B., & Louden, K. E. 2000. Deep structure of the ocean-continent transition in the southern Iberia Abyssal Plain from seismic refraction profiles: The IAM-9 transect at 40°20'N. *Journal of Geophysical Research*, **105(B3)**, 5859–5885.

Denham, J. I., & Brown, B. R. 1976. A new look at the Otway Basin. *APEA Journal*, **16(1)**, 91–98.

Direen, N. G., & Crawford, A. J. 2003. The Tasman Line: where is it, what is it, and is it Australia's Rodinian breakup boundary. *Australian Journal of Earth Sciences*, **50**, 491–502.

Domack, E. W., & Anderson, J. B. 1983. Marine geology of the George V continental margin: combined results of Deep Freeze 79 and the 1911-14 Australasian Expedition. *Pages 402–406 of:* Oliver, R. L., James, P. R., & Jago, J. B. (eds), *Antarctic Earth Sciences*. Canberra: Australian Academy of Science.

Donda, F., Brancolini, G., Santis, L. De, & Trincardi, F. 2003. Seismic facies and sedimentary processes on the continental rise off Wilkes Land (East Antarctica): evidence of bottom current activity. *Deep-Sea Research II*, **50(8-9)**, 1509–1527.

Drewry, D. J. 1976. Sedimentary Basins of the East Antarctic Craton from Geophysical Evidence. *Tectonophysics*, **36**, 301–314.

Du Toit, A. L. 1937. *Our Wandering Continents*. Oliver and Boyd.

Dunlop, D. J. 1995. Magnetism in rocks. *Journal of Geophysical Research*, **100(B2)**, 2161–2174.

Dziewonski, A. M., & Anderson, D. L. 1981. Preliminary Reference Earth Model. *Physics of the Earth and Planetary Interiors*, **25**, 297–356.

Ebinger, C. J., Karner, G. D., & Weissel, J. K. 1991. Mechanical strength of extended continental lithosphere: constraints from the western rift system, Africa. *Tectonics*, **10**, 1239–1256.

Eittreim, S. L., & Hampton, M. A. 1987. *The Antarctic Continental Margin Geology and Geophysics of Offshore Wilkes Land*. Circum-Pacific Council for Energy and Mineral resources.

Eittreim, S. L., & Smith, G. L. 1987. Seismic Sequences and Their Distribution on the Wilkes Land Margin. *Pages 15–43 of:* Eittreim, S. L., & Hampton, M. A. (eds), *The Antarctic Continental Margin Geology and Geophysics of Offshore Wilkes Land*. Houston, Texas, USA: Circum-Pacific Council for Energy and Mineral resources.

Eittreim, S. L., Gordon, A. L., Ewing, M., Thorndike, E. M., & Bruchhausen, P. 1972. The nepholoid layer and observed bottom currents in the Indian-Pacific Antarctic Sea. *Pages 19–35 of:* Gordon, A. L. (ed), *Studies in Physical Oceanography*. New York: Gordon and Breach.

Eittreim, S.L. 1994. Transition from continental to oceanic crust on the Wilkes-Adelie margin of Antarctica. *Journal of Geophysical Research*, **99**, 24,189–25,205.

Eittreim, S.L., Cooper, A. K., & Wannesson, J. 1995. Seismic stratigraphic evidence of ice-sheet advances on the Wilkes Land margin of Antarctica. *Sedimentary Geology*, **96**, 131–156.

Eldholm, O., Sundvor, E., & Myhre, A. M. 1979. Continental margin off Lofoten-Vesteralen. *Marine Geophysical Research*, **4**, 3–35.

Eldholm, O., Skogseid, J., Planke, S., & Gladczenko, T. P. 1995. Volcanic margin concepts. *Pages 1–16 of:* Banda, E., Torné, M., , & Talwani, M. (eds), *Rifted Ocean-Continent Boundaries*. Dordrecht: Kluwer Academic Publishers.

Elliot, D. H. 1975. Tectonics of Antarctica: a review. *American Journal of Science*, **275**, 45–106.

Elliot, D. H. 1992. Jurassic magmatism and tectonism associated with Gondwanaland breakup: an Antarctic perspective. *Pages 165–184 of:* Storey, B., Alabaster, T., & Pankhurst, P. J. (eds), *Magmatism and the Causes of Gondwana Break-up*. London: Geol. Soc. Special Publ.

Embley, R. W., & Langseth, M. G. 1977. Sedimentation processes on the continental rise of northeastern South America. *Marine Geology*, **25**, 279–297.

Emery, K. O. 1980. Continental margins - classification and petroleum prospects. *AAPG Bulletin*, **64**, 297–315.

Escutia, C., Eittreim, S. L., & Cooper, A. K. 1997. Cenozoic Sedimentation on the Wilkes Land Continental Rise, Antarctica. *Pages 791–795 of:* Ricci, C. A. (ed), *The Antarctic Region: Geological Evolution and Processes*. Siena: Terra Antarctica Publication.

Escutia, C., Eittreim, S. L., Cooper, A. K., & Nelson, C. H. 2000. Morphology and Acoustic Characteristic of the Antarctic Wilkes Land Turbidite Systems: Ice-Sheet-Source versus River-Sourced Fans. *Journal of Sedimentary Research*, **70, No.1**, 84–93.

Etheridge, M. A., Symonds, P. A., & Lister, G. S. 1989. Application of the Detachment Model to Reconstruction of Conjugate Passive Margins. *Pages 23–40 of:* Tankard, A. J., & Balkwill, H. R. (eds), *Extensional Tectonics and Stratigraphy of the North Atlantic Margins*. The American Association of Petroleum Geologists and The Canadian Geological Foundation.

Evans, D. A. D. 2003. True polar wander and supercontinents. *Tectonophysics*, **1-4**, 303–320.

Exon, N., *et al.* 2002. Drilling Reveals Climatic Consequences of Tasmanian Gateway Opening. *EOS Transactions*, **83; No 23**, 253–259.

Falvey, D. A. 1974. The development of continental margins in plate tectonic theory. *Australian Petroleum Exploration Association Journal*, **14**, 95–106.

Ferraccioli, F., Coren, F., Bozzo, E., Zanolla, C., Gandolfi, S., Tabacco, I., & Frezzotti, M. 2001. Rifted(?) crust at the East Antarctic Craton margin: gravity and magnetic interpretation along a traverse across the Wilkes Subglacial Basin region. *Earth and Planetary Science Letters*, **192**, 407–421.

Finlayson, D. M., Collins, C. D. N., Lukaszyk, I., & Chudyk, E. C. 1998. A transect across Australia's southern margin in the Otway Basin region: crustal architecture and the nature of rifting from wide-angle seismic profiling. *Earth and Planetary Science Letters*, **288**, 177–189.

Fitzgerald, P. G. 2002. Tectonics and landscape evolution of the Antarctic plate since the breakup of Gondwana, with an emphaisis on the West Antarcti Rift System and the Transantarctic Mountains. *Royal Sociey of New Zealand Bulletin*, **35**, 453–469.

Fitzgerald, P. G., & Baldwin, S. L. 1997. Detachment fault model for the evolution of the Ross Embayment. *Pages 555–564 of:* Ricci, C. A. (ed), *The Antarctic region: geological evolution and processes*. Sienna: Terra Antarctica Publications.

Fitzgerald, P. G., Sandiford, M., Barrett, P. J., & Gleadow, A. J. W. 1986. Asymmetric extension associated with uplift and subsidence in the Transantarcitic Mountains and the Ross Embayment. *Earth and Planetary Science Letters*, **81**, 67–78.

Forsyth, D. W. 1985. Subsurface loading and estimates of the flexural rigidity of continental lithosphere. *Journal of Geophysical Research*, **90**, 12,623–12,632.

Foucher, J.-P., Le Pichon, X., & Sibuet, J.-C. 1982. The ocean-continent transition in the uniform lithosphere stretching model: role of partial melting in the mantle. *Philosophical Transactions of the Royal Society of London*, **A305**, 27–43.

Fowler, S. R., White, R. S., Spence, G. D., & Westbrook, G. K. 1989. The Hatton Bank continental margin – II: Deep structure from two-ship expanding spread seismic profiles. *Geophysical Journal International*, **96**, 295–309.

Gaina, C., Müller, R. D., Royer, J. Y., Stock, J., Hardebeck, J., & Symonds, P. 1998. The tectonic history of the Tasman Sea: A puzzle with thirteen pieces. *Journal of Geophysical Research*, **103**, 12,413–12,433.

Gee, J., Staudigel, H., & Tauxe, L. 1989. Contribution of induced magnetization to magnetization of seamounts. *Nature*, **342**, 170–173.

Green, R., Schmidt, P. W., & McDougall, I. 1978. Palaeomagnetic and potassium-argon dating studies of the Tasmanian dolerites; discussion and reply. *Journal of the Geological Society of Australia*, **25(5-6)**, 365–367.

Grindley, G. W., & Davey, F. J. 1982. The Reconstruction of New Zealand, Australia and Antarctica. *Pages 15–29 of:* Craddock, C. (ed), *Antarctic Geoscience*. University of Wisconsin Press.

Groushinsky, N. P., & Sazhina, N. B. 1982. Some features of Antarctic crustal structure. *In:* Craddock, C. (ed), *Antarctic Geoscience*. University of Wisconsin Press.

Gunn, B. M., & Warren, G. 1962. Geology of Victoria Land between the Mawson and Mulock Glaciers, Antarcitca. *New Zealand Geological Survey Bulletin*, **71**, 157.

Gurnis, M., & Müller, R. D. 2003. Origin of the Australian-Antarctic Discordance from an ancient slab and mantle wedge. *Pages 417–430 of:* Hillis, R. R., & Müller, R. D. (eds), *Evolution and Dynamics of the Australian Plate. Geological Society of Australia Special Publication 22 and Geological Society of America Special Paper 372.*

Gurnis, M., Müller, R. D., & Moresi, L. 1998. Cretaceous Vertical Motion of Australia and the Australian-Antarctic Discordance. *Science*, **279**, 1499–1504.

Hamilton, E. L. 1976. Variations of density and porosity with depth in deep-sea sediments. *Journal of Sedimentary Petrology*, **46, No. 2**, 280–300.

Hamilton, E. L., & Bachman, R. T. 1982. Sound velocity and related properties of marine sediments. *Journal of Acoustic Society of America*, **72(6)**, 1891–1904.

Hampton, M. A., Eittreim, S. L., & Richmond, B. M. 1987. Seismic Sequences and Their Distribution on the Wilkes Land Margin. *Pages 75–87 of:* Eittreim, S. L., & Hampton, M. A. (eds), *The Antarctic Continental Margin Geology and Geophysics of Offshore Wilkes Land*. Houston, Texas, USA: Circum-Pacific Council for Energy and Mineral resources.

Hatton, L., Worthington, M. H., & Makin, J. 1986. *Seismic Data Processing - Theory and Practice*. Blackwell Scientific Publications.

Hayes, D. E., & Conolly, J. R. 1972. Morphology of the southeast Indian Ocean. *Pages 125–145 of:* Hayes, D. E. (ed), *Antarctic Oceanology II: The Australian-New Zealand Sector, Antarctic Research Series, 19*. Washington: AGU.

Hayes, D. E., & Frakes, L. A. 1975. General synthesis Deep-Sea Drilling Project Leg 28. *In:* Hayes, D. E., & Frakes, L. A. (eds), *Initial reports of the Deep-Sea Drilling Project*. Washington, D. C.: U. S. Government Printing Office.

Heezen, B. C. 1974. Atlantic-Type Continental Margins. *Pages 13–24 of:* Burke, C. A., & Drake, C. L. (eds), *The Geology of Continental Margins*. Springer-Verlag.

Hegarty, K. A., Weissel, J. K., & Mutter, J. C. 1988. Subsidence history of Australia's southern margin: constraints on basin models. *AAPG Bulletin*, **72 (5)**, 615–633.

Heirtzler, J. R., Dickson, G. E., Herron, E. M., & Pitman III, W. C. 1968. Marine magnetic anomalies, geomagnetic field reversals, and motions of the ocean floor and continents. *Journal of Geophysical Research*, **73(6)**, 2119–2136.

Henning, A., Sawyer, D., & Templeton, D. C. 2004. Exhumed upper mantle within the ocean-continent transition on the northern West Iberia margin: Evidence from prestack depth migration and total tectonic subsidence analyses. *Journal of Geophysical Research*, **109(B5)**. doi:10.1029/2003JB002526.

Hillier, J., & Watts, A. B. 2005. Relationship between depth and age in the North Pacific Ocean. *Journal of Geophysical Research*, **110(B02405)**. doi:10.1029/2004JB003406.

Hinz, K., Willcox, J. B., Whiticar, M., Kudrass, H., Exon, N. F., & Feary, D. 1986. The west Tasmanian margin: an underrated petroleum province? *Pages 395–410 of:* Glenie, R. C. (ed), *Second southe-eastern Australia oil exploration symposium*. PESA.

Holbrook, W. S., Purdy, G. M., Sheridan, R. E., Glover, III, L., Talwani, M., Ewing, J., & Hutchinson, D. 1994. Seismic structure of the U.S. Mid-Atlantic continental margin. *Journal of Geophysical Research*, **99**, 17871–17891.

Hooper, P. R., Rehacek, J., & Duncam, R. A. 1993. The basalts of Lesotho, Karoo Province, Southern Africa (abstract). *EOS, Transactions of the American Geophysical Union*, **74**, 553.

Horen, H., Zamora, M., & Dubuisson, G. 1996. Seismic waves velocities and anisotropy in serpentinized peridotites from Xigaze ophiolite: Abundance of serpentine in slow spreading ridge. *Geophsyical Research Letters*, **23(1)**, 9–12.

Hospers, J. 1965. Gravity field and structure of the Niger Delta, Nigeria, West Africa. *Geological Society of America Bulletin*, **76**, 407–422.

Huchon, P., Nguyen, T. N. H., & Chamot-Rooke, N. 2001. Propogation of continentl break-up in the southwestern South China Sea. *Pages 31–50 of:* Wilson, R. C. L., Whitmarsh, R. B., Taylor, B., & Froitzheim, N. (eds), *Continental Margins: A Comparison of Evidence from Land and Sea. Special Publication 187.* London: Geological Society London.

Hudec, M. R., & Jackson, M. P. A. 2002. Structural segmentation, inversion, and salt tectonics on a passive margin: evolution of the Inner Kwanza Basin, Angola. *Geological Society of America Bulletin*, **114**, 1222–1244.

Hutchinson, D. R., Grow, J. A., Klitgord, K. D., & Swift, B. A. 1982. Deep structure and evolution of the Carolina Trough. *Pages 129–152 of:* Watkins, J. S., & Drake, C. L. (eds), *Studies in Continental Margin Geology.* AAPG Memoir 34. Tulsa, OK: American Association of Petroleum Geologists.

IAGA, Working Group 8. 2000. International Geomagnetic Reference Field 2000. *Geophysical Journal International*, **141(1)**, 259–262. International Association of Geomagnetism and Aeronomy (IAGA) Division V.

Ikami, A., Ito, K., & Kaminuma, K. Shibuya K. 1983. Crustal structure of the Mizuho Plateau, Antarctica, revealed by explosion seismic measurements. *In:* Oliver, R. L., James, P. R., & Jago, J. B. (eds), *Antarctic Earth Science.* Australian Academy of Science, Canberra.

IOC, IHO, & BODC. 2003. *Centenary Edition of the GEBCO Digital Atlas.* Published on CD-ROM on behalf of the Intergovernmental Oceanoographic Commission and the International Hydrographic Organization as part of the General Bathymetric Chart of the Oceans; British Oceanographic Data Centre, Liverpool.

Irving, E. 1970. Oxidation and magnetic properties of basalt; review and discussion. *Canadian Journal of Earth Sciences*, **7**, 1528–1538.

Jarrard, R. D., Dadey, K.A., & Busch, W.H. 1989. Velocity and Density of Sediments of Erik Ridge, Labrador Sea: Control by Porosity and Mineralogy. *Pages 811–835 of:* Srivastava, S. P., Arthur, M.A., & Clement, B. (eds), *Proceedings of ODP Scientific Results, 105.* Ocean Drilling Program.

Jones, E. J. W. 1999. *Marine Geophysics.* Wiley.

Kagami, H. 1995. Topogrpaphic character of the East Antarctic continental margin off Wilkes Land. *Pages 181–192 of: Proceedings of the National Institute for Polar Research Symposium on Antarctic Geoscience*. Japan: NIPR.

Karner, G. D. 1991. Sediment blanketing and the flexural strength of extended continental lithosphere. *Basin Research*, **3**, 177–185.

Karner, G. D., & Watts, A. B. 1982. Gravity anomalies and flexure of the lithosphere at mountain ranges. *Journal of Geophysical research*, **88**, 10,449–10,477.

Karner, G.D., & Watts, A.B. 1983. Gravity Anomalies and Flexure of the Lithosphere at Mountain Ranges. *Journal of Geophysical Research*, **88**(B12), 10449–10477.

Keen, C., Peddy, C., De Voogd, B., & Matthews, D. H. 1989. Conjugate margins of Canada and Europe: results from deep reflection profiling. *Geology*, **17**, 173–176.

Keen, C. E., & Dehler, S. A. 1997. Extensional styles and gravity anomalies at rifted continental margins: Some North Atlantic examples. *Tectonics*, **16**, 744–754.

Keen, C. E., Loncarevic, B. D., Reid, I., Woodside, J., Haworth, R. T., & Williams, H. 1990. Tectonic and geophysical overview. *Pages 31–85 of:* Keen, M. J., & Williams, G. L. (eds), *Geology of the Continental Margin off Eastern Canada*. The Geology of North America, vol. 2. Ottowa: Geol. Surv. of Can.

Kennett, J. 1982. *Marine Geology*. Prentice-Hall.

Kennett, J. P. 1977. Cenozoic evolution of Antarctic glaciation, the Circum-Antarctic Ocean, and their impact on global paleoceanography. *Journal of Geophysical research*, **82**, 3843–3859.

Kent, D. V., & Gee, J. 1994. Grain Size-Dependent Alteration and the Magnetization of Oceanic Basalts. *Science*, **265**, 1561–1563.

Klein, E. M., & Langmuir, C. H. 1987. Global correlations of ocean ridge basalt chemistry with axial depth and crustal thickness. *Journal of Geophysical Research*, **92(8)**, 8089–8115.

Kogan, A. L. 1972. Results of deep seismic soundings of the earth's crust in East Antarctica. *Pages 485–489 of:* Adie, R. J. (ed), *Antarctic geology and geophysics*. Universitetsforlaget.

Kong, L. S. L., Detrick, R. S., Fox, P. J., Mayer, L. A., & Ryan, W. B. F. 1988. The morphology and tectonics of the Mark area from the Sea Beam and Sea MARK I observations, Mid-Atlantic Ridge 23°N. *Marine Geophysical Research*, **10**, 59–90.

König, M. 1980. *Geophysical Investigations of the Southern Continental Margin of Australia and the Conjugate Sector of East Antarctica*. Ph.D. thesis, Lamont Doherty Earth Observatory, Columbia University, NY, USA. unpublished.

König, M., & Talwani, M. 1977. A geophysical study of the southern continental margin of Australia: Great Australian Bight and western sections. *Geological Society of America Bulleting*, **88**, 1000–1014.

Kooi, H., Cloetingh, S., & Burrus, J. 1992. Lithospheric necking and regional isostasy at extensional basins1. Subsidence and gravity modeling with an application to the Gulf of Lions Margin (SE France). *Journal of Geophysical research*, **97**, 17,553–17,571.

Krawczyk, C. M., Reston, T. J., Beslier, M., & Boillot, G. 1996. Evidence for detachment tectonics on the Iberia Abyssal Plain rifted margin. *Pages 603–615 of:* Whitmarsh, R. B., Sawyer, D. S., Klaus, A., & Masson, D. G. (eds), *Proceedings of the Ocean Drilling Program, Scientific Results 149*. Ocean Drilling Program.

Krishna, M. R., Chand, S., & Subrahmanyam, C. 2000. Gravity anomalies, sediment loading and lithospheric flexure associated with the Krishna-Godavari basin, eastern continental margin of India. *Earth and Planetary Science Letters*, **175**, 223–232.

Kumar, N. 1978. Sediment Distribution in Western Atlantic Off Northern Brazil - Structural Controls and Evolution. *AAPG Bulletin*, **62(2)**, 273–294.

Kusznir, N. J., & Egan, S. S. 1990. Simple-shear and pure-shear models of continental extensional sedimentary basin formation: application to the Jeanne d'Arc Basin, Grand Banks of Newfoundland. *Pages 305–322 of:* Tankard, A. J., & Blakwill, H. R. (eds), *Extensional Tectonics of the North Atlantic Margins*. Am. Assoc. Pet. Geol., Mem. 46.

Kusznir, N. J., & Park, R. G. 1987. The extensional strength of the continental lithoshpere: its dependence on geothermal gradient, and crustal composition and thickness. *Pages 35–52 of:* Coward, M. P., Dewey, J. F., & Hancock, P. L. (eds), *Continental Extensional Tectonics*. Geological Society of London Special Publication.

Lambeck, K. 1972. Gravity anomalies over ocean ridges. *Geophysical Journal of the Royal Astronomical Society*, **30**, 37–53.

Larson, P. A., Mudie, J. D., & Larson, R. L. 1972. Magnetic anomalies and fracture zone trends in the Gulf of California. *Geological Society of America Bulletin*, **83**, 3361–3368.

Larson, R. L., & Chase, C. G. 1972. Late Mesozoic evolution of the western Pacific Ocean. *Geological Society of America Bulletin*, **83**, 3627–3644.

Larter, R. D., & Barker, P. F. 1989. Effects of ridge crest-trench interaction on Antarctic-Phoenix spreading: forces on a young subducting plate. *Journal of Geophysical Research*, **17**, 19,583–19,607.

Larter, R. D., Cunningham, A. P., & Hardy, R. J. J. 1990. The sea-floor multiple problem in multichannel seismic reflection data acquired on the Antarctic continental shelf: its causes and treatment. *Pages 187–193 of:* Cooper, A. K., & Webb, P. N. (eds), *International Workshop on Antarctic Offshore Seismic Stratigraphy (ANTOSTRAT): Overview and Extended Abstracts*. USGS.

Larter, R. D., Rebesco, M., Vanneste, L. E., Gamboa, L. A. P., & Barkere, P. F. 1997. Cenozoic tectonic, sedimentary and glacial history of the continental shelf west of Graham

Land, Antarctic Peninsula. *Pages 1–27 of:* Cooper, A. K., Barker, P. F., & Brancolini, G. (eds), *Geology and Seismic Stratigraphy of the Antarctic margin, Part 2. Antarctic Research Series. 71.* American Geophysical Union.

LASE Study Group. 1986. The structure of the U.S. East coast passive margin from large aperature seismic experiments (LASE). *Marine and Petroleum Geology*, **3**, 234–242.

Lavier, L. L., & Steckler, M. S. 1997. The effect of sedimentary cover on the flexural strength of continental lithosphere. *Nature*, **389**, 476–479.

Lawver, L. A., & Gahagan, L. M. 2003. Evolution of Cenozoic seaways in the circum-Antarctic region. *Paelaeogeography, Palaeoclimatology, Paleaecology*, **198**, 11–37.

Lawver, L. A., & Scotese, C. R. 1987. A Revised Reconstruction of Gondwanaland. *Pages 17–24 of:* McKenzie, G. D. (ed), *Geophys. Monogr. 40.* American Geophysical Union.

Lawver, L. A., Gahahgan, L. M., & Coffin, M. F. 1992. Development of paleoseaways around Antarctica. *Pages 7–30 of: The Antarctic paleoenvironment: a perspective on global change.* Washington D.C.: American Geophysical Union. Antarctic Research Series Volume 56.

Lawver, L. A., Gahahgan, L. M., & Dalziel, I. W. D. 1998. A tight fit–Early Mesozoic Gondwana: a plate tectonic perspective. *In: Origin and evolution of continents. Memoirs of the National Institute of Polar Research.* Tokyo: NIPR.

Laxon, S., & McAdoo, D. 1994. Arctic Ocean Gravity Field Derived From ERS-1 Satellite Altimetry. *Science*, **265**, 621–624.

LeMasurier, W. E., & Rex, D. C. 1991. The Marie Byrd Land volcanic province and its relation to the cainozoic West Antarctic Rift System. *Pages 249–281 of:* Tingey, R. J. (ed), *The Geology of Antarctica.* Clarendon Press, Oxford.

Levi, S. 1983. Paleomagnetism and rock magnetism of submarine basalts from the Galapagos spreading centre near 86°W. *Pages 429–435 of: Initial reports of the Deep Sea Drilling Project: Volume 70.* Washington D.C.: U.S. Government Printing Office.

Levi, S., & Riddhough, R. 1986. Why are marine magnetic anomalies suppressed over sedimented spreading centers. *Geology*, **14**, 651–654.

Lin, A. T., & Watts, A. B. 2002. Origin of the West Taiwan basin by orogenic loading and flexure of a rifted continental margin. *Journal of Geophysical Research*, **107(B9)**.

Lin, J., & Phipps Morgan, J. 1992. The spreading rate dependence of three-dimensional mid-ocean ridge gravity structure. *Geophysical Research Letters*, **19**, 13–16.

Lister, C. R. B. 1972. On the thermal balance of a mid-ocean ridge. *Royal Astronomical Society Geophysical Journal*, **26**, 515–535.

Lister, G. S., Etheridge, M. A., & Symonds, P. A. 1991. Detachment models for the formation of passive continental margins. *Tectonics*, **10**, 1038–1064.

Ludbrook, N. H. 1980. *A Guide to the Geology and Mineral Resources of South Australia*. Dept. of Mines and Energy South Australia.

Luyendyk, B. P. 1997. Slab capture versus ridge collision as an explanation for Cretaceous extension and rifting of east Gondwana. *Pages 467–474 of:* Ricci, C. A. (ed), *The Antarctic Region: Geological Evolution and Processes, Proceed. VII Symp. on Antarctic Earth Sci.* Siena.

Lythe, M. B., Vaughan, D. G., & the BEDMAP Consortium. 2000. BEDMAP - bed topography of the Antarctic. 1:10,000,000 scale map. *BAS (Misc) 9*.

Macdonald, K. C. 1982. Mid-ocean ridges: Fine scale tectonics, volcanic and hydrothermal processes within the plate boundary zone. *Annu. Rev. Earth Planet. Sci.*, **10**, 155–190.

Maggi, A., Jackson, J.A., McKenzie, D., & Priestley, K. 2000. Earthquake focal depths, effective elastic thickness, and the strength of the continental lithosphere. *Geology*, **28**(6), 495–498.

Manatschal, G. 2004. New models for evolution of magma-poor rifted margins based on a review of data and concepts from West Iberia and the Alps. *International Journal of Earth Science*, **93**, 432–466.

Marty, J. C., & Cazenave, A. 1989. Regional variations in subsidence rate of oceanic plates: a global analysis. *Earth and Planetary Science Letters*, **94**, 301–315.

Mawson, D. 1940. Sedimentary Rocks. *Australasian Antarctic Expedition 1911-14 Scientific Reports*, **Series A, IV(II)**, 347–367.

McAdoo, D., & Laxon, S. 1996. Satellite Gravity in the Weddell Sea. *Pages 155–164 of:* Storey, B. C., King, E. C., & Livermore, R. A. (eds), *Weddell Sea Tectonics and Gondwana Breakup*. Geological Society Special Publication NO. 108.

McAdoo, D., & Laxon, S. 1997. Antarctic Tectonics: Constraints From an ERS-1 Satellite Marine Gravity Field. *Science*, **276**, 556–560.

McKenzie, D. 1978. Some Remarks on the Development of Sedimentary Basins. *Earth and Planetary Science Letters*, **40**, 25–32.

McKenzie, D. P. 2003. Estimating Te in the presence of internal loads. *Journal of Geophysical Research*, **108(B9)**, 10.1029/2002JB001766.

McKenzie, D. P., & Fairhead, J. D. 1997. Estimates of the effective elastic thickness of the continental lithosphere from Bouguer and free air gravity anomalies. *Journal of Geophysical Research*, **102**, 27,523–27,552.

Meffre, S., Berry, R. F., & Hall, M. 2000. Cambrian metamorphic complexes in Tasmania: tectonic implications. *Australian Journal of Earth Sciences*, **47(6)**, 971–985.

Melhuish, A., Henrys, S. A., Bannister, A., & Davey, F. J. 1995. Seismic profiling adjacent to Ross Island: Constraints on late Cenozoic stratigraphy and tectonics. *Journal of Geophysical Research*, **94**, 10,473–10,500.

Menzies, M. A., Klemperer, S. L., Ebinger, C. J., & Baker, J. 2002. Characteristics of volcanic rifted margins. *Pages 1–14 of:* Menzies, M. A., & Baker, J. (eds), *Volcanic Rifted Margins*. Geological Society of America Special Publication.

Michon, L., & Merle, O. 2003. Mode of lithospheric extension: Conceptual models from analogue modeling. *Tectonics*, **22(4)**, 1028.

Minshull, T. A., Muller, M. R., Robinson, C. J., White, R. S, & Bickle, M. J. 1998. Is the oceanic Moho a serpentinisation front? *Pages 71–80 of:* Mills, R. A., & Harrison, K. (eds), *Modern Ocean Floor Processes and Geological Record*. Geological Society of London Special Publication.

Mishra, D. C., Sekhar, D. V. Chandra, Raju, D. Ch. Venkata, & Kumar, V. Vijaya. 1999. Crustal structure based on gravity-magnetic modelling constrained from seismic studies under Lambert Rift, Antarctica and Godavari and Mahanadi rifts, India and their interrelationship. *Earth and Planetary Science Letters*, **172**, 287–300.

Mohriank, W., & Talwani, M. (eds). 2000. Inferences Regarding Initiation of Oceanic Crust Formation From the U.S. East Coast Margin and Conjugate South Atlantic Margins. *Pages 211–234 of:* Mohriank, W., & Talwani, M. (eds), *Atlantic Rifts and Continental Margins*. M. Talwani and V. Abreu: AGU.

Moore, A. M. G., Stagg, H. M. J., & Norvick, M. S. 2000. Deep-water Otway basin: a new assessment of the tectonics and hydrocarbon prospectivity. *APPEA Journal*, **40**, 66–84.

Morris, E., Detrick, R. S., Minshull, T. A., Mutter, J. C., White, R. S., Su, W., & Buhl, P. 1993. Seismic Structure of Oceanic Crust in the Western North Atlantic. *Journal of Geophysical Research*, **98(B8)**, 13,879–13,903.

Murray, C. G., Scheibner, E., & Walker, R. N. 1989. Regional geological interpretation of a digital coloured residual Bouguer gravity image of easter Australia with a wavelength cut-off of 250 km. *Australian Journal of Earth Sciences*, **36**, 423–449.

Mutter, C. Z., & Mutter, J. C. 1993. Variations in thickness of layer 3 dominate oceanic crustal structure. *Earth and Planetary Science Letters*, **117**, 295–317.

Mutter, J., Talwani, M., & Stoffa, P. 1982. Origin of seaward-dipping reflectors in oceanic crust off the Norwegian margin by subaerial seafloor spreading. *Geology*, **10**, 137–157.

Mutter, J. C., & Karson, J. A. 1992. Structural processes at slow-spreading ridges. *Science*, **257**, 627–634.

Neidell, N. S., & Taner, M. T. 1971. Semblance and other coherency measures for multichannel data. *Geophysics*, **36**, 482–497.

Newman, P. 1993. Divergence effects in a layered earth. *Geophysics*, **38**, 481–488.

Nichols, I. A., Ferguson, J., Jones, H., Marks, G. P., & Mutter, J. C. 1981. Ultramafic blocks from the ocean floor southwest of Australia. *Earth and Planetary Science Letters*, **56**, 362–374.

Normack, W. R., Hess, G. R., Stow, D. A. V., & Bowen, A. J. 1980. Sediment waves on the Monterey fan levee: a preliminary physical interpretation. *Marine Geology*, **37**, 1–18.

Nur, A., & Ben-Avraham, Z. 1982. Oceanic Plateaus, the Fragmentation of Continents, and Mountain Building. *Journal of Geophsyical Research*, **87(B5)**, 3644–3661.

Oliver, R. L., & Fanning, C. M. 1997. Australia and Antarctica: precise correlation of Palaeoproterozoic Terrains. *Pages 163–172 of:* Ricci, C. A. (ed), *The Antarctic Region: Geological Evolution and Processes*. Sienna: Terra Antarctica Publication.

Oufi, O., & Cannat, M. 2002. Magnetic properties of variably serpentinized abyssal peridotites. *Journal of Geophysical Research*, **107(B5)**, EPM3–20.

Özdemir, Ö., & Dunlop, D. J. 1985. An experimental study of chemical remanent magnetizations of synthetic monodomain titanomaghemites with initial thermoremanent magnetizations. *Journal of Geophsyical Research*, **90**, 11,513–11,523.

Parker, R. L. 1972. The rapid calculation of potential anomalies. *Geophysical Journal of the Royal Astronomical Society*, **31**, 447–455.

Parrish, J. T. 1990. Gondwanan Paleogeography and Paleoclimatology. *Pages 15–26 of:* Taylor, T. N., & Taylor, E. L. (eds), *Antarctic Paleobilology*. Springer-Verlag.

Parsons, B. E., & Molnar, P. 1976. The origin of outer topographic rises associated with trenches. *Geophysical Journal of the Royal Astronomical Society*, **45**, 707–712.

Parsons, B. E., & Sclater, J. G. 1977. An analysis of the variation of ocean floor bathymetry and heat flow with age. *Journal of Geophysical Research*, **82**, 803–827.

Pérez-Gussinyé, M., Reston, T., & Morgan, J. Phipps. 2001. Serpentinization and magmatism during extension at non-volcanic margins: the effect of initial lithospheric structure. *Pages 551–576 of:* Wilson, R. C. L., Whitmarsh, R. B., Taylor, B., & Froitzheim, N. (eds), *Continental Margins: A Comparison of Evidence from Land and Sea. Special Publication 187*. London: Geological Society London.

Perez-Gussinye, M., Lowry, A. R., Watts, A. B., & Velicogna, I. 2004. On the recovery of effective elastic thickness using spectral methods: Examples from synthetic data and from the Fennoscandian Shield. *Journal of Geophysical Research*, **109(B10409)**. doi:10.1029/2003JB002788.

Pinheiro, L. M., Wilson, R. C. L., Pena dos Reis, R., Whitmarsh, R. B., & Ribeiro, A. 1996. The western Iberia Margin: a geophysical and geological overview. *Pages 3–27 of:*

Whitmarsh, R. B., Sawyer, D. S., Klaus, A., & Masson, D. G. (eds), *Proceedings of the Ocean Drilling Program, Scientific Results 149*. Ocean Drilling Program.

Pitman, W. C. 1978. The relationship between eustacy and stratigraphic sequences of passive margins. *Geological Society of America Bulletin*, **89**, 1389–1403.

Poehls, K. A., Luyendyk, B. P., & Heirtzler, J. R. 1973. Magnetic smooth zones in the world's oceans. *Journal of Geophysical Research*, **78**, 6985–6997.

Powell, R. D. 1984. Glacimarine processes and inductinve lithofacies modelling of ice shelf and tidewater glacier sediments based on Quaternary examples. *Marine Geology*, **57(1)**, 1–52.

Pratt, J. H. 1855. On the attraction of the Himalaya Mountains, and of the elevated regions beyond them upon a plumb-line in India. *Philosophical Transactions of the Royal Society of London*, **145**, 53–101.

ProMAX. 1998a. *2D Advanced Techniques User Training Manual*. Landmark.

ProMAX. 1998b. *2D Seismic Processing and Analysis*.

Quilty, P. 1986. Australia's Antarctic Basins - Identification and Evolution. *Petroleum Exploration Society of Australia*, **8**, 20–46.

Rabinowitz, P. D., & LaBrecque, J. L. 1977. The isostatic gravity anomaly: A key to the evolution of the ocean-continent boundary. *Earth and Planetary Science Letters*, **35**, 145–150.

Rabinowitz, P. D., & LaBreque, J. L. 1979. The Mesozoic south Atlantic Ocean and evolution of its continental margins. *Journal of Geophysical Research*, **84**, 5973–6002.

Raitt, R. W. 1963. The crustal rocks. *Pages 85–102 of:* Hill, M. N. (ed), *The Sea*. Interscience.

Rapp, R. H., & Pavlis, N. K. 1990. The Development and Analysis of Geopotential Coefficient Models to Spherical Harmonic Degree 360. *Journal of Geophysical Research*, **95, B13**, 21,885–21,911.

Rebesco, M., Larter, R. D., Barker, P. F., Camerlenghi, A., & Vanneste, L. E. 1997. The history of sedimentation on the continental rise west of the Antarctic Peninsula. *Pages 29–49 of:* Cooper, A. K., Barker, P. F., & Brancolini, G. (eds), *Geology and Seismic Stratigraphy of the Antarctic margin, Part 2. Antarctic Research Series. 71.* American Geophysical Union.

Ritsema, J., van Heijst, H. J., & Woodhouse, J. H. 1999. Complex shear wave velocity structure imaged beneath Africa and Iceland. *Science*, **286**, 1925–1928.

Rosendahl, B. R., & Groschel-Becker, H. 2000. Architecture of the Continental Margin in the Gulf of Guinea as Revealed by reprocessed Deep-Imaging Seismic Data. *Pages 85–104 of:* Mohriank, W., & Talwani, M. (eds), *Atlantic Rifts and Continental Margins*. AGU.

Royer, J., & Rollet, N. 1997. Plate tectonic setting of the Tasmanian region. *Australian Journal of Earth Science*, **44**, 543–560.

Sandwell, D. T., & Smith, W. H. F. 1997. Marine gravity anomaly from Geosat and ERS 1 satellite altimetry. *Journal of Geophysical Research*, **102(B5)**, 10,039–10,054.

Sangree, J. B., & Widmier, J. M. 1977. Seismic stratigraphy and global changes of sea level. Part 9. Seismic interpretation of clastic depositional facies. *Pages 165–184 of:* Payton, C. E. (ed), *Seismic stratigraphy - applications to hydrocarbon exploration. AAPG Memoir 29.* AAPG.

Sawyer, D. 1985. Total tectonic subsidence: A parameter for distinguishing crust type a the U.S. Atlantic continental margin. *Journal of Geophysical Research*, **90**, 7751–7769.

Sayers, J., Symonds, P. A., Direen, N. G., & Bernadrel, G. 2001. Nature of the continent-ocean transitionon the non-volcanic rifted margin of the central Great Australian Bight. *Pages 51–77 of:* Wilson, R. C. L., Whitmarsh, R. B., Taylor, B., & Froitzheim, N. (eds), *Continental Margins: A Comparison of Evidence from Land and Sea. Special Publication 187.* London: Geological Society London.

Schouten, H., & McCamy, K. 1972. Filtering Marine Magnetic Anomalies. *Journal of Geophysical Research*, **77;35**, 7089–7099.

Sclater, J. G., & Francheteau, J. 1970. The implications of terrestrial heat flow observation on current tectonic and geochemical models of the crustal and upper mantle of the earth. *Geophysical Journal of the Royal Astronomical Society*, **20**, 509–542.

Sleep, N. H. 1971. Thermal effects of the formation of Atlantic continental margins by continental breakup. *Journal of the Royal Astronomical Society*, **24**, 325–350.

Smith, A. G., & Drewry, D. J. 1984. Delayed phase change due to hot asthenosphere causes Transantarctic uplift? *Nature*, **309**, 536–538.

Smith, G., & Hallam, A. 1970. The Fit of the Southern Continents. *Nature*, **225**, 139–144.

Smith, G. M., & Banerjee, S. K. 1986. Magnetic Structure of the Upper Kilometer of the Marine Crust at Deep Sea Drilling Project Hole 504B, Eastern Pacific Ocean. *Journal of Geophysical Research*, **91(B10)**, 10,337–10,354.

Smith, W. H. F., & Sandwell, D. T. 1994. Bathymetric prediction from dense satellite altimetry and sparse shipboard bathymetry. *Journal of Geophysical Research*, **99(B11)**, 21,083–10,824.

Stacey, F. D. 1967. The Koenigsberger Ratio and the Nature of Thermoremanence in Igneous Rocks. *Earth and Planetary Science Letters*, **2**, 67–68.

Stagg, H. M. J. 1985. The structure and origin of Prydz Bay and the Mac.Robertson Shelf, East Antarctica. *Tectonophysics*, **114**, 315–340.

Stagg, H. M. J., Willcox, J. B., Symonds, P. A., O'Brien, G. W., Colwell, J. B>, Hill, P. J., s. Clee, C, Moore, A. M. G., & Struckmeyer, H. I. M. 1999. Architecture and evolution of the Australian continental margin. *AGSO Journal of Australian Geology & Geophysics*, **17(5/6)**, 17–33.

Stagg, H. M. J., Colwell, J. B., Direen, N. G., O'Brien, P. E., Brown, B. J., Bernadel, G., Borissova, I., & Ishihara, T. in press. Geology of the continental margin of Enderby and Mac. Robertson Lands, East Antarctica: insights from a regional data set. *In:* Jokat, W. (ed), *Proceedings Workshop East-West Antarctic Tectonics and Gondwana Break-up: 60W to 60E, Potsdam, 2003.* Marine Geophysical Researches.

Steckler, M. S. 1985. Uplift and extension at the Gulf of Suez: indication of induced mantle convection. *Nature*, **317**, 135–139.

Steckler, M. S., & Ten Brink, U. S. 1986. Lithospheric strength variation as a control on new plate boundaries: examples from the Gulf of Suez. *Earth and Planetary Science Letters*, **79**, 120–132.

Steckler, M. S., & Watts, A. B. 1978. Subsidence of the Atlantic-type continental margin off New York. *Earth and Planetary Science Letters*, **41**, 1–13.

Steckler, M. S., & Watts, A.B. 1981. Subsidence history and tectonic evolution of Atlantic-type continental margins. *Pages 184–19 of:* Scrutton, R.A. (ed), *Dynamics of Passive Margins, Geodynamics Series, Vol. 6.* Washington D.C.: American Geophysical Union.

Steed, R. 1980. *Geophysical investigation of Wilkes Land, Antarctica.* Ph.D. thesis, University of Cambridge, U. K. unpublished.

Stern, T. A., & ten Brink, U. S. 1989. Flexural Uplift of the Transantarctic Mountains. *Journal of Geophysical Research*, **94, B8**, 10,315–10,330.

Stern, T. A., & ten Brink, U. S. 1992. Rift flank uplifts and hinterland basins: comparison of the Transantarctic Mountains with the Great Escarpment of Southern Africa. *Journal of Geophysical Research*, **97**, 569–585.

Stewart, J. 1998. *Gravity Anomalies and Lithospheric Flexure: Implications for the Thermal and Mechanical Evolution of the Continental Lithosphere.* Ph.D. thesis, University of Oxford, U. K. unpublished.

Stewart, J., Watts, A. B., & Bagguley, J. G. 2000. Three-dimensional subsidence analysis and gravity modelling of the continental margin offshore Namibia. *Geophysical Journal International*, 724–746.

Stock, J., & Molnar, P. 1987. Revised history if early Tertiary plate motion in the southwest Pacific. *Nature*, **325**, 495–499.

Storey, B. C., Dalziel, I. W. D., Garrett, S. W., Grunow, A. M., Pankhurst, R. J., & Vennum, W. R. 1998. West Antarctica in Gondwanaland: crustal blocks, reconstruction and breakup processes. *Tectonophysics*, **155**, 381–390.

Storey, B.C., & Kyle, P.R. 1999. The Weddell Sea region: a plume impact site and source for Gondwana magmas during the initial stages of Gondwana breakup. *Page 292 of:* Skinner, D. N. B. (ed), *8th International Symposium on Antarctic Earth Sciences, 5-9 July 1999, programme and abstracts.* Victoria University of Wellington, New Zealand.

Strand, K., Passchier, S., & Nasi, J. 2003. Implications of quartz grain microtextures for onset of Eocene/Oligocene glaciation in Prydz Bay, ODP Site 1166, Antarctica. *Paelaeogeography, Palaeoclimatology, Paleaoecology*, **198**, 101–112.

Suess, E. 1904. *The face of the earth (Das Antlitz der Erde).* Oxford University Press.

Symonds, P. A., Eldholm, O., Mascle, J., & Moore, G. F. 2000. Characeristics of Continental Margins. *Pages 25–63 of:* Cook, P. J., & Carleton, C. (eds), *Continental shelf limits: the legal and scientific interface.* Oxford University Press.

Talwani, M., & Eldholm, O. 1972. The continental margin off Norway: A geophysical study. *Geological Society of America Bulletin*, **83**, 3573–3606.

Talwani, M., & Eldholm, O. 1973. The boundary between continental and oceanic crust at the margin of rifted continents. *Nature*, **241**, 325–330.

Talwani, M., & Heirtzler, J. R. 1964. Computation of magnetic anomalies caused by two dimensional structures of arbitrary shape. *Computers in the Mineral Industries*, **9(1)**, 464–480.

Talwani, M., Worzel, J. L., & Landisman, M. 1959. Rapid computation for two dimensional bodies with application to the Mendocino submarine fracture zone. *Journal of Geophysical Research*, **64**, 19–59.

Talwani, M., Mutter, M., Houtz, R., & Konig, M. 1978. The Crustal Structure and Evolution of the Area Underlying The Magnetic Quiet Zone on the Margin South of Australia. *Pages 151–175 of:* watkins, J., Montadert, L., & Dickenson, P. (eds), *Geological and Geophysical Investigations of Continental Margins. Memoirs. American Association of Petroleum geologists. 29.* AAPG.

Tanahashi, M., Saki, T., Oikawa, N., & Sato, S. 1987. An Interpretation of the Multichannel Seismic Reflection Profiles across the Continental Margin of the Dumont d'Urville Sea, off Wilkes Land, east Antarctica. *Pages 1–13 of:* Eittreim, S. L., & Hampton, M. A. (eds), *The Antarctic Continental Margin Geology and Geophysics of Offshore Wilkes Land.* Houston, Texas, USA: Circum-Pacific Council for Energy and Mineral resources.

Tanahashi, M., Eittreim, S., & Wannesson, J. 1994. Seismic stratigraphic sequences of the Wilkes Land margin. *Terra Antarctica*, **1**, 391–393.

Tanahashi, M., Ishihara, T., Yuasa, M., Murakami, F., & Nishimura, A. 1997. Preliminary reoport of the TH95 geological and geophysical survey results in the Ross Sea nd Dumont D'Urville Sea. *Pages 36–58 of: Proceedings NIPR Symp. Antarctic Geoscience*. NIPR.

Taylor, B., Goodliffe, A., Martinez, F., & Hey, R. 1995. Continental rifting and initial sea-floor spreading in the Woodlark basin. *Nature*, **374**, 534–537.

Telford, W. M., Geldart, L. P., & Sherriff, R. E. 1990. *Applied Geophysics: Second Edition*. Cambridge University Press.

ten Brink, U. S., Schneider, C., & Johnson, A. H. 1995. Morphology and stratal geometry of the Antarctic Continental Shelf: Insights from models. *Pages 1–25 of:* Cooper, A. K., Barker, P. F., & Brancolini, G. (eds), *Geology and Seismic Stratigraphy of the Antarctic Margin: Antarctic Research Series, Volume 68*. American Geophysical Union.

ten Brink, U. S., Hackney, R. I., Bannister, S., Stern, T. A., & Makovsky, Y. 1997. Uplift of the Transantarctic Mountains and the bedrock beneath the East Antarctic ice sheet. *Journal of Geophysical Research*, **102, B12**, 27,603–27,621.

Tikku, A. A., & Cande, S. C. 1999. The oldest magnetic anomalies in the Australian-Antarctic Basin: Are they isochrons? *Journal of Geophysical Research*, **104, B1**, 661–677.

Tingey, R. J. 1991a. Mesozoic tholeiitic igneous rocks in Antarctica: The Ferrar (Super) Group and related rocks. *Pages 153–170 of:* Tingey, R. J. (ed), *The Geology of Antarctica*. Clarendon Press, Oxford.

Tingey, R. J. 1991b. The Regional Geology of Archaean and Proterozoic rocks in Antarctica. *Chap. GEBCO, pages 1–58 of:* Tingey, R. J. (ed), *The Geology of Antarctica*. Clarendon Press, Oxford.

Totterdell, J. M., & Bradshaw, B. E. 2004. The structural framework and tectonic evolution of the Bight Basin. *Pages 41–61 of:* Boult, P. J., Johns, D. R., & Lang, S. C. (eds), *Eastern Australasian Basins Symposium II*. Petroleum Exploration Society of Australia.

Totterdell, J. M., & Krassay, A. A. 2003. *Sequence stratigraphic correlation of onshore and offshore Bight Basin successions*. Geoscience Australia Record.

Totterdell, J. M., Blevin, J. E., Struckmeyer, H. I. M., Bradshaw, B. E., Colwell, J. B., & Kennard, J. M. 2000. A new sequence framework for the Great Australian Bight: starting with a clean slate. *APPEA Journal*, **4**, 95–117.

Tsumaraya, Y., Tanahashi, M., Saki, T., Machihara, T., & Asakura, N. 1985. Preliminary report of the marine geophysical and geological surveys off Wilkes Land, Antarctica in 1983-1984. *Pages 48–62 of: Memoirs of National Institute of Polar Research Issue 37*. National Institute of Polar Research, Japan.

Tucholke, B. E., & Lin, J. 1994. A geological model for the structure of ridge segments in slow spreading ocean crust. *Journal of Geophysical Research*, **99**, 11,937–11,958.

Vail, P. R., Mitchum, R. M., & Thompson, S. 1977. Seismic stratigraphy and global changes of sea level, 4. *Pages 83–97 of: Seismic Stratigraphy-Application to Hydrocarbon Exploration.* American Association of Petroleum Geology Memoirs.

van der Beek, P. S., Cloetingh, S., & Andriessen, P. 1995. Mechanisms of extionsional basin formation and vertical motion at rift flanks: constraints from tectonic modeling and fission track thermochronology. *Earth and Planetary Science Letters*, **121**, 417–433.

Veevers, J. J. 1982. Austrlian-Antarctic depression from the mid-ocean to adjacent continents. *Nature*, **295(5847)**, 315–317.

Veevers, J. J. 1986. Breakup of Australia and Antarctica estimated as mid-Cretaceous (95Ma) from magnetic and seismic data at the continental margin. *Earth and Planetary Science Letters*, **77**, 91–99.

Veevers, J. J. 1987. The Antarctic Continental Margin Geology and Geophysics of Offshore Wilkes Land. *Pages 45–73 of:* Eittreim, S. L., & Hampton, M. A. (eds), *The Antarctic Continental Margin Geology and Geophysics of Offshore Wilkes Land.* Houston, Texas, USA: Circum-Pacific Council for Energy and Mineral resources.

Veevers, J. J., Stagg, H. M. J., Willcox, J. B., & Davies, H. L. 1990. Pattern of slow seafloor spreading (<4 mm/year) from breakup (96 Ma) to A20 (44.5 Ma) off the southern margin of Australia. *BMR Journal of Australian Geology and Geophysics*, **11**, 499–507.

Veevers, J. J., McA. Powell, C., & Roots, S. R. 1991. review of seafloor spreading around Australia. I. Synthesis of the patterns of spreading. *Australian Journal of Earth Sciences*, **38**, 373–389.

Vening Meinesz, F. A. 1932. Comments on Isostasy. *Page 27 of:* Bowie, W. (ed), *Comments on Isostasy.* National Research Council.

Vine, F. J., & Matthews, D. H. 1963. Magnetic anomalies over oceanic ridges. *Nature*, **199**, 947–949.

Vogt, P. R., Anderson, C. N., Bracey, D. R., & Schneider, E. D. 1970. North Atlantic magnetic smooth zones. *Journal of Geophysical Research*, **75**, 3955–3968.

Volpi, V., Camerlenghi, A., Hillenbrand, C. D., Rebesco, M., & Ivaldi, R. 2003. The effect of biogenic silica on sediment consolidation and slope instability, Pacific margin of the Antarctic Peninsula. *Basin Research*, **15**, 339–354.

Walcott, R. 1972. Gravity, flexure, and the growth of sedimentary basins at a continental edge. *Geol. Soc. Am. Bull.*, **83**, 1845–1848.

Walcott, R. 1973. Structure of the Earth from glacio-isostatic rebound. *Annual Review of Planetary Physics*, 15–38.

Wannesson, J., Pelras, M., Petitperrin, B., Perret, M., & Segoufin, J. 1985. A geophysical transect of the Adelie Margin, East Antarctica. *Marine and Petroleum Geology*, **2**, 192–201.

Watts, A. B. 1978. An analyisis of isostasy in the world's oceans: 1. Hawaiian-Emperor Seamount Chain. *Journal of Geophysical Research*, **83**, 5989–6004.

Watts, A. B. 1988. Gravity anomalies, crustal structure and flexure of the lithosphere at the Baltimore Canyon Trough. *Earth and Planetary Science Letters*, **89**, 221–238.

Watts, A. B. 2001. *Isostasy and Flexure of the Lithosphere*. Cambridge University Press.

Watts, A. B., & Burov, E. B. 2003. Lithospheric strength and its relationship to the elastic and seismogenic layer thickness. *Earth and Planetary Science Letters*, **213**, 113–131.

Watts, A. B., & Fairhead, J. D. 1997. Gravity anomalies and magmatism along the western continental margin of the British Isles. *Journal of the Geological Society of London*, **154**, 523–529.

Watts, A. B., & Fairhead, J. D. 1999. A process-oriented approach to modeling the gravity signature of continental margins. *The Leading Edge*, **Feb**, 258–263.

Watts, A. B., & Marr, C. 1995. Gravity anomalies and the thermal and mechanical structure of rifted continental margins. *Pages 65–94 of:* et al., E. Banda (ed), *Rifted Ocean-Continent Boundaries*. Kluwer Academic Publishers.

Watts, A. B., & Ryan, W. B. F. 1976. Flexure of the lithosphere and continental margin basins. *Tectonophysics*, **36**, 25–44.

Watts, A. B., & Torné, M. 1992. Subsidence history, crustal structure and thermal evolution of the Valencia Trough: A young extensional basin in the western Mediterranean. *Journal of Geophysical Research*, **97**, 20,021–20,041.

Watts, A.B., & Stewart, J. 1998. Gravity anomalies and the segmentation of the continental margin offshore West Africa. *Earth and Planetary Science Letters*, **156**, 239–252.

Watts, A.B., Karner, G.D., & Steckler, M.S. 1982. Lithospheric flexure and the evolution of sedimentary basins. *Philosophical Transactions of the Royal Society of London*, **305**, 249–281.

Wegener, A. 1912. Die Enstehung der Kontinente. *Petermanns Mitteilungen*, 185–195,253–256,305–309.

Wegener, A. 1915. *Die Ehtstehung der Kontinente*. Friedrich Vieweg & Sohn. (*First English translation in 1924 from the 3rd (1922) German edition*).

Weissel, J. K., & Hayes, D. E. 1971. Asymmetric Seafloor Spreading South of Australia. *Nature*, **231(5304)**, 518–522.

Weissel, J. K., & Hayes, D. E. 1972. Magnetic anomalies in the Southeast Indian Ocean. *Page 196 of:* Hayes, D. E. (ed), *Antarctic Oceanology II. The Australian-New Zealand Sector.* American Geophyscial Union, Antarctic Research Series, 19.

Weissel, J. K., & Hayes, D. E. 1974. The Australian-Antarctic Discordance: New results and Implications. *Journal of Geophysical Research*, **79(17)**, 2579–2587.

Weissel, J. K., & Karner, G. D. 1989. Flexural uplift of rift flanks due to mechanical unloading of the lithosphere during extension. *Journal of Geophysical Research*, **94**, 13,919–13,950.

Weissel, J. K., Hayes, D. E., & Herron, E. M. 1977. Plate tectonics synthesis, the displacements between Australia, New Zealand, and Antarctica since the Late Cretaceous. *Marine Geology*, **25**, 231–277.

Wernicke, B. 1985. Uniform-sense normal simple shear of the continental lithosphere. *Canadian Journal of Earth Science*, **22**, 108–125.

White, R. S. 1984. Atlantic oceanic crust: Seismic structure of a slow spreading ridge. *Pages 34–44 of:* Gass, I. G., Lippard, S. J., & Shelton, A. W. (eds), *Ophiolites and oceanic lithosphere.* Geological Society of London.

White, R. S., & McKenzie, D. 1989. Magmatism at rift zones: the generation of volcanic continental margins and flood basalts. *Journal of Geophysical Research*, **94**, 7685–7729.

White, R. S., McKenzie, D., & O'Nioins, R. K. 1992. Oceanic crustal thickness from seismic measurements and rare earth element inversions. *Journal of Geophysical Research*, **97(B13)**, 19,683–19,715.

Willcox, J. B. 1978. The Great Australia Bight - a regional interpretation of graivty, magnetic, and seismic data from the Continental Margin Survey. *Bureau of Mineral Resources, Australia. Report 201.*

Willcox, J. B., & Stagg, H. M. J. 1990. Australia's southern margin: a product of oblique extension. *Tectonophysics*, **173**, 269–281.

Willcox, J. B., Baillie, P., Exon, N., Lee, C. S., & Thomas, B. 1989. *The geology of western Tasmania and its continental margin - with particular reference to petroleum potential.* Geoscience Australia Record.

Wilson, R. C. L., Manatschal, G., & Wise, S. 2001. Rifting along non-volcanic passive margins: stratigraphic and seismic evidence from the Mesozoic successions of the Alps and western Iberia. *Pages 429–452 of:* Wilson, R. C. L., Whitmarsh, R. B., Taylor, B., & Froitzheim, N. (eds), *Continental Margins: A Comparison of Evidence from Land and Sea. Special Publication 187.* London: Geological Society London.

Worzel, J. L. 1968. Advances in marine geophysical research of continental margins. *Can. J. Earth Sci.*, **5**, 963–983.

Wyer, P. 2003. *Gravity anomalies and segmentation of the Eastern USA passive continental margin*. Ph.D. thesis, University of Oxford, U. K. unpublished.

Yilmaz, Ö. 2001. *In:* Doherty, S. M. (ed), *Seismic Data Analysis: Processing, Inversion, and Interpretation of Seismic Data*. SEG, Investigations in Geophysics, No. 10.

Yuasa, M., Niida, K., Ishihara, T., Kisimoto, K., & Murakami, F. 1997. Peridotite Dredged from a Seamount off Wilkes Land, the Antarctic: Emplacement of Fertile Mantle Fragment at Early Rifting Stage between Australia and Antarctica during the Final Breakup of Gondwanaland. *Pages 725–730 of:* Ricci, C. A. (ed), *The Antarctic Region: Geological Evolution and Processes*. Terra Antarctica.

Zachos, J. C., Quinn, T. M., & Salamy, K. A. 2001. Trends, rhythms, and aberrations in global climate 65 Ma to present. *Science*, **292**, 251–266.

Appendix A

USGS Survey L184 Seismic Reflection Data Processing

A.0.4 Processing Sequence Summary

In the following sections a typical processing sequence (e.g. Yilmaz [2001]) is tested and demonstrated on L184 survey data. Data were processed from field SEGY to fully time migrated sections using *ProMAX (v1998.6)*. Acquisition parameters and the original processing sequence applied are outlined in Chapter 3.

A.1 Survey L184 Data Processing

A.1.1 Preprocessing

Data received for this study had been transcribed from field tapes, demultiplexed and re-written as SEGY. Subsequently, the significant preprocessing steps remaining to be applied were field geometry setup, deep-water delay (DWD) correction, trace editing, and geometric spreading correction.

Field Geometry Setup

Limited field geometry information was included within the SEGY headers of these data. Separate navigation files including location and time information were provided separately as ASCII text files. Thus, shot and receiver locations prescribed during the geometry setup were relative only. CMP binning was performed and the relative locations of CMPs assigned based on shot-receiver geometries initialised during setup. The CMP binning process assigns all traces at the midpoint of a given shot-receiver pair to one CMP.

Deep Water Delay Correction

Data were recorded in water depths varying from less than 400 m (∼0.5 sec TWT) to over 4000 m (∼5 sec TWT) during this survey. Data acquired in deeper water had a deep water delay (DWD) of 1-3 s applied, this simply delays the start of data recording after shot firing. The DWD was recorded in the observer's log and could be easily confirmed via single trace analyses. A near trace display of the data prior to DWD correction is shown in Figure A.1, the water bottom reflection is offset at a number of shot locations by 1 s intervals.

To correct for the DWD, and ensure that the water bottom was not offset for each change in the DWD, static corrections were applied. The amount of the DWD was added to each section of the line it was applied to, however, firstly the record length was increased by the magnitude of the maximum DWD to ensure that no data were lost once the record start point was reset. The correction transforms the variably offset water bottom reflector to its true TWT position (Figure A.1).

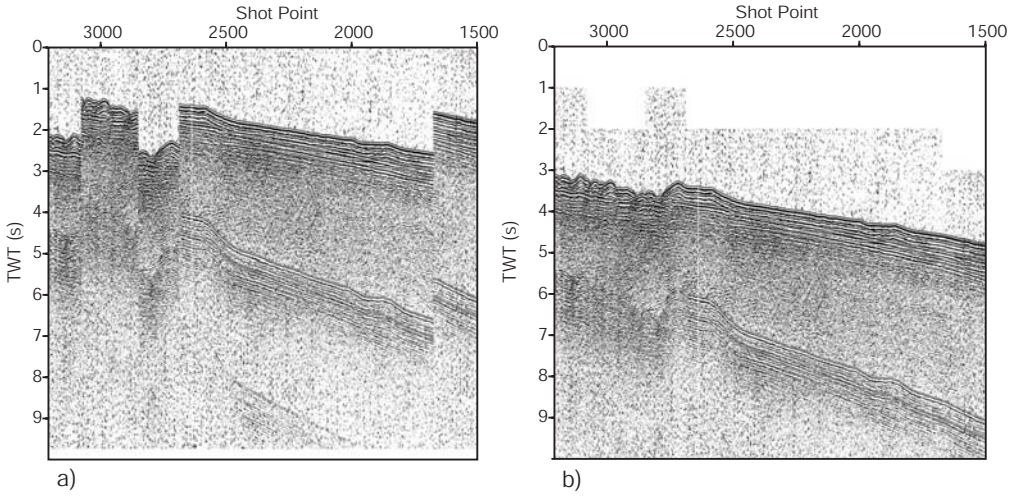

Figure A.1: Near trace display (channel 1) a) before correction, and b) after correction of the deep-water delay (DWD).

Trace Editing

Trace data were edited to remove noisy and/or spiky traces and to check that no traces had been recorded with reverse polarity. Trace statistics were calculated for the entire raw trace dataset to assist in the editing process. They allow statistical outliers, typically associated with traces exhibiting high noise levels and spikes, to be identified without checking every trace individually.

The interactive trace statistic analysis used to locate noisy traces is illustrated in Figure A.2. The histograms represent energy decay, first-break energy, dominant data frequency, frequency deviation, pre first-break average energy, pre first-break average frequency, average trace energy, and spikiness. The mean and standard deviation of these quantities are also displayed on the histograms. The data frequency and average trace energy histograms were most useful in interactively selecting traces which were particularly noisy or spiky. Undesired traces were deleted from the dataset.

True Amplitude Recovery

Seismic energy decays as it propagates from its source. In a homogeneous halfspace energy is lost due to both spherical divergence (frequency independent) and attenuation (frequency dependent) [Yilmaz, 2001]. The Earth generally acts as a low pass filter and attenuates higher frequency signals most rapidly. Seismic energy decreases proportional to $1/r^2$ and amplitude proportional

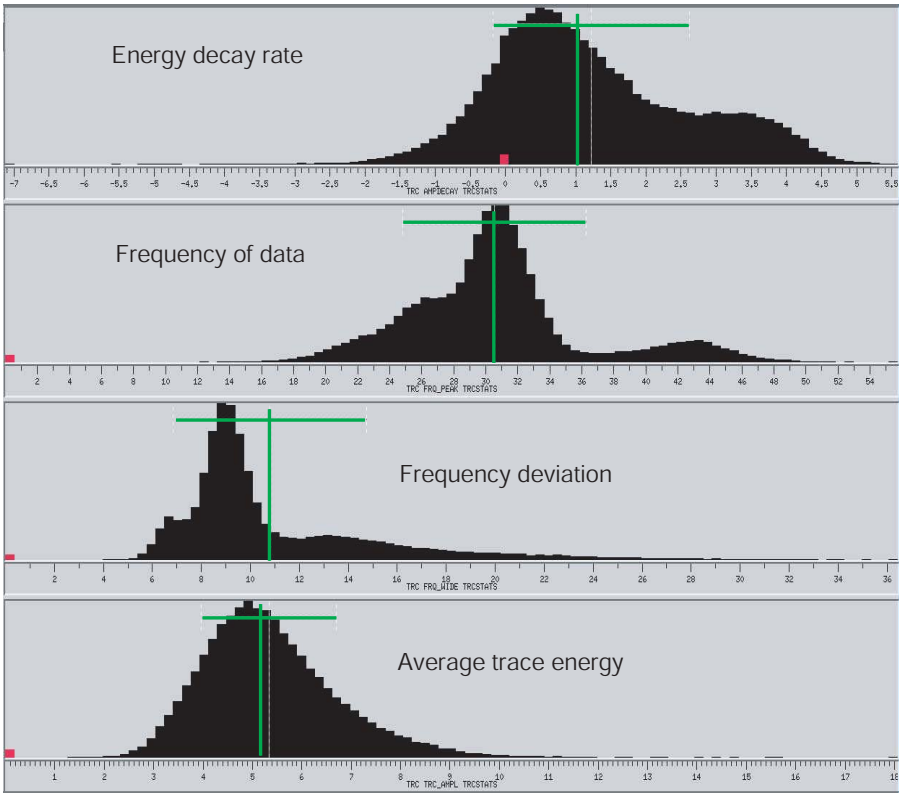

Figure A.2: Analysis of the trace statistics (calculated using the *ProMAX* database statistics functionality) for the entire seismic line allows statistically outlying traces to be interactively selected and edited. Histograms represent different trace attribute variations of amplitude, frequency and energy as labelled. Vertical green lines represent the mean and horizontal green lines show the standard deviation. The red traces have been selected from the entire dataset (black) and can be viewed in a different but interactively connected window.

to $1/r$, where r is the radius of the wavefront. True Amplitude Recovery (TAR) is a process applied to seismic data to compensate for these effects.

For a layered Earth, amplitude decay is a function of the RMS velocity of primary reflections and the two-way travel time (TWT); it can be described approximately by $1/(v^2.t)$, where t is the TWT and v is the RMS velocity at time t [Newman, 1993]. This function was used to correct for spherical divergence in this dataset.

TAR was first applied to all shot data using a simple, assumed velocity function. Due to the high energy multiple reflections affecting this dataset TAR was applied to a depth such that amplitude recovery was not performed on or below the water bottom multiple. To apply TAR only above the water bottom multiple ensures that the high energy multiple is not amplified further through the application of this time dependent gain function. Selected shot gathers following the application of spherical divergence correction are shown in Figure A.3. Primary reflection amplitude is increased. However, undesirable noise in the data is also boosted. As

higher frequencies are also subject to greater attenuation by the Earth, the recovery of higher frequency data is not as successful as for lower frequencies.

This initial TAR function was removed following velocity analysis and repeated with the interpreted RMS velocity structure. The imaging differences associated with this change are relatively minor.

A.1.2 Pre-Stack Processing

Deconvolution

The signal recorded in seismic reflection surveying is a function of the source wavelet, the Earth impulse response function, and random background noise [Yilmaz, 2001]. The convolution model for seismic reflections can be expressed as,

$$x(t) \quad = \quad w(t) * e(t) + n(t)$$

where *x(t)* denotes the recorded seismic signal, *w(t)* is the seismic source wavelet, *e(t)* is the Earth response function, *n(t)* represents random noise, and the * denotes convolution in the time domain or multiplication in the frequency domain.

The Earth impulse response function imposes some undesirable effects on the data such as attenuation (particularly of higher frequencies) and multiple reflections. Deconvolution attempts to recognise these effects as linear filters and apply appropriate inverse filters to remove them. Deterministic inverse filtering is only applicable where the form of the seismic source wavelet is known explicitly and it is assumed to propagate through the subsurface without distortion. When the form of the source wavelet is unknown more sophisticated deconvolution techniques, such as predictive deconvolution, are required [Yilmaz, 2001].

Predictive deconvolution attempts to predict repeated sequences in a given time series associated with the form of the original source signal. It is assumed the components of the signal to be removed (i.e. original source signature and noise) follow a repeatable pattern with a linear offset or lag. Applying predictive deconvolution requires the definition of three main parameters
i) one or many time gates over which to apply the deconvolution,
ii) the active operator length, and
iii) the gap or minimum lag.
The choice of the deconvolution gate length defines how much of the original time series is deconvolved. An optimum time gate excludes the early parts of any record affected by energy from direct arrivals and also the deeper parts of a record where incoherent noise dominates.

There is no theoretical minimum or maximum operator length which controls the limits of this parameter [Hatton *et al.*, 1986]. Short operators often yield spikey amplitude spectra. Whereas, amplitude spectra created with longer operators begin to approximate the spectrum of the impulse response. However, increasing operator length does not indefinitely improve the success of deconvolution; typically more and more spurious spikes are actually introduced beyond some optimum operator length [Yilmaz, 2001]. Selecting an appropriate operator length can be quantitatively assessed by examining autocorrelograms of the recorded seismic wavelet. The autocorrelation of the unknown source wavelet should resemble the first transient zone in the

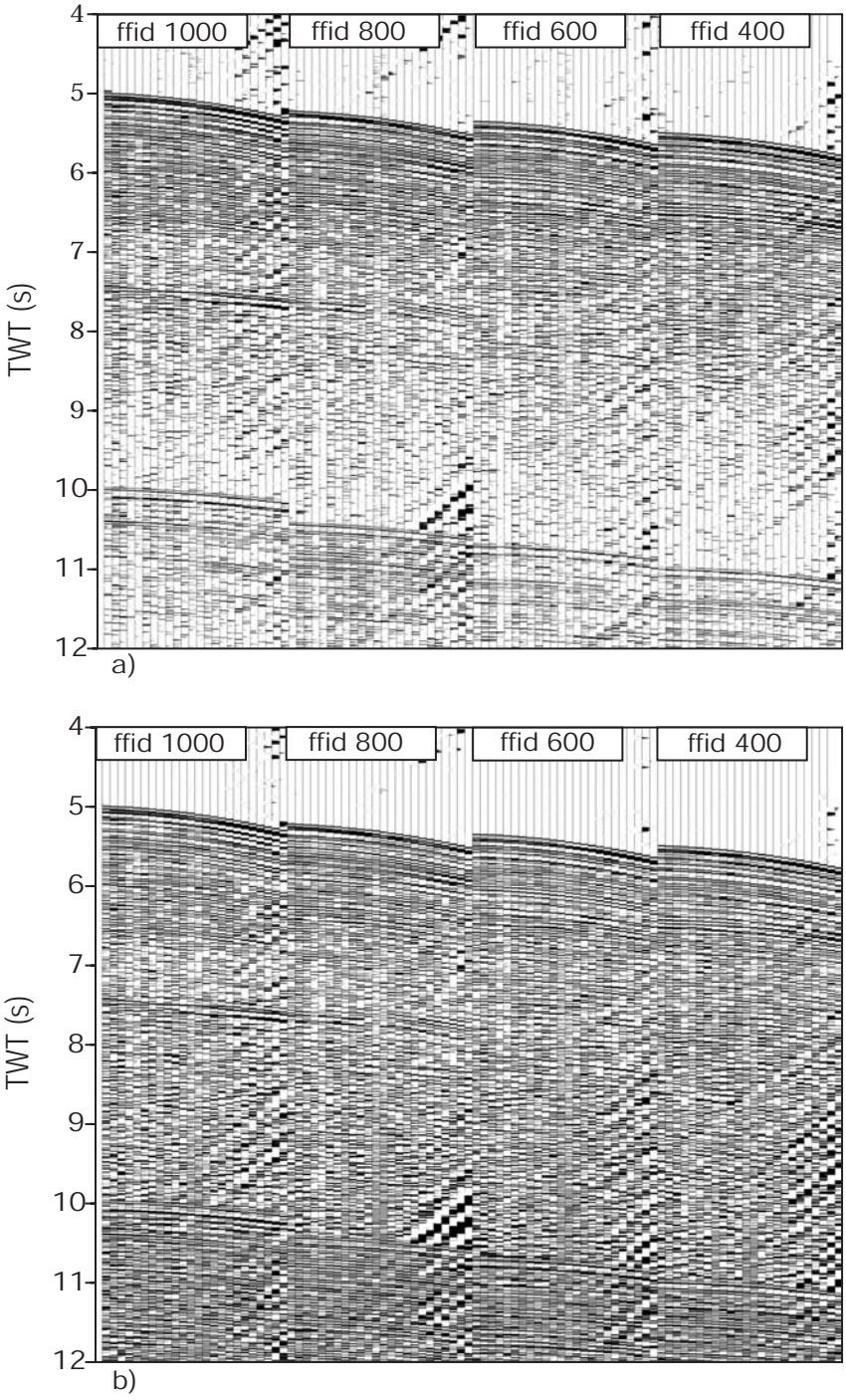

Figure A.3: Comparison of four shot gathers (ffid = field file identifier) a) before any correction for spherical divergence, and b) following the application of true amplitude recovery (TAR) to correct for spherical divergence. Noise and signal are both amplified by this gain function.

autocorrelation [Yilmaz, 2001]. Hence, if the extent of the seismic source wavelet can be inferred then an operator length can be chosen to include only autocorrelation lags associated with the seismic source wavelet. In practice then, the operator length is generally chosen to include the first distinct energy packet in the autocorrelation.

Analyses of autocorrelograms allows an absolute minimum operator length of 100 ms to be inferred. However, it is likely that in practice the optimal operator length is greater than 100 ms.

Prediction lag controls the resolution of the deconvolution output and the power distribution of the output frequency spectrum. A unit prediction lag, that is where the prediction lag is chosen to be equal to the sampling interval (2 ms for this dataset), is equivalent to spiking deconvolution and implies the highest resolution. Any larger prediction lag implies less than full resolution. In reality, the signal-to-noise ratio controls how close to unity the prediction lag can be forced [Yilmaz, 2001]. Deconvolved signals using a unit prediction lag contain high frequencies, this may actually degrade signal-to-noise ratios in situations where high frequency energy is mostly noise [ProMAX, 1998b]. As the prediction lag is increased the amplitude spectra become increasingly band-limited and approximate more closely the input wavelet, i.e. the deconvolution process has no effect on the data.

The effect of varying the prediction lag from unity to approximately equal to operator length is demonstrated by the power spectra shown in Figure A.4. A unit lag operator length (2 ms) creates a very broadband deconvolved power spectrum with significant spikiness. Similarly, a lag of 6 ms fails to remove major spikes in the output spectrum between 20-40 Hz and fails to preserve the overall spectral shape of the input data. The very long prediction lag of 90 ms has little effect on the data, the output power spectrum for this lag resembles the control power spectra. The optimum prediction lag is ∼20-30 ms, for these lag values the high frequency end of the spectrum is suppressed, spikiness is decreased from the original power spectra, and the overall shape of the input power spectra is maintained.

Varying the operator length, using a constant prediction lag, has a lesser relative effect on the deconvolved power spectra. Figure A.5 illustrates the effect of varying the deconvolution operator length from 100-500 ms. The power spectra indicate that the output is largely inssensitive to changes in operator length between 200-400 ms. An operator length of 100 ms does not boost the power enough for some mid range frequencies leaving a relatively spikey output spectrum. Operators of 500 ms and greater begin to alter the input spectral range to an extent where unacceptable amounts of noise are introduced, boosting the power of higher frequency components.

Predictive deconvolution is required on this dataset as the airgun source signal was not explicitly recorded. A deconvolution time gate was defined every 25 shots and excludes data deeper than 8.5 sec TWT in the record and also excludes the earliest part of the signal in shallow water where direct wave energy is superimposed on primary reflected energy in the recorded signal. Analysis of the power spectra indicate appropriate parameters for the application of predictive deconvolution are an operator distance of 200-300 ms and a prediction lag of ∼24 ms.

Utilising the parameters indicated by the spectral analyses as initial values, a selection of CMP gathers were deconvolved and analysed in the time-space (t-x) domain. The imaging of CMP gathers in the t-x domain shows very little sensitivity to variations in operator length.

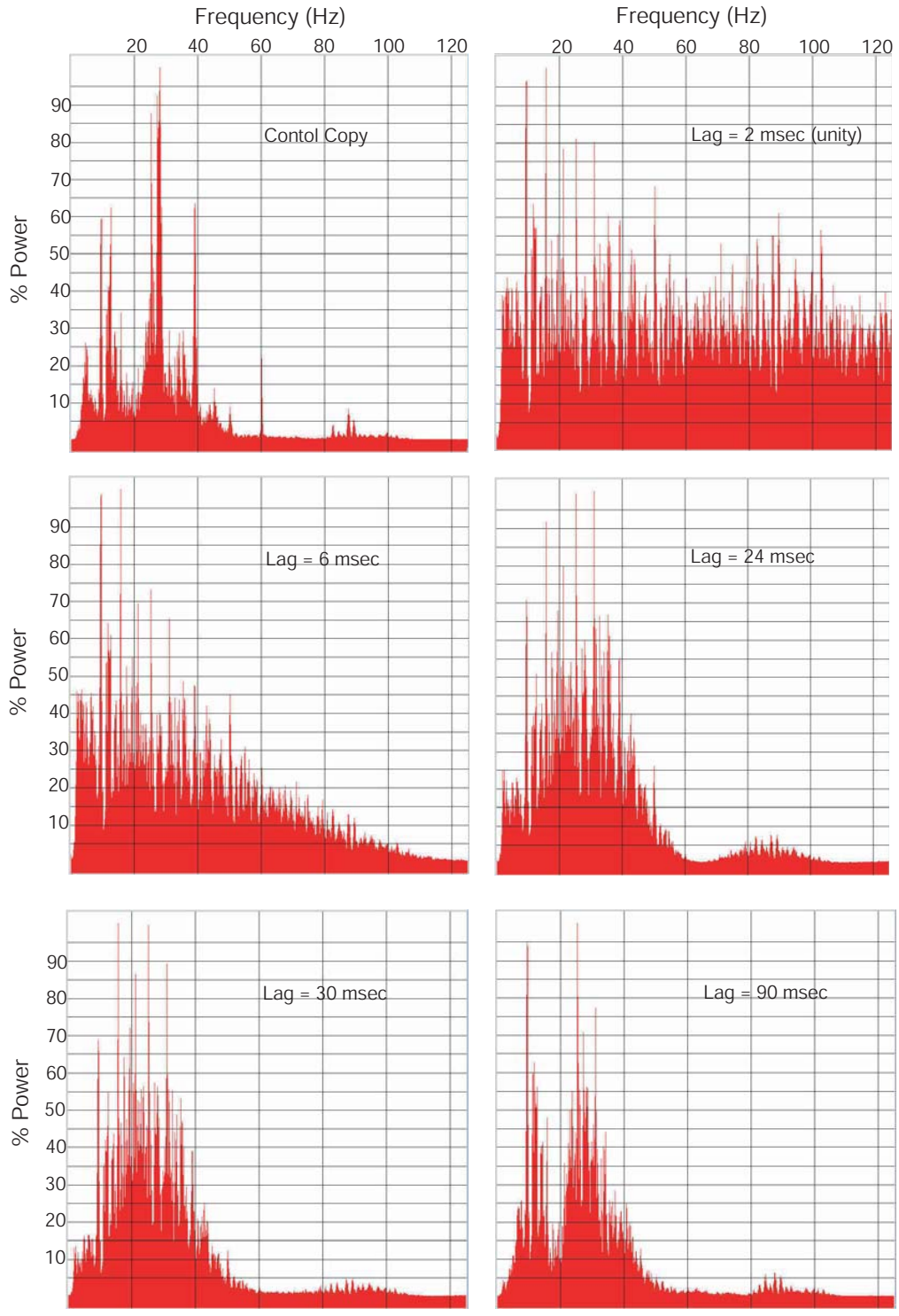

Figure A.4: Comparison at CMP 800 of original power spectra and five spectra calculated following predictive deconvolution with different prediction lag values and a constant operator distance of 200 ms. Short lags (i.e. unity) retain the significant spikiness of the original spectra, whereas long lags are band limited and do not significantly alter the original spectra. A lag distance of 24-30 ms is appropriate for these data.

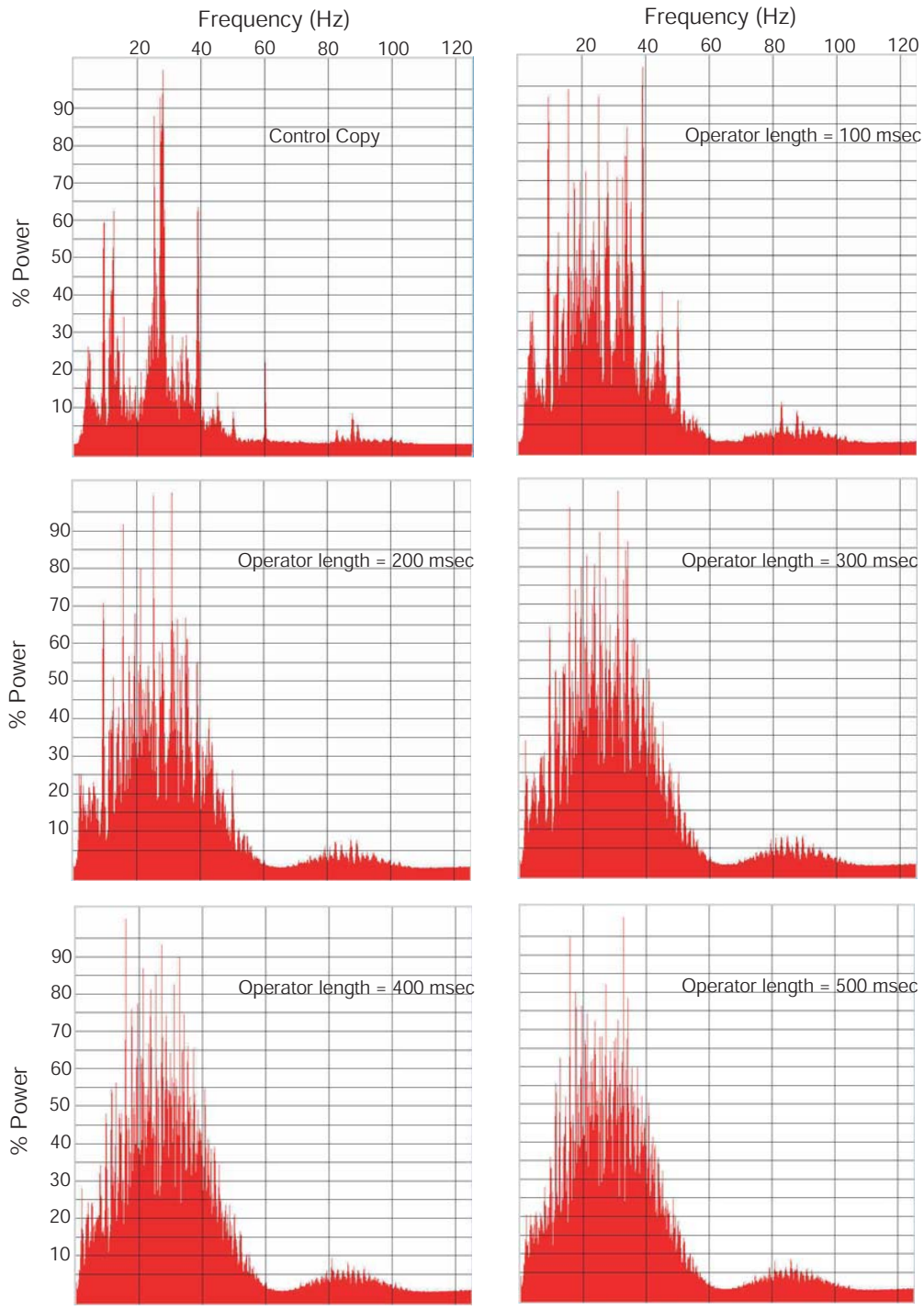

Figure A.5: Comparison at CMP 800 of original power spectra and five spectra calculated following predictive deconvolution with different operator distances and a constant prediction lag of 24 ms.

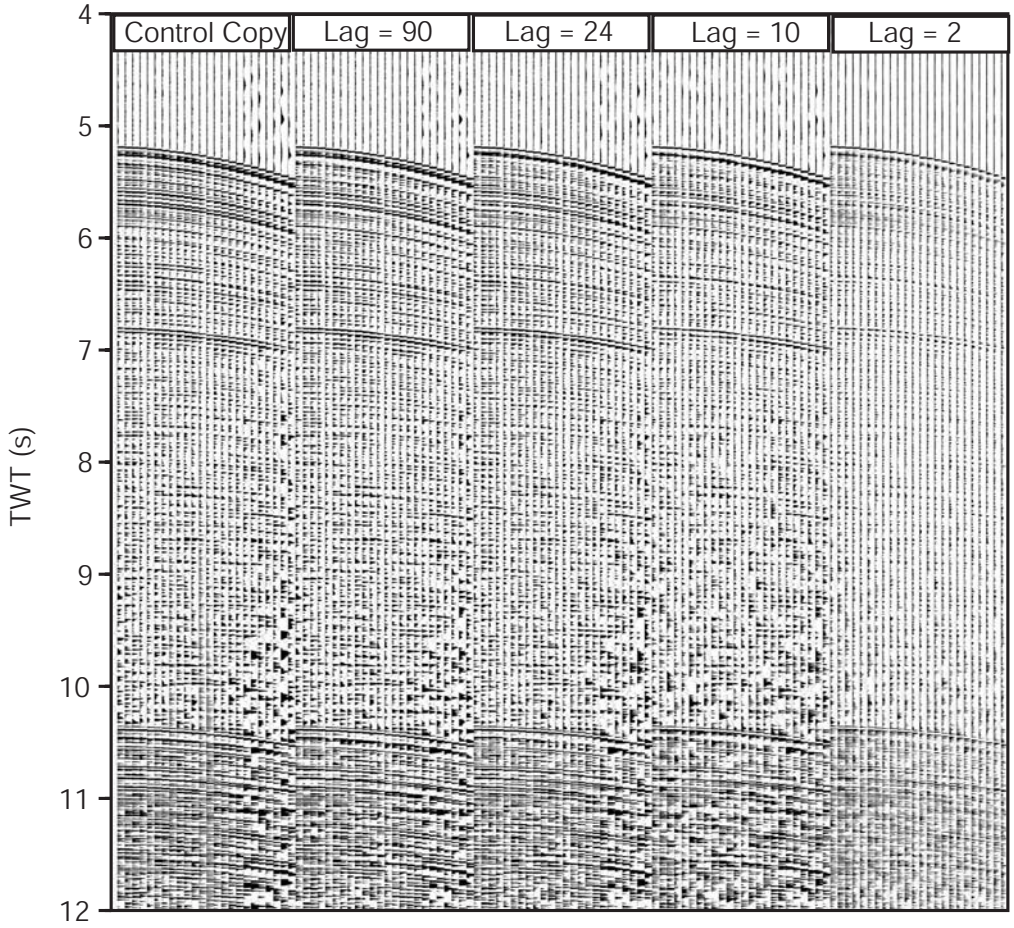

Figure A.6: Comparison of CMP 800 following deconvolution with prediction lags as labelled and an operator distance of 250 ms. Although imaging of the subtle differences is difficult, analysis of these gathers and corresponding amplitude spectra (Figure A.4) indicate a prediction lag of 24 ms provides the best data enhancement.

Variations in prediction lag have a greater impact on CMP gathers. Figure A.6 illustrates the effect on CMP 800 of varying prediction lag from 2-90 ms for an operator distance of 250 ms. The unity prediction lag does not enhance the signal amplitude relative to the noise and produces a 'washed-out' output gather. The 90 ms lag does not alter the imaging relative to the control copy, indicating that this lag is too great. Deconvolution applied with lags between 12-30 ms produce very similar output gathers, from this analysis alone it would be difficult to select an appropriate value for the prediction lag.

Imaging the subtle changes affected by altering prediction lag and particularly operator distance in shot gathers is very difficult. Utilising power spectra calculated for differing parameters provides a far more quantitative assessment of parameter selection. Following the parameter testing process, predictive deconvolution was applied to the entire line using an operator distance of 250 ms and a prediction lag of 24 ms.

Velocity analysis and Normal Moveout (NMO) correction

Semblance velocity analysis [Neidell & Taner, 1971] was carried out to create stacking velocity sections at regular intervals along each line. Stacking velocities allow correction of moveout associated with the hyperbolic moveout, in t-x space, of events associated with flat reflectors. Velocity analysis using semblance is based on the calculation of a velocity spectrum that represents a measure of signal coherency as a function of velocity and two-way zero offset time. A number of acquisition factors affect velocity analysis. Spread length has a significant control on velocity analysis as short streamers which do not provide far offset information exhibit little moveout and poor resolution in the velocity spectrum, this is particularly problematic at greater seafloor depths where moveout is the smallest. The fold of a dataset also constrains the resolution of the velocity spectrum, lower folds typically allow less accurate stacking velocity determination. Departures from hyperbolic moveout, generally associated with dipping reflectors, also negatively impact on the quality of velocity spectra [Yilmaz, 2001].

Semblance analyses were performed on super-gathers created by combining nine adjacent CMPs at a maximum spacing of four kilometres, more frequent analyses were completed in areas of rapid change in bathymetry or basement depth. The velocity spectrum typically shows high levels of coherence up until the arrival of the first water bottom multiple (Figure A.7). The short streamer of only 2400 m used to acquire this data and the fold of only 24 does not allow significant moveout differences between primary energy reflections and the water bottom multiple which makes accurately defining stacking velocities below this multiple reflection difficult. Refraction and wide-angle reflection velocity data were available on some lines from sonobuoys deployed during surveying [Childs & Stagg, 1987]. Where available these data were considered during semblance analyses to provide improved constraints.

Figure A.7 shows the semblance velocity analysis for CMP 640 without NMO applied, and with NMO applied using the displayed velocity profile. Typically, RMS velocity increases with depth. However, the semblance shows maximum coherence at relatively lower velocities at and below the arrival of the first water bottom multiple due to the greater energy contained in the water bottom multiple relative to primary reflections. Quality control of stacking velocities was carried out by applying NMO to the relevant CMP supergather as the velocities were picked. Further real time quality control was achieved by viewing the two-dimensional velocity field as it was created with a brute stack displayed in the background (Figure A.8). This allows spuriously high or low velocity picks to be readily identified and re-examined where necessary.

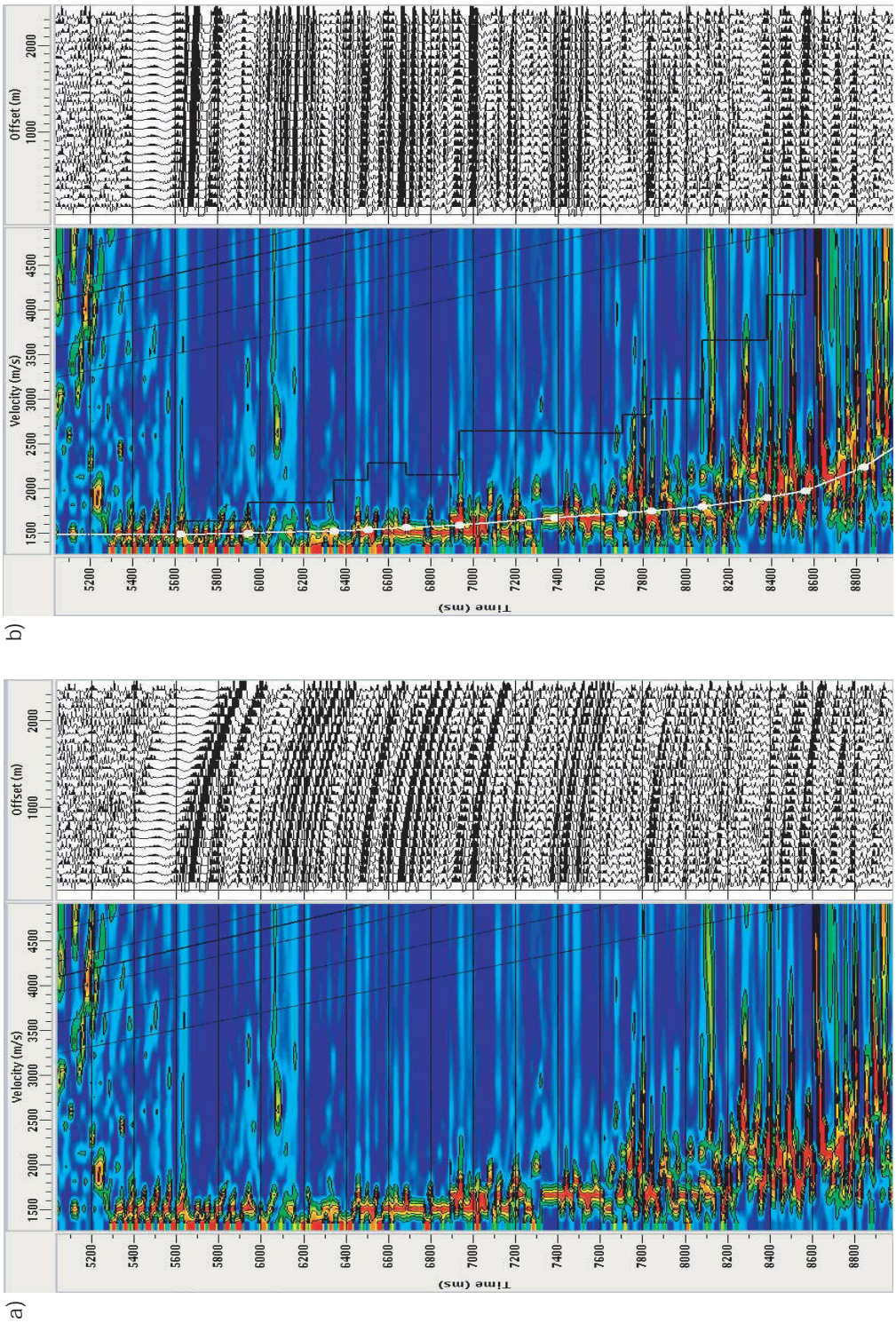

Figure A.7: a) Semblance analysis and corresponding CMP super-gather composed of 9 adjacent CMP gathers at CMP 640, and b) estimated velocity function, and NMO corrected CMP super gather. RMS velocity profile (white) and interval velocities, derived from conversion of RMS velocities using the Dix equation, (black) are shown.

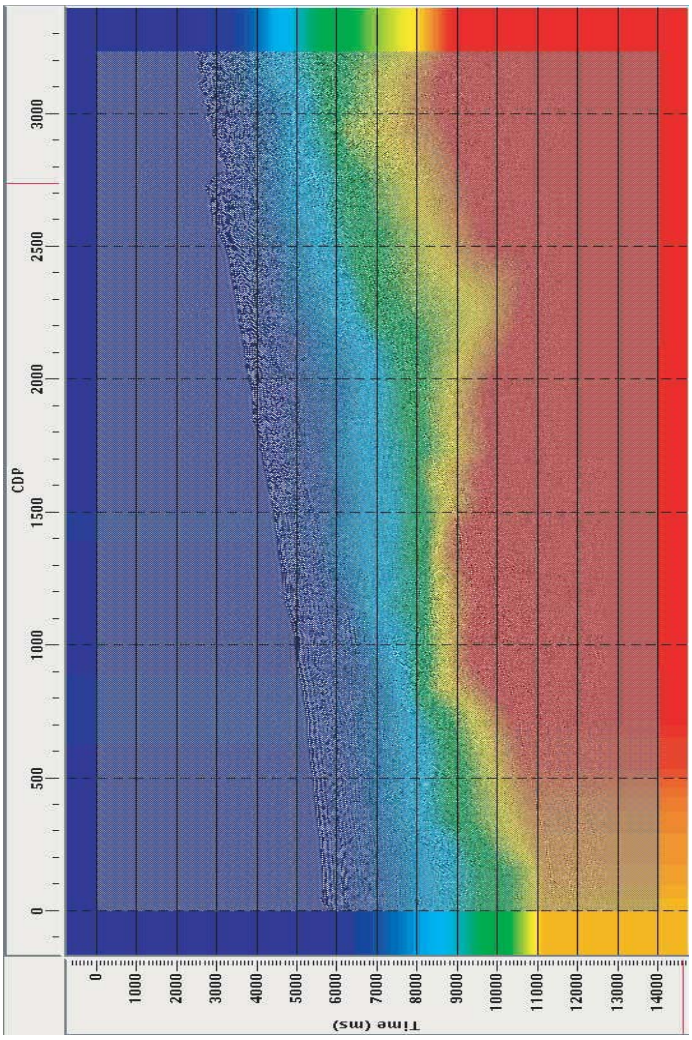

Figure A.8: Interactive velocity volume viewer used to quality control stacking velocities picked every 4 km. Colours represent velocity, red = 4000 m/s and blue = 1480 m/s. Brute stack of seismic data (calculated using an assumed velocity-depth profile) is visible as the image background.

The NMO correction was applied using the stacking velocities. The NMO correction applies a time variant stretching to each input trace to correct for offset and simulate a zero offset section. For a single horizontal layer the NMO correction is, after Yilmaz [2001]

$$\begin{aligned} \Delta t_{nmo} &= t(x) - t(0) \\ &= t(0)[(1 + [x/v_{nmo}t(0)]^2)^{0.5} - 1] \end{aligned}$$

where *t(x)* is the time at offset x, *t(0)* is the time at zero offset, and v_{nmo} is the normal moveout velocity.

As the NMO correction is a time dependent stretching of time data dimension, the frequency content of reflections can be altered, literally stretched from an actual wavelength to a greater apparent wavelength. The adverse effects of stretching are most apparent at early times for larger

offsets. To minimise the stretching effects of the NMO all samples in a gather for which stretching exceeds a threshold value of 30% were muted.

Dip Moveout

Dip moveout (DMO) is a form of partial prestack migration whereby each data sample is migrated to its zero offset position. This process collapses the smear associated with CMP stacking of dipping reflectors. Testing of DMO on these data indicates that very little benefit in data imaging is achieved through the application of this process. This is most likely a function of the geometry of the survey. The appropriate offset bin interval of 100 m (2×shot interval) [**?**] equals the channel spacing for this survey. Typically, offset bins would include more than 3 channels of data. Further DMO processing was not applied due to the minimal impact of this technique.

Common Mid Point (CMP) Stacking

Common midpoint (CMP) stacking is the single most important step in improving data imaging. The stacking process takes advantage of the acquisition practice of 'redundant recording', a process whereby a single point on any given reflector is imaged by multiple shot-receiver combinations, the number of these combinations is the fold of the data. Theoretically the signal to noise ratio is increased by a factor of $\sqrt{N}$ for a survey with an N-fold stack, however, in practice this value is always somewhat lower than $\sqrt{N}$ [Yilmaz, 2001]. A CMP stack is created by combining traces in each CMP gather to form a stacked trace at the midpoint location of that gather, and then combining (stacking) each of these CMP traces. The fold of the data in this survey was 24.

As well as increasing the signal to noise ratio, CMP stacking also attenuates coherent noise such as multiples. Multiples spend more of their travel time in the low velocity water column relative to primaries with the same arrival time, and hence usually have lower stacking velocities than the primaries and do not align on the NMO corrected gather, subsequently they are severely attenuated by the stacking process [Hatton *et al.*, 1986].

A.1.3 Post-Stack Processing

Post-Stack Deconvolution

Post stack deconvolution can improve data imaging for two main reasons. Firstly, it restores higher frequency components of the data which are attenuated by the CMP stacking process. Secondly, the stacked section approximates a zero-offset section, hence predictive deconvolution has the potential to compress the source wavelet more efficiently than when applied to CMP gathers [Yilmaz, 2001].

Parameter testing demonstrated that post stack deconvolution was again more sensitive to variation in prediction lag relative to changes in operator length. An operator distance of 250 ms was selected following testing of this parameter. A stacked section of 1000 CMP gathers (1500-2500) was deconvolved using a number of prediction lags of 2-90 ms, Figure A.9. It is not possible to optimally diplay each of the test panels in hardcopy without altering the gain and display settings between each panel, a process that would effectively remove the imaging differences resulting from deconvolution with different parameters. A lag of 2 ms introduces significant amounts of high frequency noise, particularly after the arrival of the first water bottom multiple. The sections deconvolved with lags of 10, 16 and 24 ms have similar results on the imaging quality of the section; the first water bottom multiple is suppressed relative to the control copy and the imaging of reflectors between 4-7 ms is also improved. The 90 ms lag is too long to have any noticeable effect on imaging relative to the control copy. A prediction lag of 16 ms and an operator length of 250 ms were selected for the deconvolution of the entire line.

Frequency Filtering

Application of frequency filtering is standard practice in seismic processing [Yilmaz, 2001]. It is applied here after deconvolution to remove noise introduced by the deconvolution process. Frequencies outside the 5-120 Hz range were not recorded during acquisition, thus, any signal outside of this range must be noise introduced by previous processing steps.

The frequency dependent absorption of seismic energy results in deeper arrivals comprising a lower frequency power peak relative to shallow arrivals. Hence, higher frequency bands of signal are confined to the shallow part of the section. The time-variant nature of the seismic signal bandwidth requires the application of frequency filters that are time variant. Time variant filters allow a band-pass filter with different frequency cut-offs to be applied to the data in different time sections. Typically the high frequency cut-off will be greater for shallow data, relative to deeper data which is subject to greater natural attenuation of high frequency data. Test panels, Figure A.13, illustrate the effect of varying the frequency pass gate of the band-pass filter. The optimally filtered test panel shows much greater reflector fidelity throughout the section. The individual reflectors in the upper sequence are more clearly defined and deep reflectors are much clearer due to the removal of high frequency noise at greater depths.

After analysis of test panels it was evident that a low frequency tapered cut-off from 5-12 Hz was appropriate for both the early and late time gates. The high frequency cut off tapered from 70-77 Hz in the upper time gate for optimal data enhancement. For the later time gate a lower

high frequency cut-off of 40-60 Hz was optimal. When applied to the entire line the filter was designed to be spatially variant as well as time variant to ensure that as the depth of the water bottom changed approximately the upper 3 s of data were included in the early time gate.

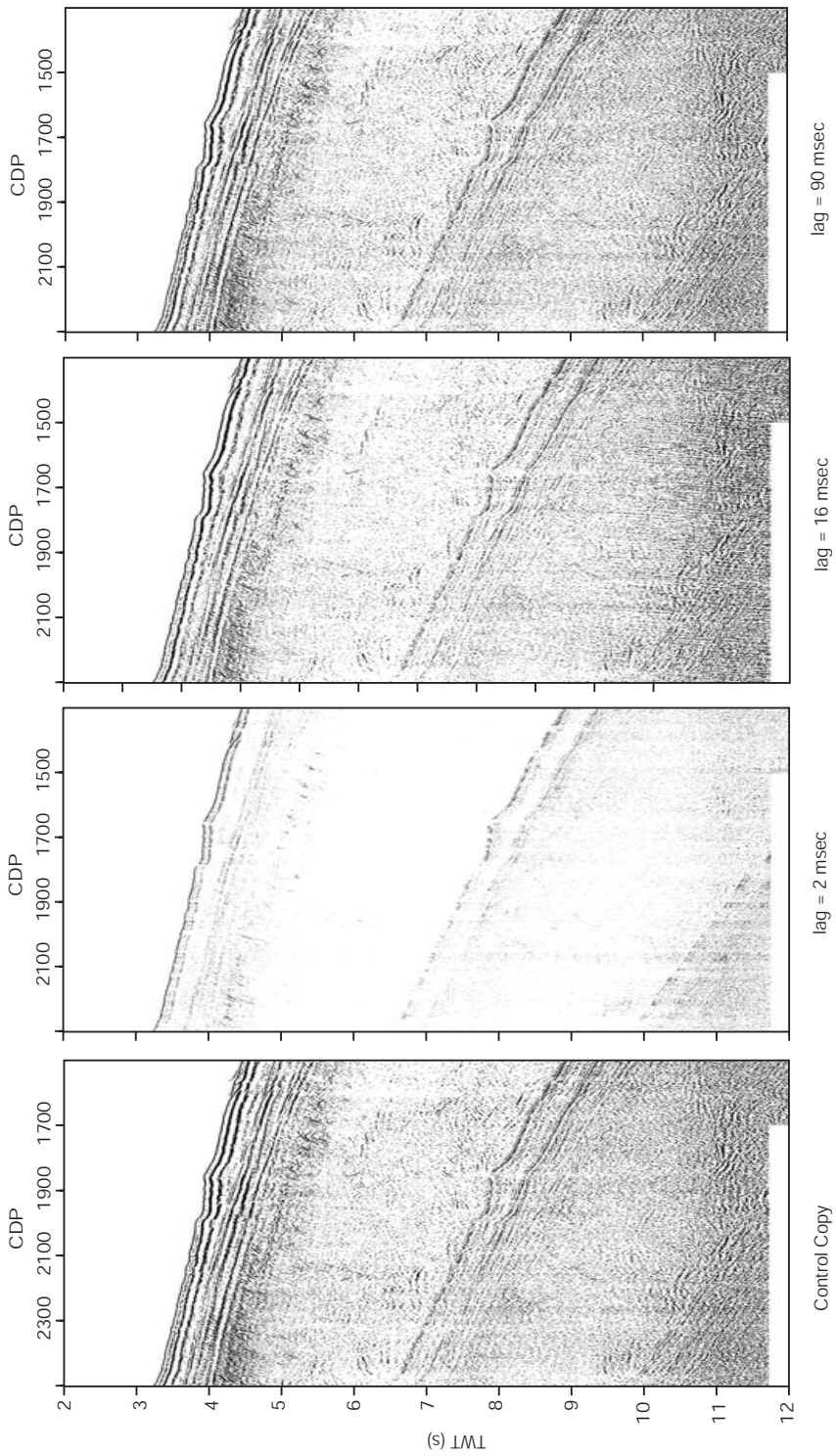

Figure A.9: Comparison of the effect of predictive deconvolution on a stacked section of line L184-5 utilising varying prediction lag lengths, as labelled. Display settings are equal for each panel resulting in non-optimal imaging for the 2 ms lag panel. A lag of between 10-24 ms provides best data imaging improvements.

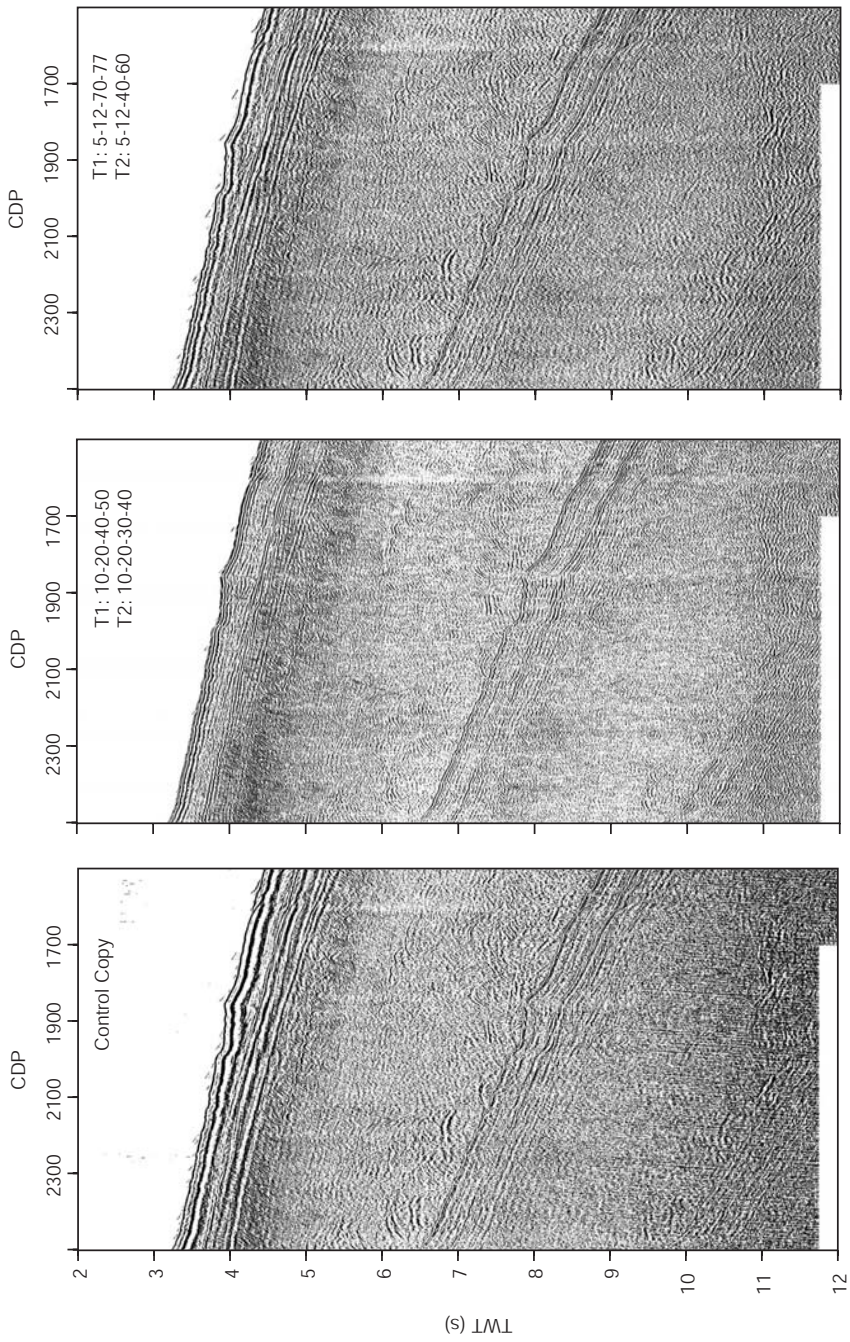

Figure A.10: Test panels for band-pass frequency filtering of CMP gathers 1500-2500. T1 and T2 are time gates from 0-6 s and 6-12 s respectively. The optimal frequency gates reduce the high frequency noise at later times without removing the high frequency signal component at early times.

A.1.4 Migration

Migration is typically the final step in a standard seismic processing sequence. The two major aims of migration are, i) to position reflectors in their correct subsurface position in t-x space, and ii) to collapse diffractions associated with geological discontinuities [Yilmaz, 2001]. Migration attempts to correct the position of reflectors by compensating for the assumption in the CMP stacking process that all reflectors are horizontal and continuous. Obviously in a geologic environment all reflectors do not meet these assumptions and are subsequently imaged in an incorrect subsurface location.

Using simple geometric constructions it can be shown that a number of basic principles are always true of migrated data. The dip angle of the reflector in a geological section is greater than in the recorded time section, that is; migration steepens reflectors. The length of a reflector in a geological section is shorter than in a time section, that is; migration shortens reflectors. A reflector in a geologic section is positioned up dip of its image in a time section, hence; migration moves reflectors up dip.

Accurate velocity information is paramount to the effectiveness of the migration process. Typically a means of direct velocity analysis, independent from the indirect velocities of semblance analysis (i.e. refraction or sonic logs) is utilised in creating the velocity field for migration. This is particularly true of depth migration. As semblance analysis was the only major source of velocity information for this data, depth migration was not attempted.

Many algorithms exist for performing time migration. Common migration algorithms include phase shift, Stolt Frequency-Wavenumber (FK), Kirchoff, fast explicit finite difference (FD), and steep dip explicit FD. Important factors in selecting the optimal migration technique include the required computational time (which can differ by factors of more than 20), the accuracy of velocity structure, and expected dip angles (steepness). Detailed descriptions of the technical differences between algorithms are not included here (see Yilmaz [2001] for detailed analysis), however, test panels of a section of the stacked data illustrate the different results obtained via different migration algorithms A.11.

Comparable results were produced by the FK, phase-shift, and reverse-time migration techniques. Whereas Kirchoff and steep-dip algorithms reduced the amplitude of important reflectors significantly. The three former methods collapse diffractions and improve dipping reflector resolution between the sea-floor and the first water-bottom multiple. The phase-shift algorithm provides optimal imaging enhancement.

Below the first water-bottom multiple the improvements introduced by migration relative to the control panel are negligible, this is due to inaccuracies in the velocity function below the very strong water-bottom multiple. The deep reflector between 10-12 sec is over-migrated by each algorithm, indicating that the velocity used for migration at this depth is too high. Phase-shift migration was re-applied with a velocity scaling factor of 80%, Figure A.12. The resulting migration does not over-migrate the deep reflector. Final migration was conducted using the phase-shift algorithm with and without velocity scaling.

A.1.5 Trace mixing and Display

Trace mixing is a technique commonly applied to amplify coherent events in seismic data and improve the signal to noise ratio. It is effective as from trace to trace coherent reflections should interfere more constructively than incoherent noise. Mixing large number of traces causes lateral smearing and provides the practical limitation for the enhancement possible from this technique.

The two important parameters in this processing step are the number of traces being mixed, and the weighting given to each of the mixed traces. After testing several mixing combinations, Figure **??**, a three trace mix with a 1:2:1 weighting distribution was deemed most appropriate for maximum imaging improvement. The 5 and 9 trace mixes remove signal as well as noise and smear high-amplitude, non-continuous reflectors.

A comparison of the processed and migrated stacked section, and a pre-processed only stack (after NMO at 1480 m/s) is shown in Figure A.14. Both sections have had automatic gain control (AGC) applied to optimise data imaging. AGC is applied post processing only and prior to display as it can not be removed through the application of any filter-inverse mathematical function as with other types of gain applications. The final stacked section exhibits improved signal to noise ratio and imaging of reflectors relative to the brute stack. Imaging of the sedimentary section is improved and deep reflectors become visible in the migrated section relative to the brute stack.

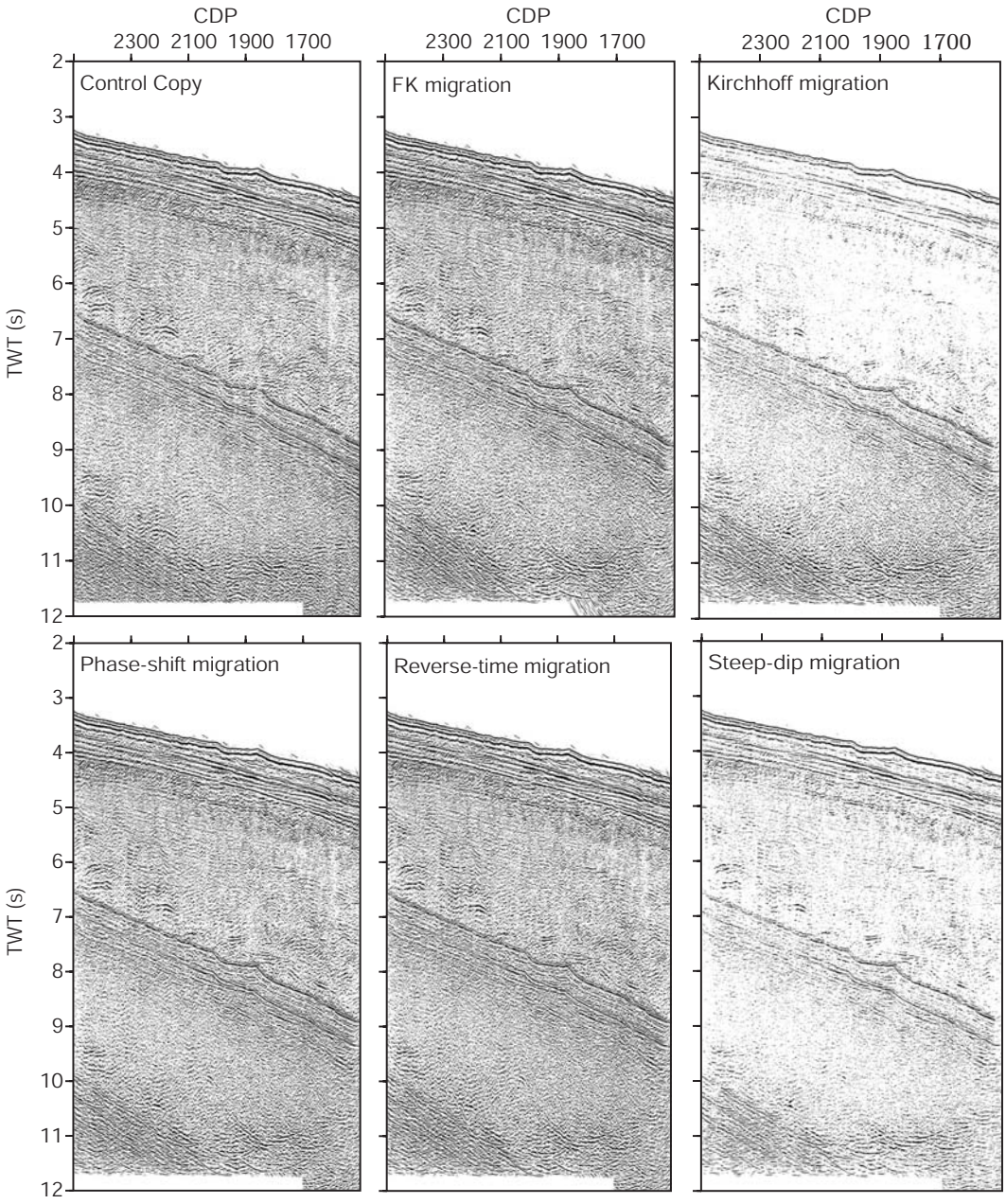

Figure A.11: Test panels of migration algorithms as labelled with no gain applied before display. Phase-shift, FK, and reverse-time migrations provide similar imaging enhancements. Deep reflectors are all overmigrated as indicated by the introduction of upward-inflected 'smiles' relative to the control panel.

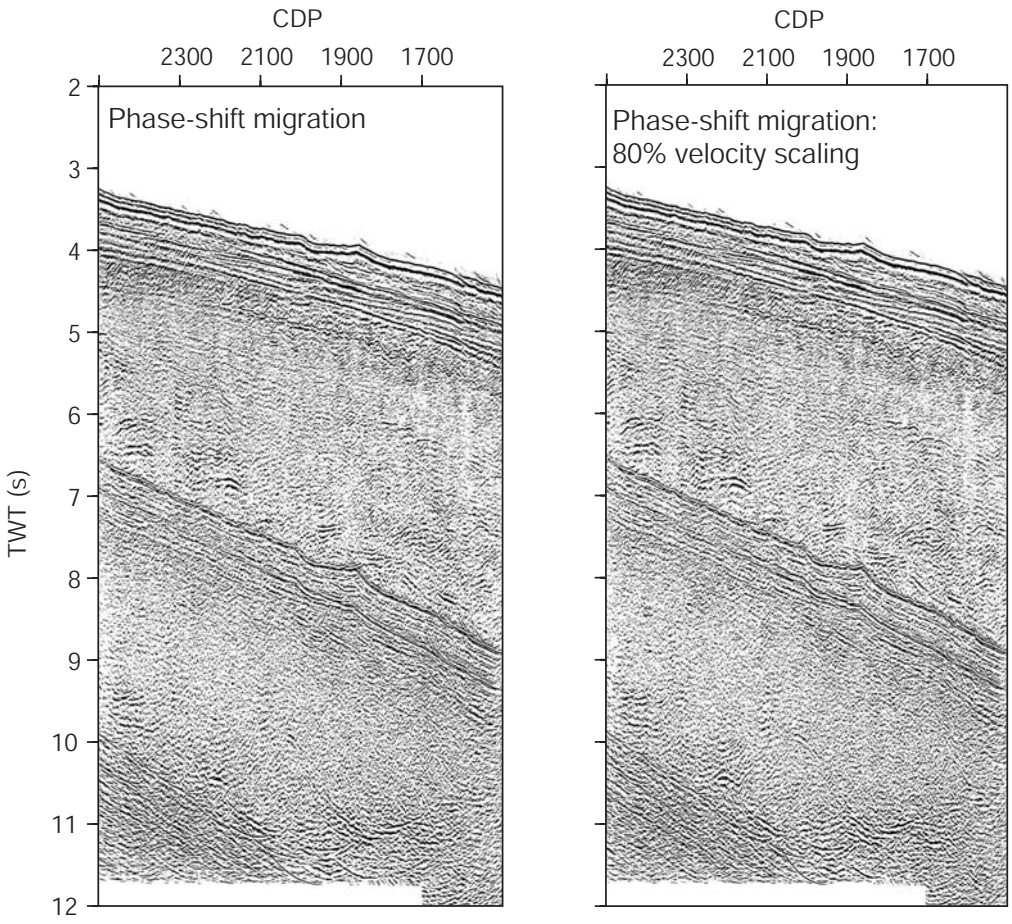

Figure A.12: Phase-shift migrated section with no and 80% velocity scaling applied as labelled. The scale-reduced velocities do not overmigrate deep reflectors between the first and second water-bottom multiples.

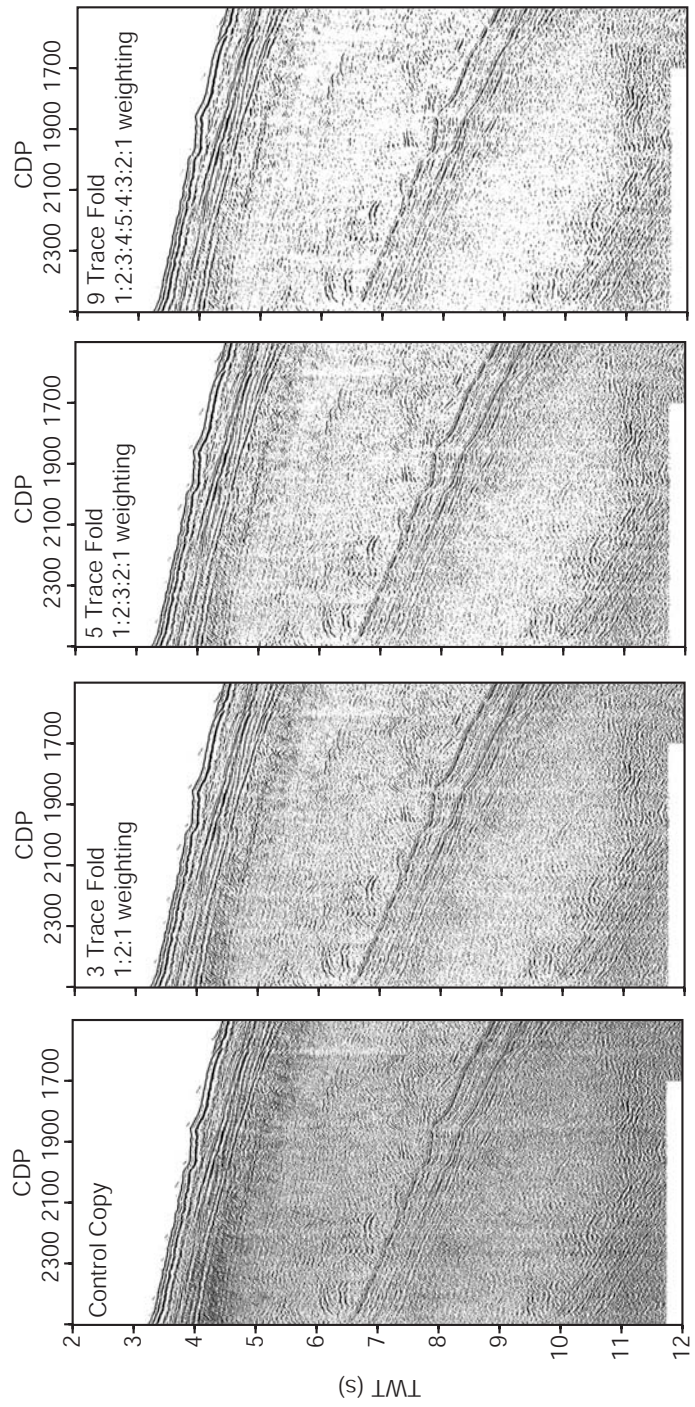

Figure A.13: Test panels for trace mixing stacked data between CMP gathers 1500-2500. 3, 5, and 9 trace mixes are tested with differing weighting distributions. The 3 trace fold with a 1:2:1 weighting provides optimal imaging enhancement.

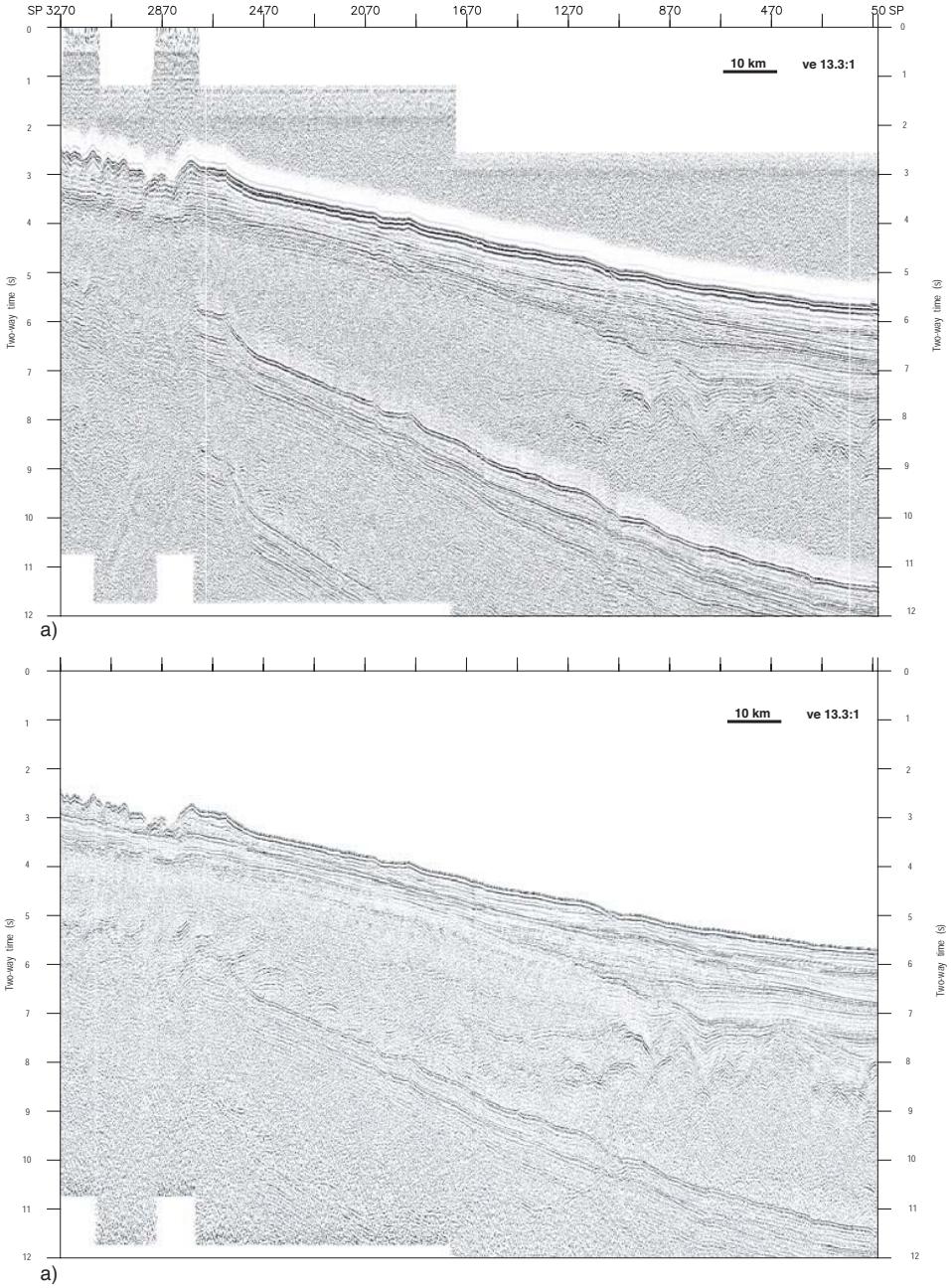

Figure A.14: Stacked sections of L184-5 data a) after basic pre-processing and NMO correction at water velocity, and b) following the processing sequence outlined herein. Definition of reflectors is greatly improved in the fully processed section and the amplitude of the water bottom multiple is massively reduced.

A.2 Multiple Suppression

Two L184 survey lines, L184-11 and L184-12, traverse the outer part of the continental shelf. Data from both these lines exhibit large amplitude water bottom multiples at similar TWT depths to primary reflectors. A number of processing steps were tested on these lines in an attempt to reduce the amplitude of the water bottom multiple relative to the primary reflectors. Strong multiples are common on the Antarctic margins, MCS data acquired over the Antarctic continental shelf at a number of locations including Prydz Bay [Stagg, 1985], the Ross Sea [Cooper *et al.*, 1987], and the Antarctic Peninsula margins [Larter *et al.*, 1990] are effected by strong water bottom multiples also.

The primary geological factors specific to the Antarctic Margins that cause exceptionally strong water bottom multiples are, after Larter *et al.* [1990]:
i) The overdeepened continental shelf, a result of isostatic loading by the proximal Antarctic ice sheet , and ii) Overcompacted sediments on the shelf, a result of loading by grounded ice sheets during periods of glacial maxima and ice sheet migration across the shelf.
The geophysical consequences of these factors are water bottom multiples of longer wavelengths (relative to shallower continental shelves at lower altitudes) and greater amplitude water bottom reflections (and hence multiples also) due to the increased acoustic impedance difference between the water and shallow sediments due to their ice load increased compaction.

Traditional methods of decreasing the amplitude of the water bottom multiple on continental shelves include deconvolution (pre- and post-stack) and CMP stacking. Long predictive deconvolution operators applied pre-stack have little effect except for near channel traces as the multiple is not truly periodic at larger offsets. The stacking process utilising primary velocities distorts the phase of the water bottom multiple and ensures that post-stack deconvolution fails to remove large amounts multiple energy. CMP stacking is typically the most powerful method of removing significant amounts of multiple energy, however, this too fails to remove much of the multiple energy on Antarctic margins [Larter *et al.*, 1990].

A number of multiple suppression techniques were applied to the MCS data from lines L184-11 and L184-12 to investigate possible imaging benefits. These lines had the standard processing sequence outlined above applied, in addition, techniques such as wave equation multiple rejection (WEMR), frequency-wavenumber domain (f-k) filtering, Radon filtering, and near trace mutes (NTM) were tested.

Wave Equation Multiple Rejection

Wave Equation Multiple Rejection (WEMR) is designed specifically to attenuate water bottom multiples in marine data. The process uses water depths and f-k extrapolation to model water bottom multiples which can then be subtracted from the original data [ProMAX, 1998a]. This process must be applied prior to TAR as the data can not have had any amplitude altering steps previously applied.

The WEMR algorithm requires water depth information in the trace headers and an accurately picked top mute just above the seafloor. As water depth values were not included in the

trace headers of this dataset they were picked off a near trace stacked section, with normal moveout (NMO) correction applied at water velocity. Water depth values were then projected from the picked horizon file into the trace header, with the application of the appropriate conversion from TWT to depth in metres.

A comparison of a section of stacked data with and without the application of WEMR, Figure A.15, with normal moveout applied at water velocity (1480 m/sec), shows the impact of the WEMR filter. The amplitude of the primary multiple reverberation is reduced somewhat by the process, however, significant multiple energy remains. Although computationally expensive, WEMR was applied to both lines 11 and 12 as they are relatively short and the improvement, although minor, was evident.

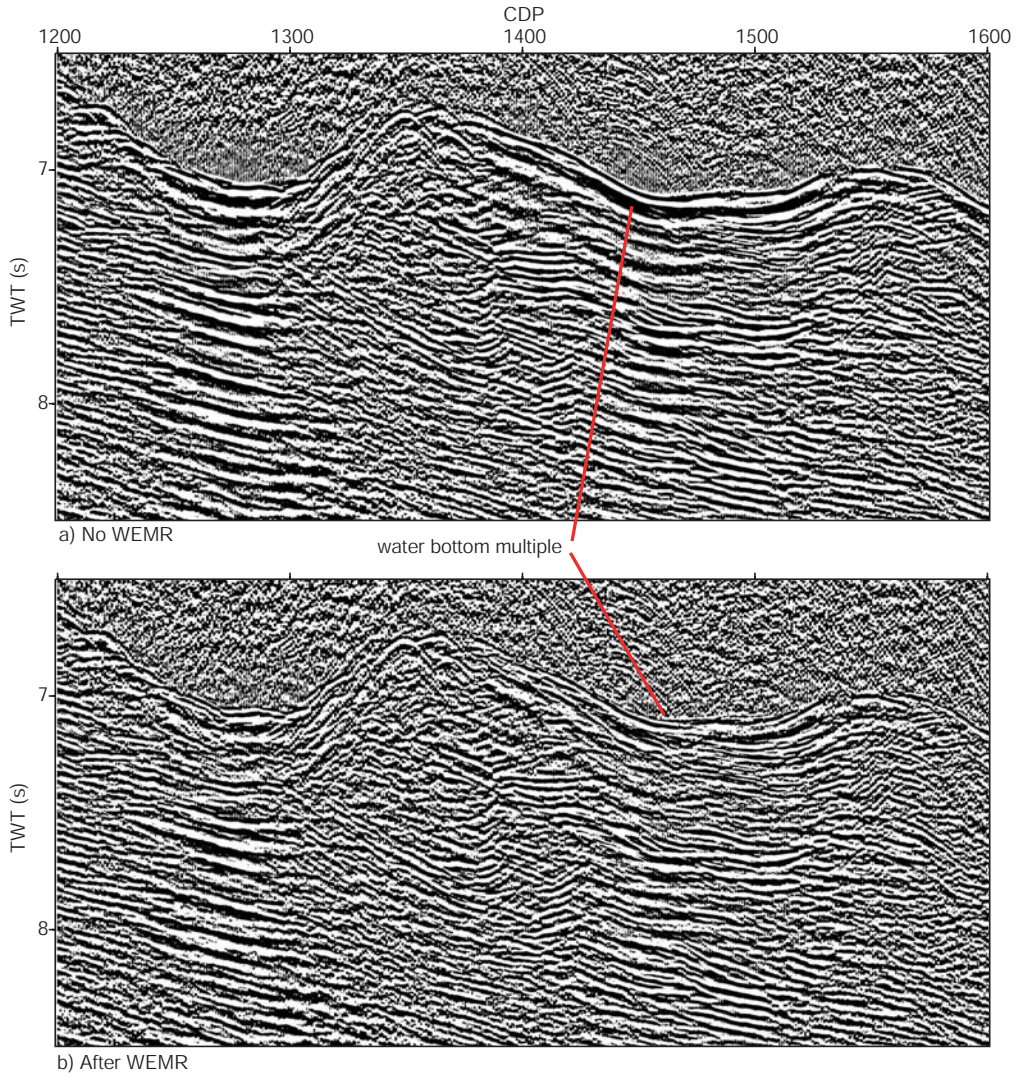

Figure A.15: Comparison of a stacked (nmo at 1480 m/sec)section of Line 12, a) with no multiple suppression, and b) following the application of wave equation multiple rejection (WEMR) filtering. The amplitude of the first water bottom multiple is reduced by the application of WEMR, although significant amounts of multiple energy remain.

F-K Filtering

Decreasing the amplitude of the water bottom multiple using f-k filtering was not possible without eliminating important primary data. Far offsets could be filtered with some success, however, the relative benefit of this is much less than that gained by stacking far offsets. The non-zero dip of much of the sedimentary section on the outer-shelf and upper-rise also create difficulties in attempting to apply f-k filtering, because the NMO correction will cause dipping primary events to appear as multiple data when mapped into f-k space. After extensive testing it was evident that f-k filtering was not an appropriate method of multiple suppression for this data set.

Radon Filtering

Radon analysis involves transforming seismic data from time-distance (t-x) space into time-moveout (t-mo) space. Following NMO correction with a primary velocity field all primary reflectors exhibit zero moveout (ideally), that is they are entirely flat in t-x space, however, multiples still exhibit moveout and resemble parabolas in t-x space. Radon analysis models an input gather using the Radon transform, and maps events of an image or data set with different characteristics (in this case curvatures) into different locations of a new space, the Radon model [ProMAX, 1998a]. Accordingly as primaries exhibit zero moveout and multiples exhibit non-zero moveout they are separated in t-mo space. When the modelled data is displayed in t-mo space multiples and primaries plot as points rather than lines, Figure A.16.

Data points occur in the t-mo space at equal times to coherent reflectors in t-x space. Water bottom multiples plot at predictable times after the primary water bottom reflection, and at positive moveouts. The filter in Figure A.16 is designed to remove this multiple energy and pass the primary energy which plots close to the zero moveout axis.

It is difficult to image the minor improvement produced by Radon filtering the data from these two lines in the t-x domain. However, a small reduction in the amplitude of multiples was evident, particularly on the southern end of Line L184-11 on the continental shelf. Accordingly, both lines were Radon filtered prior to CMP stacking.

Near Trace Mute

Far offset multiple energy is far more effectively suppressed by the stacking process and filter application than near offset multiple energy. At near offsets multiple energy is far more difficult to remove as the moveout of the multiple reflections, relative to primary reflectors, is much smaller. A near trace mute can help eliminate remaining multiple energy at near offsets. A surgical mute with an upper surface just above the arrival of the first water bottom multiple is generally most appropriate. For near trace muting to improve imaging, the acoustic source utilised during surveying must have been sufficient to produce coherent, reflectors at far offsets.

Obviously a near trace mute can not distinguish between primary and multiple energy, hence, primary and multiple energy alike are muted. A near trace mute was not necessary for Line L184-12 as the multiple energy was efficiently removed by the previous processing steps and by stacking. However, as Line L184-11 still contained significant multiple energy a near trace

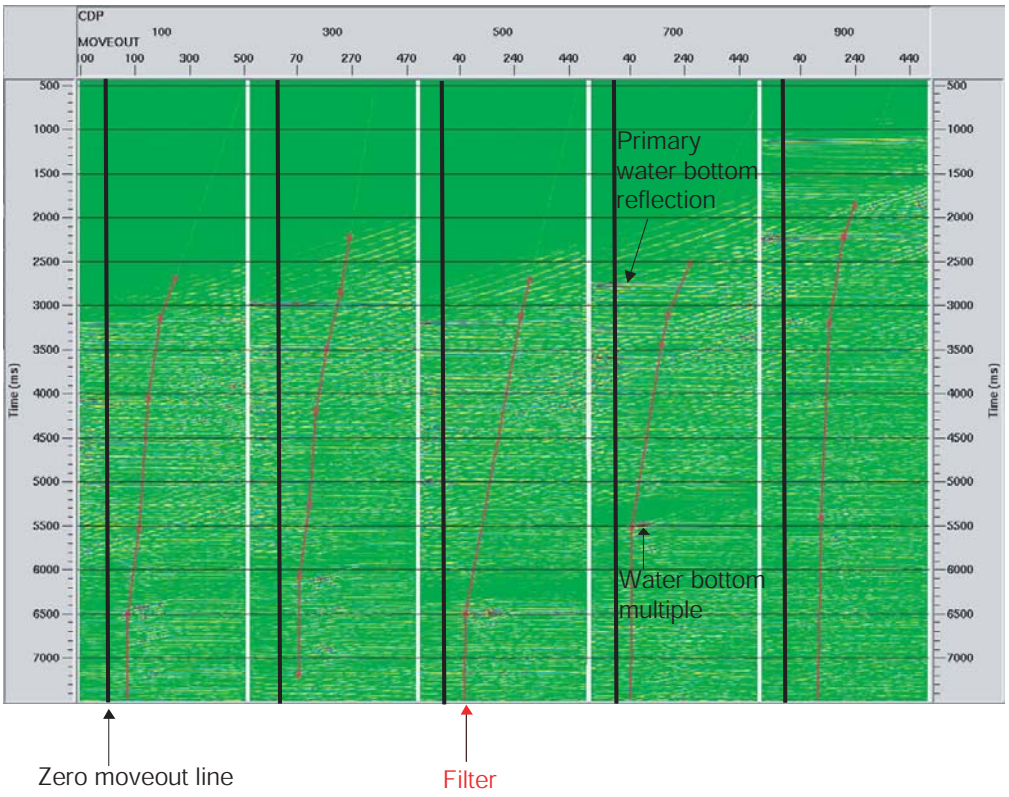

Figure A.16: Five NMO corrected CMP gathers in time-moveout (t-mo) space. Non-zero data in t-mo space corresponds to parabolic/curved events in t-x space, that is multiples. The filter mutes information to the positive direction (right) of the red line.

mute was tested on CMP gathers prior to stack. Significant amounts of multiple energy can be removed, however, the amplitude of important primary reflectors are also significantly reduced by the muting process, particularly in the shallow waters of the continental shelf. The overall signal-to-noise ratio was worsened by the application of the near trace mute, accordingly it was not applied before the final stack.